ABSTRACT

GONG, BO. Atomic Layer Deposition and Molecular Layer Deposition on Polymers. (Under the direction of Gregory N. Parsons).

Atomic layer deposition (ALD) is a vapor phase thin film deposition technique based on sequential self limiting surface reactions. In a typical ALD process, two reactants are introduced alternatively to a substrate, resulting in formation of a single atomic layer each exposure cycle. Repeating the surface-limiting reaction cycle allows ultra-uniform nanoscale films to be formed with precise thickness control over complex 3D surfaces. Similar self limiting surface reactions have been used for the deposition of polymer or organic-inorganic hybrid films. This extended ALD process is described as molecular layer deposition (MLD).

In our studies, we are exploring new chemistry and applications of ALD/MLD. Arrays of ALD/MLD processes have been conducted on various polymer substrates. By coating the substrates with different materials, we were able to give new functionalities to the polymers. For example, hydrophilic, conductive, and photocatalytic coatings have been deposited. Moreover, recent studies of ALD on polymers showed that metal organic precursors often diffuse sub-surface into the polymer. This sub-surface diffusion and reaction could result in the change of the chemical composition and the physical properties of the bulk polymer.

Surface functionalization and chemistry modification of polymers by ALD/MLD enabled a large number of new applications of polymers. In this work, several demonstration applications will be presented, and the mechanism of the ALD/MLD process on polymers will be discussed.

© Copyright 2012 by Bo Gong

All Rights Reserved

Atomic Layer Deposition and Molecular Layer Deposition on Polymers

by
Bo Gong

A dissertation submitted to the Graduate Faculty of
North Carolina State University
in partial fulfillment of the
requirements for the degree of
Doctor of Philosophy

Chemical Engineering

Raleigh, North Carolina

2012

APPROVED BY:

_____	_____
Dr. Gregory N. Parsons Committee Chair	Dr. Saad A. Khan
_____	_____
Dr. Orlin D. Velev	Dr. Michael D. Dickey

DEDICATION

To my parents, Weizhen Gong and Quanzhen Shi,

and my wife, Shu Jiang.

BIOGRAPHY

Bo Gong was born in Jiuquan, Gansu province, China on Oct 22nd, 1984. He graduated with a Bachelor of Science in Chemical Engineering from Tianjin University in July 2007. Following graduation he joined the Chemical and Biomolecular Engineering Department at North Carolina State University. He will work with Novellus Systems Inc. after graduation.

ACKNOWLEDGMENTS

I would like first to express my sincere appreciation to my advisor, Dr. Gregory N. Parsons, for the freedom and his endless support and guidance through my PhD research and studies. I also want to thank my committees, Dr. Saad A. Khan, Dr. Orlin D. Velev and Dr. Michael D. Dickey, for their inspiring discussion and comments.

I would like to thank past members of the Parsons research group, Dr. Qing Peng, Dr. Jeong-seok Na, Dr. Giovanna Scarel, Dr. Kevin Hyde, Dr. Kim Roberts, Dr. Sang-jeong Oh, Dr. Jesse S. Jur, and Dr. Joe C. Spagnola, for their mentoring and instruction. I want to give special thanks to Dr. Qing Peng. He introduced me to the ALD and helped me to get familiar with everything in the lab. I also want to thank current members of the group, Dr. Chris Oldham, Dr. Mark Losego, Christina Devine, Dohan Kim, Kyoungmi Lee, Will Sweet, Berc Kalanyan, Moataz Mousa, Sarah Atanasov, and Junjie Zhao, for their helpful discussion and collaborations.

I also want to thank staff at AIF (NCSU) and SMIF (DUKE), Chuck Mooney, Roberto Garcia, Fred Stevie, Michelle Gignac, and Mark D. Walters, for their help with some materials characterization. I am grateful to Laura Beth Dong for helping me understand the BET equipment and analysis.

Last but not the least, I must acknowledge my family. I could not finish my PhD without their unconditional love and support.

TABLE OF CONTENTS

LIST OF TABLES ..... **x**
LIST OF FIGURES ..... **xi**
CHAPTER 1. Introduction **1**
1.1 Overview of Thin Film Deposition Techniques on Polymers 1
1.1.1 Sol-gel 2
1.1.2 Hydrothermal 3
1.1.3 Layer by Layer 4
1.1.4 Electroless Plating 5
1.1.5 Spraying 5
1.1.6 Dip Coating 5
1.1.7 Physical Vapor Deposition 6
1.1.8 Chemical Vapor Deposition 6
1.2 Atomic Layer Deposition and Molecular Layer Deposition 7
1.2.1 Atomic Layer Deposition 7
1.2.2 Molecular Layer Deposition 8
1.3 Atomic Layer Deposition on Polymers and Sequential Vapor Infiltration 9
1.3.1 ALD Growth on Polymer Substrates 9
1.3.2 Sequential Vapor Infiltration 10
1.4 Integration of Atomic Layer Deposition and Liquid Phase Deposition Techniques 13
1.4.1 ZnO ALD and Hydrothermal Growth of ZnO Nanorods 13
1.4.2 Al_2O_3 ALD and Layer by Layer Growth of Metal Organic Frameworks 14
1.5 Opportunities of Atomic Layer Deposition and Related Processes. 15
References 22
CHAPTER 2. Experimental Tools **34**
2.1 Atomic Layer Deposition and Molecular Layer Deposition Systems 34
2.2 Spin-coating and Electro-spinning of Polymers 35
2.2.1 Spin-coating of Polymer Films 35
2.2.2 Electro-spinning of Polymer Fibers 36
2.3 Liquid Phase Deposition Techniques 36
2.3.1 Hydrothermal 36

2.3.2 Layer by Layer MOF Assembly 37
2.4 Materials Characterization 37
2.4.1 Ellipsometry 37
2.4.2 Quartz Crystal Microbalance 38
2.4.3 Vibration Spectroscopy (FTIR, UV-Vis) 38
2.4.4 Electron Microscopes (SEM, TEM) 41
2.4.5 Atomic Force Microscope 42
2.4.6 Nitrogen Adsorption/ Desorption Analysis (BET) 42
2.4.7 Water Contact Angle 43
2.4.8 X-ray Photoelectron Spectroscopy (XPS) 44
2.4.9 X-ray Diffraction (XRD) 44
2.4.10 Mechanical Tensile Test 44
2.4.11 Thermal Gravity Analysis (TGA) and Differential Scanning Calorimetry (DSC) 45
References 49
CHAPTER 3. Overview of Key Results of the Dissertation 51
3.1 Conformal Organic-Inorganic Hybrid Network Polymer Thin Films by Molecular Layer Deposition using Trimethylaluminum and Glycidol 51
3.2 A Two-Step Lewis Acid-Catalyzed ε-Caprolactone Ring-Opening Molecular Layer Deposition Process for Hybrid Organic-Aluminum Oxide Polymer Thin Films 52
3.3 Highly Active Photocatalytic ZnO Nanocrystalline Rods Supported on Polymer Fiber Mats: Synthesis Using ZnO Atomic Layer Deposition and Hydrothermal Crystal Growth 53
3.4 Layer by Layer Growth of HKUST-1 on Nonwoven Polypropylene Fiber Mat 54
3.5 Atomic Layer Deposition of Aluminum Oxide on Metal Organic Framework $Cu_3(BTC)_2$ 56
3.6 Quantitative Analysis of Reaction of Trimethyl-aluminum towards Polymer Substrates during Al_2O_3 Atomic Layer Deposition by In-situ FTIR 57
3.7 Sequential Vapor Infiltration of Metal Oxides into Sacrificial Polyester Fibers: Shape Replication and Controlled Porosity of Micro/Mesoporous Oxide Monoliths 59
3.8 Hydrophilic Mechanical Buffer Layers and Stable Hydrophilic Finishes on Polydimethylsiloxane using Combined Sequential Vapor Infiltration and Atomic/Molecular Layer Deposition 61
3.9 Directed Mesoporous Metal Oxides by Vapor Phase Atomic Layer Deposition and Infiltration of Ordered Surfactant Thin Films 63

3.10 Core Sheath Nanocomposite Structures Enabled by Aluminum Oxide Atomic Layer Deposition on Bicomponent Polymer Fibers 64

CHAPTER 4. Conformal Organic-Inorganic Hybrid Network Polymer Thin Films by Molecular Layer Deposition using Trimethylaluminum and Glycidol 82

Abstract 83

4.1. Introduction 84

4.2. Experimental Section 87

4.3. Results and Discussion 90

4.4. Summary and Conclusions 99

Acknowledgments 99

References 114

CHAPTER 5. A Two-Step Lewis Acid-Catalyzed ε-Caprolactone Ring-Opening Molecular Layer Deposition Process for Hybrid Organic-Aluminum Oxide Polymer Thin Films 119

Abstract 120

5.1. Introduction 121

5.2. Experimental Details 123

5.3. Experimental Results 126

5.4. Conclusions 131

Acknowledgments 132

References 144

CHAPTER 6. Highly Active Photocatalytic ZnO Nanocrystalline Rods Supported on Polymer Fiber Mats: Synthesis Using ZnO Atomic Layer Deposition and Hydrothermal Crystal Growth 149

Abstract 150

6.1. Introduction 151

6.2. Experimental Procedures 153

6.3. Results and Discussion 156

6.4. Summary and Conclusions 161

Acknowledgements 161

References 168

CHAPTER 7. Layer by Layer Growth of HKUST-1 on Nonwoven Polypropylene Fiber Mat 173

Abstract 174

7.1. Introduction 175
7.2. Experimental 176
7.3. Experimental Results 179
7.4. Conclusions 183
Acknowlegment 183
References 189
CHAPTER 8. Atomic Layer Deposition of Aluminum Oxide on Metal Organic Framework $Cu_3(BTC)_2$ 195
Abstract 196
8.1. Introduction 197
8.2. Experimental 198
8.3. Results and Discussion 201
8.4. Conclusion 204
References 212
CHAPTER 9. Quantitative Analysis of Reaction of Trimethyl-aluminum towards Polymer Substrates during Al_2O_3 Atomic Layer Deposition by In-situ FTIR 216
Abstract 217
9.1. Introduction 218
9.2. Experimental Section 220
9.3. Experimental Results 224
9.4. Discussion 234
9.5. Summary 239
Acknowledgements 240
References 259
CHAPTER 10. Sequential Vapor Infiltration of Metal Oxides into Sacrificial Polyester Fibers: Shape Replication and Controlled Porosity of Micro/Mesoporous Oxide Monoliths 265
Abstract 266
10.1. Introduction 267
10.2. Experimental Procedures 269
10.3. Results and Discussion 274
10.4. Conclusions 282
Acknowledgments 283

References 295
CHAPTER 11. Hydrophilic Mechanical Buffer Layers and Stable Hydrophilic Finishes on Polydimethylsiloxane using Combined Sequential Vapor Infiltration and Atomic/Molecular Layer Deposition 301
Abstract 302
11.1. Introduction 303
11.2. Experimental Methods 305
11.3. Results and Discussion 307
11.4. Summary and Conclusions 312
Acknowledgements 313
References 319
CHAPTER 12. Directed Mesoporous Metal Oxides by Vapor Phase Atomic Layer Deposition and Infiltration of Ordered Surfactant Thin Films 322
Abstract 323
12.1. Introduction 324
12.2. Experimental Methods 326
12.3. Results and Discussion 329
12.4. Summary and Conclusions 334
References 344
CHAPTER 13. Core Sheath Nanocomposite Structures Enabled by Aluminum Oxide Atomic Layer Deposition on Bicomponent Polymer Fibers 349
Abstract 350
13.1. Introduction 351
13.2. Experimental Section 352
13.3. Experimental Results and Discussion: 356
13.4. Conclusion 359
Acknowledgments 359
References 366

LIST OF TABLES

Table 3.1. Summary of polymer substrates studied, characteristic functional groups, and reactivity toward TMA/water ALD process. For each polymer, the TMA exposure was approximately 60seconds at 2 Torr. 75
Table 7.1. Summary of mass increase from MOF coating and the measured BET surface area. 187
Table 9.1. Summary of polymer substrates studied, characteristic functional groups, and reactivity toward TMA/water ALD process. For each polymer, the TMA exposure was approximately 60seconds at 2 Torr. 258
Table 10.1. Summary of porous metal oxide samples prepared by vapor phase infiltration. BET surface area, total pore volume and mode pore width of TMA/water and $TiCl_4$/water soaked polyester fibers are listed. 288
Table 12.1. Summary of porous metal oxide samples prepared by vapor phase infiltration and atomic layer deposition on surfactants after post annealing at 450 °C for 12hr. BET surface area, total pore volume and mode pore width are listed. 342

LIST OF FIGURES

Figure 1.1. A overview of the sol gel process. In sol gel chemistry, molecular precursors are converted to nanoparticles to form a colloidal suspension, or sol. The gel network can be produced by further condensation. The gel can be processed by various drying methods to develop materials with distinct properties. (https://www.llnl.gov/str/May05/Satcher.html).. 18
Figure 1.2. The layer by layer (LBL) process and the structure of LBL films. 1) solution of positive polyelectrolyte, 2) pure deionized water, 3) solution of negative polyelectrolyte, 4) pure deionized water. 19
Figure 1.3. A schematic diagram of atomic layer deposition (ALD) of Al_2O_3. Trimethyl aluminum (TMA) and water are used as precursors to react with surface alternatively. 20
Figure 1.4. A schematic diagram for molecular layer deposition (MLD). (A) Organic precursor A reacts with surface functional groups. (B) Organic precursor B reacts with precursor A saturated surface..... 21
Figure 2.1. A schematic view of the viscous flow ALD/MLD reactor. The precursors are delivered into the reactor with Ar carrier gas. On the reactor exhaust line, computer controlled gate values are used to direct the exhaust from the EG pulse into a liquid nitrogen trap before entering the pump. 46
Figure 2.2. Schematic diagram of In-situ FTIR ALD/MLD reactor. The precursors are delivered into the reactor with high purity Ar. In the middle part of the chamber, two CsI IR windows are attached, and two gate valves are installed between the IR window and reactor chamber to prevent the deposition of ALD/MLD film on the windows. During the measurement, the IR beam is directed through the planar sample and focused into a MCT-A detector. Before each dose, a background spectrum was collected as reference, and differential spectra were employed to show the surface chemistry change after each pulse.. 47
Figure 2.3. (a) An example nitrogen adsorption/ desorption isotherm collected by Autosorb-1C at 77K. **(b)** BET plot calculated from the adsorption isotherm.($0.05<P/P_0<0.35$) The BET surface area can be calculated from the intercept and the slope of the plot..... 48
Figure 3.1. Schematic of the surface reactions during TMA/GLY MLD process consistent with the FTIR data in Figure 4.6(a). Exposing the –OH surface to TMA produced surface Al-CH_3. The following glycidol exposure consumes Al-CH_3 surface units, including reactions with both the OH and epoxy end of the molecule. The aluminum can help catalyze the ring opening. Available OH groups are then available to react with TMA during the next exposure step. Not shown in this diagram is the expected sub-surface diffusion of TMA and reaction with available lone pair sites producing Lewis acid/base O**:** $Al(CH_3)_3$ adducts that can react during the next glycidol exposure step. 66
Figure 3.2. Direct comparison between in-situ QCM data collected during TMA/GLY, TMA/water/GLY and DEZ/GLY sequences following TMA/water (or DEZ/water) ALD. TMA (DEZ)/Ar/GLY/Ar = 1/40/2/40 s is used for TMA/GLY and DEZ/GLY, and TMA/Ar/Water/Ar/GLY/Ar = 1/40/1/40/2/40 s is used for TMA/Water/GLY. The TMA/GLY produced an induction period followed by a large mass uptake. The TMA/water/GLY sequence showed a much lower mass uptake per cycle, without an induction period.

Negligible mass uptake is observed for the DEZ/GLY sequence, demonstrating the importance of the Al-CH_3 as a growth catalyst. 67
Figure 3.3. Film thickness for TMA/LAC MLD films on silicon wafers is plotted versus number of MLD cycles at various growth temperatures. Film thickness was determined using ellipsometry. For all the samples on Si wafer the deposition sequence was TMA/Ar/LAC/Ar = 1/40/2/40 seconds. The growth rate decreased from 0.75 Å /cycle to 0.08Å/cycle as the substrate temperature increased from 60 to 120°C. 68
Figure 3.4. Scanning electron micrographs obtained from: (a) and (b), untreated PBT fibers after hydrothermal ZnO nanorod crystal growth; (c) and (d), PBT fibers after 100 ALD cycles of ZnO (~20 nm thick), followed by hydrothermal ZnO nanorod growth. Nanorod crystals are visible primarily on the top-most fibers in the fiber mat. Panels (e) and (f) show PBT fibers after 200 cycles (~40 nm) of ALD ZnO, followed by ZnO nanorod growth. Nanorod growth is visible on all the fibers. In panel (b) a circle highlights a large crystal, similar in size to the one shown in Figure 2(b), formed on the untreated fiber. 69
Figure 3.5. Normalized absorbance of organic dye at 525 nm plotted versus UV radiation exposure time. PBT fiber substrates with various surface treatments were immersed in the aqueous solution containing the azo dye (acid red 40), and illuminated using a UV lamp. The fibers with ALD ZnO and ZnO nanorod crystals produced the most rapid photocatalytic dye degradation. The inset shows a photograph of the dye solutions in contact with the different substrates after 2 hr of illumination. The red dye is nearly completely removed from the solution in contact with the nanorod-coated fibers. 70
Figure 3.6. Optical images of HKUST-1 coated PP fiber mat. (a) The fiber mat on the left is the direct LBL growth of MOF on PP fiber mat. The mat on the right is the PP fiber mat pretreated with ALO, then coated with MOF by LBL technique. (b) MOF coated PP fiber mat before vacuum dry. (c) MOF coated PP fiber mat after vacuum dry. 71
Figure 3.7. The Fourier transform infrared (FTIR) spectra collected from the HKUST-1 films on Al_2O_3 coated Si wafers. Slow growth was detected for the first 2 deposition cycles. Then the linear increase of IR absorbance vs. LBL deposition cycles was observed. 72
Figure 3.8. In-situ QCM data collected from water/N_2 process on bare QCM and $Cu_3(BTC)_2$ particle coated QCM. Bare QCM crystal showed negligible mass uptake during water exposures, while the $Cu_3(BTC)_2$ coated QCM crystal showed very large mass uptake and decreasing. The MOF with 5 cycles of TMA/water ALD process showed smaller mass uptake during water exposure, and this could be explained by the shrinking of pore volume and size after ALD. 73
Figure 3.9. The Al-CH_3 deformation (~1200 cm^{-1}) and CH_3 asymmetric stretching (~2960 cm^{-1}) absorbance increase after first TMA pulse on different polymer substrate. The magnitude of the $\nu_a(CH_3)$ and $\delta_a(CH_3)$ intensity also displays the relative extent of reaction between the various polymers and TMA. 74
Figure 3.10. Panel (a) presents a picture of polybutylene terephthalate (PBT) nonwoven fiber mats: (left) as received; (middle) after TMA/water infiltration; and (right) after infiltration and anneal at 450°C. The starting size for all samples was approximately the same. After infiltration, the fiber mat becomes yellow in color, shrinks in size and becomes mechanically stiffer. Annealing causes more shrinkage, and the sample becomes more brittle, consistent

with transformation of the polymer to micron-sized alumina fibers. Panel (b) shows a scanning electron microscope image of the as-received PBT nonwoven. Panels (c) and (d) show a similar sample after 1 h TMA/water soaking and 12 h 450°C anneal. The images in (c) and (d) show that the soaking and annealing preserves the starting fiber morphology. Some connectivity between the fibers likely results from polymer flow during the soaking process. More connectivity was observed with higher process temperature and longer precursor exposure. The cross-sectional view in panel (d) confirms that the fibers are uniform after calcination, indicating full penetration of the precursor throughout the 3 μm diameter starting fiber. 76
Figure 3.11. FTIR transmission spectra collected in situ from the a starting PBT film cast onto a silicon substrate (bottom trace) and after exposing the film to TMA (middle) and water (upper trace) at 80°C. The TMA exposure removes ester (1720 and 1270cm^{-1}) and ether (1100 cm^{-1}) bonding units indicating high reactivity between TMA and ester bonds in the PBT. The CH_3 (2860 and 2930 cm^{-1}) and Al-CH_3 modes (1200 cm^{-1}) increase upon TMA treatment, confirming Al-CH_3 present in the soaked PBT film. After water dosing, the decrease in CH_3 and Al-CH_3 absorbance and an increase in Al-O modes shows water reacting with the Al-CH_3 groups to form Al-OH. 77
Figure 3.12. Stress strain curve of TMA/water and DEZ/water soaked PDMS and pristine PDMS. The slope of the stress strain curve is the measure of the Young's modules, we can see after soak with metal organic precursor, the modules of PDMS is significant increased. This increase of young's modulus will form a mechanical buffer layer between ALD coating and bulk PDMS, which will stabilize the ALD coating and keep the ALD layer intact. 78
Figure 3.13. Schematic diagram of surface treatment of PDMS with ALD only or sequential vapor infiltration followed by ALD. The top scenario shows direct aluminum oxide ALD on PDMS resulting in cracked aluminum oxide coating. The bottom scenario shows ALD after sequential vapor infiltration, producing a smooth and uniform coating on the PDMS. The sequential vapor infiltration before the ALD helps maintain the surface in a hydrophilic state. 79
Figure 3.14. Schematic diagram for the preparation of mesoporous metal oxide materials from vapor phase infiltration method. 80
Figure 3.15. Schematic diagram of the "short" and "long" TMA/water ALD cycles on PLA/PP core/sheath bi-component fibers. When the core/sheath fiber was exposed to "short" TMA/water exposures, precursor vapors were not given enough time to diffuse into the PP layer. Minimal subsurface diffusion and reaction occurred, and thin Al2O3 ALD layer was deposited on PP surface. However, when the "long" precursor exposures were used, TMA and water vapors could diffuse through the PP, and react with PLA core. 81
Figure 4.1. Schematic diagram of the in-situ FTIR ALD/MLD reactor. The precursors are delivered into the reactor with high purity Ar. In the middle part of the chamber, two CsI IR windows are attached, and two gate valves are installed between the IR window and reactor chamber to prevent the deposition of ALD/MLD film on the windows. During the measurement, the IR beam is directed through the planar sample and focused into a MCT-A detector. Before each dose, a background spectrum was collected as reference, and differential spectra were employed to show the surface chemistry change after each pulse.101

Figure 4.2. (a) Film thickness for TMA/GLY MLD films on silicon wafers is plotted versus number of MLD cycles at various growth temperatures. Film thickness was determined using ellipsometry. For all the samples on Si wafer the deposition sequence was TMA/Ar/GLY/Ar = 1/40/2/40 seconds. The growth rate decreased from 2.4 nm/cycle to 0.6 nm/cycle as the substrate temperature increased from 90 to 150 °C. (b) More careful examination shows the growth rate of the MLD film on silicon starts off slowly and increases over the first 100 cycles at 120 °C, before reaching steady state. The reflective index decreased with growth time, consistent with a less dense film structure and overall change in the growth reaction mechanism as deposition proceeds. 102
Figure 4.3. In-situ QCM mass uptake results for TMA/water ALD and TMA/GLY MLD sequences. Gas pulse and purge times were 1/40/2/40 seconds. (a) TMA/water ALD at 120 °C under steady-state growth, shows an average mass uptake during the TMA and water pulses of ~80 ng/cm^2 and ~12 ng/cm^2 respectively; (b) TMA/GLY MLD at 120 °C under steady-state growth shows a larger average mass uptake of ~210 ng/cm^2 and ~118 ng/cm^2 during the TMA and GLY pulses, respectively; (c) 100 cycles of TMA/GLY MLD at 90 to 150 °C on an Al-OH surface (formed using TMA/water ALD) shows an increase in deposition rate at lower temperatures, and a growth incubation time. (d) Mass uptake per step for 100 cycles of TMA/GLY MLD at 120 °C on Al-OH surface. Approximately 60 cycles was needed for the TMA/GLY MLD process to reach steady growth, which is consistent with growth rate data collected from film on Si wafers. The small mass uptake of TMA and GLY at the very beginning implied the "double" reaction is happening on the surface. 103
Figure 4.4. In-situ QCM data for TMA and glycidol dose saturation during the TMA/GLY MLD process at 120 °C. **(a)** After multiple repeated cycles of TMA/GLY, the surface was repeatedly exposed to TMA/Ar pulses (TMA/Ar = 1/82 s). More than 16 pulses were needed to saturate the surface. **(b)** Similar experiments for glycidol dose saturation on TMA saturated surface (GLY/Ar = 2/81 s). Both reagents showed high mass uptake for the first pulse. The data shows that after many growth cycles, both the TMA and GLY reagents diffuse subsurface and react during film growth. The subsurface diffusion is more prevalent in thicker films than in thinner films, but it becomes kinetically limited as film thickness increases. 104
Figure 4.5. Direct comparison between in-situ QCM data collected during TMA/GLY, TMA/water/GLY and DEZ/GLY sequences following TMA/water (or DEZ/water) ALD. TMA (DEZ)/Ar/GLY/Ar = 1/40/2/40 s is used for TMA/GLY and DEZ/GLY, and TMA/Ar/Water/Ar/GLY/Ar = 1/40/1/40/2/40 s is used for TMA/Water/GLY. The TMA/GLY produced an induction period followed by a large mass uptake. The TMA/water/GLY sequence showed a much lower mass uptake per cycle, without an induction period. Negligible mass uptake is observed for the DEZ/GLY sequence, demonstrating the importance of the Al-CH_3 as a growth catalyst. 105
Figure 4.6. In-situ differential FTIR spectra collected during **(a)** the first TMA/GLY sequence on an Al-OH surface; and **(b)** the TMA/water/GLY sequence. In panel **(a)** the differential spectrum collected after the TMA dose (labeled TMA-water) shows Al-CH_3 modes on the surface, indicated by the Al-CH_3 deformation absorbance at 1200 cm^{-1}. Upon glycidol exposure (GLY-TMA) the CH_3 is removed from the surface by reaction with the OH

or epoxy groups on GLY. The increase of CH_2 modes at 2865 and 2928 cm^{-1} confirms the attachment of GLY on the surface. In panel **(b)** the GLY dose after the water exposure produced an obvious decrease of surface -OH peak at 3700 cm^{-1} and increase of CH_2 modes at 2865 and 2928 cm^{-1}. The decrease of –OH indicates a reaction between the -OH on GLY and the Al-OH surface. (Fringes on the spectra is due to the interference from the AAO membrane). 106
Figure 4.7. Schematic of the surface reactions during TMA/GLY MLD process consistent with the FTIR data in Figure 4.6(a). Exposing the –OH surface to TMA produced surface Al-CH_3. The following glycidol exposure consumes Al-CH_3 surface units, including reactions with both the OH and epoxy end of the molecule. The aluminum can help catalyze the ring opening. Available OH groups are then available to react with TMA during the next exposure step. Not shown in this diagram is the expected sub-surface diffusion of TMA and reaction with available lone pair sites producing Lewis acid/base O**:** $Al(CH_3)_3$ adducts that can react during the next glycidol exposure step. By placing a water exposure step after the TMA exposure, the subsurface Al-CH_3 groups become "quenched" and result in more steady growth at a reduced growth rate, as shown in the QCM data in Figure 4.5. 107
Figure 4.8. **(a)** Ex-situ FTIR spectra collected from MLD films after deposition on Si wafers. The process sequence was TMA/Ar/GLY/Ar = 1/40/2/40 seconds at 120 °C. Spectra show modes associated with -CH_2- asymmetric and symmetric stretching at 2928 cm^{-1} and 2865 cm^{-1}, C-O at 1100 cm^{-1} and Al-O stretching near 700 cm^{-1} consistent with the polymer composition: (-Al-O-(C_4H_8)-O-)$_n$. Mode intensity increased with the number of deposition cycles. **(b)** The intensity of the CH_2 asymmetric stretching mode at 2928 cm^{-1} is plotted versus number of MLD cycles. This peak was selected as a characteristic absorbance for MLD film, and the intensity of this peak is increased with the number of MLD cycles. The absorbance increased more slowly during the first 50 cycles, which is consistent with increasing growth rate as deposition proceeds..... 108
Figure 4.9. (a) XPS survey scan of the TMA/GLY MLD film on Si (200 cycles at 120 °C) displayed a relatively low Al concentration compared to C and O. **(b)** The C 1s detail scan from the same sample showed a bonding distribution consistent with the polymer structure (-Al-O-(C_4H_8)-O-), with little C=O present. 109
Figure 4.10. Atomic force micrographs of MLD films (100 cycles at 120 °C) on a Si wafer. The film showed a relative smooth surface with RMS of ~5 Å. 110
Figure 4.11. Transmission electron microscopy images of MLD coating (25 cycles at 120 °C, TMA/Ar/GLY/Ar=2/40/4/40 s) on electrospun PVA nanofibers after calcination in air at 400 °C for ~48 hours. The polymer fibers were removed upon calcination, resulting in hollow porous microtubes. The images show that the MLD network polymer reaction leads to a uniform film on the complex, high aspect-ratio nanostructured fiber matrix. The thickness of the tube wall is ~ 20 nm and is uniform from tube to tube throughout the whole sample. The scale bars are 500 and 20 nm respectively. 111
Figure 4.12. Pore size distribution determined from N_2 adsorption/desorption studies. Separate experiments analyzed: **(a)** pore size distribution in the micropore range (< 2nm) calculated by the Hovarth Kawazoe (HK) method; and **(b)** in the mesopore range (between 2 and 20) calculated by the Barrett Joyner Halenda (BJH) method. Materials were 400 cycles

of MLD coated electrospun PVA fibers after calcinations at 400 °C for 48 hours. The microtubes are predominantly microporous with an average pore size of ~5 Å, with few mesopores present. 112
Figure 4.13. The stability of hybrid materials under ambient environment and thermal annealing conditions. **(a)** Ex-situ FTIR spectra and **(b)** thickness of deposited TMA/glycidol films (100 cycles at 120 °C) on silicon, with different ambient exposure time. **c)** Ex-situ FTIR spectra and **(d)** thickness of the same TMA/GLY films on silicon annealed in air at the indicated temperature for 2 hours. The data showed the hybrid network polymer films are stable in ambient environment for more than 1 week. Thermal treatment at temperatures above 200 °C eliminates the organic components in the films. 113
Figure 5.1. Film thickness for TMA/LAC MLD films on silicon wafers is plotted versus number of MLD cycles at various growth temperatures. Film thickness was determined using ellipsometry. For all the samples on Si wafer the deposition sequence was TMA/Ar/LAC/Ar = 1/40/2/40 seconds. The growth rate decreased from 0.75 Å /cycle to 0.08Å/cycle as the substrate temperature increased from 60 to 120°C. 133
Figure 5.2. (a) Ex-situ FTIR spectra collected after deposition from MLD films on Si wafers using TMA/Ar/LAC/Ar = 1/40/2/40 seconds at 60°C. Spectra show modes associated with -CH_2- asymmetric and symmetric stretching at 2928 $cm^{-1}$and 2865cm^{-1}, C-O at 1100 cm^{-1} and Al-O stretching near 700cm^{-1} consistent with the polymer composition: (-Al-O-(C_8H_{16})-O-)$_n$. Mode intensity increased with the number of deposition cycles. (b) The intensity of the CH_2 asymmetric stretching mode at 2928 cm^{-1} is plotted versus number of MLD cycles, was selected as a characterization absorbance for MLD film, and the intensity of this peak is increased with the number of MLD cycles. 134
Figure 5.3. In-situ QCM mass uptake results for TMA/LAC MLD sequences. Gas pulse and purge times were 1/40/2/40 seconds. 100 cycles of TMA/GLY MLD at 60 to 120 °C on Al-OH surface formed using the TMA/water ALD process. 135
Figure 5.4. In-situ differential FTIR spectra collected during TMA/LAC sequence at 60°C. Differential spectra collected after LAC dose showed an increase of CH_2 modes at 2865 and 2928 cm^{-1} ,C=O mode at 1732 cm^{-1} and very little decrease of CH_3 absorbance at 2895 cm^{-1} and 2940 cm^{-1}, which indicate the selective reaction of C-O-C on LAC with Al-CH_3. 136
Figure 5.5. In-situ differential FTIR spectra collected after each TMA/LAC cycle at 60°C. Differential spectra collected after LAC dose showed an increase of CH_2 modes at 2865, 2928 and 1463 cm^{-1} ,OH mide at 3100-3600 cm^{-1}, C=O mode at 1732 cm^{-1}. Absorbance increase with deposition cycles. 137
Figure 5.6. In-situ differential FTIR spectra collected during TMA/LAC sequence at 120°C. Differential spectra collected after LAC dose showed an increase of CH_2 modes at 2865 and 2928 cm^{-1} ,C-O-C mode at 1600 cm^{-1} and very little decrease of CH_3 absorbance at 2895 cm^{-1} and 2940 cm^{-1}, which indicate the selective reaction of C=O on LAC with Al-CH_3. Or both C-O-C and C=O on LAC will react with Al-CH_3. 138
Figure 5.7. In-situ differential FTIR spectra collected after each TMA/LAC cycle at 120°C. Differential spectra collected after LAC dose showed an increase of CH_2 modes at 2865, 2928 and 1463 cm^{-1} ,OH mide at 3100-3600 cm^{-1}, C=O mode at 1732 cm^{-1}. Absorbance increase with deposition cycles. 139

Figure 5.8. Schematic of the surface reactions during TMA/LAC MLD process at 120°C. Exposing the –OH surface to TMA produced Al-CH_3 features visible in the IR in Figure 5.6. Upon exposure to LAC, the IR data showed increase of CH2 related features, O-C-O aluminum carbonate absorbance and no obvious increase of carbonyl absorbance, indicating the surface Al-CH_3 reacts with the (C=O)-O group on the LAC molecule to produce aluminum carbonate groups. During the following TMA dose, the O-C-O asymmetric stretching mode in aluminum carbonate decreased. This is imply the reaction between Al-O-C groups will TMA, and formation of Al-CH_3 terminations. 140
Figure 5.9. (a) XPS survey scan of the TMA/LAC MLD film on Si (400 cycles at 60°C). (b) The C 1s detail scan from the same sample showed a bonding distribution consistent with the polymer structure (Al-O-(C_4H_8)-), with little C=O present. 141
Figure 5.10. (a) XPS survey scan of the TMA/LAC MLD film on Si (400 cycles at 90°C). (b) The C 1s detail scan from the same sample showed a bonding distribution consistent with the polymer structure (Al-O-(C_4H_8)-), with little C=O present. 142
Figure 5.11. Atomic force micrographs of TMA/LAC MLD films (400 cycles at 120°C) on a Si wafer (1μm × 1μm). MLD film showed a larger surface roughness with RMS of ~5Å.. 143
Figure 6.1. Schematic view of the viscous flow ALD reactor used for these studies. In one ALD cycle, two co-reactants (e.g. diethyl zinc and water for ZnO formation) are introduced alternatively, with an inert gas purge step in between, allowing formation of one atomic layer of ZnO. Desired thickness could be achieved by repeating the ALD cycles. 162
Figure 6.2. Scanning electron microscopy images of silicon wafers after ZnO hydrothermal growth. Images (a) and (b) were collected from samples without an ALD ZnO nucleation layer. Alternatively, images (c) and (d) were from silicon samples that were coated with 100 cycles of ALD ZnO before hydrothermal ZnO nanorod crystal growth. 163
Figure 6.3. Scanning electron micrographs obtained from: (a) and (b), untreated PBT fibers after hydrothermal ZnO nanorod crystal growth; (c) and (d), PBT fibers after 100 ALD cycles of ZnO (~20 nm thick), followed by hydrothermal ZnO nanorod growth. Nanorod crystals are visible primarily on the top-most fibers in the fiber mat. Panels (e) and (f) show PBT fibers after 200 cycles (~40 nm) of ALD ZnO, followed by ZnO nanorod growth. Nanorod growth is visible on all the fibers. In panel (b) a circle highlights a large crystal, similar in size to the one shown in Figure 6.2(b), formed on the untreated fiber. 164
Figure 6.4. Transmission electron microscopy images obtained from ZnO nanorod crystals on PBT fibers where the polymer was removed by calcination before imaging. In image (a), the nanorods are visible protruding from the ZnO thin film layer that remains after calcination. The arrow on the left in image (a) points to a region of ALD ZnO coating without nanorod crystal growth. The image in (b) was collected from the tip of a nanocrystal rod, as indicated by the region circled in (a). The HRTEM image shows the lattice spacing is 0.32 nm, indicating wurtzite ZnO. 165
Figure 6.5. Normalized absorbance of organic dye at 525 nm plotted versus UV radiation exposure time. PBT fiber substrates with various surface treatments were immersed in the aqueous solution containing the azo dye (acid red 40), and illuminated using a UV lamp. The fibers with ALD ZnO and ZnO nanorod crystals produced the most rapid photocatalytic dye degradation. The inset shows a photograph of the dye solutions in contact with the different

substrates after 2 hr of illumination. The red dye is nearly completely removed from the solution in contact with the nanorod-coated fibers. 166
Figure 6.6. Reusability of ZnO treated PBT fiber mat for photocatalytic dye degradation. The PBT fiber mats with ZnO treatment showed repeatable photocatalytic activity. However, small decreases of efficiency were observed for both ZnO ALD coated and ZnO ALD/nanorods coated samples in three consecutive tests. 167
Figure 7.1. The Fourier transform infrared (FTIR) spectra collected from the HKUST-1 films on Al_2O_3 coated Si wafers. Slow growth was detected for the first 2 deposition cycles. Then the linear increase of IR absorbance vs. deposition cycles was observed. 184
Figure 7.2. Optical images of HKUST-1 coated PP fiber mat. (a) The fiber mat on the left is the direct LBL growth of MOF on PP fiber mat. The mat on the right is the PP fiber mat pretreated with ALO, then coated with MOF by LBL technique. (b) MOF coated PP fiber mat before vacuum dry. (c) MOF coated PP fiber mat after vacuum dry. 185
Figure 7.3. (a) The XRD patterns collected from the PP fiber mats. (b) The simulated XRD pattern from the reported HKUST-1 structure. Diffraction peaks from HKUST-1 was observed from PP fiber mat with Al_2O_3 seed layer. Very small diffraction peaks were measured from the PP fiber mat without the Al_2O_3 seed layer. The measured XRD pattern from the MOF coating match the reported HKUST-1 structure. 186
Figure 7.4. SEM images of PP fiber mat with different HKUST-1 coating. (a) untreated PP fiber mat. (b) ALO coated PP fiber mat with 20 LBL HKUST-1. (c) APTES treated PP fiber mat with ALO, and 20 LBL HKUST-1. (d) Direct hydrothermal growth of HKUST in ALO coated PP fiber mat. 188
Figure 8.1. Structure and images of HKUST-1 (or $Cu_3(BTC)_2$). (a) The schematic diagram of the molecular structure of the $Cu_3(BTC)_2$. (b) Optical image collected from $Cu_3(BTC)_2$ crystals supported on a glass slide. (c) Scanning electron microscope image collected from the synthesized $Cu_3(BTC)_2$ crystals. 206
Figure 8.2. Nitrogen sorption data collected from the HKUST particles. (a) The adsorption/ desorption isotherm curve of the outgassed $Cu_3(BTC)_2$. (b) Pore size distribution of $Cu_3(BTC)_2$ calculated from the isotherm curve. (DFT method) 207
Figure 8.3. X-ray diffraction patterns collected from the (a) glass substrate and (b) $Cu_3(BTC)_2$ particles supported on the glass substrate. The curve (c) was simulated from the reported molecular structure of $Cu_3(BTC)_2$. The collected XRD pattern fits very well with the literature report, which confirmed the formation of $Cu_3(BTC)_2$ 208
Figure 8.4. In-situ QCM and FTIR analysis of Al_2O_3 ALD on $Cu_3(BTC)_2$. The bottom curve related to the in-situ QCM data collected from TMA/water ALD process on the untreated QCM crystal. The top trace is corresponding to the TMA/water ALD on $Cu_3(BTC)_2$ supported QCM crystal. Much larger mass uptake was observed on MOF coated QCM, which consistent with the larger amount of TMA and water diffuse and reaction in the particles. 209
Figure 8.5. In-situ FTIR spectra collected during ALD on MOFs, The spectrum from $Cu_3(BTC)_2$ showed symmetric (1645, 1590 cm-1) and asymmetric (1450, 1370 cm-1) stretching of carboxylate groups, which is consistent with the reported chemical composition.

TMA/water showed small reaction with MOFs, and the features around (3020 and 1306 cm^{-1}) corresponding to the formed methane trapped in MOFs. 210
Figure 8.6. In-situ QCM data collected from water/Ar process on bare QCM and $Cu_3(BTC)_2$ particle coated QCM. Bare QCM crystal showed negligible mass uptake during water exposures, while the $Cu_3(BTC)_2$ coated QCM crystal showed very large mass uptake and decreasing. The MOF with 5 cycles of TMA/water ALD process showed smaller mass uptake during water exposure, and this could be explained by the shrinking of pore volume and size after ALD. 211
Figure 9.1. In-situ differential FTIR spectra of TMA/water deposition on AAO membranes. After TMA pulse, we observe the absorbance increase of CH_3 stretching feature at ~2960 cm^{-1} and the decrease of -OH related features between 3700 and 3000 cm^{-1}. In the following water pulse, we can see a mirrored spectrum, which corresponding to increase of -OH and decrease of CH_3 on the surface. Multiple layers of AAO membrane were used to quantitative analysis the relation between the absorbance and surface area. A linear relation between number of AAO membrane and CH_3 asymmetric stretching absorbance has been measured and plotted in panel (b). 241
Figure 9.2. In-situ FTIR differential Spectra of TMA/water deposition on spin coated PP film. Negligible interactions between TMA and PP were observed. The peak intensity of CH_3 asymmetric stretching at ~2960cm^{-1} is not detectable (< 2×10^{-4}) after 1st TMA exposure. . 242
Figure 9.3. C 1s peak detail scan of PP film on Si wafer, before (a) and after (b) TMA/water soaking. No observable change in peak shape. The TMA/water soaked PP film showed no detectable Al. 243
Figure 9.4. In-situ FTIR differential spectra of TMA/water deposition on spin coated PVA film. For clarity, differential spectra after precursor dose were magnified 20 times. We found TMA will react with C-OH and C=O on the PVA fiber in the first ALD cycle. The peak intensity of CH_3 stretching at ~2960 cm^{-1} is ~ $4.0\pm0.5\times 10^{-4}$ after the first TMA exposure. 244
Figure 9.5. SEM images of electrospun PVA fiber before (a) and after (b) 1 cycle of TMA/water "long exposure" cycle, and annealing at 450 °C overnight. Alumina "nanobelts" are observed after annealing, indicating the formation of a thin layer of continuous film on the PVA electro-spun fiber. 245
Figure 9.6. C 1s peak analysis of PVA film on Si wafer, before (a) and after (b) 1 cycle of TMA/water soaking. Significant decrease of C=O and C-OH features support the conclusion that TMA reacts with C-OH and C=O in the PVA. 246
Figure 9.7. In-situ FTIR differential spectra of TMA/water deposition on spin coated Nylon-6 film. The absorbance scale is the same for all spectra. The spectra show hydrogen bonded NH stretching (3304 cm^{-1}), CH_2 stretching (2930 cm^{-1}), amide I (CO stretching) (1640 cm^{-1}), C-H stretching (2860-2930 cm^{-1}), CH_3 bending (1437 cm^{-1}, 1190 cm^{-1}) and CH_3 rocking (690 cm^{-1}). The large signal strength is consistent with a larger extent of reaction between Nylon-6 and TMA during the first ALD cycle. The peak intensity of CH_3 stretching at ~2960 cm^{-1} is ~ $1.0\pm0.3\times10^{-2}$ after the first TMA exposure. 247
Figure 9.8. C 1s peak analysis of Nylon-6 film on Si wafer, before (a) and after (b) 1 cycle of TMA/water soaking. 248

Figure 9.9. In-situ FTIR differential spectra of TMA/water deposition on PBT film on Si. After the TMA pulse, almost all the ester characteristic peaks (1720 cm^{-1} and 1260 cm^{-1}) are removed, indicating high reactivity of ester groups towards TMA vapor. The ether bond, which has a characteristic frequency of 1100 cm^{-1}, also dramatically decreased. This implies that the TMA vapor will also attach the ether bonds in PBT film. During water pulse, removal of the CH_3 related features (~2960 cm^{-1} and 1200 cm^{-1}) indicates the reaction between Al-CH_3 and water vapor. The peak intensity of CH_3 stretching at ~2960 cm^{-1} is ~0.30±0.05 after the TMA exposure..... 249
Figure 9.10. SEM images of nonwoven PBT fiber before (a) and after (b) 1 cycle of TMA/water soaking, and annealing at 450 °C overnight. Solid fibers were recovered after calcination, which indicated the TMA vapor penetrated all way through into the PBT fiber. A porous alumina fiber structure was formed which has been confirmed by N_2 adsorption/desorption analysis..... 250
Figure 9.11. C 1s peak analysis of PBT film on Si wafer, before (a) and after (b) 1 cycle of TMA/water soaking. Complete removal of C=O and the formation of C-O-Al is consistent with the in-situ FTIR analysis..... 251
Figure 9.12. In-situ FTIR differential Spectra of TMA/water deposition on PET film on Si. Similar differential spectra were collected compared with PBT film. After the first TMA pulse, the peak intensity of CH_3 stretching at ~2960 cm^{-1} is ~ 1.42±0.1..... 252
Figure 9.13. In-situ FTIR differential spectra of TMA/water deposition on spin coated PLA film on Si. Total removal of the ester characteristic peaks after TMA pulse, and new features at 1600 cm^{-1} are observed related to aluminum carbonate. After the water pulse, the CH_3 related features are removed, and the new mode at 1600 cm^{-1} is consistent with the reaction with water. The peak intensity of CH_3 asymmetric stretching at ~2960 cm^{-1} is ~ 5.3±0.5× 10^{-2}..... 253
Figure 9.14. In-situ FTIR differential spectra of TMA/water deposition on polycarbonate membranes on Si. The data shows complete removal of ester characteristic peaks after the TMA pulse, and new features at 1600 cm^{-1} associated with the carbonyl-aluminum complex. After water pulse, the remove of CH_3 related features and the new mode at 1600 cm^{-1} is consistent with the reaction between Al-CH_3 and water. The peak intensity of CH_3 stretching at ~2960 cm^{-1} is ~0.31±0.06. 254
Figure 9.15. In-situ FTIR differential spectra of TMA/water deposition on PMMA film on Si. After TMA pulse, we find partial removal of the ester peaks, and again, Al-C mode at 1600 cm^{-1}. In the following water pulse, the Al-CH_3 groups react with water and form Al-OH. The peak intensity of CH_3 stretching at ~2960 cm^{-1} is ~ 1.7±0.3× 10^{-2} after the first TMA pulse. 255
Figure 9.16. In-situ FTIR differential spectra of TMA/water deposition on PEO film on Si. Removal of ether bond at 1100 cm^{-1} shows the TMA inserts to break the C-O-C linkage in the polymer. Similarly, after the water pulse, the decrease of CH_3 stretching mode corresponds to the reaction of Al-CH_3 with water to form Al-OH. The peak intensity of CH_3 stretching at ~2960 cm^{-1} is ~ 1.10±0.1 after the first TMA exposure..... 256
Figure 9.17. The Al-CH_3 deformation (~1200 cm^{-1}) and CH_3 asymmetric stretching (~2960 cm^{-1}) absorbance increase after first TMA pulse on different polymer substrate. The

magnitude of the $\nu_a(CH_3)$ and $\delta_a(CH_3)$ intensity also displays the relative extent of reaction between the various polymers and TMA. 257
Figure 10.1. Panel (a) presents a picture of polybutylene terephthalate (PBT) nonwoven fiber mats: (left) as received; (middle) after TMA/water infiltration; and (right) after infiltration and anneal at 450°C. The starting size for all samples was approximately the same. After infiltration, the fiber mat becomes yellow in color, shrinks in size and becomes mechanically stiffer. Annealing causes more shrinkage, and the sample becomes more brittle, consistent with transformation of the polymer to micron-sized alumina fibers. Panel (b) shows a scanning electron microscope image of the as-received PBT nonwoven. Panels (c) and (d) show a similar sample after 1 h TMA/water soaking and 12 h 450°C anneal. The images in (c) and (d) show that the soaking and annealing preserves the starting fiber morphology. Some connectivity between the fibers likely results from polymer flow during the soaking process. More connectivity was observed with higher process temperature and longer precursor exposure. The cross-sectional view in panel (d) confirms that the fibers are uniform after calcination, indicating full penetration of the precursor throughout the 3 μm diameter starting fiber. 284
Figure 10.2. Cross-sectional TEM images of a PBT fiber after 1h TMA/water exposure at 80°C, and 450°C anneal. The dark region on the lower resolution image is platinum deposited during TEM sample preparation. Some contrast in image (a) in the radial direction may be present. A closer look of the outer edge of the fiber in figure (b) shows a uniform distributed mesoporous structure. The insect shows a high magnification of the mesoporous structure, and it is consistent with a pore diameter of 5-10 nm. 285
Figure 10.3. Nitrogen/hydrogen adsorption/desorption results collected at 77K from PBT samples. Figure (a) Nitrogen and hydrogen isotherm from PBT samples after 18 hr TMA/water soaking at 80°C and 24 hr anneal 450°C. The hydrogen adsorption/desorption analysis shows 24.4 standard cc/g adsorption at atmosphere pressure, corresponding to ~ 0.22 weight % hydrogen. Figure(b) Pore size distribution results from PBT soaked in TMA vapor with different duration, with fixed infiltration (80°C) and post annealing temperature (450°C). The longer soak time leads to smaller pores and higher pore volume, consistent with more TMA incorporation. Figure (c) Pore size distribution results from PBT soaked in TMA vapor at different temperatures, with other conditions fixed (Table 10.1). Higher soaking temperature also results in porous alumina with smaller pores, which is attributed to the increased reactivity between the TMA and the polymers. Figure (d) Additional pore size analysis for PBT samples annealed at different temperatures after soaking under same condition (details given in Table 10.1). The higher anneal temperature produces larger pores. 286
Figure 10.4. Panel (a): nitrogen isothermal adsorption/desorption data obtained from porous titania. The plot shows the amount of vapor adsorbed as a function of pressure up to one atmosphere. The sample was prepared by soaking of PBT polymer fibers at 160°C for 18 hr in $TiCl_4$, then annealing at 450 °C for 12 hr. Panel (b): pore size distribution of the porous titania calculated from the isotherm. The pore size is larger than obtained for the same polymer soaked in TMA and annealed under the same conditions. 287

Figure 10.5. Mass increase during TMA/water infiltration at 80°C on a cast PBT film, measured in situ using a quartz crystal microbalance. Figure (a) shows that the mass increase saturates after 400 micro-doses (2 sec each) of TMA, with ~ 90 µg overall mass uptake. This amount of mass increase is more than 1000× larger than ~40 ng measured for a typical TMA/water ALD process on a planar solid substrate (i.e. with no subsurface reaction). Likewise, the water reaction saturates after ~ 100 micro-doses. Figure (b) shows a closer view of first 30 TMA micro-doses on a PBT film. A large mass uptake occurs for the first several cycles then decreases as exposure proceeds. 289
Figure 10.6. FTIR transmission spectra collected in situ from the a starting PBT film cast onto a silicon substrate (bottom trace) and after exposing the film to TMA (middle) and water (upper trace) at 80°C. The TMA exposure removes ester (1720 and 1270cm^{-1}) and ether (1100 cm^{-1}) bonding units indicating high reactivity between TMA and ester bonds in the PBT. The CH_3 (2860 and 2930 cm^{-1}) and Al-CH_3 modes (1200 cm^{-1}) increase upon TMA treatment, confirming Al-CH_3 present in the soaked PBT film. After water dosing, the decrease in CH_3 and Al-CH_3 absorbance and an increase in Al-O modes shows water reacting with the Al-CH_3 groups to form Al-OH. 290
Figure 10.7. Proposed scheme for the PBT/TMA and PBT/TMA/water reactions consistent with the IR data shown in Figure 10.6. TMA is a strong Lewis acid and will likely attack nucleophilic carbonyl groups in the polyester to break the C=O ester bond and formation of aluminum alkyl oxide. Likewise, TMA can also insert into the C-O-C backbone linkage in the PBT to break the polymer chain and produce a methyl termination and a corresponding Al-$(CH_3)_2$ terminal group. During water pulses, the Al-CH_3 groups readily react with water to form Al-OH..... 291
Figure 10.8. X-ray photoelectron spectra of the C 1s feature in: (a) an untreated PBT film; and (b) a PBT film after TMA/water infiltration. The spectra collected after TMA/water show negligible C=O at 289 eV and formation of Al-O-C at ~283.5 eV consistent with mechanism in Figure 10.7. 292
Figure 10.9. Differential scanning calorimetry and thermal gravimetric analysis of: (a), (b) untreated PBT fibers; and (c), (d) TMA/water infiltrated PBT fibers. Results in panel (a) show increased heatflow at approximately 220 °C, consistent with the PBT melting point. Whereas, in panel (c) for the TMA/water soaked PBT, no obvious T_m was observed up to 275 °C. The TGA curve for untreated PBT in panel (b) shows rapid mass decrease at ~400 °C, with ~0 % residue after 900 °C. However, after TMA/water soaking, panel (d) shows a more gradual mass loss, continuing until ~550 °C with ~25 % of mass remaining after 900 °C. 293
Figure 10.10. Ex-situ FTIR spectra showing the ambient and thermal stability of a TMA/water infiltrated PBT film. The TMA/water soaked PBT continues to absorb water from the ambient during one hour of air exposure. Annealing at 450 °C removes water and the organic component, leaving primarily Al-O modes near 700 cm^{-1}..... 294
Figure 11.1. Water contact angle behavior measured over time. The symbols correspond to samples as follows: *purple dots:* PDMS with 100 cycles aluminum oxide ALD at 120 °C; *Blue squares:* Si wafer with 100 cycles aluminum oxide ALD at 120 °C; *Red dots:* Si wafer coated with liquid water soaked 200 cycles "alucone" at 120 °C; *Green triangles:* liquid

water soaked 200 cycles “alucone” on Si wafer at 150 °C; *Black squares:* liquid water soaked 200 cycles “alucone” on Si wafer at 90 °C. All ALD treated samples showed increased contact angle over time during exposure to laboratory air. It is interesting to note the water contact angle is kept at a very low value for the MLD coatings, possible because of the micro porous morphology formed from the hydroxylation of the MLD coating. 314
Figure 11.2. Water contact angle behavior measured over time. The symbols correspond to samples as follows: *Red squares:* TMA/water soak and 100 cycles aluminum oxide ALD at 120 °C; *blue squares:* TMA/water soak and 100 cycles aluminum oxide ALD at 60 °C and purge with Ar for 48 hours; *Black squares:* DEZ/water soak and 100 cycles Zinc oxide ALD at 60 °C: *Gray squares*: TMA/water soak + 100 cycles aluminum oxide ALD + 100 cycles “alucone” at 60 °C. All the treated samples showed increased contact angle over time during exposure to laboratory air, except the “alucone” coated sample. 315
Figure 11.3. (a) Optical microscopy images of PDMS after TMA/water soak and 100 cycles aluminum oxide ALD at 120 °C. Visible cracks and buckle of the surface is observed. (b) Optical microscopy images of PDMS after TMA/water soak and 100 cycles aluminum oxide ALD at 60 °C. Smooth and crack free coating was formed on the PDMS, this could attribute to the smaller thermal expansion at lower process temperature. (c) Optical microscopy images of PDMS after DEZ/water soak and 100cycles Zinc oxide ALD at 60°C. Buckles and cracks were formed on the PDMS surface during the DEZ treatment. 316
Figure 11.4. Stress strain curve of TMA/water and DEZ/water soaked PDMS and pristine PDMS. The slope of the stress strain curve is the measure of the Young’s modules, we can see after soak with metal organic precursor, the modules of PDMS is significant increased. This increase of Young’s modulus will form a mechanical buffer layer between ALD coating and bulk PDMS, which will stabilize the ALD coating and keep the ALD layer intact. 317
Figure 11.5. Schematic diagram of surface treatment of PDMS with ALD only or sequential vapor infiltration followed by ALD. The top scenario shows direct aluminum oxide ALD on PDMS resulting in cracked aluminum oxide coating. The bottom scenario shows ALD after sequential vapor infiltration, producing a smooth and uniform coating on the PDMS. The sequential vapor infiltration before the ALD helps maintain the surface in a hydrophilic state. 318
Figure 12.1. Scanning electron microscope images collected from the vapor phase infiltrated F127 surfactants film on the Si wafer. Panel (a), (b) showed the morphology of F127 surfactants film after TMA/water vapor infiltration. Panel (c), (d) showed the mesoporous aluminum oxide film formed on the Si wafer after calcinations of infiltrated film at 400 °C overnight. The pore size is measured from 3nm-10nm. The openings of the pores are mostly on the edge of the film. 336
Figure 12.2. TEM images collected from the mesoporous aluminum oxide samples for N_2 adsoprtion/desorption analysis. The sample was prepared by TMA/water vapor phase infiltration of F127 surfactant dipcoated on PP fiber mat, and post calcinations at 400 °C overnight. PP fiber mat and surfactant template have been removed by the calcinations.... 337
Figure 12.3. (a). Nitrogen adsorption/desorption isotherms for mesoporous alumina prepared by vapor phase infiltration of F127 surfactant with TMA/water. The BET surface area is measured 631.3 m2/g. **(b)** Nitrogen adsorption/desorption isotherms for mesoporous alumina

prepared by 100 cycles of TMA/water (1/60/1/60) ALD on F127 surfactant. The BET surface area is measured as 417.3 m2/g. **(c)**, Pore sized distribution calculated from the N2 adsorption/desorption isotherm in Figure (a) with the BJH method. **(d)** Pore sized distribution of ALD coated F127 calculated from the N2 desorption isotherm with the BJH method.... 338
Figure 12.4. In-situ FTIR spectra collected from the **(a)** F127 surfactant film on Si wafer, **(b)** TMA vapor soaked F127 surfactant film, **(c)** TMA/water vapor soaked F127 surfactant film, and **(d)** 400 °C annealed mesoporous alumina film on silicon wafer. The increase of CH_3 related feature at 2930, 1200 and 700 cm^{-1} is corresponding to the large amount incorporation of TMA in the surfactant film. The removed of CH_3 related absorbance and the increase of hydroxyl related absorbance after water dose is related to the conversion of Al-CH_3 to Al-OH..... 339
Figure 12.5. XRD patterns collected from **(a)** CTAB surfactant film, **(b)** TMA/water vapor infiltrated CTAB surfactant film, **(c)** A calcined mesoporous alumina film. Calcination temperature was 400 °C. A low angle diffraction peak is observed for CTAB films, corresponding to the laminar structures of the CTAB surfactant. However, the TMA/water vapor phase infiltration induced the phase changed from laminar to cylindrical structure. The formed mesoporous alumina is characterized as amorphous..... 340
Figure 12.6, Schematic diagram for the preparation of mesoporous metal oxide materials from vapor phase infiltration method. 341
Figure 12.7. DSSC performance for mesoporous TiO_2 electrode by vapor phase infiltration of F127 surfactants with $TiCl_4$ vapor at 45 °C. The light color of the DSSC electrode is due to the small thickness of porous TiO_2 layer(~150 nm in thickness), which would inhibit the performance of the solar cell. An overall solar energy conversion efficiency of 0.04% was measured. The small pore size and the two-dimensionally pore structure could also have prevented the dye from diffuse in and adsorb on the TiO_2 porous electrode. The conventional DSSC made from TiO_2 nanoparticle electrode (~5-10 μm in thickness) showed ~5-8 % overall efficiency. 343
Figure 13.1. Scanning electron microscope images collected from core/sheath bi-component fibers with 100 "short" TMA/water ALD cycles. Image (a) is collected from coated PLA/PP core/sheath fibers. The coated fibers showed almost identical morphology to the untreated fibers (not shown). Image (b) is collected from coated PP/PLA core/sheath fibers. PLA sheath melted together with adjacent fibers resulting in a cracked and nonuniform coating, whereas the smaller the PP core fibers remained intact and are readily visible in the image. 360
Figure 13.2. In-situ FTIR spectra collected during the first two "long" TMA/water ALD cycles on PLA and PP films. Panel (a) showed the IR spectra collected from the PLA. The spectrum at the very bottom is from the untreated PLA film on Si wafer. Differential spectra collected after each pulse of reagents were listed from bottom to the top. Significant reaction between TMA and carbonyls in PLA was measured. Panel (b) displayed the IR spectra collected from the PP. Similarly, the bottom spectrum is collected from the untreated PP film on Si wafer, and the differential spectra collected after each pulse of reagents were listed from bottom to the top. The minimal reaction between TMA and PP is not detectable. 361

Figure 13.3. XPS spectra collected from the PLA film on Si wafer. The survey scans of (a) untreated and (b) treated PLA film were displayed on the top. After one "long" TMA/water ALD cycle, significant increase of Al atom percentage (12%) was measured. The detailed C 1s scan of untreated and treated PLA film were shown in figure (c) and (d). The spectrum of PLA film showed peaks at 284.5 eV (C-C) and 289 eV (C=O). After one "long" TMA/water exposure, the peak at 289 eV is removed, corresponding to the reaction between the TMA with C=O bond in the PLA. 362
Figure 13.4. The cross-section TEM image collected from (a) untreated PLA/PP core/sheath fiber, (b) PLA/PP core/sheath fiber with 500 "short" TMA/water ALD cycles and (c) PLA/PP core/sheath fiber with 100 "long" TMA/water cycles. After 500 "short" ALD cycles, thin Al2O3 film was deposited on PP surface. However, for 100 "long" ALD cycles coated sample, different contrast in PLA core was observed..... 363
Figure 13.5. The SEM images and EDS line scans collected from the cross-section of PLA/PP core/sheath fibers. Figure (a) showed the cross-section of an untreated PLA/PP fiber. The EDS line scan along the diameter of the fiber showed no detectable aluminum. The SEM image in figure (b) was collected from the cross-section PLA/PP core/sheath fiber with 500 "short" TMA/water ALD cycles. The EDS line scan showed two distinctive aluminum peaks located on PP surface. This is consistent with conformal Al2O3 coating on PP. Figure (c) displayed the SEM image collected from the cross-section of 100 cycles of "long" TMA/water coated PLA/PP core/sheath fiber. In addition to the two aluminum peaks located on PP surface, the EDS line scan along the diameter showed aluminum peaks in PLA core. These additional aluminum peaks consistent with TMA diffuse through PP and react with PLA core. 364
Figure 13.6. Schematic diagram of the "short" and "long" TMA/water ALD cycles on PLA/PP core/sheath bi-component fibers. When the core/sheath fiber was exposed to "short" TMA/water exposures, precursor vapors were not given enough time to diffuse into the PP layer. Minimal subsurface diffusion and reaction occurred, and thin Al2O3 ALD layer was deposited on PP surface. However, when the "long" precursor exposures were used, TMA and water vapors could diffuse through the PP, and react with PLA core. 365

CHAPTER 1. Introduction

Natural polymeric materials such as cotton, paper, rubber and so on have been in use for several centuries. They have been important materials since their discovery. Since the 20th century, the development of synthetic polymers and the plastics significantly expanded the properties and the applications of the material. Nowadays, synthetic polymers are ubiquitous in our everyday life. A great number of polymers have been synthesized by tuning the monomers, microstructures, monomer arrangement, and the chain length.

Another approach to further extend the applications of polymers is by applying functional coatings. The coating could fine tune the surface properties and greatly broaden the application fields of the polymeric materials. New functionalities, like diffusion barrier, chemical resistance, conductivity, abrasion resistance, and photocatalytic could be incorporated into the materials. So far, a large number of coating techniques have been developed for polymer materials.

1.1 Overview of Thin Film Deposition Techniques on Polymers

The thin film deposition techniques can be categorized into two groups, liquid solvent based processes and vapor phase based methods. In the liquid solvent based processes, precursors are dissolved in water or organic solvents, and a solid coating is condenses or reacts on the surface to deposit a film coating. Example liquid-phase coating methods include sol gel, hydrothermal, layer by layer, plating and spraying techniques. In the vapor phase based methods, vaporized gas phase precursors are used for the film deposition, including physical vapor deposition, chemical vapor deposition and atomic layer deposition. These techniques are typically used for high quality inorganic coatings, such as metal, metal oxide

and metal nitride, and they have been extensively used in microelectronic fabrications. In the following sections, an overview of thin film deposition techniques on polymers will be provided.

1.1.1 Sol-gel

One of the important coating techniques applied to polymer substrates is the sol-gel method. The term "sol" refers to the colloid particles in solution, and the term "gel" refers to the networked growth of particles. Sol-gel is a wet chemical method, and it has been widely used for the deposition of silica and metal oxide materials.[1-4] A typical sol-gel process includes the following steps as shown in Figure 1.1. Firstly, the suspension of colloidal powders, or sol is prepared. The suspension is typically formed by mechanical mixing of colloidal particles in water at a pH that prevents precipitation. It could also be prepared by mixing the metal oxide precursor, such as metal alkoxides and metal salts, with water. Secondly, the sol solution is then casted on to the substrate. With time the colloidal particles and condensed species link together to become a three-dimensional network, or gel. Finally, the aged gel is dried carefully. The dehydration reaction happens in the gel network. The technique offers unique advantages for preparing nanoparticles, bulk ceramic and coatings. However, the method is very sensitive to detailed process conditions, such as pH, precursor concentration, aging time, and temperatures. Another main drawback of this technique is the long processing time required. [1]

So far, a number of sol-gel processes have been developed for the polymer substrates.[5,6] However, because the sol-gel method is based on homogeneous liquid phase reaction, it is difficult to get uniform and conformal thin coating onto substrates with

complex 3D structure. The capillary force often prevents the uniform distribution of precursor solution, resulting in non-conformal coatings. The precise control of film thickness is also a challenge for the sol gel process, because the precursor concentration, pH and temperature need to be very carefully controlled for each thickness.[7,8]

1.1.2 Hydrothermal

The hydrothermal method is another versatile liquid phase approach for the formation of crystalline metal oxide materials.[2,9-12] In a typical hydrothermal process, the metal oxide precursors, such as metal alkoxides and metal salts, are mixed with water and transferred into a pressurized autoclave. At elevated temperature, the metal precursor will react with water to form metal oxide.[2] The pH of the aqueous solution, temperature and the pressure of the process will affect the structure and the properties of the resultingmaterials. Various metal oxide hydrothermal growth process have been developed for polymer substrates. The substrate surface chemistry is critical for the metal oxide growth.[13-15]

Surfactant molecules can be added into the hydrothermal growth solutions. These amphiphilic molecules direct the orientation of the crystal growth.[16] The surfactants micelles have also been demonstrated as structure templates for the formation of porous materials by hydrothermal method.[17-20] A great number of porous silica and metal oxide materials have been successfully prepared by this method.

Metal organic frameworks (MOFs) were also synthesized by hydrothermal methods. Metal organic frameworks (MOFs) are new emerging porous materials with advanced properties. Compare to pure inorganic porous materials, such as zeolites, MOFs have high specific surface area, regular pore structures and custom-defined surface chemistry. [21-24] In a

typically MOF synthesis, metal ions and carboxylic acid linkers were self-assembled into ordered open frameworks. By selecting the metal ions and organic linkers, MOFs with different structure and properties can be prepared. For example, metal ions with different coordination preference could induce the different pore structures by determine how many organic linker could connect to the metal center. A large number of structures can be synthesized by choosing different metal ions and organic linkers.[21-24]

1.1.3 Layer by Layer

The layer by layer (LBL) assembly technique was developed by Gero Decher in the 1990s.[25] Figure 1.2 shows the schematic of the process. The substrate is sequentially introduced to two polyelectrolytes with complementary positive and negative charges.[25] The electrostatic force between the two polyelectrolytes leadto film to build up in a layer by layer manner.[25] A number of polymer materials have been deposited by this technique, enabling many functionalities including mechanical, optical and electronic properties.[26-28] Moreover, inorganic nanoparticles, biomolecules could incorporate into the film very easily.[27,29-32] Although LBL is a versatile technique, there are a lot of limitations. For instance, as in other wet chemical processes, it is not easy to form uniform and conformal films over large surface, especially onto the 3D complex structures.[25,27] Moreover, the method is limited to chaged polymer (polyelectrolyte) films, and it is easy to introduce contaminants into the film.[25]

1.1.4 Electroless Plating

Electroless plating is a widely used metal deposition technique on nonconductive surfaces. Instead of using electric current to reduce the metal ions in the plating solution, a reducing agent is added. The most common metals deposited through electroless plating are copper (Cu) and nickel (Ni),[33-35] although gold (Au) and silver (Ag) are also deposited in this way.[36 37] Plasma surface pretreatment is typically conducted to faciliate the film nucleation and growth.[36]

1.1.5 Spraying

Spraying is another technique widely used in industry for large surface coating. In the spray process, the liquid or solid coating materials are brought to the surface by compressed air. The following evaporation of solvent or heat treatment keeps the coating stay on the surface.

1.1.6 Dip Coating

Dip coating is another technique widely used for creating thin films on various substrates. Uniform films could be applied by dipping the substrate into the coating solution, which contains the coating materials. After removing the substrate from the solution carefully, the coated substrates were dried in ambient to remove the solvent residue. The concentration of the coating solution, the withdrawing speed and the post thermal treatment are critical for the thickness and the quality of the coatings.

1.1.7 Physical Vapor Deposition

Physical vapor deposition (PVD) is a vacuum deposition technique to deposit thin films by the condensation of a vaporized material onto various substrates. A large number of metal, metal oxide and metal nitride can be deposited by this technique. In the PVD process, the target materials were evaporated by high temperature or plasma sputter bombardment.[38,39] When the vaporized materials reach the substrates, they would condense on the surface. Because there is not chemical reaction in the process, the material deposited can be very pure. However, one drawback of PVD process is that the technique is a line-of-sight method. It is difficult to get conformal and uniform coating on high aspect ratio surface. Moreover, most PVD processes involved the using high temperature or plasma bombardment, which is incompatible to most polymer substrates.

1.1.8 Chemical Vapor Deposition

Chemical vapor deposition (CVD) is a thin film deposition technique involved the chemical reaction of vapor phase reactants on near the vicinity of a heated substrates surface. It is capable of produce various coating materials, such as metal, metal oxide and metal nitride, with good control of composition and thickness.[40-42] Moreover, the unique feature of CVD over PVD technique is that CVD is not a line-of-sight method. It is capable of coating of substrates with complex shape. The versatility of CVD make it became one of the main processing methods for thin film deposition. A great number of applications have been enabled by the CVD technique, such as semiconductors for microelectronics, gas diffusion barriers and optical coatings.[43] However, due to the CVD process is still based on homogeneous gas phase reaction, it is still challenge for it to get very conformal and uniform

coatings on high aspect ratio substrates, such as long trenches, nanoporous materials, and nanofibers. [43] To get better film coverage on high aspect ratio surfaces, a modified CVD process, atomic layer deposition (ALD), has been developed.

1.2 Atomic Layer Deposition and Molecular Layer Deposition

1.2.1 Atomic Layer Deposition

Atomic layer deposition (ALD) is a vapor phase thin film deposition technique based on sequential self-limiting surface reactions. In the typical ALD process, as shown in Figure 1.3, two reactants are introduced alternatively to the substrate, and forming a single layer of molecular each time. The Al_2O_3 film deposited by trimethy-aluminum (TMA) and water is the most studied ALD process. In which you first exposed the substrate to TMA vapor, TMA will react with surface OH and form Al-CH_3 terminated surface. In the following water pulse, these Al-CH_3 groups will react with water and change the surface back the OH terminated. Conformal films with desired thickness and composition can be deposited by control reaction cycles. So far, a great number of materials have been deposited by ALD, such as metal, metal oxide, metal nitride, and semiconductors. The ALD process has enabled many advanced applications, especially in microelectronic industry.

The history of ALD dates back to the 1970s in Finland and the work of Suntola. ZnS was deposited by using vaporized zinc and sulfur elements. The material was used for thin film transistor (TFT) displays.[44] After the introduction of ALD, the research area showed great advancements in the last 40 years. The early research of ALD is mainly focused on electronic, optoelectronic, and light emitting diode applications.[44-50] Nowadays, more and

more researchers are exploring new ALD materials and ALD-related processes, which could greatly extend applications of ALD. For example, ALD has found applications in nanomaterials, solar energy, batteries, optics, biomedicine, and microelectromechanical systems.

1.2.2 Molecular Layer Deposition

Following the principles of atomic layer deposition (ALD),[44,51,52] researchers are currently exploring vapor phase molecular layer deposition (MLD) approaches for organic or hybrid materials deposition and integration.[53-58] The MLD approach utilizes alternating self-limited heterogeneous surface reactions to build up a solid-state thin film though a sequence of molecular adsorption/reaction steps. Figure 1.4 displays a schematic diagram for molecular layer deposition process.[56] Under mild temperature conditions, exposing an excess single component vapor phase reagent to well-defined surface bound reactive ligands results in a self-saturating half-reaction that prepares the surface for a subsequent complementary half-reaction. The complete sequence constitutes one reaction cycle, and with sufficient precursor exposure, the extent of half-reactions is determined by the number of available reactive sites on the growth surface. This progression thereby allows a film to be conformally constructed on surfaces with arbitrary shape and surface area.

Organic polymer films including polyamides, [55,59] polyimides[60] and polyureas[61] can be formed. Reports show formation of polyamide nylon 66 [55] using adipoyl chloride (ClOC-$(CH_2)_4$-COCl) and 1, 6-hexanediamine (H_2N-$(CH_2)_6$-NH_2), as well as formation of poly (p-phenylene terephthalamide) films.[59] In-situ infrared (IR) transmission analysis confirms the

sequence of proposed sequential steps. Recent work also report polyurea MLD using 1,4-phenylene diisocyanate (PDIC) and ethylene diamine (ED).[61]

In addition to pure organic films, several hybrid organic-inorganic polymer films can be synthesized by MLD. Trimethyl aluminum reacts readily with ethylene glycol to form a coordination polymer of the form $(Al\text{-}O\text{-}CH_2\text{-}CH_2\text{-}O)_n$. In-situ IR and quartz crystal microgravimetry (QCM) provided insight into the growth reaction mechanism.[54] In addition to well defined vertical film growth, results demonstrate that homo-bifunctional organic reactants, such as ethylene glycol, undergo a "double reaction",[54,58,62] where both hydroxyl groups on the ethylene glycol react with surface. The double reaction decreases the reactive site density and result in low growth rates and films with low density and poor stability under ambient exposure. To avoid double reactions associated with homo-bifunctional reactants, Yoon et al. used two hetero-bifunctional reactants, ethanolamine and maleic anhydride, along with trimethyl aluminum in a three-reactant sequence to form aluminum oxide organic hybrid films.[63] In this dissertation, we described MLD reaction studies using TMA and heterogeneous glycidol (GLY) or ε-caprolactone (LAC) in a two-step molecular vapor/surface reaction, forming solid organic-inorganic network thin films.

1.3 Atomic Layer Deposition on Polymers and Sequential Vapor Infiltration

1.3.1 ALD Growth on Polymer Substrates

Recently developed low temperature ALD processes, which can be conducted at temperature as low as room temperature, make coating of a variety of thermal sensitive substrates possible. An array of ALD deposition processes have been conducted on polymers

substrates. For examples, polymer substrates were serving as templates for ALD to replicate complex 3D structures, such as polyethylene particles,[64] patterned polystyrene spheres,[65] electro-spun PVA fiber,[66] block copolymers,[67,68] and virus shells.[69] Other research was focused on the surface fictionalization of polymer substrates by ALD coatings, for example, butterfly wing[70] and polymer fibers[66,71-73] were coated by Al_2O_3 ALD to tune the surface energy of these structures.[71] The incorpration of ALD chemistry make polymer materals can be used in many new applications, such as flexible electronics, solar cells, chemical resistant layers, antomicrobial coatings and gas diffusion barriers.

Recent studies of ALD on polymers demonstrated that metal oxide precursors often diffuse sub-surface into the polymer, creating a graded organic/inorganic interface region.[74-76] The extent of subsurface diffusion and deposition during ALD on polymers is known to be affected by reaction temperature, extent of precursor exposure and the specific chemical interactions between the precursors and reactive groups in the polymer.[71-73] Other studies show that vapor infiltration alters the chemical and mechanical properties of natural polymer materials.[75,76] We can control subsurface species diffusion and reaction during vapor exposure, for example by carefully selecting the polymer template, metal organic precursor, and the extent of precursor exposure.[77,78]

1.3.2 Sequential Vapor Infiltration

To further understand the subsurface deposition during ALD on polymers, a modified ALD process was developed. Sequential vapor infiltration (SVI) is proceeding by allowing the subsurface precursor diffusion/reaction and sequence co-reactant diffusion to approach saturation. In this dissertation, we reported using SVI to modify polyester fibers. After

infiltrate polyester fibers with metal organic precursors (TMA/$TiCl_4$), we find out that TMA could diffuse and react through the polymer bulk and produce a homogeneous organic-inorganic hybrid material that retains the form and shape of the starting polymer template. Calcination yields a porous inorganic solid with pore size and pore size distribution controlled by the details of the infiltration and calcination process steps, where again, the shape of the resulting solid matrix directly mimics the starting polymer fiber web. Using higher temperature and longer infiltration times during metal organic exposure we find that the pore size shrinks and the size distribution narrows, where the size approaches the monomer unit dimension in the starting polymer. This indicates that polymer structure acts to template the porous oxide structure. Thus, by choosing the starting polyester monomer length, the pore size could be pre-selected and adjusted which will be useful for separations, vapor adsorption, and other important applications. [77]

More interesting, we found that different polymers showed dramatic different response to metal organic vapor infiltration, which enabled selective modify the certain polymer segment by SVI. For example, amphiphilic surfactants moleculars have been widely used as structure direct template for the preparation of metal oxide from solution. The interaction between the hydrophilic head of the surfactants molecular and the metal oxide precursor helped the self-assemble of ordered micelles/metal oxide hybrid materials, and after post template remove, well defined porous materials could be prepared. Recently, this selective interaction between metal oxide precursor and certain polymer segment was also discovered during vapor phase sequential vapor infiltration (SVI) and atomic layer deposition (ALD) of metal oxide onto polymers, In this dissertation, we reported the preparation of

mesoporous aluminum oxide and titanium oxide material by the vapor phase infiltration of trimethyl aluminum or titanium tetrachloride and water vapor into the nonionic (F127 $EO_{106}PO_{70}EO_{106}$) and ionic surfactants (cetyltrimethylammonium bromide CTAB and sodium dodecyl sulfate SDS). In-situ FTIR was used to monitor the chemistry change during the vapor infiltration, SEM, TEM and XRD were used to characterize the morphology and structure change, and the nitrogen adsorption and desorption measurement was employed to analysis the specific surface area and the pore size distribution of the porous metal oxide. Besides vapor phase infiltration procedure, conventional ALD process has also been tested to prepare the mesoporous metal oxide materials.

Similarly, SVI of TMA/water on bi-component fiber also demonstrated the selective reactivity of TMA toward certain polymer segments. Previous research in our group has proved that PP is an inert polymer with little or no reaction with TMA/water. However, PLA shows drastic reaction with TMA vapor. After SVI of TMA/water on core (PLA) sheath (PP) bi-component fiber, we observed that TMA could diffuse through the inert PP sheath and react with PLA core.

Sequential vapor phase infiltration provides a new approach for preparation of inorganic-organic hybrid materials from polymers. After removing of organic components by post annealing, micro/mesoporous materials were synthesized. Moreover, the selective reaction between ALD precursors and polymers enabled selective modification of certain polymer segments.

1.4 Integration of Atomic Layer Deposition and Liquid Phase Deposition Techniques

The substrate surface chemistry is critical for many liquid phase deposition techniques. To facilitate the nucleation and growth of the coatings, desired surface functional groups were always introduced onto the surface, such as OH, COOH, SH or NH_2 groups. Many approaches have been developed for surface pretreatment, such as UV-ozone, Oxygen plasma, and self assemble monolayers. Atomic layer deposition (ALD) functionalized surface could help the further film growth from liquid phase. ALD provides a solvent free vapor phase technique for the formation of conformal metal oxide surface. This fresh deposited metal oxide layer gives a high density OH surface, which could further decorated with other functional groups. Moreover, the metal oxide deposited on the substrate by ALD could also serve as a seed layer for further crystal growth from the surface.

1.4.1 ZnO ALD and Hydrothermal Growth of ZnO Nanorods

Aqueous hydrothermal techniques for ZnO nanorod crystal growth can proceed rapidly at relatively mild temperatures (<150 °C), and the processing permits surface-selective growth that drives nanostructure evolution.[79] For most hydrothermal methods, an oxide seed layer is essential to initiate and continue crystal evolution. The seed layer presents nucleation sites, lowering the thermodynamic barrier for ZnO nano- and micro-crystal growth and further enhancing the growth direction selectivity and aspect ratio.[14,15] Previous researchers form nucleation sites by applying ZnO particles or a nanocrystalline film by dip coating, spin coating[80] or sputtering.[81] These approaches can work for deposition on planar surfaces, but for complex 3-D substrates, these methods are not expected to yield uniform seed layers and homogeneous seed layer distribution.

Atomic layer deposition (ALD) is a vapor phase thin film deposition technique which can deposit materials uniformly on complex 3D surfaces. In the ALD process, two co-reactants (e.g. diethyl zinc and water for ZnO formation) are introduced alternatively, separated by an inert gas purge step, allowing the surface to react with each reagent in a series of self-limiting adsorption/reaction steps.[82,83-86,] Repeating this sequence builds up a coating with desired thickness on the substrate. Several research groups recently showed that this process yields uniform metal oxide thin film coatings on high aspect ratio polymer fiber substrates.[83-89] Some of these reports also show photocatalytic performance of the resulting polymer/oxide structures.[87,88] For this study, we show that the ALD layer provides an ideal seed layer for hydrothermal growth of ZnO nanorod crystals on fiber structures, and that these nanocrystal-coated fibers show high photocatalytic activity compared to previous structures.

1.4.2 Al_2O_3 ALD and Layer by Layer Growth of Metal Organic Frameworks

Metal organic frameworks (MOFs) were conventionally synthesized by solvent thermal batch process, which result in the formation of MOFs in free standing particle morphology. However, more and more chemical sensing and adsorption applications required the attachment of MOFs on supporting materials, such as flexible polymer fiber mat.[90,91] Some developments of attachment of MOF on polymer fibers have been reported. Küsgen et al. reported the direct hydrothermal growth of MOFs on pulp fibers.[90] Rose et al. recently demonstrated a route to polymer fibers by electro-spin MOFs particles with the polymer solution.[91] However, these methods did not provide a very good control of MOFs attachment and the mechanical properties of the polymer substrates dramatically affected by

these attaching processes.[90,91] A new method developed by Shekhah, O et al. enabled the well controlled surface attachment of MOFs, which could enable the conformal attachment with precise thickness control.[92-97]

The surface chemistry of the supporting materials is critical for the formation of MOFs on surface. Previous research demonstrated that the NH_2 or COOH groups would help the nucleation on the surface, and affect the crystal growth orientation.[93,95-97] Other report showed that certain metal oxide or nitride surface could also enable the surface attachment of MOFs.[98] Previous research also showed Al_2O_3 coating on Si wafer could help with the nucleation during hydrothermal growth of MOF-5.[99]

ALD is an ideal technique for surface functionalization of high aspect ratio substrates, such as polymer fiber mat. This has been demonstrated by the previous research in our group.[66,84,100,101] In this paper, we demonstrated a method for the surface attachment of MOFs on polypropylene fiber mat by using Al_2O_3 ALD and LBL growth of MOFs. The metal organic framework HKUST-1 [Copper benzene-1,3,5-tricarboxylate $Cu_3(BTC)_2$] will be used as the demonstration material in this study.

1.5 Opportunities of Atomic Layer Deposition and Related Processes.

Atomic layer deposition (ALD) is a chemical vapor based thin film deposition technique. By employing self-limiting surface reaction, conformal and uniform coatings could be applied on complex 3D surfaces.[52,102] The thickness of the coating could also be precisely controlled at sub-nanometer scale by varying the deposition cycles.[52,102]

The continuous miniaturization of device dimensions in microelectronics has been pushing the development of advandced thin film deposition techniques. The needs for good

surface coverage on high aspect ratio substrates, and the precise control of film thickness would drive more and more processes shifting from PVD and CVD to ALD. For example, so far, ALD processes have been developed and commercialized for high-k dielectric layers, TaN diffusion barriers and Cu electroplating seed layers.

Low temperature ALD and ALD related processes have greatly expanded the fields of ALD. ALD on polymer, biological, and hybrid materials has become a sustainable and important research area. More and more researchers start using ALD as a platform technique to get conformal functional coatings. Although many ALD process are known on a wide range of polymer substrates, the nucleation and growth mechanism on polymers needs to be carefully studied. Moreover, the interaction between ALD precursors and polymer substrates during the ALD process need to be explored.

A number of ALD related processes have been introduced in the last several years, such as molecular layer deposition, multipulse vapor infiltration and sequential vapor infiltration. The introduction of these process could further expand the application fields of ALD chemistry.

Although a large number of materials have been deposited by ALD, there are some important materials haven't been demonstrated by ALD process. New ALD/MLD chemistries and processes would keep driving the advancement of ALD.

One of the important drawbacks of ALD process is its slowness. The slow growth rate of ALD film has limited its comercialization. More and more research has been focused on improving the throughput of ALD process. For example, various spacial ALD process and atomosphere process have been developed.

Prospects of ALD are promising. We would see more ALD and related processes in the near future. it is going to find more and more applications in bio, energy and nanomaterials.

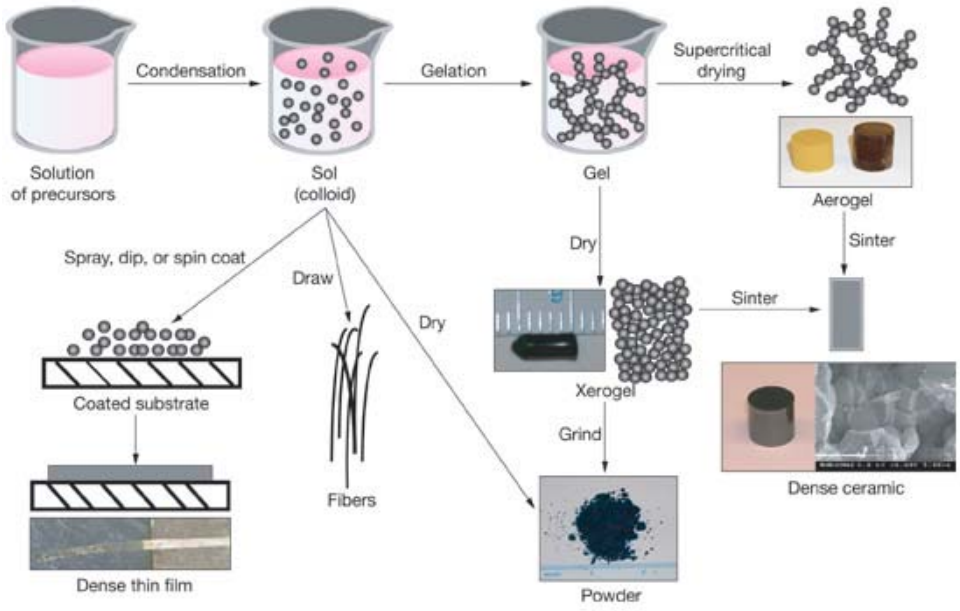


Figure 1.1. A overview of the sol gel process. In sol gel chemistry, molecular precursors are converted to nanoparticles to form a colloidal suspension, or sol. The gel network can be produced by further condensation. The gel can be processed by various drying methods to develop materials with distinct properties. (https://www.llnl.gov/str/May05/Satcher.html)

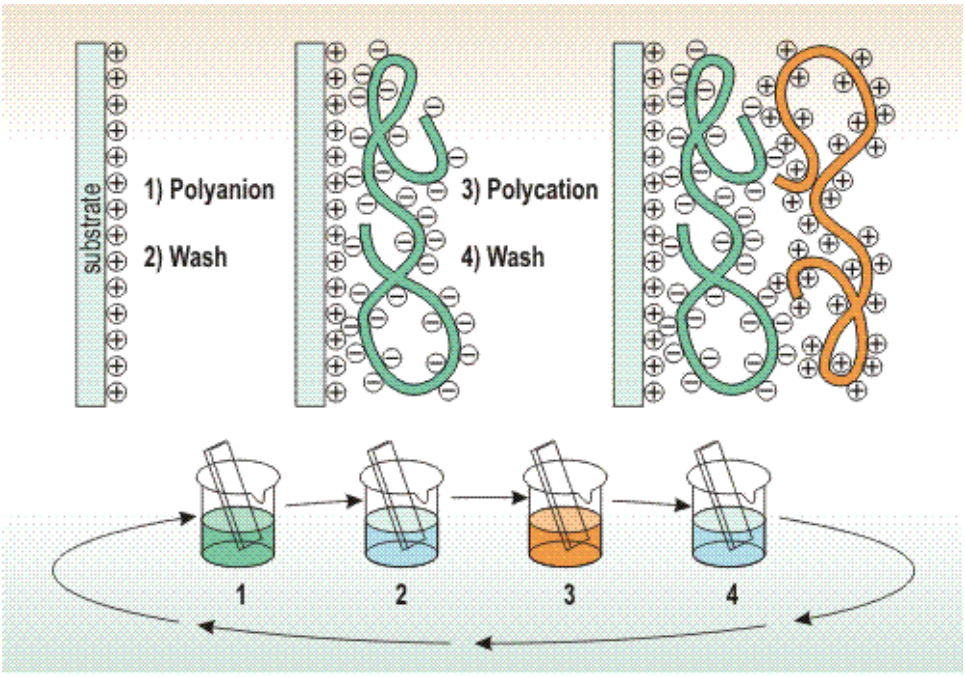


Figure 1.2. The layer by layer (LBL) process and the structure of LBL films. 1) solution of positive polyelectrolyte, 2) pure deionized water, 3) solution of negative polyelectrolyte, 4) pure deionized water.

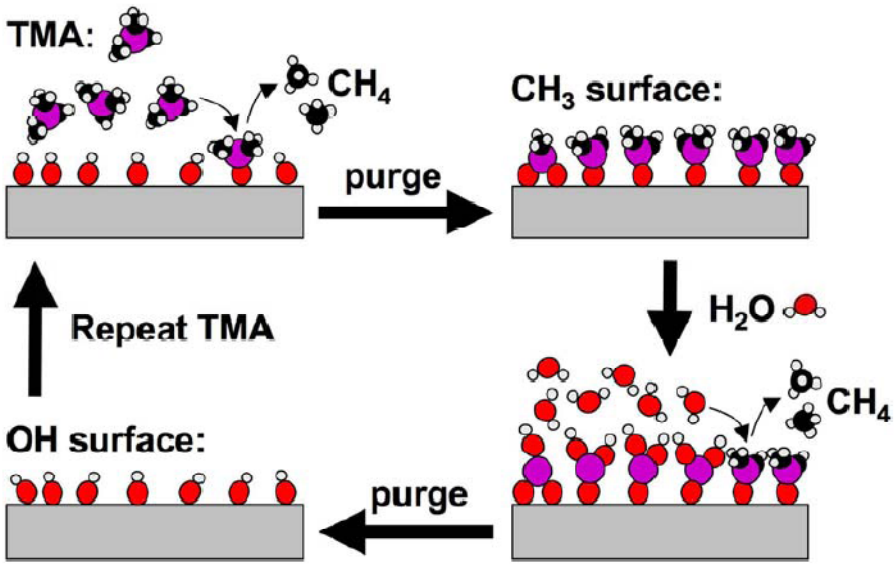


Figure 1.3. A schematic diagram of atomic layer deposition (ALD) of Al_2O_3. Trimethyl aluminum (TMA) and water are used as precursors to react with surface alternatively.

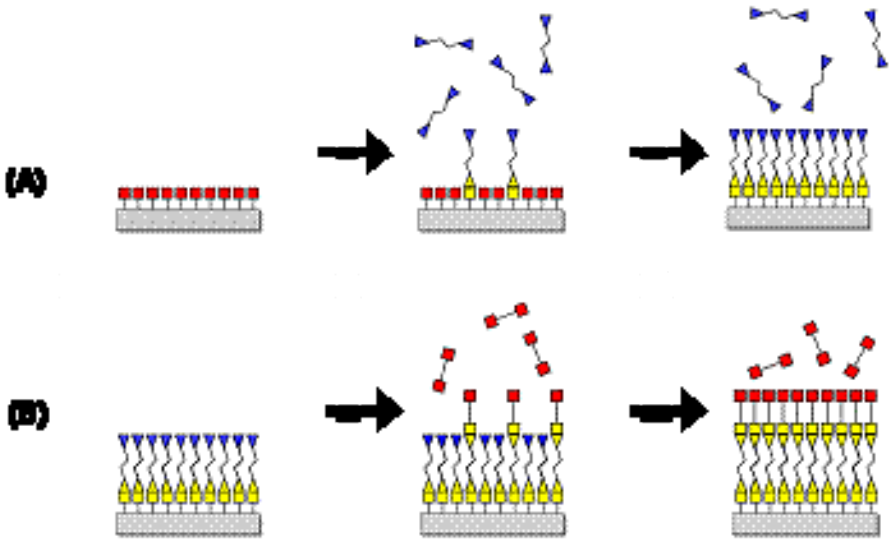


Figure 1.4. A schematic diagram for molecular layer deposition (MLD). (A) Organic precursor A reacts with surface functional groups. (B) Organic precursor B reacts with precursor A saturated surface.

References

1 L. L. Hench; J. K. West; The sol-gel process, *Chemical Reviews,* **1990**. *90*, 33.

2 B. L. Cushing; V. L. Kolesnichenko; C. J. O'Connor; Recent advances in the liquid-phase syntheses of inorganic nanoparticles, *Chemical Reviews,* **2004**. *104*, 3893.

3 J. Livage; M. Henry; C. Sanchez; Sol-gel chemistry of transition-metal oxides, *Progress in Solid State Chemistry,* **1988**. *18*, 259.

4 Y. F. Lu; R. Ganguli; C. A. Drewien; M. T. Anderson; C. J. Brinker; W. L. Gong; Y. X. Guo; H. Soyez; B. Dunn; M. H. Huang; J. I. Zink; Continuous formation of supported cubic and hexagonal mesoporous films by sol gel dip-coating, *Nature,* **1997**. *389*, 364.

5 R. A. Caruso; M. Antonietti; Sol-gel nanocoating: An approach to the preparation of structured materials, *Chemistry of Materials,* **2001**. *13*, 3272.

6 R. A. Caruso; J. H. Schattka; A. Greiner; Titanium dioxide tubes from sol-gel coating of electrospun polymer fibers, *Advanced Materials,* **2001**. *13*, 1577.

7 I. Ichinose; H. Senzu; T. Kunitake; A surface sol-gel process of TiO2 and other metal oxide films with molecular precision, *Chemistry of Materials,* **1997**. *9*, 1296.

8 H. Brunner; T. Vallant; U. Mayer; H. Hoffmann; Stepwise Growth of Ultrathin SiOx Films on Si(100) Surfaces through Sequential Adsorption/Oxidation Cycles of Alkylsiloxane Monolayers, *Langmuir,* **1996**. *12*, 4614.

9 T. Chirayil; P. Y. Zavalij; M. S. Whittingham; Hydrothermal synthesis of vanadium oxides, *Chemistry of Materials,* **1998**. *10*, 2629.

10 L. Kavan; M. Kalbac; M. Zukalova; I. Exnar; V. Lorenzen; R. Nesper; M. Graetzel; Lithium storage in nanostructured TiO2 made by hydrothermal growth, *Chemistry of Materials,* **2004**. *16*, 477.

11 F. F. Lange; Chemical solution routes to single-crystal thin films, *Science,* **1996**. *273*, 903.

12 M.-M. Titirici; M. Antonietti; A. Thomas; A generalized synthesis of metal oxide hollow spheres using a hydrothermal approach, *Chemistry of Materials,* **2006**. *18*, 3808.

13 N. Ishizawa; H. Banno; M. Hayashi; S. E. Yoo; M. Yoshimura; Preparation of BaTiO3 and SrTiO3 polycrystalline thin-films on flexible polymer film substrate by hydrothermal method, *Japanese Journal of Applied Physics Part 1-Regular Papers Short Notes & Review Papers,* **1990**. *29*, 2467.

14 C. Y. Lee; S. Y. Li; P. Lin; T. Y. Tseng; ZnO nanowires hydrothermally grown on PET polymer substrates and their characteristics, *Journal of Nanoscience and Nanotechnology,* **2005**. *5*, 1088.

15 Z. B. Wu; N. Kumagai; M. Yoshimura; Hydrothermal formation and growth of single- and double-layer BaTiO3 and SrTiO3 films on the flexible polymer film substrates from sol-gel amorphous titanium oxide films, *Chemistry of Materials,* **2000**. *12*, 3356.

16 H. Zhang; D. Yang; Y. J. Ji; X. Y. Ma; J. Xu; D. L. Que; Low temperature synthesis of flowerlike ZnO nanostructures by cetyltrimethylammonium bromide-assisted hydrothermal process, *Journal of Physical Chemistry B,* **2004**. *108*, 3955.

17 S. Inagaki; S. Guan; T. Ohsuna; O. Terasaki; An ordered mesoporous organosilica hybrid material with a crystal-like wall structure, *Nature,* **2002**. *416*, 304.

18 M. H. Lim; A. Stein; Comparative studies of grafting and direct syntheses of inorganic-organic hybrid mesoporous materials, *Chemistry of Materials,* **1999**. *11*, 3285.

19 D. Margolese; J. A. Melero; S. C. Christiansen; B. F. Chmelka; G. D. Stucky; Direct syntheses of ordered SBA-15 mesoporous silica containing sulfonic acid groups, *Chemistry of Materials,* **2000**. *12*, 2448.

20 P. T. Tanev; T. J. Pinnavaia; Mesoporous silica molecular sieves prepared by ionic and neutral surfactant templating: A comparison of physical properties, *Chemistry of Materials,* **1996**. *8*, 2068.

21 H. K. Chae; D. Y. Siberio-Perez; J. Kim; Y. Go; M. Eddaoudi; A. J. Matzger; M. O'Keeffe; O. M. Yaghi; A route to high surface area, porosity and inclusion of large molecules in crystals, *Nature,* **2004**. *427*, 523.

22 M. Eddaoudi; J. Kim; N. Rosi; D. Vodak; J. Wachter; M. O'Keeffe; O. M. Yaghi; Systematic design of pore size and functionality in isoreticular MOFs and their application in methane storage, *Science,* **2002**. *295*, 469.

23 N. W. Ockwig; O. Delgado-Friedrichs; M. O'Keeffe; O. M. Yaghi; Reticular chemistry: Occurrence and taxonomy of nets and grammar for the design of frameworks, *Accounts of Chemical Research,* **2005**. *38*, 176.

24 N. L. Rosi; J. Eckert; M. Eddaoudi; D. T. Vodak; J. Kim; M. O'Keeffe; O. M. Yaghi; Hydrogen storage in microporous metal-organic frameworks, *Science,* **2003**. *300*, 1127.

25 G. Decher; Fuzzy nanoassemblies: Toward layered polymeric multicomposites, *Science,* **1997**. *277*, 1232.

26 E. Donath; G. B. Sukhorukov; F. Caruso; S. A. Davis; H. Mohwald; Novel hollow polymer shells by colloid-templated assembly of polyelectrolytes, *Angewandte Chemie-International Edition,* **1998**. *37*, 2202.

27 P. T. Hammond; Form and function in multilayer assembly: New applications at the nanoscale, *Advanced Materials,* **2004**. *16*, 1271.

28 C. S. Peyratout; L. Dahne; Tailor-made polyelectrolyte microcapsules: From multilayers to smart containers, *Angewandte Chemie-International Edition,* **2004**. *43*, 3762.

29 R. A. Caruso; A. Susha; F. Caruso; Multilayered titania, silica, and Laponite nanoparticle coatings on polystyrene colloidal templates and resulting inorganic hollow spheres, *Chemistry of Materials,* **2001**. *13*, 400.

30 H. Lee; S. M. Dellatore; W. M. Miller; P. B. Messersmith; Mussel-inspired surface chemistry for multifunctional coatings, *Science,* **2007**. *318*, 426.

31 M. A. C. Stuart; W. T. S. Huck; J. Genzer; M. Mueller; C. Ober; M. Stamm; G. B. Sukhorukov; I. Szleifer; V. V. Tsukruk; M. Urban; F. Winnik; S. Zauscher; I. Luzinov; S. Minko; Emerging applications of stimuli-responsive polymer materials, *Nature Materials,* **2010**. *9*, 101.

32 L. Y. Wang; R. X. Yan; Z. Y. Hao; L. Wang; J. H. Zeng; H. Bao; X. Wang; Q. Peng; Y. D. Li; Fluorescence resonant energy transfer biosensor based on upconversion-luminescent nanoparticles, *Angewandte Chemie-International Edition,* **2005**. *44*, 6054.

33 L. M. Ang; T. S. A. Hor; G. Q. Xu; C. H. Tung; S. P. Zhao; J. L. S. Wang; Decoration of activated carbon nanotubes with copper and nickel, *Carbon,* **2000**. *38*, 363.

34 V. M. Dubin; Y. ShachamDiamand; B. Zhao; P. K. Vasudev; C. H. Ting; Selective and blanket electroless copper deposition for ultralarge scale integration, *Journal of the Electrochemical Society,* **1997**. *144*, 898.

35 F. Z. Kong; X. B. Zhang; W. Q. Xiong; F. Liu; W. Z. Huang; Y. L. Sun; J. P. Tu; X. W. Chen; Continuous Ni-layer on multiwall carbon nanotubes by an electroless plating method, *Surface & Coatings Technology,* **2002**. *155*, 33.

36 Y. Kobayashi; V. Salgueirino-Maceira; L. M. Liz-Marzan; Deposition of sliver nanoparticles on silica spheres by pretreatment steps in electroless plating, *Chemistry of Materials,* **2001**. *13*, 1630.

37 L. A. Porter; H. C. Choi; A. E. Ribbe; J. M. Buriak; Controlled electroless deposition of noble metal nanoparticle films on germanium surfaces, *Nano Letters,* **2002**. *2*, 1067.

38 K. Sarakinos; J. Alami; S. Konstantinidis; High power pulsed magnetron sputtering: A review on scientific and engineering state of the art, *Surface & Coatings Technology,* **2010**. *204*, 1661.

39 A. Matthews; Plasma-based physical vapor deposition surface engineering processes, *Journal of Vacuum Science & Technology A,* **2003**. *21*, S224.

40 M. J. Hampdensmith; T. T. Kodas; Chemical-Vapor-Deposition of Metals .1. An Overview of CVD Processes, *Chemical Vapor Deposition,* **1995**. *1*, 8.

41 J. Murota; M. Sakuraba; B. Tillack; Atomically controlled processing for group IV semiconductors by chemical vapor deposition, *Japanese Journal of Applied Physics Part 1-Regular Papers Brief Communications & Review Papers,* **2006**. *45*, 6767.

42 D. R. Cote; S. V. Nguyen; A. K. Stamper; D. S. Armbrust; D. Tobben; R. A. Conti; G. Y. Lee; Plasma-assisted chemical vapor deposition of dielectric thin films for ULSI semiconductor circuits, *Ibm Journal of Research and Development,* **1999**. *43*, 5.

43 K. L. Choy; Chemical vapour deposition of coatings, *Progress in Materials Science,* **2003**. *48*, 57.

44 T. Suntola; ATOMIC LAYER EPITAXY, *Thin Solid Films,* **1992**. *216*, 84.

45 G. Stuyven; P. De Visschere; A. Hikavyy; K. Neyts; Atomic layer deposition of ZnS thin films based on diethyl zinc and hydrogen sulfide, *Journal of Crystal Growth,* **2002**. *234*, 690.

46 L. Niinisto; J. Paivasaari; J. Niinisto; M. Putkonen; M. Nieminen; Advanced electronic and optoelectronic materials by Atomic Layer Deposition: An overview with special emphasis on recent progress in processing of high-k dielectrics and other oxide materials, *Physica Status Solidi a-Applied Research,* **2004**. *201*, 1443.

47 J. P. Chang; Y. S. Lin; Dielectric property and conduction mechanism of ultrathin zirconium oxide films, *Applied Physics Letters,* **2001**. *79*, 3666.

48 M. D. Groner; J. W. Elam; F. H. Fabreguette; S. M. George; Electrical characterization of thin Al2O3 films grown by atomic layer deposition on silicon and various metal substrates, *Thin Solid Films,* **2002**. *413*, 186.

49 S. K. Kim; W. D. Kim; K. M. Kim; C. S. Hwang; J. Jeong; High dielectric constant TiO2 thin films on a Ru electrode grown at 250 degrees C by atomic-layer deposition, *Applied Physics Letters,* **2004**. *85*, 4112.

50 J. Robertson; High dielectric constant oxides, *European Physical Journal-Applied Physics,* **2004**. *28*, 265.

51 M. D. Groner; F. H. Fabreguette; J. W. Elam; S. M. George; Low-temperature Al2O3 atomic layer deposition, *Chemistry of Materials,* **2004**. *16*, 639.

52 R. L. Puurunen; Surface chemistry of atomic layer deposition: A case study for the trimethylaluminum/water process, *Journal of Applied Physics,* **2005**. *97*,

53 N. M. Adamczyk; A. A. Dameron; S. M. George; Molecular layer deposition of poly(p-phenylene terephthalamide) films using terephthaloyl chloride and p-phenylenediamine, *Langmuir : the ACS journal of surfaces and colloids,* **2008**. *24*, 2081.

54 A. A. Dameron; D. Seghete; B. B. Burton; S. D. Davidson; A. S. Cavanagh; J. A. Bertrand; S. M. George; Molecular layer deposition of alucone polymer films using trimethylaluminum and ethylene glycol, *Chemistry of Materials,* **2008**. *20*, 3315.

55 Y. Du; S. M. George; Molecular layer deposition of nylon 66 films examined using in situ FTIR spectroscopy, *Journal of Physical Chemistry C,* **2007**. *111*, 8509.

56 S. M. George; B. Yoon; A. A. Dameron; Surface Chemistry for Molecular Layer Deposition of Organic and Hybrid Organic-Inorganic Polymers, *Accounts of Chemical Research,* **2009**. *42*, 498.

57 B. H. Lee; M. K. Ryu; S.-Y. Choi; K.-H. Lee; S. Im; M. M. Sung; Rapid vapor-phase fabrication of organic-inorganic hybrid superlattices with monolayer precision, *Journal of the American Chemical Society,* **2007**. *129*, 16034.

58 Q. Peng; B. Gong; R. M. VanGundy; G. N. Parsons; "Zincone" Zinc Oxide-Organic Hybrid Polymer Thin Films Formed by Molecular Layer Deposition, *Chemistry of Materials,* **2009**. *21*, 820.

59 N. M. Adarnczyk; A. A. Dameron; S. M. George; Molecular layer deposition of poly(p-phenylene terephthalamide) films using terephthaloyl chloride and p-phenylenediamine, *Langmuir,* **2008**. *24*, 2081.

60 T. Bitzer; N. V. Richardson; Demonstration of an imide coupling reaction on a Si(100)-2x1 surface by molecular layer deposition, *Applied Physics Letters,* **1997**. *71*, 662.

61 P. W. Loscutoff; H. Zhou; S. B. Clendenning; S. F. Bent; Formation of Organic Nanoscale Laminates and Blends by Molecular Layer Deposition, *Acs Nano,* **2010**. *4*, 331.

62 B. Yoon; J. L. O'Patchen; D. Seghete; A. S. Cavanagh; S. M. George; Molecular Layer Deposition of Hybrid Organic-Inorganic Polymer Films using Diethylzinc and Ethylene Glycol, *Chemical Vapor Deposition,* **2009**. *15*, 112.

63 B. Yoon; D. Seghete; A. S. Cavanagh; S. M. George; Molecular Layer Deposition of Hybrid Organic-Inorganic Alucone Polymer Films Using a Three-Step ABC Reaction Sequence, *Chemistry of Materials,* **2009**. *21*, 5365.

64 J. D. Ferguson; A. W. Weimer; S. M. George; Atomic layer deposition of Al2O3 films on polyethylene particles, *Chemistry of Materials,* **2004**. *16*, 5602.

65 X. D. Wang; C. S. Lao; E. Graugnard; C. J. Summers; Z. L. Wang; Large-size liftable inverted-nanobowl sheets as reusable masks for nanolithiography, *Nano Letters,* **2005**. *5*, 1784.

66 Q. Peng; X.-Y. Sun; J. C. Spagnola; G. K. Hyde; R. J. Spontak; G. N. Parsons; Atomic layer deposition on electrospun polymer fibers as a direct route to Al2O3 microtubes with precise wall thickness control, *Nano Letters,* **2007**. *7*, 719.

67 Q. Peng; Y.-C. Tseng; S. B. Darling; J. W. Elam; Nanoscopic Patterned Materials with Tunable Dimensions via Atomic Layer Deposition on Block Copolymers, *Advanced Materials,* **2010**. *22*, 5129.

68 R. H. A. Ras; M. Kemell; J. de Wit; M. Ritala; G. ten Brinke; M. Leskela; O. Ikkala; Hollow inorganic nanospheres and nanotubes with tunable wall thicknesses by atomic layer deposition on self-assembled polymeric templates, *Advanced Materials,* **2007**. *19*, 102.

69 M. Knez; A. Kadri; C. Wege; U. Gosele; H. Jeske; K. Nielsch; Atomic layer deposition on biological macromolecules: Metal oxide coating of tobacco mosaic virus and ferritin, *Nano Letters,* **2006**. *6*, 1172.

70 D. P. Gaillot; O. Deparis; V. Welch; B. K. Wagner; J. P. Vigneron; C. J. Summers; Composite organic-inorganic butterfly scales: Production of photonic structures with atomic layer deposition, *Physical Review E,* **2008**. *78*,

71 G. K. Hyde; G. Scarel; J. C. Spagnola; Q. Peng; K. Lee; B. Gong; K. G. Roberts; K. M. Roth; C. A. Hanson; C. K. Devine; S. M. Stewart; D. Hojo; J.-S. Na; J. S. Jur; G. N. Parsons; Atomic Layer Deposition and Abrupt Wetting Transitions on Nonwoven Polypropylene and Woven Cotton Fabrics, *Langmuir,* **2010**. *26*, 2550.

72 J. S. Jur; J. C. Spagnola; K. Lee; B. Gong; Q. Peng; G. N. Parsons; Temperature-Dependent Subsurface Growth during Atomic Layer Deposition on Polypropylene and Cellulose Fibers, *Langmuir,* **2010**. *26*, 8239.

73 J. C. Spagnola; B. Gong; S. A. Arvidson; J. S. Jur; S. A. Khan; G. N. Parsons; Surface and sub-surface reactions during low temperature aluminium oxide atomic layer deposition on fiber-forming polymers, *Journal of Materials Chemistry,* **2010**. *20*, 4213.

74 C. A. Wilson; R. K. Grubbs; S. M. George; Nucleation and growth during Al2O3 atomic layer deposition on polymers, *Chemistry of Materials,* **2005**. *17*, 5625.

75 L. Zhang; A. J. Patil; L. Li; A. Schierhorn; S. Mann; U. Goesele; M. Knez; Chemical Infiltration during Atomic Layer Deposition: Metalation of Porphyrins as Model Substrates, *Angewandte Chemie-International Edition,* **2009**. *48*, 4982.

76 S.-M. Lee; E. Pippel; U. Goesele; C. Dresbach; Y. Qin; C. V. Chandran; T. Braeuniger; G. Hause; M. Knez; Greatly Increased Toughness of Infiltrated Spider Silk, *Science,* **2009**. *324*, 488.

77 B. Gong; Q. Peng; J. S. Jur; C. K. Devine; K. Lee; G. N. Parsons; Sequential Vapor Infiltration of Metal Oxides into Sacrificial Polyester Fibers: Shape Replication and Controlled Porosity of Microporous/Mesoporous Oxide Monoliths, *Chemistry of Materials,* **2011**. *23*, 3476.

78 B. Gong; J. C. Spagnola; G. N. Parsons; Hydrophilic mechanical buffer layers and stable hydrophilic finishes on polydimethylsiloxane using combined sequential vapor infiltration and atomic/molecular layer deposition, *Journal of Vacuum Science & Technology A,* **2012**. *30*,

79 X. Y. Zhang; J. Y. Dai; H. C. Ong; N. Wang; H. L. W. Chan; C. L. Choy; Hydrothermal synthesis of oriented ZnO nanobelts and their temperature dependent photoluminescence, *Chemical Physics Letters,* **2004**. *393*, 17.

80 L. Vayssieres; K. Keis; S. E. Lindquist; A. Hagfeldt; Purpose-built anisotropic metal oxide material: 3D highly oriented microrod array of ZnO, *Journal of Physical Chemistry B,* **2001**. *105*, 3350.

81 R. B. M. Cross; M. M. De Souza; E. M. S. Narayanan; A low temperature combination method for the production of ZnO nanowires, *Nanotechnology,* **2005**. *16*, 2188.

82 J.-S. Na; B. Gong; G. Scarel; G. N. Parsons; Surface Polarity Shielding and Hierarchical ZnO Nano-Architecture Engineering using Sequential Hydrothermal Crystal Synthesis and Thin Film Atomic Layer Deposition, *ACS Nano,* **2009**. *3*, 3191.

83 G. K. Hyde; K. J. Park; S. M. Stewart; J. P. Hinestroza; G. N. Parsons; Atomic layer deposition of Conformal inorganic nanoscale coatings on three-dimensional natural fiber systems: Effect of surface topology on film growth characteristics, *Langmuir,* **2007**. *23*, 9844.

84 G. K. Hyde; G. Scarel; J. C. Spagnola; Q. Peng; K. Lee; B. Gong; K. G. Roberts; K. M. Roth; C. A. Hanson; C. K. Devine; S. M. Stewart; D. Hojo; J. S. Na; J. S. Jur; G. N. Parsons; Atomic Layer Deposition and Abrupt Wetting Transitions on Nonwoven Polypropylene and Woven Cotton Fabrics, *Langmuir,* **2010**. *26*, 2550.

85 M. Kemell; V. Pore; M. Ritala; M. Leskela; M. Linden; Atomic Layer Deposition in Nanometer-Level Replication of Cellulosic Substances and Preparation of Photocatalytic TiO2/Cellulose Composites, *Journal of the American Chemical Society,* **2005**. *127*, 14178.

86 Q. Peng; X. Y. Sun; J. C. Spagnola; G. K. Hyde; R. J. Spontak; G. N. Parsons; Atomic layer deposition on electrospun polymer fibers as a direct route to Al2O3 microtubes with precise wall thickness control, *Nano Letters,* **2007**. *7*, 719.

87 M. Kemell; V. Pore; M. Ritala; M. Leskela; Ir/Oxide/Cellulose Composites for Catalytic Purposes Prepared by Atomic Layer Deposition, *Chemical Vapor Deposition,* **2006**. *12*, 419.

88 S. M. Lee; G. Grass; G. M. Kim; C. Dresbach; L. B. Zhang; U. Gosele; M. Knez; Low-temperature ZnO atomic layer deposition on biotemplates: flexible photocatalytic ZnO structures from eggshell membranes, *Physical Chemistry Chemical Physics,* **2009**. *11*, 3608.

89 S. M. Lee; E. Pippel; U. Gosele; C. Dresbach; Y. Qin; C. V. Chandran; T. Brauniger; G. Hause; M. Knez; Greatly Increased Toughness of Infiltrated Spider Silk, *Science,* **2009**. *324*, 488.

90 P. Küsgens; S. Siegle; S. Kaskel; Crystal Growth of the Metal—Organic Framework Cu3(BTC)2 on the Surface of Pulp Fibers, *Advanced Engineering Materials,* **2009**. *11*, 93.

91 M. Rose; B. Böhringer; M. Jolly; R. Fischer; S. Kaskel; MOF Processing by Electrospinning for Functional Textiles, *Advanced Engineering Materials,* **2011**. *13*, 356.

92 O. Shekhah; H. Wang; S. Kowarik; F. Schreiber; M. Paulus; M. Tolan; C. Sternemann; F. Evers; D. Zacher; R. A. Fischer; C. Woll; Step-by-step route for the synthesis of metal-organic frameworks, *Journal of the American Chemical Society,* **2007**. *129*, 15118.

93 C. Munuera; O. Shekhah; H. Wang; C. Woell; C. Ocal; The controlled growth of oriented metal-organic frameworks on functionalized surfaces as followed by scanning force microscopy, *Physical Chemistry Chemical Physics,* **2008**. *10*, 7257.

94 O. Shekhah; J. Liu; R. A. Fischer; C. Woell; MOF thin films: existing and future applications, *Chemical Society Reviews,* **2011**. *40*, 1081.

95 O. Shekhah; H. Wang; M. Paradinas; C. Ocal; B. Schuepbach; A. Terfort; D. Zacher; R. A. Fischer; C. Woell; Controlling interpenetration in metal-organic frameworks by liquid-phase epitaxy, *Nature Materials,* **2009**. *8*, 481.

96 O. Shekhah; H. Wang; T. Strunskus; P. Cyganik; D. Zacher; R. Fischer; C. Woell; Layer-by-layer growth of oriented metal organic polymers on a functionalized organic surface, *Langmuir,* **2007**. *23*, 7440.

97 O. Shekhah; H. Wang; D. Zacher; R. A. Fischer; C. Woell; Growth Mechanism of Metal-Organic Frameworks: Insights into the Nucleation by Employing a Step-by-Step Route, *Angewandte Chemie-International Edition,* **2009**. *48*, 5038.

98 K. Yusenko; M. Meilikhov; D. Zacher; F. Wieland; C. Sternemann; X. Stammer; T. Ladnorg; C. Woell; R. A. Fischer; Step-by-step growth of highly oriented and continuous seeding layers of Cu(2)(ndc)(2)(dabco) on bare oxide and nitride substrates, *Crystengcomm,* **2010**. *12*, 2086.

99 S. Hermes; D. Zacher; A. Baunemann; C. Woell; R. A. Fischer; Selective growth and MOCVD loading of small single crystals of MOF-5 at alumina and silica surfaces modified with organic self-assembled monolayers, *Chemistry of Materials,* **2007**. *19*, 2168.

100 B. Gong; Q. Peng; G. N. Parsons; Conformal Organic - Inorganic Hybrid Network Polymer Thin Films by Molecular Layer Deposition using Trimethylaluminum and Glycidol, *Journal of Physical Chemistry B,* **2011**. *115*, 5930.

101 B. Gong; Q. Peng; J. S. Na; G. N. Parsons; Highly active photocatalytic ZnO nanocrystalline rods supported on polymer fiber mats: Synthesis using atomic layer deposition and hydrothermal crystal growth, *Applied Catalysis a-General,* **2011**. *407*, 211.

102 M. Leskela; M. Ritala; Atomic layer deposition (ALD): from precursors to thin film structures, *Thin Solid Films,* **2002**. *409*, 138.

CHAPTER 2. Experimental Tools

2.1 Atomic Layer Deposition and Molecular Layer Deposition Systems

Atomic and molecular layer thin film deposition studies were carried out in a homemade hot wall viscous flow vacuum reactor equipped with in-situ quartz crystal microbalance (QCM) as described in Figure 2.1.[1] To protect the pump system during reaction, the exhaust from the organic and metal-organic exposure steps were pumped through independent exhaust lines using computer-controlled gate valves. A liquid nitrogen trap was installed in the organic exhaust line before the pump to trap any organic effluent before it reached the pump. The film deposition precursors (TMA, DEZ and DI–H_2O) were stored in separate stainless steel bottles and evaporated at 25 °C. During the predetermined gas exposure time, a computer–controlled ALD solenoid valve opened to allow the effluent vapor to mix into flowing argon carrier gas. The glycidol liquid was loaded into a gas bubbler and heated at 60°C, and during the glycidol exposure period, argon gas bubbled through the vessel and into the reactor. After each precursor or reactant exposure step, argon gas continued to flow to purge the reactor or any remaining reactant or product vapor. The steady-state process pressure was ~1.1 Torr and the total argon flow rate was approximately 200 standard cubic centimeters per minute. During TMA, DEZ, H_2O and GYL dose times, the reactor pressure increased by approximately 150, 100, 50 and 50 mTorr, respectively. A range of reactant exposure times were evaluated during steady state growth. A typical deposition cycle followed a TMA/Ar/glycidol/Ar sequence where the exposure or purge times were 1/40/2/40 seconds, respectively. As shown below, we obtained fully saturated

growth resulting in ~8 nm per cycle at 90°C using TMA/Ar/glycidol/Ar exposure times of 5/90/10/90 seconds. For conciseness, the written reaction sequences include only the pertinent reactants, i.e., "TMA/Ar/glycidol/Ar" is written as "TMA/GLY" or "TMA/glycidol".[2]

Sequential vapor infiltration was conducted in the same ALD/MLD reactor. A modified precursor exposure sequence was used for SVI experiment. SVI process used a sequence of 60 exposure steps, where each exposure step included flowing TMA into the reactor for 10 seconds followed by sealing the reactor at fixed pressure (~ 2 Torr) for 60 seconds, then purging the reactor with argon for 20 seconds. This sequence corresponded to one TMA "soak" cycle. After 60 TMA soak steps (a total soak time of one hour), the reactor was purged with Ar for 15 mins, then 20 water soak steps were performed using the same timing sequence before removing the sample from the reactor. For some fiber samples, a long continuous soak scheme was used, which included a exposure the sample to ~7 Torr of TMA or TiCl4 vapor for ~ 18 hr, followed by a purge with Ar for 30 mins and a soak in 5 Torr of water vapor for ~1 hr.

2.2 Spin-coating and Electro-spinning of Polymers

2.2.1 Spin-coating of Polymer Films

Polymer films on Si wafer were prepared by dissolve the polymer fibers or powder in organic solvent, and then spin coated on Si wafer at the room temperature, using a Laurell WS-400-6NPP ø150mm spin coater. All the Si wafer used for film casting, was first dip into a JTP® cleaning solution for 2 mins, and rinse under DI water for 5 mins, and blow dry

under the high purity N_2 (99%). For example, PP film on Si wafer was prepared by first dissolve PP nonwoven fibers mat in DHN at 80 °C to get 1 w% solution, and then spin cast into film on Si wafer. Similarly, PVA and PEO were dissolved in water, PBT and PET were dissolved in trifluoroacetic acid (TFA), PLA was dissolved in chloroform, PMMA was dissolved in Toluene and Nylon-6 was dissolved in formic acid to cast the object film.

2.2.2 Electro-spinning of Polymer Fibers

Poly(vinyl alcohol) (PVA) with a molecular weight of 127 kDa and a degree of hydrolysis of 88% was purchased from Aldrich and used without further purification. A 7 wt % PVA aqueous solution was prepared by dissolving PVA in deionized water (DI H_2O) at 60 °C and stirring gently for 2 h. Electrospinning was performed using the parallel-plate setup. A stable jet was formed at a flow rate of 7 μL/min and an electric field of 1 kV/cm.[3]

2.3 Liquid Phase Deposition Techniques

2.3.1 Hydrothermal

Hydrothermal growth of ZnO nanorods on PBT fiber mat was conducted in a Teflon beaker. After ZnO ALD coating, the PBT fibers and silicon control wafer were transferred into a Teflon vessel containing 30 ml aqueous solution of equimolar (20mM) zinc nitrate hexahydrate ($Zn(NO_3)\cdot 6H_2O$, 99% Aldrich) and hexamethylene tetramine ($C_6H_{12}N_4$, 99% Aldrich). The vessel was left open and held in an oven at 96 °C for 6 hr resulting in the growth of ZnO nanorod crystals on the ZnO coated silicon and PBT substrates. The silicon wafer was held face-down in the solution to prevent the precipitation of any ZnO particles that may have formed in the solution bulk. After growth, the PBT fiber mat and Si wafer

were rinsed with deionized water for 2 mins, and then dried in N_2 flow at room temperature. Seed layer thicknesses of ~20 and 40 nm were investigated.[4,5]

Hydrothermal growth of MOF (HKUST-1) was conducted in a stainless pressured vessel. Firstly, 4mM of Benzene tri carboxylic acid (BTC) was dissolved in 24 ml of ethanol, and 7.2mM of copper nitrate trihydrate [$Cu(NO_3)_2 \cdot 3H_2O$] was dissolved in 24ml water. The two solutions were mixed together in the pressured vessel with the PP fiber samples. Then the pressured vessel was heated to 120 °C for 18 hours. After cooled down, the sample was rinsed with ethanol for 3 times.[6]

2.3.2 Layer by Layer MOF Assembly

We attached the metal organic framework HKUST-1 [$Cu_3(btc)_2$] in a layer by layer (LBL) fashion. The ALD seeded PP fiber mat was first dipped in a 1mM benzene tri-carboxylic acid (BTC) ethanol solution for 1 hour. After washed with ethanol for 5 mins, the PP fiber mat was then dipped in a 1mM copper acetate monohydrate [$Cu(CH_3COO)_2 \cdot H_2O$] ethanol solution for another 1 hour. Finally, the fiber mat was washed again with ethanol for 5 mins. This dip and wash process was considered as a growth cycle. Various MOF loading amount could be achieved by controlling the growth cycles. [7]

2.4 Materials Characterization

2.4.1 Ellipsometry

A variable-angle alpha-SE spectroscopic ellipsometry (J.A. Woollam Co., Inc.), including a three-layer (ALD,MLD film/native oxide/silicon) Cauchy model, allowed for

film thickness and reactive index measurement. In the model, thickness of native oxide was 20 Å, and the Si substrate was 400 microns.

2.4.2 Quartz Crystal Microbalance

Quartz crystal microbalance (QCM) measures the mass change by detecting the vibration frequency of the quartz crystal resonator. There is a linear relation between the mass change and the frequency shift. By measuring the frequency shift, we could calculate the mass uptake or remove on the quartz crystal surface.[8]

The in-situ QCM was installed onto the deposition reactor system through the inlet of the reactor as show in Figure 2.1. Polished QCM crystal sensors with Au coating (Colorado Crystal Corp.) were mounted in the Maxtek BSH-150 bakeable sensor head. The sensor head was modified to allow ~10 sccm of Ar flow over the back side of the sensor, and the crystal was sealed to the QCM housing using conductive epoxy to prevents material from depositing onto the backside of the crystal surface.[1,8] The mass change signals were detected and recorded by a film thickness monitor (Maxtek TM-400), using a home designed LABVIEW program to record the data.[1,2] Two kinds of quartz crystals were used for experiment. One with polished gold surface, and another one with unpolished surface. The unpolished crystal will give larger mass uptake values due to the surface roughness.

2.4.3 Vibration Spectroscopy (FTIR, UV-Vis)

The infrared (IR) transmittance spectroscopy is used to measure how much a sample absorbs infrared at each wavelength. When the IR radiation frequency matches the vibration frequency of certain chemical structures, the resonance effect would result in absorption of

IR radiation in this frequency. Because this vibration frequency is determined by the molecular structure, bond energy, and the atom weight, the IR spectroscopy could be used to characterize this information. Since a molecule could vibrate in different ways, such as stretching, bending, rocking, and wagging, a number of vibration modes could be measured by IR spectroscopy.

In our studies, material chemical composition was analyzed using transmission Fourier transform infrared spectroscopy (FTIR). Instead using a monochromatic infrared source, in the FTIR system, a polychromatic infrared source and Michelson interferometer was used. The interferometer allows some wavelengths to pass through but blocks others. By moving one of the mirrors in the interferometer, a series of wavelengths got blocked. After computer processing, the absorbance vs. wavelength can be calculated. The FTIR is less expensive than monochromatic infrared spectroscopy, and capable of measuring a range of infrared frequencies at the same time.

A Thermo Scientific Nicolet IR bench with a deuterated triglycine sulfate (DTGS) detector and KBr bean splitter was used in the transmission mode with 2050 scans at 4 cm^{-1} resolution for ex-situ measurement. The measuring chamber was continuously purged with purified dry air (ambient without water moisture). A background spectrum was collected using the starting Si wafer before the deposition.[1]

A special designed IR reactor was used for in-situ FTIR analysis in transmission mode, as shown in Figure 2.2. The IR beam was directed out from a FTIR spectrometer (Nicolet 6700, Thermo Scientific), through the vertically-mounted sample, reflected off a gold parabolic mirror and focused onto an external MCT-A (mercury cadmium telluride type

A) IR detector. The IR beam is transmitted through the reactor using two single crystal CsI IR windows. The windows permit the IR beam to cross horizontally through a 15 cm wide deposition analysis zone, where the beam path is perpendicular to the gas flow direction. Gate valves isolate the IR windows from precursor or product exposure during the reactant dose periods, and the valves are open and data collected during the argon gas purge period. Spectra were acquired with 4 cm-1 resolution and 200 scans. Before IR analysis, the AAO substrate was coated with 20 cycles of TMA/H_2O to form a reproducible Al_2O_3 starting surface. Spectra are displayed in differential mode by using the spectrum collected from the most recent half-cycle as the background reference. During the in-situ FTIR experiments, a typical TMA/GLY deposition cycle involved TMA and GLY gas exposure for 1 and 2 seconds respectively, with 120 s Ar purge and 150 s IR data collection period after each vapor exposure.[2]

The installation of an external detector involved adding a auxiliary experiment module (AEM) in the Nicolet IR bench. The jumpers on the external detector need to be configured as AEM for the system to recognize. The IR beam alignment is critical for successful in-situ FTIR measurement. For rough alignment, the red laser could help you locate the IR beam. To further fine tune the beam alignment, the relative position of the gold parabolic mirror and the IR detector need to be carefully optimized. After each beam alignment, the system needs to stabilize for at least 30 min to remove the moisture and CO_2 in the detector box. In this dissertation, AAO is used as high surface area substrate for in-situ experiment. However, it is not an ideal substrate for the FTIR measurement. It got strong IR absorbance at ~1000 cm^{-1}, which make the in-situ FTIR hard to detect the surface chemistry

change in the range of 650 to 1200 cm^{-1}. Moreover, the AAO membranes give fringes on the IR spectra due to interference. Other researchers used ZrO_2 nanoparticles packed in photo-etched tungsten grids as high surface area IR substrates. Because ZrO_2 particles do not have the IR absorbance in the range of 650 to 4000cm^{-1}, it is a better substrate for IR measurement. Additionally, the MCT-A detector was used in our experimental setup. It measures from 650 to 4000 cm^{-1}. To get broader measurement range, MCT-B detector could be used, which measures from 400 to 4000cm^{-1}. To further improve the in-situ FTIR set-up, we could further optimize the beam path configuration. Instead using a collimated beam, we could focus the IR beam onto the substrate. The focused IR beam could increase the incident IR intensity, and reduce the relative error.

UV-Vis spectrometer was used to measure the organic dye concentration in water, to access phtocatalytic effect of ZnO samples. A Thermo Scientific Evolution 300 UV-Vis spectrophotometer was used to measure the concentration of the dye as a function of time. We were able to quantify the relative rate of dye degradation and hence analyze the effective photocatalytic activity of the different ZnO samples.

2.4.4 Electron Microscopes (SEM, TEM)

Scanning Electron Microscope (SEM) images were collected by an FEI XL30 field emission SEM operating at 7 kV with a working distance of 5 mm. Before SEM imaging, samples sputter-coated with 5 nm of Au/Pd to reduce surface charging.

Transmission Electron Microscope (TEM) images were collected using a Hitachi HF cold field emission TEM operated at 200 kV with 0.2 nm point resolution. Another FEI Tecnai G^2 TWIN TEM is also used for TEM imaging.

2.4.5 Atomic Force Microscope

The surface morphology of resultant films was analyzed using a Q-Scope 250 scanning probe microscope (Quesant Instrument Corporation) in tapping mode. A Dimension 3000 atomic force microscope (Digital Instruments) was alse used for some measurements.

2.4.6 Nitrogen Adsorption/ Desorption Analysis (BET)

A Quantachrome Autosorb-1C surface area and pore size analyzer provided information on the Brunauer Emmett Teller (BET) surface area of the materials. Before each analysis, samples (~ 100 mg) were heated under vacuum at 100 °C for at least 4 hr to remove residual and moisture adsorbed. The nitrogen adsorption/ desorption isotherm was collected from the dried sample at 77K. An example isotherm collected was shown in Figure 2.3 (a). It showed how much nitrogen is adsorped on or desorped from the sample at given relative pressures. The specific surface area was calculated from the adsorption isotherm by BET (BET range, P/P_0 range from 0.05 – 0.35) method.[9] The pore size distribution was calculated from desorption isotherms by BJH method.

The Brunauer-Emmett-Teller (BET) method is the most widely used method for the determination of the surface area of porous materials. The measurement of the BET surface area involves the use of the BET equation.

$$\frac{1}{W((P_0/P)-1)} = \frac{1}{W_m C} + \frac{C-1}{W_m C}\left(\frac{P}{P_0}\right)$$

In which W is the weight of gas adsorbed at a relative pressure (P/P_0) and W_m is the weight of adsorbate constituting a momolayer of surface coverage. The term C (BET constant) is related to the adsorption energy. An example BET plot calculated from the

nitrogen adsorption isotherm was plotted in Figure 2.3 (b). By plotting $1/[W(P_0/P)-1]$ vs P/P_0, we could calculate W_m and C from the slope and intercept of the plot. The BET surface area can be estimated from the W_m.

The Barrett-Joyner-Halenda (BJH) method is widely used for the calculation of the pore size distribution of meso-porous materials. It is based on Kelvin equation.

$$ln\frac{P}{P_0} = \frac{2\gamma V_m}{rRT}$$

Where γ is the surface tension, V_m is the molar volume and r is the Kelvin radius. Kelvin equation predicts pressure at which nitrogen will spontaneously condense or evaporate in a cylindrical pore of a given size. The model is based on the assumption that pores have a cylindrical shape and that pore radius is equal to the sum of the Kelvin radius and the thickness of the film adsorbed on the pore surface. At given relative pressure (P/P_0), the Kelvin radius could be calculated. In return, the thickness of the condensed nitrogen in the pore could be estimated. Therefore, the pore size distribution can be calculated from the isotherm curves.

2.4.7 Water Contact Angle

The static water contact angle on the starting and modified surfaces was collected using a Model 200 Ramé Hart contact angle goniometer equipped with a CCD camera. After proper tool alignment, the water droplet was allowed to stabilize on the sample for a few seconds before more water was added while measurements were recorded as the droplet size increased and the interface between the water droplet and the surface of the substrate began

to advance. We measured at least five different points on each sample and the average value is reported.

2.4.8 X-ray Photoelectron Spectroscopy (XPS)

X-ray photoelectron spectroscopy (XPS) analysis utilized a Kratos Analytical Axis Ultra tool with a monochromatic Al Kα X-ray source. For all samples, C 1s peak was normalized to 284.5 eV as the reference. The pass energies for the survey and detail scans were 160 and 20 eV, respectively. A Riber XPS at Analytical instrumentation facility (NCSU) was also used for the XPS measurement. The tool is equipped with an Mg-Al dual X-ray source and a Mac 2 cylindrical mirror analyzer.

2.4.9 X-ray Diffraction (XRD)

The XRD patterns of the products were recorded on a Philips X' pert-MPD using Cu-Kα radiation with λ= 1.5418Å in the θ-2θ scan mode. A Rigaku SmartLab X-ray diffraction tool with Cu Kα X-ray source was also used for XRD experiments.

2.4.10 Mechanical Tensile Test

The mechanical properties of polymer stripes were measured by a TA Instruments RSA III Micro Strain Analyzer. PDMS films with a thickness of 0.5 mm were prepared by pouring the uncured PDMS in the petri dish and cured for 48 hours at room temperature. The PDMS samples were cut in to strips with dimensions of 30 mm×10 mm for tensile test. A transient analysis mode was selected to acquire the strain stress curves. The Young's modules of the materials were calculated from the slop of the strain stress curves.

2.4.11 Thermal Gravity Analysis (TGA) and Differential Scanning Calorimetry (DSC)

A TA-Instruments TGAs-Q5000 was used to test the mass loss upon heating for the samples. Before each set of TGA tests, calibration runs were recorded using 10-15 mg of platinum plate freshly cleaned and annealed under a propane torch. The temperature ramp speed was typically fixed at 10 °C/min. A TA-Instruments DSC Q2000 was employed to measure the heat flow of samples in the temperature range from 0 to 275 °C. [9]

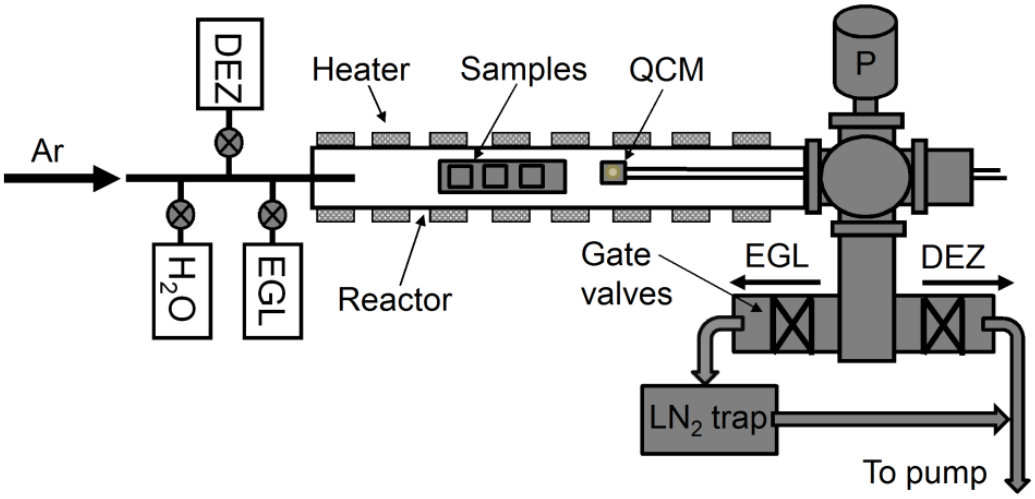


Figure 2.1. A schematic view of the viscous flow ALD/MLD reactor. The precursors are delivered into the reactor with Ar carrier gas. On the reactor exhaust line, computer controlled gate values are used to direct the exhaust from the EG pulse into a liquid nitrogen trap before entering the pump.

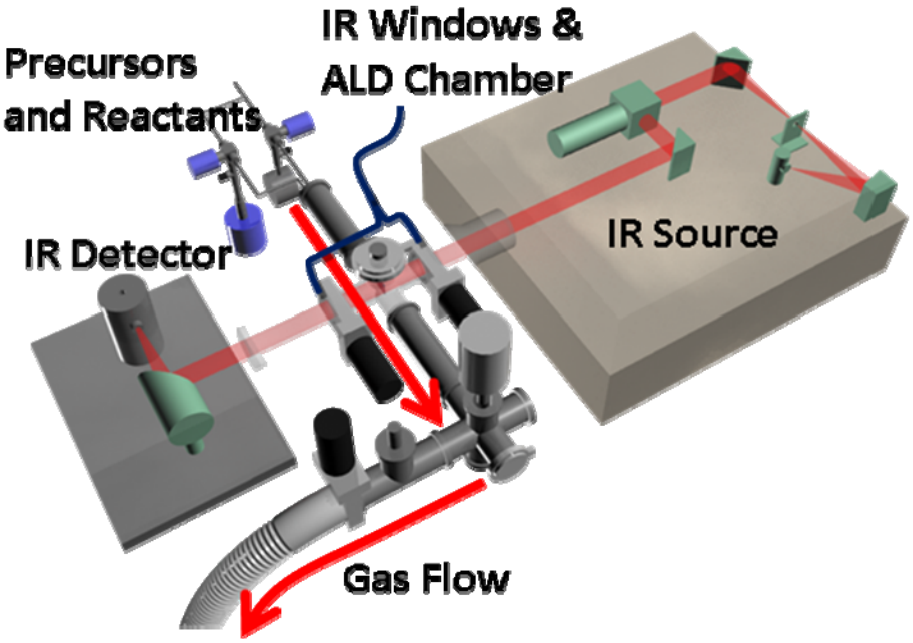


Figure 2.2. Schematic diagram of In-situ FTIR ALD/MLD reactor. The precursors are delivered into the reactor with high purity Ar. In the middle part of the chamber, two CsI IR windows are attached, and two gate valves are installed between the IR window and reactor chamber to prevent the deposition of ALD/MLD film on the windows. During the measurement, the IR beam is directed through the planar sample and focused into a MCT-A detector. Before each dose, a background spectrum was collected as reference, and differential spectra were employed to show the surface chemistry change after each pulse.

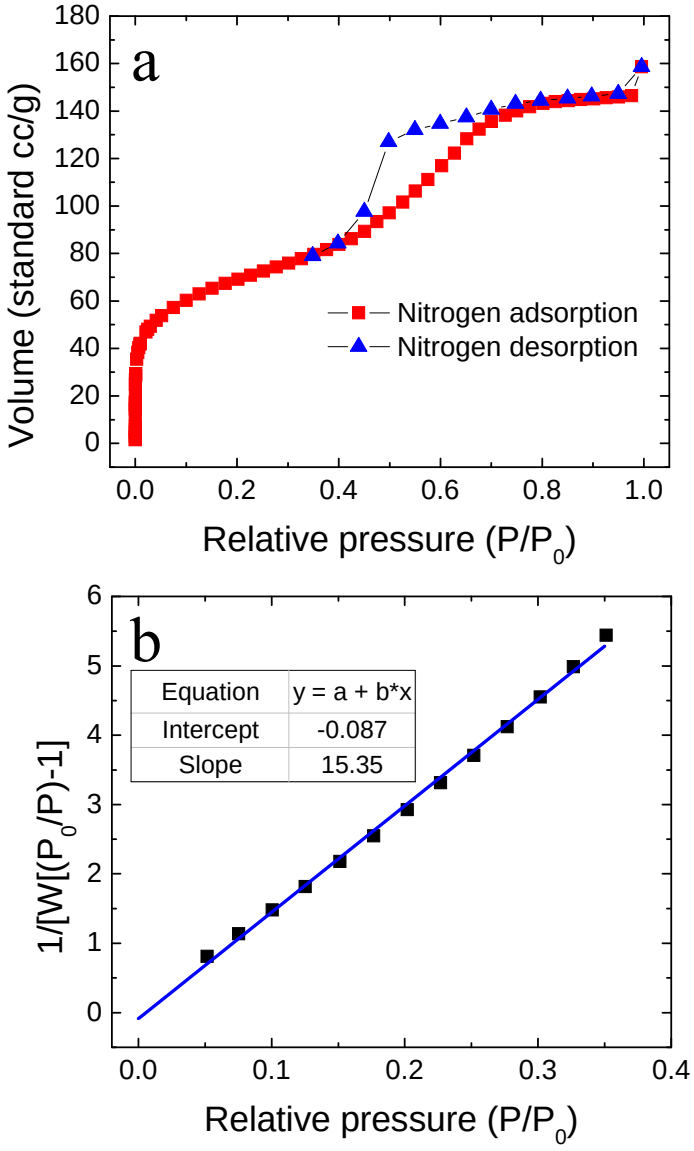


Figure 2.3. (a) An example nitrogen adsorption/ desorption isotherm collected by Autosorb-1C at 77K. **(b)** BET plot calculated from the adsorption isotherm.($0.05<P/P_0<0.35$) The BET surface area can be calculated from the intercept and the slope of the plot.

References

1 Q. Peng; B. Gong; R. M. VanGundy; G. N. Parsons; "Zincone" Zinc Oxide-Organic Hybrid Polymer Thin Films Formed by Molecular Layer Deposition, *Chemistry of Materials,* **2009**. *21*, 820.

2 B. Gong; Q. Peng; G. N. Parsons; Conformal Organic - Inorganic Hybrid Network Polymer Thin Films by Molecular Layer Deposition using Trimethylaluminum and Glycidol, *Journal of Physical Chemistry B,* **2011**. *115*, 5930.

3 Q. Peng; X. Y. Sun; J. C. Spagnola; G. K. Hyde; R. J. Spontak; G. N. Parsons; Atomic layer deposition on electrospun polymer fibers as a direct route to Al2O3 microtubes with precise wall thickness control, *Nano Letters,* **2007**. *7*, 719.

4 L. Vayssieres; Growth of arrayed nanorods and nanowires of ZnO from aqueous solutions, *Advanced Materials,* **2003**. *15*, 464.

5 B. Gong; Q. Peng; J.-S. Na; G. N. Parsons; Highly active photocatalytic ZnO nanocrystalline rods supported on polymer fiber mats: Synthesis using atomic layer deposition and hydrothermal crystal growth, *Applied Catalysis a-General,* **2011**. *407*, 211.

6 S. S. Y. Chui; S. M. F. Lo; J. P. H. Charmant; A. G. Orpen; I. D. Williams; A chemically functionalizable nanoporous material Cu-3(TMA)(2)(H2O)(3) (n), *Science,* **1999**. *283*, 1148.

7 O. Shekhah; H. Wang; S. Kowarik; F. Schreiber; M. Paulus; M. Tolan; C. Sternemann; F. Evers; D. Zacher; R. A. Fischer; C. Woll; Step-by-step route for the

synthesis of metal-organic frameworks, *Journal of the American Chemical Society*, **2007**. *129*, 15118.

8 J. W. Elam; M. D. Groner; S. M. George; Viscous flow reactor with quartz crystal microbalance for thin film growth by atomic layer deposition, *Review of Scientific Instruments*, **2002**. *73*, 2981.

9 B. Gong; Q. Peng; J. S. Jur; C. K. Devine; K. Lee; G. N. Parsons; Sequential Vapor Infiltration of Metal Oxides into Sacrificial Polyester Fibers: Shape Replication and Controlled Porosity of Microporous/Mesoporous Oxide Monoliths, *Chemistry of Materials*, **2011**. *23*, 3476.

CHAPTER 3. Overview of Key Results of the Dissertation

This dissertation explores the low-temperature atomic layer deposition (ALD) and molecular layer deposition (MLD). In this study, we developed new materials and processes for ALD and MLD. New applications of ALD and MLD coating on various polymer substrates were also studied.

3.1 Conformal Organic-Inorganic Hybrid Network Polymer Thin Films by Molecular Layer Deposition using Trimethylaluminum and Glycidol

In this work, a new molecular layer deposition process has been studied. As shown in Figure 3.1, trimethyl aluminum and hetero-bifunctional glycidol will react in an alternating surface reaction sequence to produce stable organic-inorganic hybrid thin film polymer material of the form $(\text{-Al-O-}(C_4H_8)\text{-O-})_n$. The reaction proceeds at moderate temperatures on planar and nonplanar surfaces to produce conformal and uniform films. Using in-situ spectroscopic analysis, we conclude that film growth proceeds through a combined diffusion/binding/reaction mechanism, involving sub-surface reactant accumulation during reactant dosing. The IR and growth rate data also indicate that both ends of the glycidol hetero-bifunctional reagent react with the $Al\text{-}CH_3$ surface. The mechanism is consistent with previous studies of ALD growth on polymers and three-step MLD reactions showing growth acceleration due to subsurface species transport and trapping. A water exposure step after the TMA is found to impede growth acceleration, likely by blocking TMA subsurface diffusion. The QCM data collected from these MLD sequences was plotted in Figure 3.2. Post-deposition annealing of hybrid organic-inorganic films in air results in well defined porous inorganic structures with shape that mimics the original deposition substrate. Even though

the reaction does not follow an ideal self-limiting surface reaction growth sequence, the process is still sufficiently controlled to allow highly conformal films to form on complex non-planar substrates. Such materials could find applications in fields including gas separations and diffusion barriers, biomedical scaffolds, and porous coatings.

The hetero-bifunctional glycidol did not remove the undesired double reactions. However, new phenomena were observed in this MLD process: The precursors could subsurface diffusion and reaction in the deposited MLD films. This discovery will help us understand new MLD processes in the future. The MLD process is more complex than the ALD process, the transport of precursor in the deposited film need to be considered. Moreover, the TMA/glycidol MLD is based on Lewis acid/base reactions. The understanding of the chemistry would help with the development of new MLD processes based on Lewis acid base reactions.

3.2 A Two-Step Lewis Acid-Catalyzed ε-Caprolactone Ring-Opening Molecular Layer Deposition Process for Hybrid Organic-Aluminum Oxide Polymer Thin Films

This work demonstrates that a cyclic ester ε-caprolactone (LAC) reagent can react with tri-methyl-aluminum in a vapor-phase molecular layer deposition binary reaction scheme at substrate temperatures between 60 and 120 °C to form metal-organic hybrid coordination polymer thin films of the form $(\text{-Al-O-}(C_8H_{16})\text{-O-})_n$ that are relatively stable in ambient air. Figure 3.3 displayed the film thickness versus number of MLD cycles at various growth temperatures. Ex-situ infrared transmittance spectra confirmed that films consist of Al-O and ethylene oxide units, and the deposited film showed good stability in ambient over 7 days in laboratory air. The good ambient stability will make this material of interest for

applications in gas diffusion barriers, biomedical scaffold and porous coatings. Because this catalytic mechanism depends mainly on the Lewis acid properties of the aluminum-methyl, we expect many other metals organics will show the similar catalytic activity. These results show a new method to fabricate air stable organic-inorganic hybrid materials, and novel pathways to initiate surface ring opening reactions from the vapor phase.

This work demonstrated that Lewis acid/base ring opening reaction can be employed in MLD process. The ring opening reaction is another promising method to prevent the double reactions in the MLD process. The understanding of this ring-opening surface reaction mechanism would benefit the development of new MLD processes. Moreover, the new organic precursor has relative high vapor pressure, and the process can be conducted at low temperature (60 °C). However, at low temperature, we found that the precursor condensation played important role in the MLD film growth. The condensed precursor will react with the second reagent in the following pulse step, and result in faster film building up. These observations are important for understanding of new MLD processes.

3.3 Highly Active Photocatalytic ZnO Nanocrystalline Rods Supported on Polymer Fiber Mats: Synthesis Using ZnO Atomic Layer Deposition and Hydrothermal Crystal Growth

Photocatalytically active ZnO nanorod crystals are readily grown using a low temperature hydrothermal procedure on PBT fibers mats, when the fibers are first coated with a conformal ZnO nucleation layer using atomic layer deposition. The ALD efficiently functionalized the polymer fiber to facilitate hydrothermal nanorod crystal nucleation and subsequent growth. The SEM images of ZnO nanorods supported on polymer fiber mat were

displayed in Figure 3.4. The process produces fibers with ~10× enhancement in total surface area (determined from BET analysis) on a per sample size (cm^2/cm^2) basis. We demonstrated that the ZnO film/nanorod composite will photocatalytically degrade an azo organic dye (acid red 40) in aqueous media at a rate that is nearly 2× faster than a similar fiber with only the ZnO film coating, as shown in Figure 3.5. More importantly, the functionalized polymer fiber mat could be reused very easily, and no additional particle recovery process is needed. This combination of ALD and hydrothermal processes may also be useful for other crystal growth systems, such as TiO_2, Fe_2O_3, SnO_2 and V_2O_5, where high area and ready solution access are desired.

The integration of ALD and solution based chemistry opened a broad avenue for materials synthesis. The substrate surface chemistry is critical for many liquid phase deposition techniques, and low temperature ALD provided an ideal solvent free technique for polymer surface functionalization. The incorporation of the two would produce many novel materials with advanced properties. In the future, we would see more and more integration between ALD and solution based techniques, such as sol-gel, layer by layer, and plating.

3.4 Layer by Layer Growth of HKUST-1 on Nonwoven Polypropylene Fiber Mat

Ultra-thin film of Al_2O_3 deposited by ALD on inert PP fiber mat provided an ideal nucleation layer for the subsequent growth metal organic frameworks. Figure 3.6 showed that the Al_2O_3 ALD coating significantly facilitated the LBL growth of HKUST-1 crystals on PP fiber mat. Panel (a) shows the PP fiber mat with 10 LBL HKUST-1 with and without ALD pretreatment. The fiber mat on the left is the direct LBL growth of MOF on PP fiber mat. The mat on the right is the PP fiber mat pretreated with Al_2O_3, then coated with MOF by LBL

technique. The pp fiber mat without ALD pretreatment showed almost no color change after LBL HKUST-1 growth. However, the fiber mat with Al_2O_3 ALD pretreatment showed the light green color, which is coming from the attached HKUST-1 crystals on the polymer surface. Panel (b) shows MOF coated PP fiber mat before vacuum dry in a glass tube. (c) MOF coated PP fiber mat after vacuum dry. After outgas, the color of the coated fiber changed from light green to dark blue, which is consistent with previous literature report. The FTIR spectra (as shown in Figure 3.7.) of LBL growth of MOF on Al_2O_3 ALD coated Si wafer demonstrated a linear growth of HKUST-1 vs. number of LBL cycles. The XRD patterns collected from the MOFs coated PP fiber mat confirmed that the crystal we attached is HKUST-1, and the Al_2O_3 nucleation layer is critical for this LBL attachment of MOFs. Interestingly, we found that the measured BET surface area for the HKUST-1 crystal grew by LBL technique is significantly smaller than the conventional hydrothermal method; this could due to the low processing temperature and the precursor residue in the pore structures.

This is the first report using ALD technique to facilitate the nucleation and LBL growth of HKUST-1 on polymer surface. The ALD layer proved to be a very good nucleation layer for MOF growth. Potential applications of these fiber materials include chemical storage, gas separation and catalytic conversion. I would expect other MOFs could be prepared on polymer surfaces using the similar methods. In this report, we found that the BET surface area of LBL MOF is much lower than the MOF prepared from conventional hydrothermal method. This is likely because of the LBL assembly was conducted at room temperature. Further study will explore the LBL growth at higher temperatures.

3.5 Atomic Layer Deposition of Aluminum Oxide on Metal Organic Framework $Cu_3(BTC)_2$

In this work, we conducted Al_2O_3 ALD process on the $Cu_3(BTC)_2$ MOF for the first time. We have successfully synthesized the $Cu_3(BTC)_2$ MOF crystals from the hydrothermal method. The structure and the surface area of the prepared MOF was confirmed by XRD and BET analysis. In-situ QCM was used to monitor the mass change during the ALD process. A large mass uptake was detected during the precursor pulse, which is corresponding to high surface area and porosity of the $Cu_3(BTC)_2$. In-situ FTIR spectra was also collected to study the surface chemistry. The spectra did not show strong reaction between TMA and the $Cu_3(BTC)_2$ during ALD growth. Interestingly, CH_4 IR absorbance was observed after TMA dose. This is corresponding to the adsorption of CH_4 in the MOF crystals. In the following water pulse, H_2O molecule would prefer to bind to the metal center in $Cu_3(BTC)_2$ and remove the CH_4 gas.

We also tested the moisture sensing properties of $Cu_3(BTC)_2$ by QCM. The QCM data collected from the sensing experiments was plotted in Figure 3.8. Bare QCM crystal showed negligible mass uptake during water exposures, while the $Cu_3(BTC)_2$ coated QCM crystal showed very large mass uptake and decreasing. Interestingly, after we coat the MOFs with just 5 cycle of Al_2O_3 ALD process, we found the sensitivity of this microgravity sensor decreased. This is corresponding to the shrinking of pore size and the pore volume of MOFs after the ALD. It implied we could use ALD to fine tune the moisture sensing. It also confirmed we did not destroy the MOF structure by apply thin ALD coatings.

Decorate MOFs with inorganic coatings or particles is an efficient way to prepare MOFs with novel functionalities. The characteristics of ALD make it an ideal technique for the functionalization of MOFs. The integration of ALD technique would greatly expanded the application field of MOFs. For example, we could apply noble metal particles in MOFs and using it as catalyst; we could also apply UV responsive semiconductor coatings, and make UV sensors from MOFs.

3.6 Quantitative Analysis of Reaction of Trimethyl-aluminum towards Polymer Substrates during Al_2O_3 Atomic Layer Deposition by In-situ FTIR

The reactions of trimethylaluminum (TMA) toward substrates during the Al_2O_3 atomic layer deposition (ALD) on a variety of polymers were studied by in-situ Fourier transform infrared spectroscopy (FTIR). The experiments demonstrate that TMA reacts with certain nucleophilic functional groups on the polymer surface during the first several ALD cycles. For some polymer substrates, TMA vapor penetrates into the polymer and reacts in the polymer bulk. In both cases, the initial reaction plays an important role in the nucleation and growth of Al_2O_3. For chemically inert polymers, such as polypropylene, nucleation of Al_2O_3 ALD is relative slow at the initial stage due to the lack of reactive groups on the substrate. However, polyester, polyamide and polyether are more reactive, and in-situ FTIR spectra showed a larger extent of reaction with TMA, facilitating the nucleation of ALD film on these polymers. By comparing FTIR spectra, we quantitatively estimate the extent of TMA reaction towards different polymers. Figure 3.9 showed the Al-CH_3 deformation (~1200 cm^{-1}) and CH_3 asymmetric stretching (~2960 cm^{-1}) absorbance increase after first TMA pulse on different polymer substrate. The magnitude of the $\nu_a(CH_3)$ and $\delta_a(CH_3)$

intensity also displays the relative extent of reaction between the various polymers and TMA. We also confirmed the results using X-ray photoelectron spectroscopy and scanning electron microscopy. Results give insight into the importance of polymer structure in determining the nature and extent of reaction during ALD film processing on polymer substrates.

By comparing $\nu_a(CH_3)$ absorbance intensity measured on the polymers, we could quantitatively analyze the extent of reaction for TMA with these different polymer substrates. For example, upon the first TMA pulse, the PVA film shows an $\nu_a(CH_3)$ absorbance intensity increase of ~ 0.0004. The Al-CH_3 concentration is estimated to be $0.0004/2.4\times10^{-20}cm^2 \approx 1.7\times10^{16}/cm^2$, which corresponds to $1.7\times10^{16}/7.1\times10^{14} \approx 24$ "Al-CH_3 monolayers", primarily within the polymer subsurface. The OH groups on the PVA could result in rapid formation of Al_2O_3 at the near surface, and prevent the precursor from penetrating deep into the polymer bulk. However, for TMA exposure on PET, the corresponding $\nu_a(CH_3)$ absorbance intensity increase shown in Figure 3.9 is ~1.42. This relates to an Al-CH_3 concentration of $1.42/2.4\times10^{-20}\cdot cm^2 \approx 5.9\times10^{19}/cm^2$, which is approximately equivalent to $5.9\times10^{19}/7.1\times10^{14} \approx 8.3\times10^4$ "Al-CH_3 monolayers". This shows that a large number of TMA molecules infuses and reacts in the PET bulk. By similar analysis on the other polymers, the "number of monolayers" could be used to quantitatively evaluate the extent of subsurface diffusion and reaction. This data is collected for each polymer and summarized in Table 3.1.

The extent of subsurface diffusion and reaction with TMA strongly depends on polymer chemistry. TMA will attack nucleophilic functional groups in the polymer, such as C=O in the polyesters and polyamide, and C-O-C in the polyethers. These groups will have different propensities for reaction. Many polymers contain these groups, but the location of

these reactive groups within the polymer also appears to be important. For example, PET and PMMA have similar -(C=O)-O- characteristic groups, but they show more than 10× difference in extent of reaction with TMA. In PET the ester is in the main chain so the reaction with TMA will more likely promote chain scission, facilitating further TMA infusion and reaction. In PMMA however, the ester is limited to the side chain, so reaction is less likely to break the chain, helping to maintain the polymer structure and thereby limiting diffusion. Other factors such as the overall polymer molecular weight and crystallinity may also influence the reaction extent in these and other polymer/precursor reaction systems. More ALD chemistries will be studied on polymers. The quantitative study would help in understanding the chemical interactions of ALD precursors with polymer substrates and the nucleation of ALD films, which is very important for many advanced applications of ALD films on polymers.

3.7 Sequential Vapor Infiltration of Metal Oxides into Sacrificial Polyester Fibers: Shape Replication and Controlled Porosity of Micro/Mesoporous Oxide Monoliths

This work demonstrates a new approach for synthesis of shape-controlled micro/mesoporous materials using polyesters as sacrificial templates. Vapor phase trimethyl aluminum and titanium tetrachloride precursors can diffuse into polyester fibers, including PBT, PET, PLA and PEN, and using water as a co-reactant produce a matrix network hybrid organic-inorganic polymer. This polymer readily transforms upon anneal in air to yield a porous inorganic Al_2O_3 or TiO_2 solid monolith. Moreover, the shape and macroscopic physical appearance of the inorganic solid faithfully duplicates that of the original starting polymer. Figure 3.10 shows the morphologies of PBT fiber mat before and after sequential

vapor infiltration. Figure (a) shows a photograph of an untreated PBT nonwoven fiber mesh, a similar piece of nonwoven fiber after sequential vapor infiltration, and a similar sized piece again after high temperature calcination. Note that each treatment step produces a decrease in overall sample dimension. The brownish color after annealing is likely due to a small amount of carbon residue remaining in the sample. Figure (b) presents an SEM image of the untreated nonwoven PBT, showing a uniform mat of randomly distributed individual fiber units with diameter of ~ 5 μm. Figures (c) and (d) show similar fibers after TMA (60 min) / H_2O (20 min) vapor soak at 80°C followed by 24 hr calcination in air at 450°C. After treatment, the macroscopic fiber diameter is smaller, but the overall macroscopic structure not significantly changed. Figure (c) shows some connectivity between fibers after treatment that is not present before. Some polymer flow could be expected due to polymer chain scission and/or local heating during TMA/polymer reaction. A broken fiber in Figure (d) clearly shows a uniform cross section after high temperature calcination. As will be shown below, the treatment process effectively converts the fibers from a polymer to a highly porous inorganic solid.

The proposed reaction sequence during TMA/water exposure on PBT involves a large TMA mass uptake and removal of (C=O)-O bonding units through TMA interaction with the ester bond in the PBT backbone, likely through Lewis acid/base adducts. The in-situ FTIR spectra collected during the sequential vapor phase infiltration of TMA/water was displayed in Figure 3.11. Experiments using a relatively weak Lewis acid such as diethyl zinc as the metal source do not produce similar reactions, consistent with the proposed reaction mechanism. The micro/mesoporous structure is confirmed using cross-sectional transmission

electron microscopy and nitrogen absorption/desorption experiments. The pore size and volume depend systematically on the detailed process conditions. The data shows that the starting polymer repeat unit acts to template the resulting inorganic pore size.

The ability to prepare porous inorganic solids with tunable pore size, where the monolith shape is preselected by the shape of the starting polymer template could be useful for catalytic support structures, chemical and electrochemical separations, and other porous membrane systems. This process is also open to a wide range of inorganic components and a variety of different starting polymers, allowing significant versatility over the final product design.

3.8 Hydrophilic Mechanical Buffer Layers and Stable Hydrophilic Finishes on Polydimethylsiloxane using Combined Sequential Vapor Infiltration and Atomic/Molecular Layer Deposition

Polydimethylsiloxane (PDMS) is a widely used material for many advanced applications, such as microfluidic devices, microstructure replication and soft lithography. However, PDMS is natural hydrophobic which limited it use with aqueous solutions. In this study, we exposed freshly cured polydimethylsiloxane polymer to sequential vapor infiltration of trimethylaluminum/water, then performed atomic layer deposition using TMA/water or molecular layer deposition using TMA/glycidol. We found that the TMA/water infiltration followed by ALD alumina and MLD alucone at 60 °C yields a hydrophilic coating on PDMS with advancing water contact angle of ~40 °, and the contact angle remains relatively stable in air for the ~14 day duration of our study. Vapor infiltration and reaction before the ALD + MLD increased the Young's modulus and strengthened the

polymer, creating a mechanical buffer layer at the polymer/inorganic interface that helped maintain the resulting hydrophilic structure. The mechanical stress strain curve of vapor phase infiltrated PDMS was plotted in Figure 3.12. The PDMS samples treated by infiltration and ALD (without the MLD finish layer) became hydrophobic within a few hours after exposure to air. Keeping the samples in inert Ar for up to 48 hours delayed the transition, showing that the infiltration + ALD process successfully impedes organic out-diffusion from the PDMS bulk. The ALD or MLD capping layer then provides a hydrophilic finish to the surface. Figure 3.13 showed a schematic diagram of surface treatment of PDMS with ALD only or sequential vapor infiltration followed by ALD.

PDMS treated with only the ALD coating (without the buffer layer) or with only the infiltration process (without the finish layer) were also hydrophilic after coating, but they were much less stable and rapidly became hydrophobic over time. The alucone MLD finish coating produced a more hydrophilic finish as compared to the ALD alumina. The alucone and other hybrid organic-inorganic materials are known to take up some water after processing, and some water absorption can help maintain the hydrophilic surface. The process described here, which combines sequential vapor infiltration combine with atomic layer deposition and/or molecular layer deposition on PDMS, can be a general method that could work to functionally engineer and tailor the mechanical and chemical performance polymer barriers and other important organic/inorganic material systems.

3.9 Directed Mesoporous Metal Oxides by Vapor Phase Atomic Layer Deposition and Infiltration of Ordered Surfactant Thin Films

Amphiphilic surfactants moleculars have been widely used as structure direct template for the preparation of metal oxide from solution. The interaction between the hydrophilic head of the surfactants molecular and the metal oxide precursor helped the self-assemble of ordered micelles/metal oxide hybrid materials, and after post template remove, well defined porous materials could be prepared. Recently, the selective interaction between metal oxide precursor and certain polymer segment was also discovered during vapor phase sequential vapor infiltration (SVI) and atomic layer deposition (ALD) of metal oxide onto polymers, where precursor infusion and reaction depends strongly on the interaction between the precursor and polymer starting substrate. In this work, mesoporous metal oxide materials were succesfully prepared by the sequential vapor phase infiltration (SVI) or conventional ALD on surfactant substrates. The nonionic (F127, PEO-PPO-PEO) and ionic (CTAB, SDS) surfactants were tested. Figure 3.14 displayed a schematic diagram for the preparation of mesoporous metal oxide materials from vapor phase infiltration method. In-situ FTIR was used to monitor the chemistry change during the vapor infiltration. SEM, TEM and XRD were used to characterize the structure of the porous material. The nitrogen adsorption/desorption analysis was conducted to measure the specific surface area and the pore size distribution of the porous metal oxide materials.

This approach demostrate a vapor phase approach to synthesis the mesoporous metal oxide chemistry from surfactant template. Because this chemistry is based on the Lewis acid

base interaction between metal center in the metal organic precursor and the nucleaphilic groups in surfactants, this approach could extend to other metal oxide systems.

Although we tried many surfactants and metal oxide chemistry, we haven't been able to get ordered porous metal oxide. One of the most promising combination is CTAB surfactant and Al_2O_3 (TMA/water). We were able to get ordered Al_2O_3/ CTAB surfactant hybrid materials, however, the structure got destroyed during the high temperature annealing. The possible reason is that there is not enough metal oxide dispersed into the surfactant layer. Upon calcination, the structure collapse. If we could get more metal organic precursor infuse into the surfactant layers, we should be able to get ordered metal oxide materials. To achieve this, the detailed process condition need to be fine tuned. Longer infiltration time and higher temperture might help. Moreover, alternative template removing methods can be tested on these materials, such as oxygen plasma and UV-Ozone techniques.

3.10 Core Sheath Nanocomposite Structures Enabled by Aluminum Oxide Atomic Layer Deposition on Bicomponent Polymer Fibers

Al_2O_3 ALD on polylactic (PLA) core polypropylene (PP) sheath bi-component fibers also demonstrated the selective reactivity of TMA with polymers. The PP is verified as an inert polymer with little reaction with TMA/water. However, PLA showed strong reaction towards TMA vapor. This difference in reactivity towards metal organic vapors enabled selective incorporation of aluminum oxide films and particles within different regions of bi-component PLA/PP core/sheath fibers. For long exposures, TMA will diffuse through the inert PP layer and react with PLA. Figure 3.15 showed a schematic diagram of the selective reaction between TMA and PLA core. The ALD on bi-component polymers enables a new

approach to selectively modify portions of multicomponent polymers to create unique organic/inorganic composite structures. More ALD chemistries need to be introduced.

The detailed process conditions, such as temperatures, exposure time and purge time are critical for the successful infusion of metal oxide into desired polymer segments. The detailed study of these process parameters will provide valuable information, like diffusion coefficient of precursors. This information will in return help us study the vapor phase infiltration. Moreover, we used flow tube reactor in this study, the precursors come in from one end and purge out from the other end. The gradient of precursor concentration might result in non-uniform reactions.

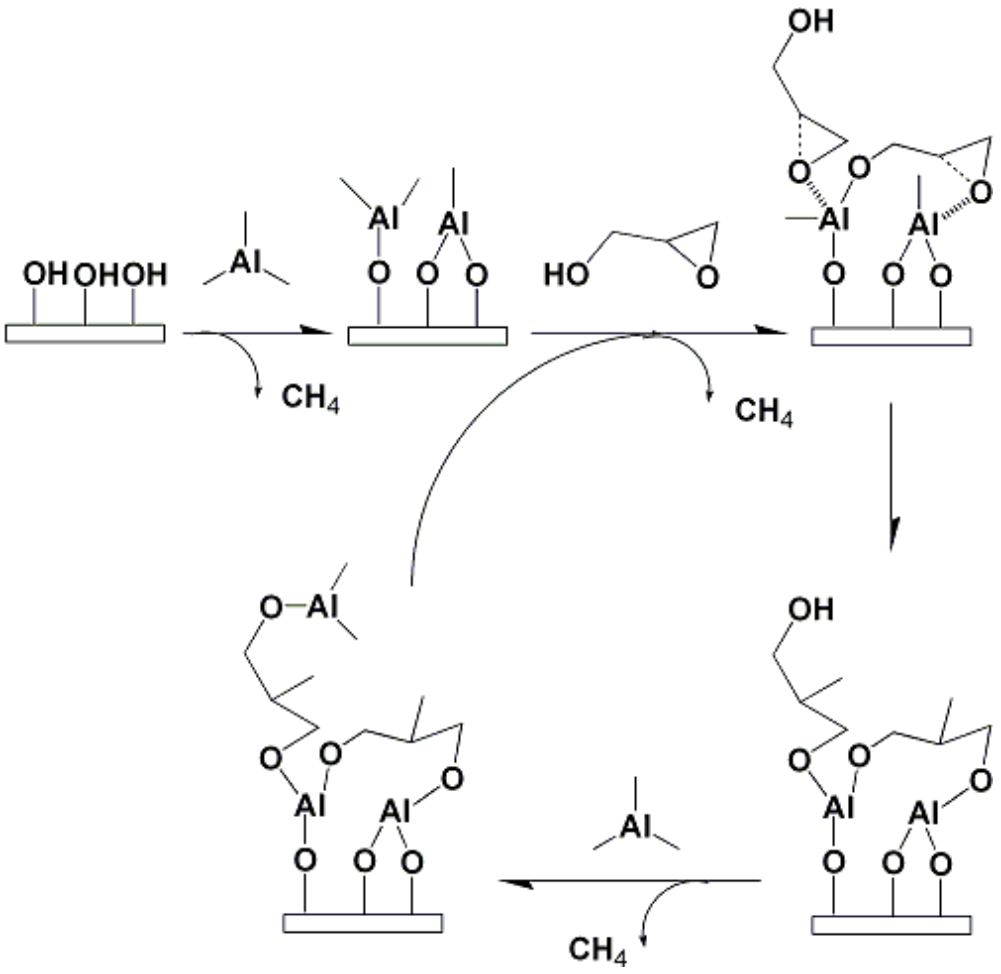


Figure 3.1. Schematic of the surface reactions during TMA/GLY MLD process consistent with the FTIR data in Figure 4.6(a). Exposing the –OH surface to TMA produced surface Al-CH_3. The following glycidol exposure consumes Al-CH_3 surface units, including reactions with both the OH and epoxy end of the molecule. The aluminum can help catalyze the ring opening. Available OH groups are then available to react with TMA during the next exposure step. Not shown in this diagram is the expected sub-surface diffusion of TMA and reaction with available lone pair sites producing Lewis acid/base O**:** $Al(CH_3)_3$ adducts that can react during the next glycidol exposure step.

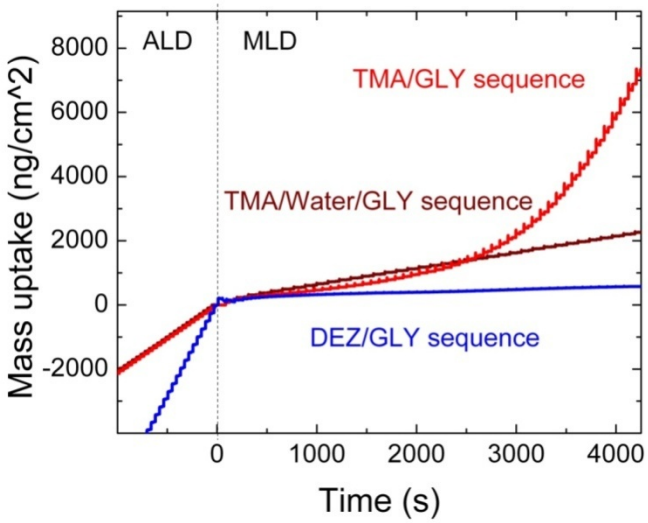


Figure 3.2. Direct comparison between in-situ QCM data collected during TMA/GLY, TMA/water/GLY and DEZ/GLY sequences following TMA/water (or DEZ/water) ALD. TMA (DEZ)/Ar/GLY/Ar = 1/40/2/40 s is used for TMA/GLY and DEZ/GLY, and TMA/Ar/Water/Ar/GLY/Ar = 1/40/1/40/2/40 s is used for TMA/Water/GLY. The TMA/GLY produced an induction period followed by a large mass uptake. The TMA/water/GLY sequence showed a much lower mass uptake per cycle, without an induction period. Negligible mass uptake is observed for the DEZ/GLY sequence, demonstrating the importance of the Al-CH_3 as a growth catalyst.

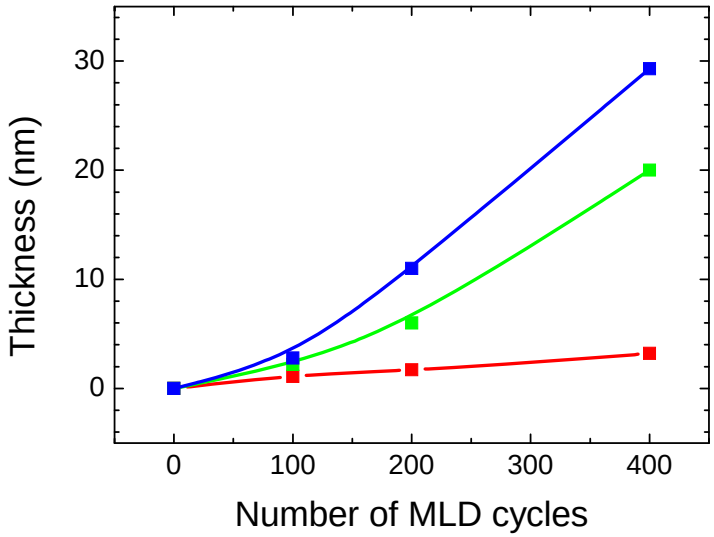


Figure 3.3. Film thickness for TMA/LAC MLD films on silicon wafers is plotted versus number of MLD cycles at various growth temperatures. Film thickness was determined using ellipsometry. For all the samples on Si wafer the deposition sequence was TMA/Ar/LAC/Ar = 1/40/2/40 seconds. The growth rate decreased from 0.75 Å /cycle to 0.08Å/cycle as the substrate temperature increased from 60 to 120°C.

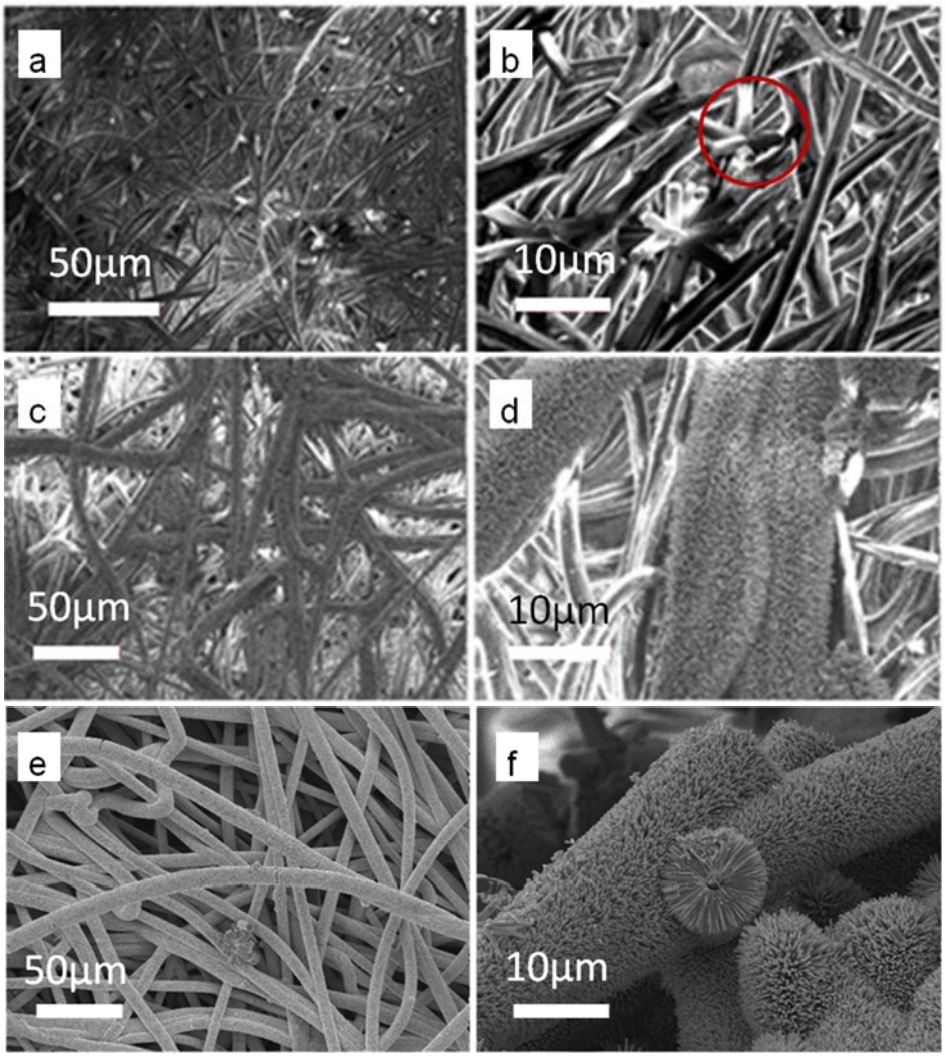


Figure 3.4. Scanning electron micrographs obtained from: (a) and (b), untreated PBT fibers after hydrothermal ZnO nanorod crystal growth; (c) and (d), PBT fibers after 100 ALD cycles of ZnO (~20 nm thick), followed by hydrothermal ZnO nanorod growth. Nanorod crystals are visible primarily on the top-most fibers in the fiber mat. Panels (e) and (f) show PBT fibers after 200 cycles (~40 nm) of ALD ZnO, followed by ZnO nanorod growth. Nanorod growth is visible on all the fibers. In panel (b) a circle highlights a large crystal, similar in size to the one shown in Figure 2(b), formed on the untreated fiber.

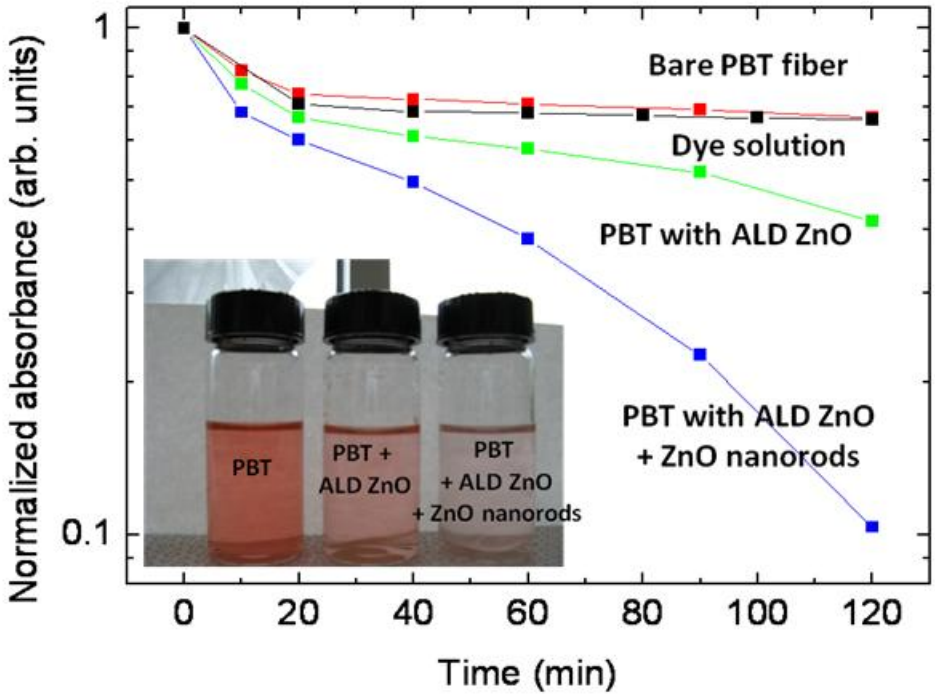


Figure 3.5. Normalized absorbance of organic dye at 525 nm plotted versus UV radiation exposure time. PBT fiber substrates with various surface treatments were immersed in the aqueous solution containing the azo dye (acid red 40), and illuminated using a UV lamp. The fibers with ALD ZnO and ZnO nanorod crystals produced the most rapid photocatalytic dye degradation. The inset shows a photograph of the dye solutions in contact with the different substrates after 2 hr of illumination. The red dye is nearly completely removed from the solution in contact with the nanorod-coated fibers.

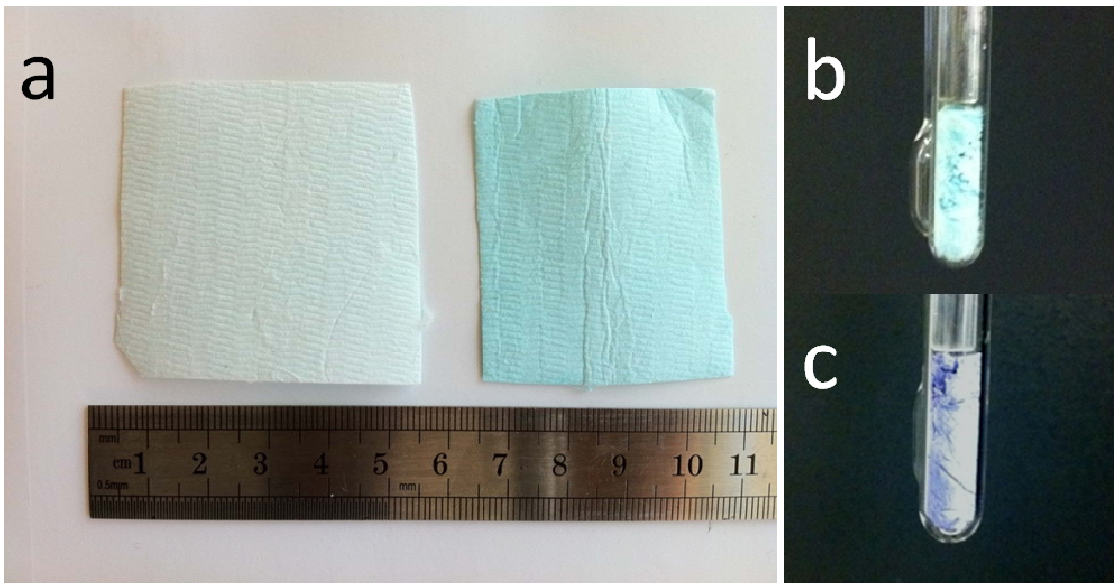


Figure 3.6. Optical images of HKUST-1 coated PP fiber mat. (a) The fiber mat on the left is the direct LBL growth of MOF on PP fiber mat. The mat on the right is the PP fiber mat pretreated with ALO, then coated with MOF by LBL technique. (b) MOF coated PP fiber mat before vacuum dry. (c) MOF coated PP fiber mat after vacuum dry.

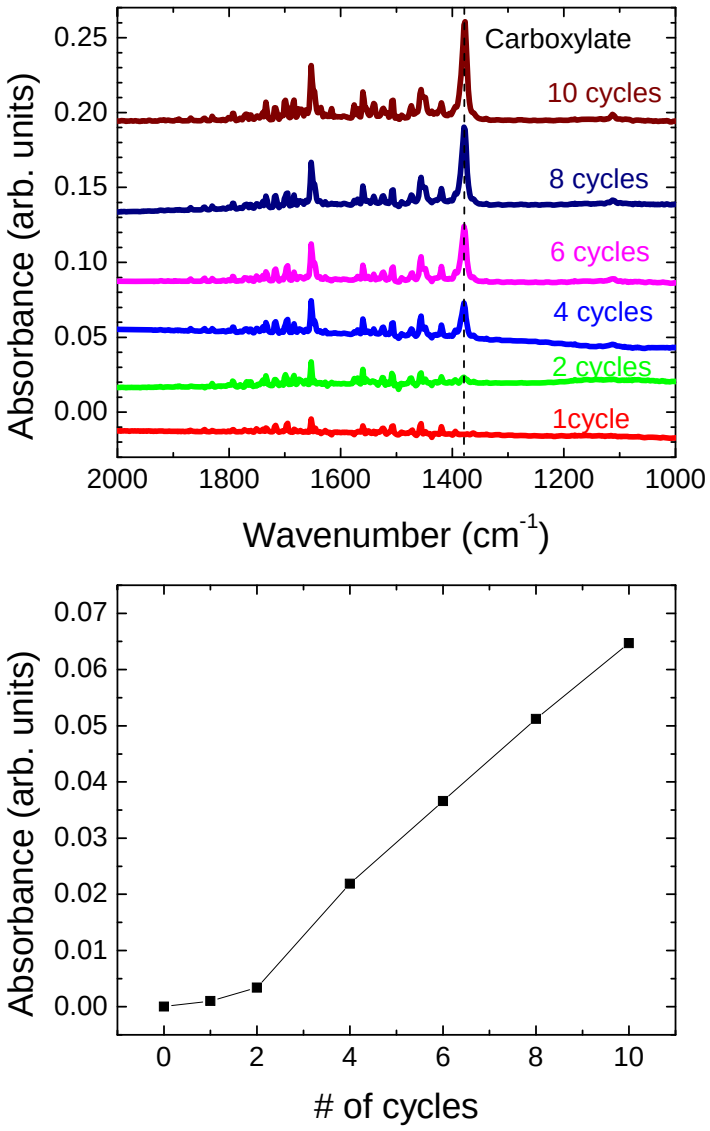


Figure 3.7. The Fourier transform infrared (FTIR) spectra collected from the HKUST-1 films on Al_2O_3 coated Si wafers. Slow growth was detected for the first 2 deposition cycles. Then the linear increase of IR absorbance vs. LBL deposition cycles was observed.

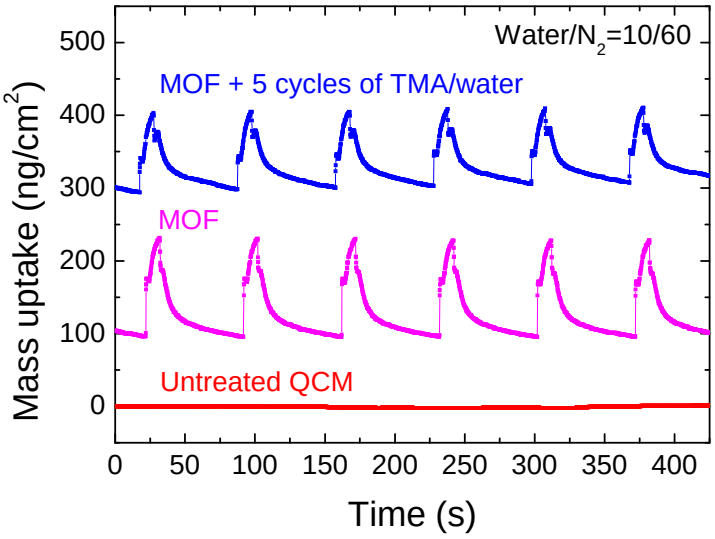


Figure 3.8. In-situ QCM data collected from water/N_2 process on bare QCM and $Cu_3(BTC)_2$ particle coated QCM. Bare QCM crystal showed negligible mass uptake during water exposures, while the $Cu_3(BTC)_2$ coated QCM crystal showed very large mass uptake and decreasing. The MOF with 5 cycles of TMA/water ALD process showed smaller mass uptake during water exposure, and this could be explained by the shrinking of pore volume and size after ALD.

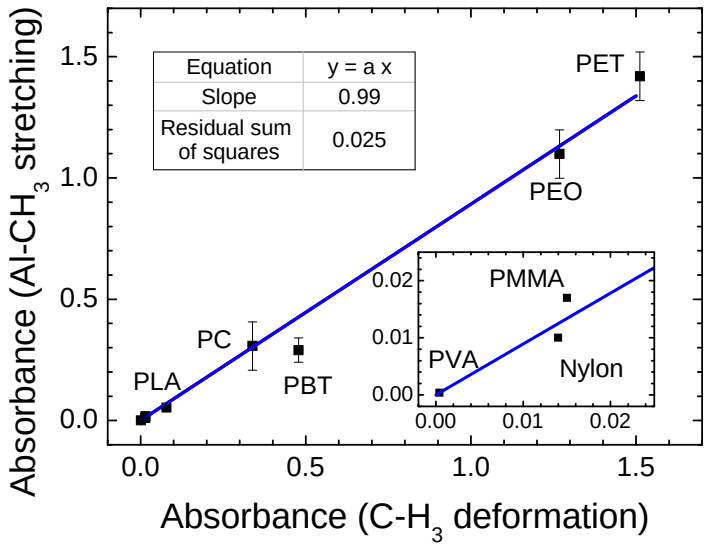


Figure 3.9. The Al-CH_3 deformation (~1200 cm^{-1}) and CH_3 asymmetric stretching (~2960 cm^{-1}) absorbance increase after first TMA pulse on different polymer substrate. The magnitude of the $\nu_a(CH_3)$ and $\delta_a(CH_3)$ intensity also displays the relative extent of reaction between the various polymers and TMA.

Table 3.1. Summary of polymer substrates studied, characteristic functional groups, and reactivity toward TMA/water ALD process. For each polymer, the TMA exposure was approximately 60seconds at 2 Torr.

Polymer	Characteristic group	# of Al-CH_3 monolayers
Polyolefin (PP fiber)	C-C	< 10
Polyvinyl Alcohol (PVA fiber)	C-OH	~ 24±6
Polyamide (PA 6)	C-(C=O)-NH-C	~ 5.9±0.9 $\times 10^2$
Polyester (PBT)	C-(C=O)-O-C	~ 1.8±0.3 $\times 10^4$
Polyester (PET)		~ 8.3±0.6 $\times 10^4$
Polyester (PLA)		~ 3.1±0.3 $\times 10^3$
Polycarbonate (PC)	C-O-(C=O)-O-C	~ 9.1±1.8 $\times 10^2$
Poly methyl methacrylate (PMMA)	C-(C=O)-O-C	~ 1.0±0.2 $\times 10^3$
Polyethylene Oxide (PEO)	C-O-C	~ 6.5±0.6 $\times 10^4$

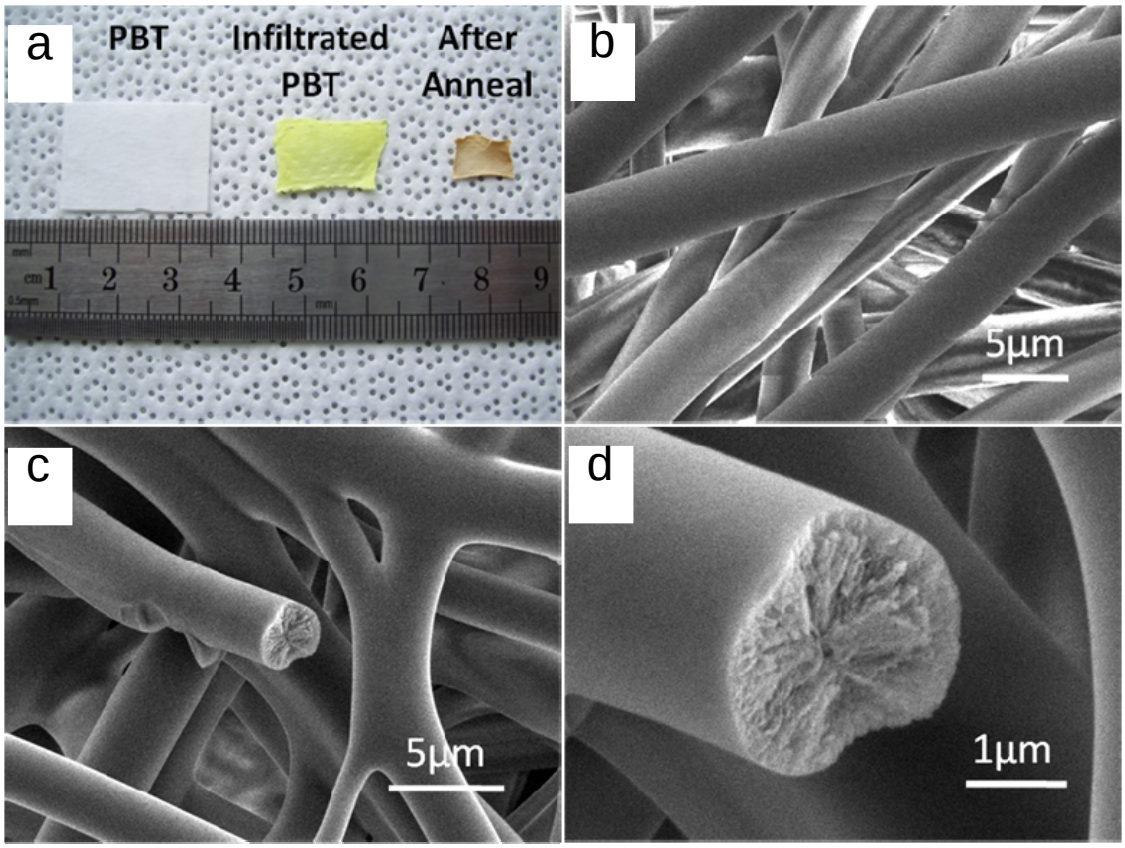


Figure 3.10. Panel (a) presents a picture of polybutylene terephthalate (PBT) nonwoven fiber mats: (left) as received; (middle) after TMA/water infiltration; and (right) after infiltration and anneal at 450°C. The starting size for all samples was approximately the same. After infiltration, the fiber mat becomes yellow in color, shrinks in size and becomes mechanically stiffer. Annealing causes more shrinkage, and the sample becomes more brittle, consistent with transformation of the polymer to micron-sized alumina fibers. Panel (b) shows a scanning electron microscope image of the as-received PBT nonwoven. Panels (c) and (d) show a similar sample after 1 h TMA/water soaking and 12 h 450°C anneal. The images in (c) and (d) show that the soaking and annealing preserves the starting fiber morphology. Some connectivity between the fibers likely results from polymer flow during the soaking process. More connectivity was observed with higher process temperature and longer precursor exposure. The cross-sectional view in panel (d) confirms that the fibers are uniform after calcination, indicating full penetration of the precursor throughout the 3 µm diameter starting fiber.

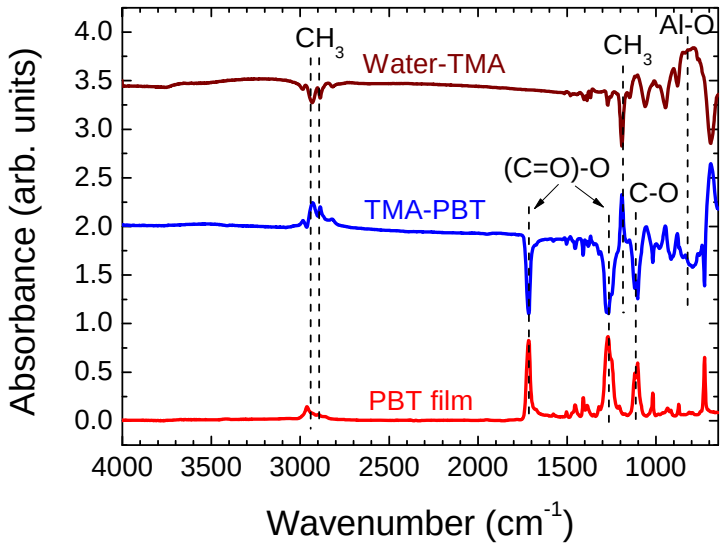


Figure 3.11. FTIR transmission spectra collected in situ from the a starting PBT film cast onto a silicon substrate (bottom trace) and after exposing the film to TMA (middle) and water (upper trace) at 80°C. The TMA exposure removes ester (1720 and 1270cm^{-1}) and ether (1100 cm^{-1}) bonding units indicating high reactivity between TMA and ester bonds in the PBT. The CH_3 (2860 and 2930 cm^{-1}) and Al-CH_3 modes (1200 cm^{-1}) increase upon TMA treatment, confirming Al-CH_3 present in the soaked PBT film. After water dosing, the decrease in CH_3 and Al-CH_3 absorbance and an increase in Al-O modes shows water reacting with the Al-CH_3 groups to form Al-OH.

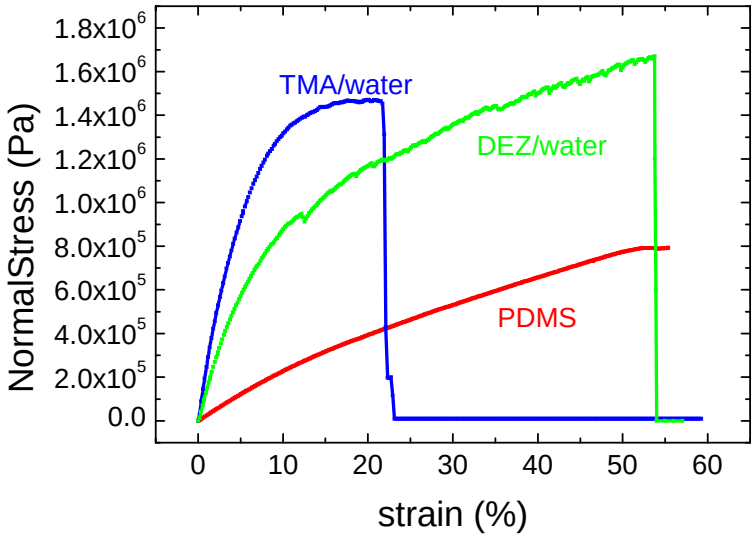


Figure 3.12. Stress strain curve of TMA/water and DEZ/water soaked PDMS and pristine PDMS. The slope of the stress strain curve is the measure of the Young's modules, we can see after soak with metal organic precursor, the modules of PDMS is significant increased. This increase of young's modulus will form a mechanical buffer layer between ALD coating and bulk PDMS, which will stabilize the ALD coating and keep the ALD layer intact.

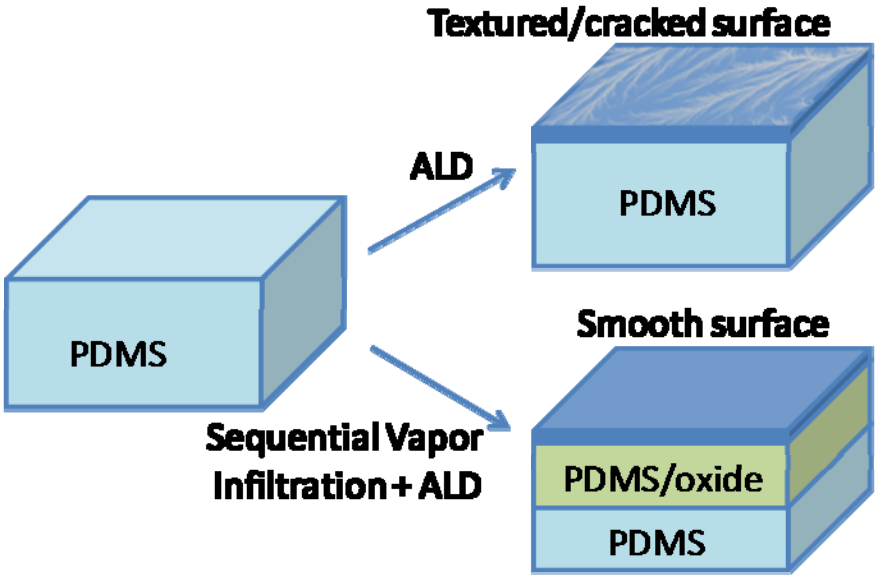


Figure 3.13. Schematic diagram of surface treatment of PDMS with ALD only or sequential vapor infiltration followed by ALD. The top scenario shows direct aluminum oxide ALD on PDMS resulting in cracked aluminum oxide coating. The bottom scenario shows ALD after sequential vapor infiltration, producing a smooth and uniform coating on the PDMS. The sequential vapor infiltration before the ALD helps maintain the surface in a hydrophilic state.

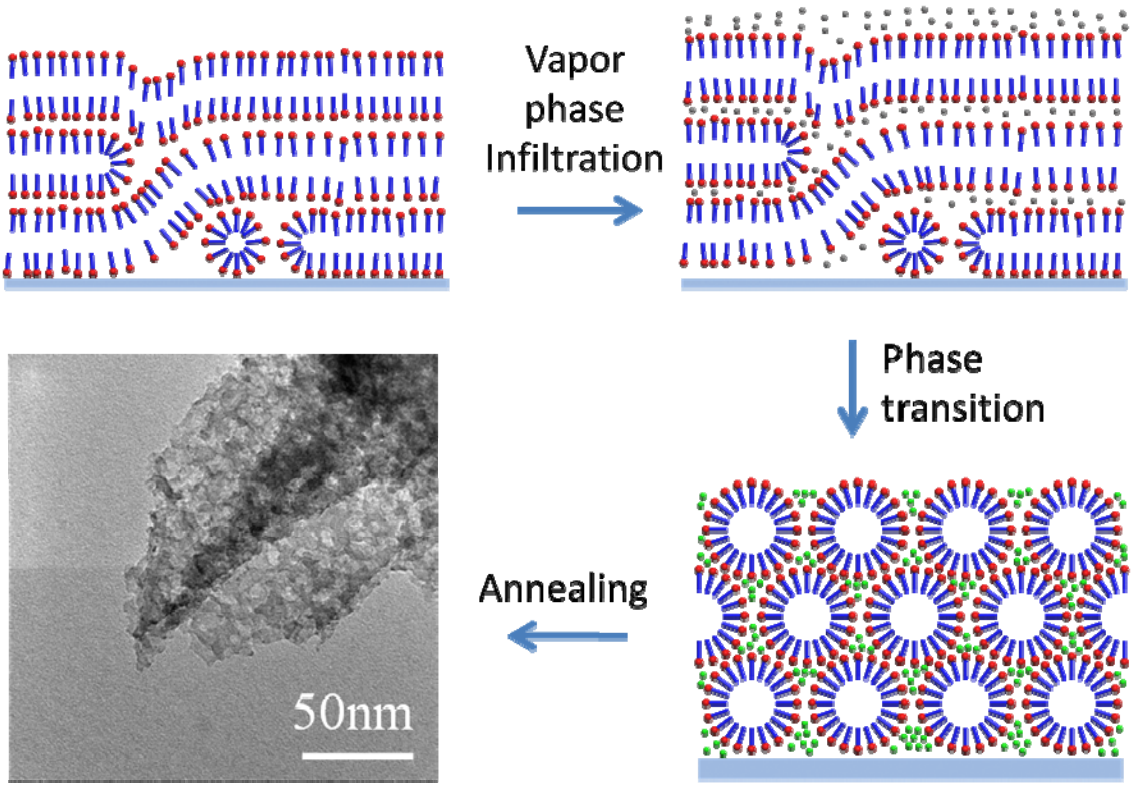


Figure 3.14. Schematic diagram for the preparation of mesoporous metal oxide materials from vapor phase infiltration method.

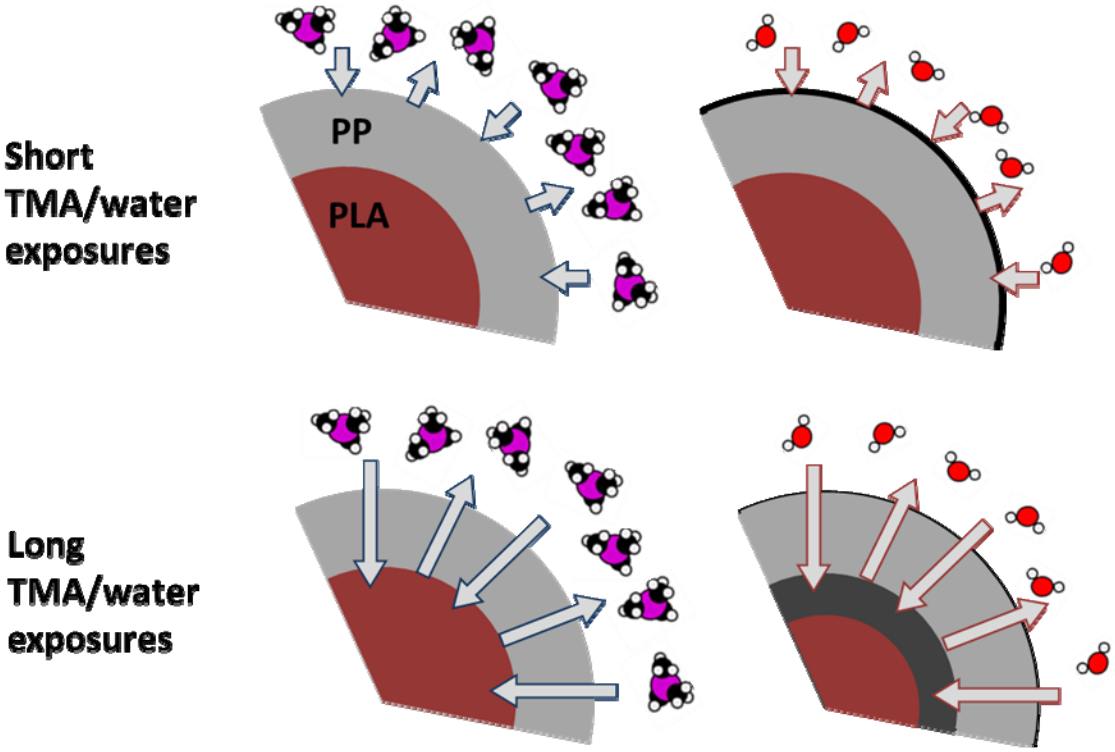


Figure 3.15. Schematic diagram of the "short" and "long" TMA/water ALD cycles on PLA/PP core/sheath bi-component fibers. When the core/sheath fiber was exposed to "short" TMA/water exposures, precursor vapors were not given enough time to diffuse into the PP layer. Minimal subsurface diffusion and reaction occurred, and thin Al2O3 ALD layer was deposited on PP surface. However, when the "long" precursor exposures were used, TMA and water vapors could diffuse through the PP, and react with PLA core.

CHAPTER 4 is a reprint of a manuscript published in JPCB.

CHAPTER 4. Conformal Organic-Inorganic Hybrid Network Polymer Thin Films by Molecular Layer Deposition using Trimethylaluminum and Glycidol

Bo Gong, Qing Peng and Gregory N. Parsons*

Department of Chemical and Biomolecular Engineering, North Carolina State University, Raleigh, North Carolina, 27695, USA

*Corresponding author: Tel: 919 515 7553, Fax: 919-515-3465,

Email: parsons@ncsu.edu

Abstract

Growing interest in nanoscale organic-inorganic hybrid network polymer materials is driving exploration of new bulk and thin film synthesis reaction mechanisms. Molecular layer deposition (MLD) is a vapor phase deposition process, based on atomic layer deposition (ALD) which proceeds by exposing a surface to an alternating sequence of two or more reactant species, where each surface half-reaction goes to completion before the next reactant exposure. This work describes film growth using trimethyl aluminum and hetero-bifunctional glycidol at moderate temperatures (90 – 150 °C) producing a relatively stable organic-inorganic network polymer of the form (-Al-O-(C4H8)-O-)n. Film growth rate and in-situ reaction analysis indicates that film growth does not initially follow a steady state rate, but increases rapidly during early film growth. The mechanism is consistent with subsurface species transport and trapping, previously documented during MLD and ALD on polymers. A water exposure step after the TMA produces a more linear growth rate, likely by blocking TMA subsurface diffusion. Uniform and conformal films are formed on complex non-planar substrates. Upon post-deposition annealing, films transform into microporous metal oxides with ~5 Å pore size and surface area as high as ~327 m^2/g, and the resulting structures duplicate the shape of the original substrate. These hybrid films and porous materials could find uses in several research fields including gas separations and diffusion barriers, biomedical scaffolds, high surface area coatings and others.

4.1. Introduction

Thin films and coatings of hybrid organic-inorganic materials are interesting for applications involving chemical absorption and detection, pre-determined stimulus response, or as surface templates for assembly of complex hierarchical nanostructures. Intensive research focused onto preparation of films containing tunable surface texture and porosity has revealed means to form films with variable non-covalent interaction groups, or capable of molecular scale shape generation.[1-5] Understanding chemical mechanisms during cooperative assembly of organic-inorganic hybrid films is critical to achieve desired function and response.[1-5] Many well known solution-based or sol-gel processes permit controlled assembly of molecule-based films or laminated organic-inorganic structures over large areas.[4-9] However, common methods for polymer film fabrications utilize organic solvents, which will degrade, swell and dissolve substrates, and raise safety and environmental concerns. Vapor phase molecule assembly methods provide an alternative route to deposit organic-inorganic thin film structures. Vapor delivery of organic and inorganic species can help ensure materials purity, and it can provide means, for example, to integrate films on substrates with arbitrary complex surfaces.[10-12] Moreover, new reaction pathways that are amendable to precise control of composition, conformality, and thickness are most challenging and of primary interest for product design. Following the principles of atomic layer deposition (ALD),[13-15] researchers are currently exploring vapor phase molecular layer deposition (MLD) approaches for organic or hybrid materials deposition and integration.[16-21] The MLD approach utilizes alternating self-limited heterogeneous surface reactions to build up a solid-state thin film though a sequence of molecular adsorption/reaction steps. Under

mild temperature conditions, exposing an excess single component vapor phase reagent to well-defined surface bound reactive ligands results in a self-saturating half-reaction that prepares the surface for a subsequent complementary half-reaction. The complete sequence constitutes one reaction cycle, and with sufficient precursor exposure, the extent of half-reactions is determined by the number of available reactive sites on the growth surface. This progression thereby allows a film to be conformally constructed on surfaces with arbitrary shape and surface area.

Based on coupling binary chemistries, MLD permits surface synthesis of homogeneous polymers and hybrid organic-inorganic thin film materials.[16-21] For example, diethyl zinc (DEZ) reacts alternatively with ethylene glycol (EG) through a ethane elimination reaction to form a thin film polymer of the form $(Zn\text{-}O\text{-}CH_2\text{-}CH_2\text{-}O)_n$. However, during the deposition process, homo-bifunctional organic reactants, such as EG, typically undergo a symmetric "double-end" surface reaction.[16,19,20] This parasitic reaction process decreases the density of reactive sites available for the following half-reaction and results in slow growth rates and poor material stability. For example, our group found that upon air exposure, films prepared from DEZ and EG decreased in film thickness changed composition, consistent with organic vaporization. In addition, Miller et al. reported that films deposited from trimethyl aluminum (TMA) and ethylene glycol (EG) became stiffer after expose to air. [22]

To help avoid the double reaction, Yoon et al. explored hetero-bifunctional reactants in three-reagent MLD reaction sequences to form aluminum oxide-organic hybrid films.[21] The parasitic reactions can be avoided, but the additional reaction steps tend to impede

significant rate enhancement. It is well know that TMA can react with hydroxyl groups through a methane elimination reaction. TMA is also a strong Lewis acid catalyst, and it is important for the selective addition of methyl into nucleophilic epoxy group to form C-C bond linkages.[23,24] We hypothesized that selective reactivity of hydroxyl or epoxy groups on glycidol towards TMA could lead to a stable two-step MLD reaction scheme that could suppress or avoid the deleterious surface double reaction. Previous studies also show that precursor subsurface diffusion and reaction can be important during ALD on polymers.[25-27] George et al. also invoked subsurface species diffusion during three-step molecular layer deposition to explain non-linear increasing growth rates.[28]

This work describes MLD reaction studies using TMA and glycidol in a two-step molecular vapor/surface reaction, forming solid organic-inorganic network thin films. We find that hetero-bifunctional glycidol does not eliminate the double reaction, but the films are stable in air and grow at a high rate compared to other reported hybrid MLD films. We monitored reaction progress using in-situ Fourier transform infrared spectroscopy (FTIR) and quartz crystal microbalance (QCM) for growth between 90 and 150 °C. In addition, the film growth rate, surface morphology, and composition were studied ex-situ. Other related reagents and sequences were also explored. We found that reactions between TMA and the glycidol hydroxyl and epoxy groups were not sufficiently selective to avoid the surface double reaction. However, we find that the deposition sequence can produce air-stable and conformal hybrid thin films, and the mechanistic studies provide interesting insight into subsurface diffusion and reaction during hybrid film deposition. Lewis acid/base interactions between TMA and oxygen lone pair sites in the deposited film likely help trap and stabilize

the TMA in the growing film bulk. The role of this interaction is confirmed by substituting diethyl zinc as a weaker Lewis acid for the TMA, which produced significant lower growth rate and no growth rate acceleration.

4.2. Experimental Section

Chemicals and Materials

Trimethyl aluminum (TMA, 98%) and diethyl zinc (DEZ, 95%) were purchased from Strem Chemicals. glycidol (GLY, 96%) was purchased from Sigma-Aldrich. All of the precursors were used as received. Deionized water (DI-H_2O) was used as the water source. Ultra-high purity Argon (99.999%, National Welders Supply Co.) was further purified with an inert gas filter (Gatekeeper®) and used for purge gas and carrier gas. Double-side-polished high resistivity (50-100 Ω-cm) n-type silicon (100) substrates with uniform ~ 60% transmittance over the middle infrared range, were used for IR substrates for ex-situ IR analysis. Before processing, silicon wafers were wet cleaned by BakerClean® JTB-100 solution (Mallinckrodt Baker Inc), followed by rinsing with DI-H_2O and blown-dry with N_2. High surface area anodic aluminum oxide (AAO) membranes (Anodisc™, 60 μm thickness, 0.1 μm pore size and 13 mm diameter) were purchased from Whatman and mounted onto an IR silicon wafer substrate for in-situ FTIR analysis. For QCM analysis, unpolished quartz crystals with gold coating (SC-101, 6 MHz) were purchased from Inficon and used as received.

Deposition Reactors and Processes

MLD and ALD deposition studies were carried out in a homemade hot wall viscous flow vacuum reactor equipped with in-situ QCM as described previously.[19] To protect the pump system during reaction, the exhaust from the organic and metal-organic exposure steps were pumped through independent exhaust lines using computer-controlled gate valves. A liquid nitrogen trap was installed in the organic exhaust line before the pump to trap any organic effluent. The film deposition precursors (TMA, DEZ and DI–H_2O) were stored in separate stainless steel bottles and evaporated at 25°C. During the predetermined gas exposure time, a computer–controlled ALD solenoid valve opened to allow the effluent vapor to mix into flowing Ar carrier gas. The GLY liquid was loaded into a bubbler and heated at 60 °C, and during the GLY exposure period, Ar gas bubbled through the vessel and into the reactor. After each precursor or reactant exposure step, Ar gas continued to flow to purge the reactor or any remaining reactant or product vapor. The steady-state process pressure was ~1.1 Torr and the total Ar flow rate was approximately 200 standard cubic centimeters per minute. During TMA, DEZ, H_2O and GLY dose times, the transition reactor pressure increase are approximately 150, 100, 50 and 50 mTorr, respectively. A range of reactant exposure times were evaluated during the growth. A typical deposition cycle followed a TMA/Ar/GLY/Ar sequence where the exposure or purge times were 1/40/2/40 seconds, respectively. For conciseness, the written reaction sequences include only the pertinent reactants, i.e., TMA/Ar/GLY/Ar is written as "TMA/GLY".

A special designed IR reactor was used for in-situ FTIR analysis in transmission mode, as showed in Figure 3.1. The IR beam was directed out from a FTIR spectrometer

(Nicolet 6700, Thermofisher), through the vertically-mounted sample, reflected off a gold parabolic mirror and focused onto an external MCT-A (mercury cadmium telluride type A) IR detector. The IR beam is transmitted through the reactor using two single crystal CsI IR windows. The windows permit the IR beam to cross horizontally through a 15 cm wide deposition analysis zone, where the beam path is perpendicular to the gas flow direction. Gate valves isolate the IR windows from precursor or product exposure during the reactant dose periods, and the values are open and data collected during the Ar gas purge period. Spectra were acquired with 4 cm^{-1} resolution and 200 scans. Before IR analysis, the AAO substrate was coated with 20 cycles of TMA/H_2O to form a reproducible Al_2O_3 starting surface. Spectra are displayed in differential mode, where the spectrum collected from the last half-cycle is used as the background reference. During the in-situ FTIR experiments, a typical TMA/GLY deposition cycle involved TMA and GLY gas exposure for 1 and 2 seconds respectively, with 120 s Ar purge and 150 s IR data collection period after each vapor exposure.

Ex-situ Characterization

Ex-situ FTIR measurements employed a Thermo scientific Nicolet 6700 IR bench in transmission mode using a deuterated triglycine sulfate (DTGS) detector and continuously purged with purified dry air. Samples were measured with 2050 scans at 4 cm^{-1} resolution. X-ray photoelectron spectroscopy (XPS) analysis utilized a Kratos Analytical Axis Ultra tool with a monochromatic Al Kα source. For all samples, C 1s peak was normalized to 284.5 eV as the reference. The pass energies for the survey and detail scans were 160 and 20 eV, respectively. The surface morphology of resultant films was analyzed using a Q-Scope 250

scanning probe microscope (Quesant Instrument Corporation) in tapping mode. A variable-angle alpha-SE spectroscopic ellipsometry (J.A. Woollam Co., Inc.) was used to determine film thickness and reactive index using a three-layer (film/native oxide/silicon) Cauchy model. In the model, thickness of the native oxide is 20 Å, and the Si substrate is 400 μm.

For conformality analysis, deposition was also performed onto three dimensional polyvinyl alcohol (PVA) electrospun fiber mats with average fiber diameter of ~ 200 nm.[12] The fiber substrates were coated with 25 cycles of TMA/GLY (2/40/4/40) at 120 °C, and then heated in air at 400 °C for 48 hours to remove the polymer template and organic component in the film and produce hollow microtubes. After dispersing the as-formed microtubes in methanol and sonicating for 1 min, several droplets were pipetted onto carbon film-coated TEM grids (Ted Pella, Inc.) then allowed to dry in lab air for several hours. Samples were then imaged in a Hitachi HF 2000 transmission electron microscope operated at 200 kV. Brunauer-Emmett-Teller (BET) surface area and the pore size distribution of the resulting microtubes were measured by nitrogen adsorption/desorption method using an Autosorb-1C surface area analyzer (Quantachrome instrument). Hirvath-Kawazoe (HK) and Barrett-Joyner-Halenda (BJH) methods were used to estimate the micropore and mesopore size distribution, respectively.

4.3. Results and Discussion

Deposition Rate

Sequentially dosing TMA and GLY onto Si wafer at temperatures between ~90 and 150 °C produced well defined thin films with thickness that depends upon precursor exposure duration, number of exposure cycles and reaction temperature. Figure 3.2(a)

displays a plot of the thickness (determined by ellipsometry) of the TMA/GLY MLD films on a silicon wafer versus number of MLD cycles at various deposition temperatures. The growth rate decreases as the substrate temperature increases. Dameron et.al [16] and Peng et.al [19] observed similar trends previously and ascribed the result to less precursor absorption at higher temperature.[16,19] We also carefully explored the film thickness and refractive index as a function of number of MLD cycles during the initial deposition cycles, and the result are presented in Figure 3.2(b). At 120 °C, the growth rate of the MLD film on silicon started off slowly and increased over the first 100 cycles before reaching steady state. The reflective index decreased as growth proceeded, consistent with a less dense film structure and overall change in the growth mechanisms. We also found that the growth rate is sensitive to the reagent exposure time and purge time. Growth was saturated at 3.3 nm/cycle at T=120 °C using TMA/Ar/GLY/Ar times of 20/90/10/90 seconds. However, a prolonged purge (300 s) decreased the growth rate to 1.2 nm/cycle. We also note that samples prepared with shorter purge time showed lower reflective index as determined by ellipsometry (n = 1.472) compared with the sample deposited with prolonged purge steps (n = 1.498). This reduced refractive index indicates more organic component in the deposited film, likely from more glycidol physisorption. All of these observations are consistent with diffusion controlled reaction kinetics, where longer purge times allow more trapped organic species to diffuse out of the film, producing less net growth.

In-situ QCM and FTIR Analysis

In-situ QCM results of TMA/water ALD and TMA/GLY MLD sequences are shown in Figure 3.3. For these runs, the process started with several cycles of TMA/water, and at

time t=0, the flow sequence was switched to TMA/GLY. In Figure 3.3a, typical QCM results for the TMA/water ALD process at 120 °C shows regular, step-wise film growth, with ~80 ng/cm^2 and ~12 ng/cm^2 mass uptake during the TMA and water pulses, respectively, as expected during ALD on our unpolished QCM crystal.[29,30] Figure 3.3b shows similar QCM results collected during the TMA/GLY cycle at 120 °C after more than 100 TMA/GLY cycles. The average mass uptake is ~210 and ~118 ng/cm^2 for the TMA and glycidol cycles, respectively. The TMA mass uptake is much larger than during similar TMA/water pulses, again consistent with excess subsurface adsorption. Figure 3.3c shows mass uptake data collected during the transition process from the TMA/water process to TMA/GLY at various substrate temperatures. Upon switching to TMA/GLY, the overall mass uptake rate stayed small for ~30-50 cycles then began to accelerate until a steady state growth is achieved. The average mass uptake from TMA and GLY during steady state growth was analyzed at different deposition temperatures. At low temperature, the ratio of TMA/GLY mass uptake is relatively low (1.60 at 90 °C), while at higher temperatures the ratio reached 2.13 at 120 °C and 2.26 at 150 °C. The low ratio at low temperature indicates more organic incorporation. More glycidol physisorption is expected at lower growth temperature.

The growth acceleration is emphasized further in Figure 3.3d where the mass uptake data for each cycle is plotted versus cycle number. It is interesting to note that the mass uptake rate is higher for the first cycle, decreases and stays small for the next 30-50 cycles, then increases before reaching a stable value after 60-70 cycles. Similar trends were reported by George et al. during an MLD sequence involving TMA, ethanolamine and maleic anhydride[31]. A surface poisoning effect after the first cycle is consistent with the “double

reaction" between surface Al-methyl sites and the two reactive ends of the GLY. The growth rate stays small because of few reactive sites on the growth surface. As growth proceeds, more film bulk becomes available as a reservoir for adsorbed TMA, allowing growth to speed up until diffusion and exposure reach a steady state balance.

The growing organic-inorganic film is sufficiently porous that TMA can diffuse subsurface and become trapped, for example, through a Lewis acid/base adduct formation with available oxygen species. The GLY in the following reactant dose can then react with the bound TMA, resulting in film growth. One mechanism likely involves an Al-CH_3 catalyzed glycidol ring-opening reaction. Considering all these processes, the steady state film growth rate is expected to depend on the overall kinetics of species diffusion, adsorption and reaction, which will change with reaction temperature as well as reactant exposure and purge conditions.

To further explore the proposed diffusion/reaction mechanism, we covered a QCM crystal surface with ~100 cycles of TMA/GLY MLD (1/40/2/40 s), then exposed it to multiple doses of TMA/Ar (1/82 s) and GLY/Ar (2/81 s). Results are presented in Figures 4.4a and b, respectively. The first TMA exposure on the TMA/GLY film produces a relatively large mass uptake, with less increase as the exposure is repeated. Similarly, after several TMA/Ar exposures, exposure to GLY/Ar (Figure 4.4b) produces a large mass uptake, followed by a smaller increase during following GLY/Ar exposure steps. Surface reaction saturation is a hallmark of ALD processes. However, the reaction between buried TMA observed here is ascribed to a balance of kinetic transport and diffusion effects, rather than dominant self-limiting surface reaction desired in an ideal ALD or MLD process.

We also used QCM to examine the deposition behavior of MLD TMA/H_2O/GLY. The mass uptake during TMA/H_2O/GLY sequence proceeds with a more steady film growth rate, with a mass uptake of ~32 ng/cm^2/cycle. This relatively small mass uptake during the TMA/H_2O/GLY sequence is explained as follows. The water dose on the TMA saturated film reacts with available Al-CH_3 sites to form Al-OH units. The glycidol can react with Al-OH through dehydration, leaving the epoxy group to react with the following TMA dose. The TMA reaction with water, however, impedes or blocks TMA diffusion, eliminating a key pathway for TMA/GLY reaction. As an additional control experiment (data in Figure 4.5), replacing the TMA with diethyl zinc results in dramatically decreased growth rate compared with TMA/GLY. The DEZ is a much weaker Lewis acid than TMA, and it is less likely to bind subsurface and will not effectively catalyze the epoxy ring opening[23,32] severely limiting growth.

The surface reaction mechanism was further studied by in-situ FTIR. Figure 4.6a shows in-situ IR spectra collected during the TMA/GLY MLD at 120 °C, where the data collection sequence proceeds up from the bottom spectrum to the top. The spectrum labeled "TMA – water" shows the spectral changes after the Al-OH surface exposed to TMA. The -OH stretching mode (near 3700 cm^{-1}) decreases, while the CH_3 symmetric (2895 cm^{-1}), asymmetric stretching (2940 cm^{-1}) modes and deformation (1200 cm^{-1}) mode increase, which are consistent with the formation -O-Al-CH_3 surface species from the reaction between TMA and surface -Al-OH.[33] The next spectrum presents the change resulted by exposing the as-formed Al-CH_3 surface to GLY. New modes at 2865 and 2920 cm^{-1} corresponding to symmetric and asymmetric CH_2 stretching, demonstrate the presence of surface bonded

GLY. Decrease of the CH_3 deformation mode intensity provides evidence for the reaction between surface Al-CH_3 groups and the glycidol hydroxyl and epoxy groups. The glycidol dose produces a small increase in hydroxyl absorbance due to unreacted hydroxyl groups, which are then available for subsequent reaction with TMA. A signal due to epoxide is expected near 913 cm^{-1}, which is outside the measurement range on the AAO substrate used. The spectrum labeled "TMA – GLY" shows the spectral change when the GLY treated surface is exposed to TMA. The positive IR peaks of -CH_3 appears while OH features become negative, consistent with TMA reaction with -C-OH to form surface Al-CH_3 units.

In-situ infrared transmission experiments were also performed using the TMA/H_2O/GLY sequence at 120 °C, and results are presented in Figure 4.6b. The bottom two spectra were collected after TMA and H_2O exposure, respectively (i.e. during Al_2O_3 ALD) producing an Al-OH saturated surface. The top-most spectrum shows the absorbance difference when the Al-OH surface reacts with GLY. The GLY exposure produces an increase in CH_2 vibrations, but there is also a distinct decrease in surface OH groups. The removal of -OH and the addition of -CH_2 groups are ascribed to reaction between Al-OH surface and the hydroxyl end group of the GLY forming a surface ethyl epoxy group and volatile H_2O. We may also expect the epoxy groups on GLY will react with surface hydroxyl through a ring-opening mechanism. However, the transfer of a hydroxyl group from the Al-OH to the epoxide carbon would not change the surface OH density. The top-most spectrum in Figure 4.6b shows a net decrease in OH density upon GLY exposure on the –OH surface, indicating GLY reaction with surface hydroxyls through the dehydration mechanism.

The proposed reaction sequence for the TMA/GLY process is shown schematically in Figure 4.7. The schematic shows during the glycidol exposure on the Al-CH_3 surface, the glycidol can bond through Lewis acid/base interaction and by methyl elimination to form Al-O-C- bonds. A ring-opening/transalkylation reaction will produce (Al-O-CH_2-CH(CH_3)-CH_2-OH) or (Al-O-CH_2-CH(CH_2-CH_3)-OH) groups. Remaining hydroxyl groups then react with TMA during the next exposure step. As film thickness increases, subsurface TMA diffusion (not shown in the schematic) becomes more prevalent. The TMA could be stabilized by bonding with available oxygen lone pair sites, or it could be kinetically trapped by random diffusion. Any TMA remaining in the film after the subsequent purge cycle (including TMA trapped sub-surface) will provide additional sites for glycidol adsorption, reaction and incorporation in the growing film.

Ex-situ Characterization

Figure 4.8(a) shows ex-situ FTIR spectra of typical MLD films deposited at 120°C. Spectral features include the characteristic CH_2 symmetric and asymmetric stretching modes at 2865 and 2925 cm^{-1}, respectively, C-O stretching at 1100 cm^{-1}, and Al-O stretching mode near 700 cm^{-1}, consistent with the expected polymer structure (-Al-O-(C_4H_8)-O-)$_n$, where the (C_4H_8) group could be (CH_2-CH(CH_3)-CH_2) or (CH_2-CH(CH_2-CH_3)). The peak intensities increase with the number of cycles, as expected for film growth. The small peaks at 844 and 913 cm^{-1} indicate that some epoxide groups may remain in the film. Figure 4.8(b) shows a trend for the absorbance of CH_2 stretching mode at 2925 cm^{-1} plotted versus number of ALD cycles. The slower absorbance increase at the beginning stage is consistent with the reduced reactivity for GLY during early film cycles as discussed above.

X-ray photoelectron spectra data in Figure 4.9 shows the composition and bonding structure of a typical hybrid film deposited at 120 °C. The survey scan indicates 41 at.% (atomic percent) carbon and 8.4 at.% aluminum for film deposited at 120 °C. The detail scan of C 1s peak shows C-C, C=O and C-O-Al related features. The C=O feature is likely due to surface carbon from the ambient, or possibly from the reformation of epoxy groups. Samples deposited at 90 °C show a reduced Al fraction of 6.6 at. %, indicating increased GLY incorporation at reduced temperature, consistent with the QCM results.

Figure 4.10 displays surface morphology after 100 cycles of film growth (1/40/2/40) at 120 °C on silicon substrate. The surface texture is relatively smooth with a root mean square roughness of ~5.6 Å. We examined conformality of the TMA/GLY film using electrospun polyvinyl alcohol (PVA) fibers as a film substrate.[12] Figure 4.11 presents transmission electron microscope images of tubular replicas formed by exposing PVA fibers to 25 TMA/GLY cycles at 120 °C, followed by calcination in air for 48 hours at 400 °C. The tubes have relatively uniform wall thickness of ~ 20 nm and provide strong evidence for good coating conformality, even under conditions where diffusion/reaction mechanisms are important. After the annealing treatment, nitrogen adsorption/desorption analysis shows that the materials are microporous with specific surface area of ~326.7 m^2/g. The micropore and mesopore size distributions were calculated from the adsorption and desorption isotherm curves and plotted in Figure 4.12. We can see that the resulting microtubes are microporous with a mode pore size of ~5 Å, with some mesopores also present. The pore size and surface area will be affected by the detailed process conditions. For example, glycidol physisorption at low deposition temperature and short purge time will produce films with higher organic

component, forming larger pores after calcination. Our findings show a narrower pore size distribution than that reported by Liang et al.[11] who characterized porosity of metal oxide structures formed by calcination of organic-inorganic hybrid thin films on silica particles.

We also studied the thermal and ambient stability of the materials formed at 120 °C using ex-situ FTIR and ellipsometry measurements, and results are displayed in Figure 4.13a and 13b. The IR results in Figure 4.13a show that prolonged air exposure produced some increase in OH absorption, but changes in other features were negligible. The film thickness measured by ellipsometry (Figure 4.13b) was also stable upon air exposure. The material stability is significantly improved compared to previous reports of inorganic-organic network polymers formed by molecular layer deposition.[16,19-21] Aluminum oxide-based network polymers, for example, formed using TMA/ethylene glycol MLD show a significant (>20%) thickness decrease after several days in laboratory air.[16] Similar instability was also observed for films deposited using DEZ and ethylene glycol.[19] The improved stability of films from the TMA/glycidol process suggests more complete precursor reactivity and cross-linking in this system. As expected, mass loss is observed when material are annealed in air at elevated temperature. When a film deposited at 120 °C is annealed in air at 100 °C for 2 hours, (Figure 4.13c) features in the IR spectrum remain unchanged. Annealing at 200 °C for 2 hours produces a loss of hydroxyl groups, and further annealing at 300 °C eliminates most of the organic C-H units. Ellipsometry shows a related decrease in film thickness upon anneals at 200 and 300 °C (Figure 4.13d).

4.4. Summary and Conclusions

Trimethyl aluminum and hetero-bifunctional glycidol will react in an alternating surface reaction sequence to produce stable organic-inorganic hybrid thin film polymer material of the form $(\text{-Al-O-}(C_4H_8)\text{-O-})_n$. The reaction proceeds at moderate temperatures on planar and nonplanar surfaces to produce conformal and uniform films. Using in-situ spectroscopic analysis, we conclude that film growth proceeds through a combined diffusion/binding/reaction mechanism, involving sub-surface reactant accumulation during reactant dosing. The IR and growth rate data also indicate that both ends of the glycidol hetero-bifunctional reagent react with the $Al\text{-}CH_3$ surface. The mechanism is consistent with previous studies of ALD growth on polymers and three-step MLD reactions showing growth acceleration due to subsurface species transport and trapping. A water exposure step after the TMA is found to impede growth acceleration, likely by blocking TMA subsurface diffusion. Post-deposition annealing of hybrid organic-inorganic films in air results in well defined porous inorganic structures with shape that mimics the original deposition substrate. Even though the reaction does not follow an ideal self-limiting surface reaction growth sequence, the process is still sufficiently controlled to allow highly conformal films to form on complex non-planar substrates. Such materials could find applications in fields including gas separations and diffusion barriers, biomedical scaffolds, and porous coatings.

Acknowledgments

This work was supported by the National Science Foundation project CBET-1034374, and DOE project #08NT0001925. We are grateful to Ying Liu, Mark D Walters and Roberto Garcia for assistance with AFM, XPS and TEM data collection, respectively.

We thank Mr. Shane DiDona for visual imaging of the FTIR reactor layout. We also thank Steve George and Charles Musgrave at UC Boulder for discussions regarding MLD reaction mechanisms.

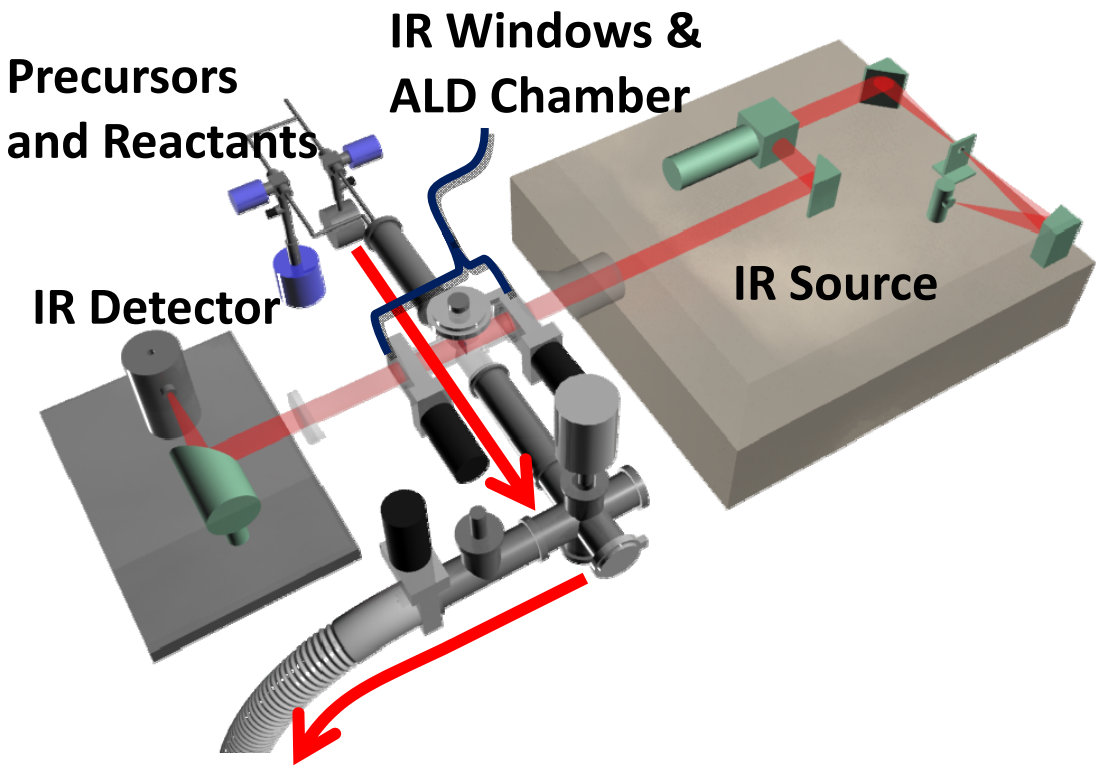


Figure 4.1. Schematic diagram of the in-situ FTIR ALD/MLD reactor. The precursors are delivered into the reactor with high purity Ar. In the middle part of the chamber, two CsI IR windows are attached, and two gate valves are installed between the IR window and reactor chamber to prevent the deposition of ALD/MLD film on the windows. During the measurement, the IR beam is directed through the planar sample and focused into a MCT-A detector. Before each dose, a background spectrum was collected as reference, and differential spectra were employed to show the surface chemistry change after each pulse.

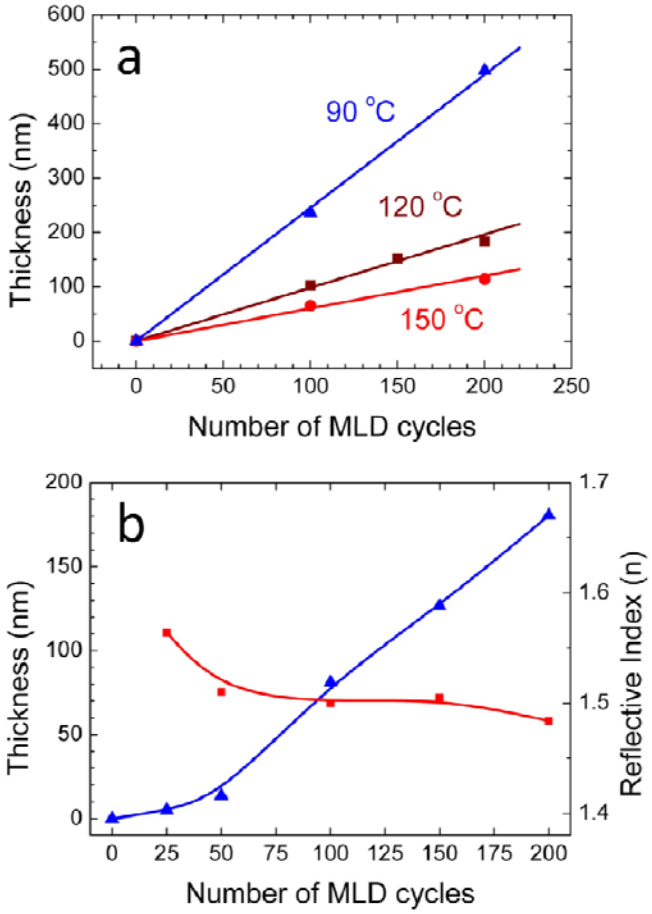


Figure 4.2. (a) Film thickness for TMA/GLY MLD films on silicon wafers is plotted versus number of MLD cycles at various growth temperatures. Film thickness was determined using ellipsometry. For all the samples on Si wafer the deposition sequence was TMA/Ar/GLY/Ar = 1/40/2/40 seconds. The growth rate decreased from 2.4 nm/cycle to 0.6 nm/cycle as the substrate temperature increased from 90 to 150 °C. (b) More careful examination shows the growth rate of the MLD film on silicon starts off slowly and increases over the first 100 cycles at 120 °C, before reaching steady state. The reflective index decreased with growth time, consistent with a less dense film structure and overall change in the growth reaction mechanism as deposition proceeds.

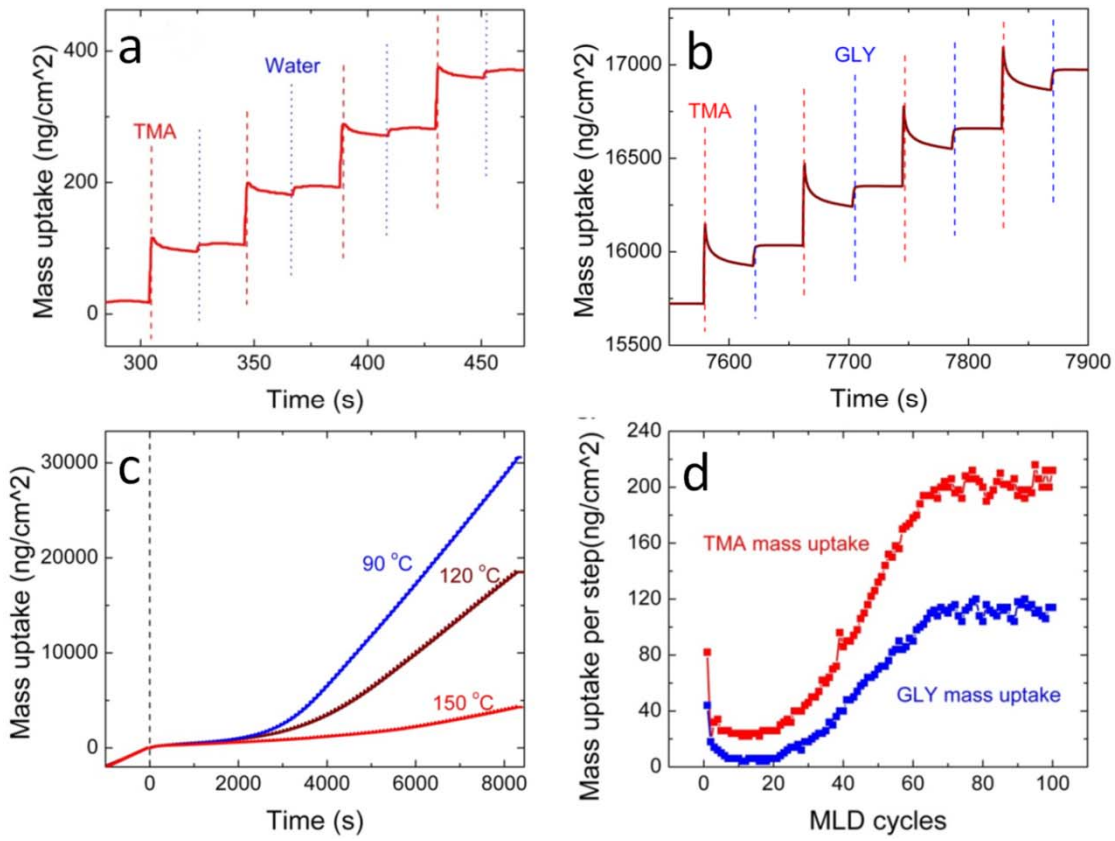


Figure 4.3. In-situ QCM mass uptake results for TMA/water ALD and TMA/GLY MLD sequences. Gas pulse and purge times were 1/40/2/40 seconds. (a) TMA/water ALD at 120 °C under steady-state growth, shows an average mass uptake during the TMA and water pulses of ~80 ng/cm^2 and ~12 ng/cm^2 respectively; (b) TMA/GLY MLD at 120 °C under steady-state growth shows a larger average mass uptake of ~210 ng/cm^2 and ~118 ng/cm^2 during the TMA and GLY pulses, respectively; (c) 100 cycles of TMA/GLY MLD at 90 to 150 °C on an Al-OH surface (formed using TMA/water ALD) shows an increase in deposition rate at lower temperatures, and a growth incubation time. (d) Mass uptake per step for 100 cycles of TMA/GLY MLD at 120 120 °C on Al-OH surface. Approximately 60 cycles was needed for the TMA/GLY MLD process to reach steady growth, which is consistent with growth rate data collected from film on Si wafers. The small mass uptake of TMA and GLY at the very beginning implied the "double" reaction is happening on the surface.

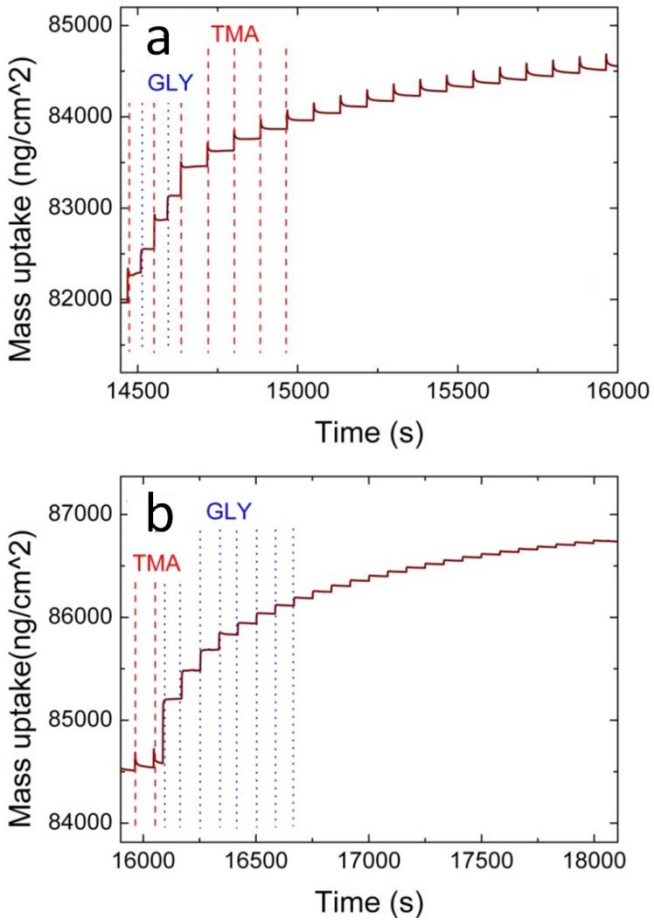


Figure 4.4. In-situ QCM data for TMA and glycidol dose saturation during the TMA/GLY MLD process at 120 °C. **(a)** After multiple repeated cycles of TMA/GLY, the surface was repeatedly exposed to TMA/Ar pulses (TMA/Ar = 1/82 s). More than 16 pulses were needed to saturate the surface. **(b)** Similar experiments for glycidol dose saturation on TMA saturated surface (GLY/Ar = 2/81 s). Both reagents showed high mass uptake for the first pulse. The data shows that after many growth cycles, both the TMA and GLY reagents diffuse subsurface and react during film growth. The subsurface diffusion is more prevalent in thicker films than in thinner films, but it becomes kinetically limited as film thickness increases.

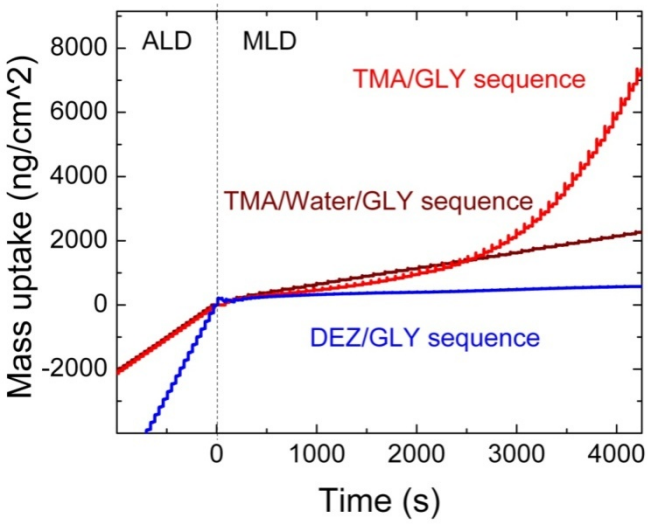


Figure 4.5. Direct comparison between in-situ QCM data collected during TMA/GLY, TMA/water/GLY and DEZ/GLY sequences following TMA/water (or DEZ/water) ALD. TMA (DEZ)/Ar/GLY/Ar = 1/40/2/40 s is used for TMA/GLY and DEZ/GLY, and TMA/Ar/Water/Ar/GLY/Ar = 1/40/1/40/2/40 s is used for TMA/Water/GLY. The TMA/GLY produced an induction period followed by a large mass uptake. The TMA/water/GLY sequence showed a much lower mass uptake per cycle, without an induction period. Negligible mass uptake is observed for the DEZ/GLY sequence, demonstrating the importance of the Al-CH_3 as a growth catalyst.

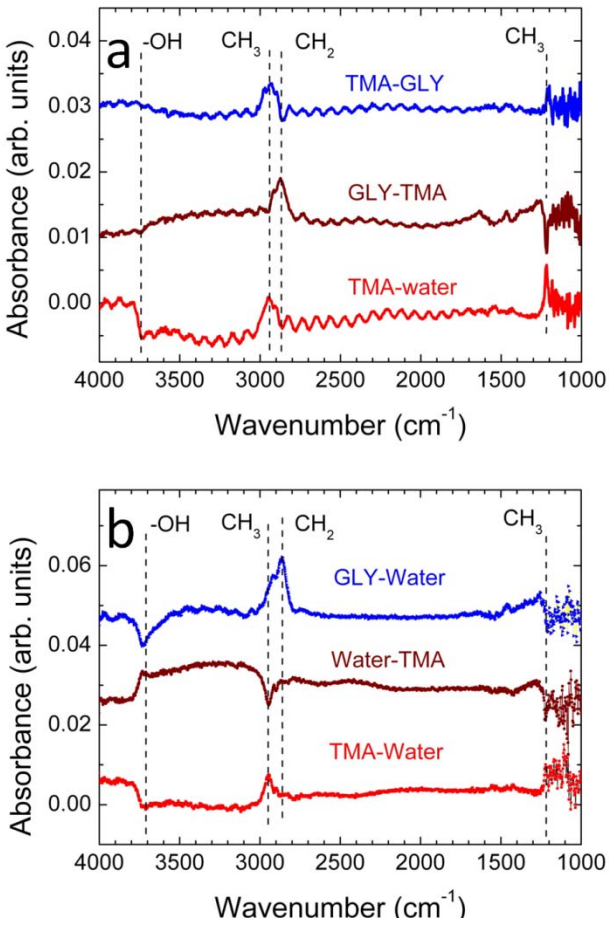


Figure 4.6. In-situ differential FTIR spectra collected during **(a)** the first TMA/GLY sequence on an Al-OH surface; and **(b)** the TMA/water/GLY sequence. In panel **(a)** the differential spectrum collected after the TMA dose (labeled TMA-water) shows Al-CH_3 modes on the surface, indicated by the Al-CH_3 deformation absorbance at 1200 cm^{-1}. Upon glycidol exposure (GLY-TMA) the CH_3 is removed from the surface by reaction with the OH or epoxy groups on GLY. The increase of CH_2 modes at 2865 and 2928 cm^{-1} confirms the attachment of GLY on the surface. In panel **(b)** the GLY dose after the water exposure produced an obvious decrease of surface -OH peak at 3700 cm^{-1} and increase of CH_2 modes at 2865 and 2928 cm^{-1}. The decrease of –OH indicates a reaction between the -OH on GLY and the Al-OH surface. (Fringes on the spectra is due to the interference from the AAO membrane).

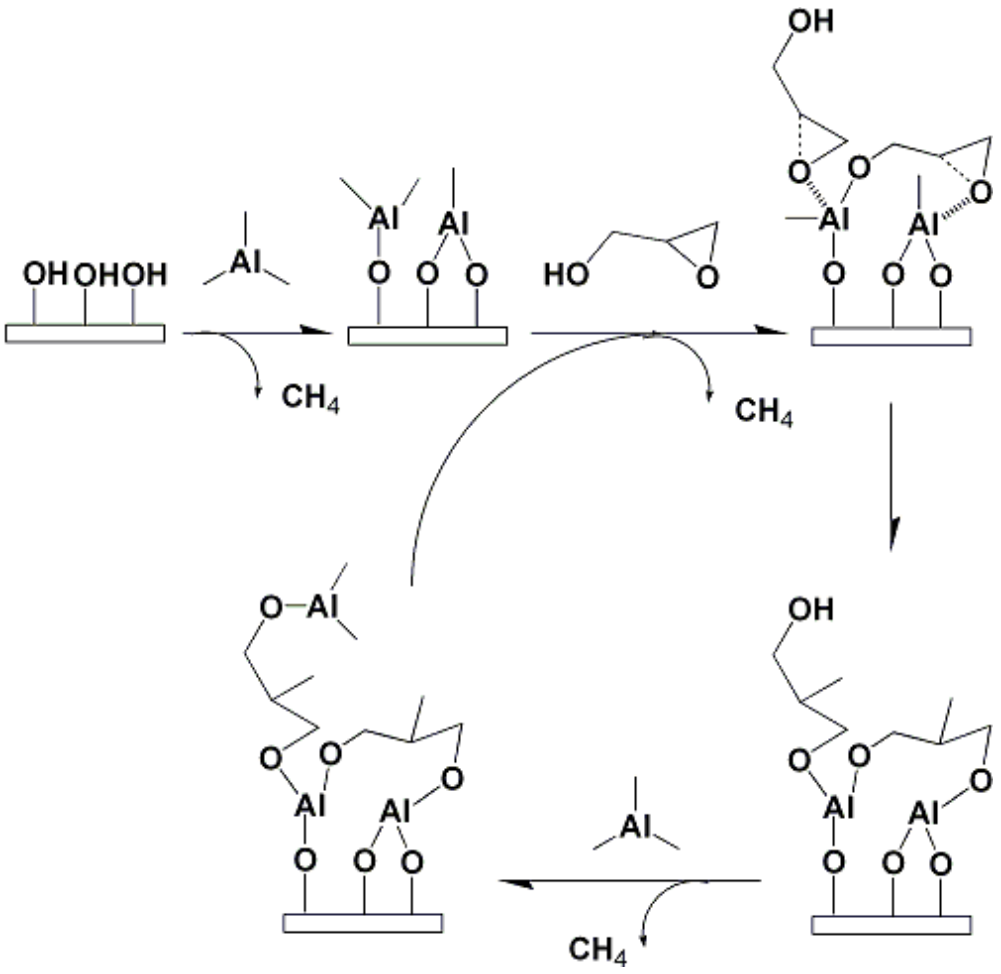


Figure 4.7. Schematic of the surface reactions during TMA/GLY MLD process consistent with the FTIR data in Figure 4.6(a). Exposing the –OH surface to TMA produced surface Al-CH_3. The following glycidol exposure consumes Al-CH_3 surface units, including reactions with both the OH and epoxy end of the molecule. The aluminum can help catalyze the ring opening. Available OH groups are then available to react with TMA during the next exposure step. Not shown in this diagram is the expected sub-surface diffusion of TMA and reaction with available lone pair sites producing Lewis acid/base O**:** $Al(CH_3)_3$ adducts that can react during the next glycidol exposure step. By placing a water exposure step after the TMA exposure, the subsurface Al-CH_3 groups become "quenched" and result in more steady growth at a reduced growth rate, as shown in the QCM data in Figure 4.5.

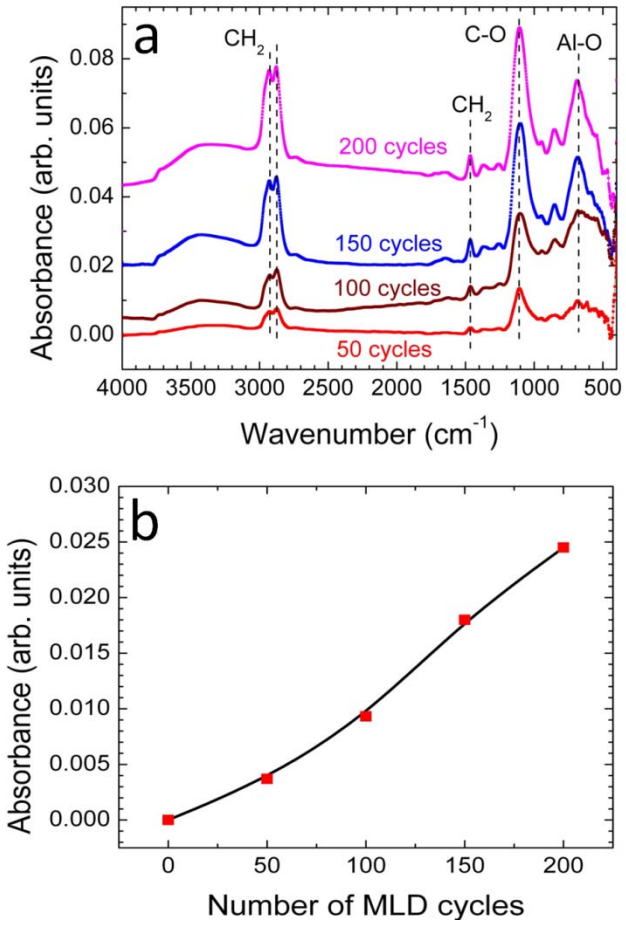


Figure 4.8. **(a)** Ex-situ FTIR spectra collected from MLD films after deposition on Si wafers. The process sequence was TMA/Ar/GLY/Ar = 1/40/2/40 seconds at 120 °C. Spectra show modes associated with -CH_2- asymmetric and symmetric stretching at 2928 cm^{-1} and 2865 cm^{-1}, C-O at 1100 cm^{-1} and Al-O stretching near 700 cm^{-1} consistent with the polymer composition: (-Al-O-(C_4H_8)-O-)$_n$. Mode intensity increased with the number of deposition cycles. **(b)** The intensity of the CH_2 asymmetric stretching mode at 2928 cm^{-1} is plotted versus number of MLD cycles. This peak was selected as a characteristic absorbance for MLD film, and the intensity of this peak is increased with the number of MLD cycles. The absorbance increased more slowly during the first 50 cycles, which is consistent with increasing growth rate as deposition proceeds.

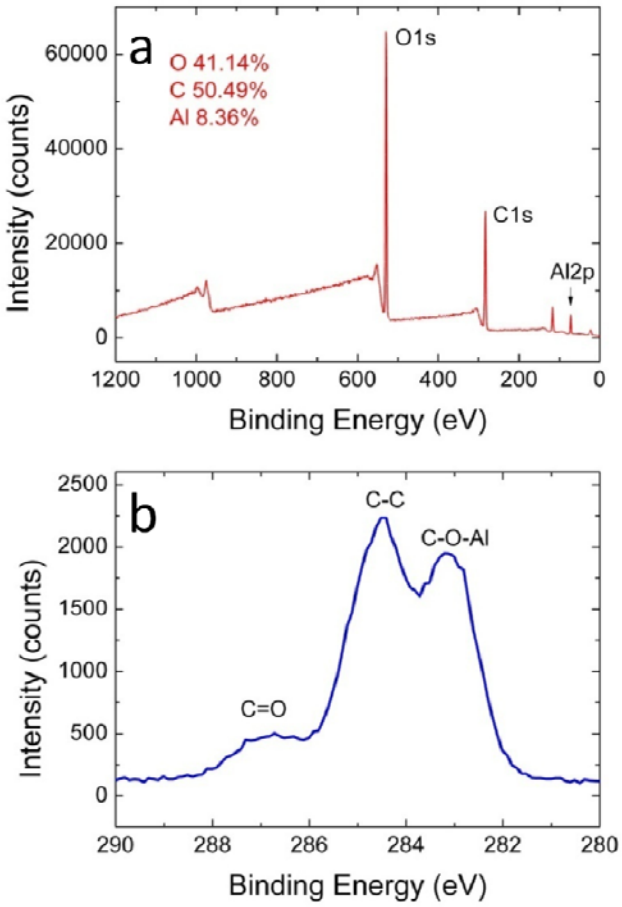


Figure 4.9. **(a)** XPS survey scan of the TMA/GLY MLD film on Si (200 cycles at 120 °C) displayed a relatively low Al concentration compared to C and O. **(b)** The C 1s detail scan from the same sample showed a bonding distribution consistent with the polymer structure (-Al-O-(C_4H_8)-O-), with little C=O present.

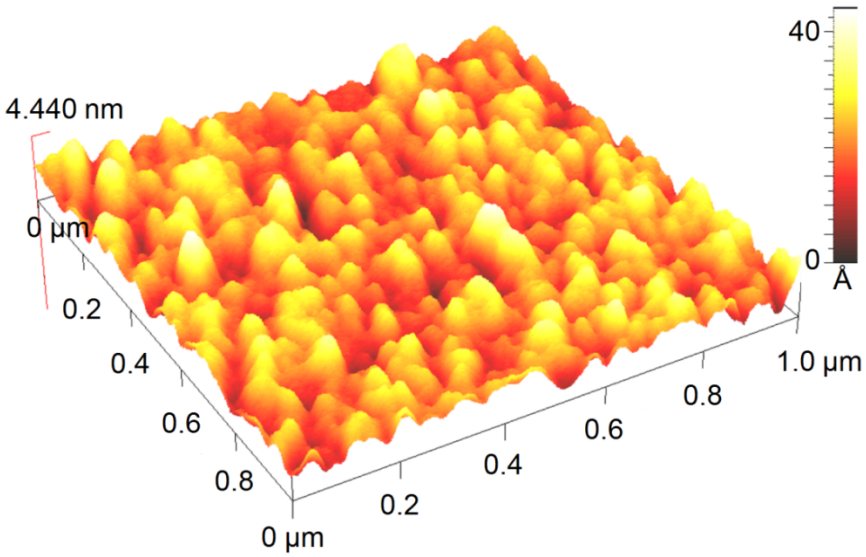


Figure 4.10. Atomic force micrographs of MLD films (100 cycles at 120 °C) on a Si wafer. The film showed a relative smooth surface with RMS of ~5 Å.

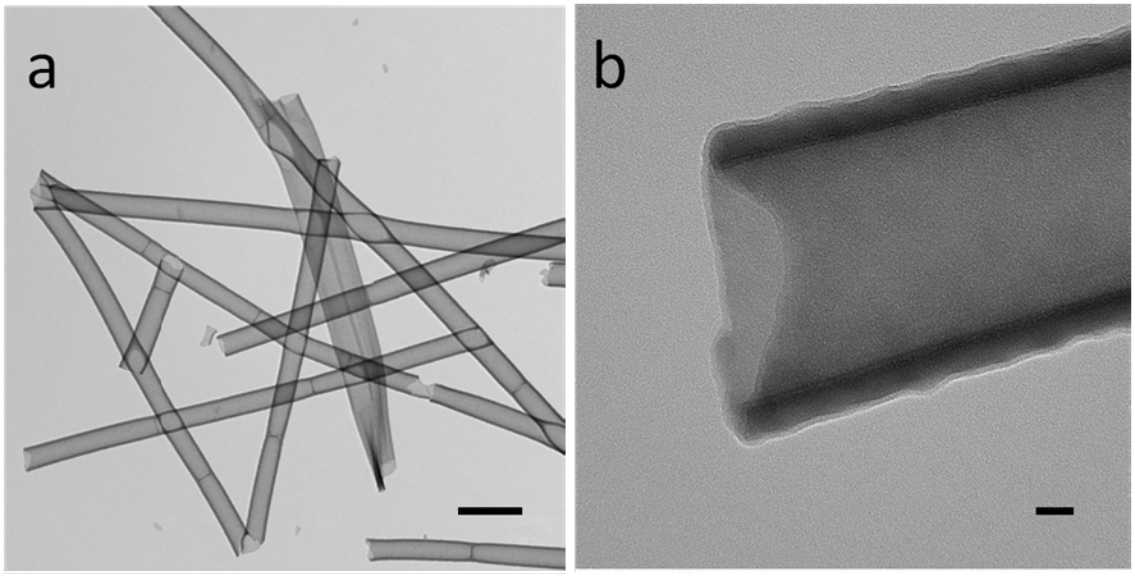


Figure 4.11. Transmission electron microscopy images of MLD coating (25 cycles at 120 °C, TMA/Ar/GLY/Ar=2/40/4/40 s) on electrospun PVA nanofibers after calcination in air at 400 °C for ~48 hours. The polymer fibers were removed upon calcination, resulting in hollow porous microtubes. The images show that the MLD network polymer reaction leads to a uniform film on the complex, high aspect-ratio nanostructured fiber matrix. The thickness of the tube wall is ~ 20 nm and is uniform from tube to tube throughout the whole sample. The scale bars are 500 and 20 nm respectively.

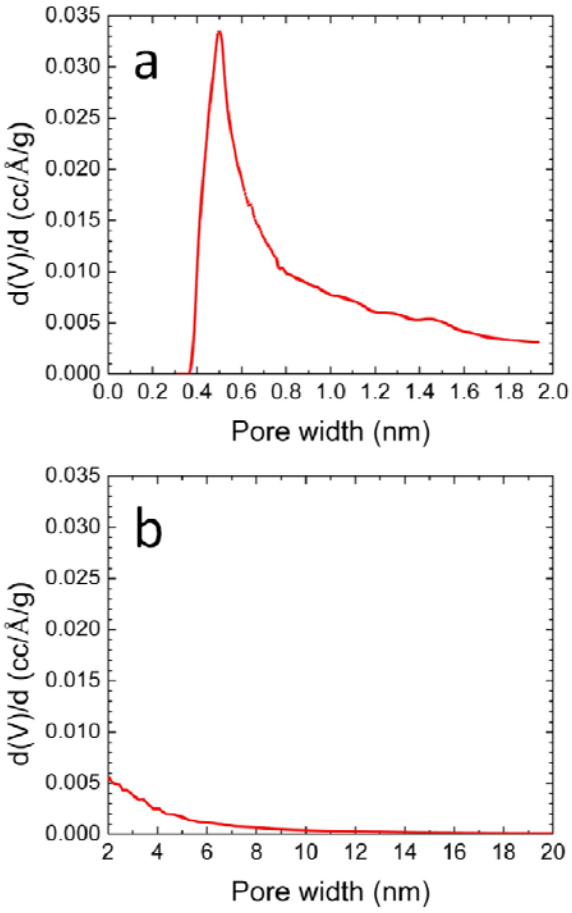


Figure 4.12. Pore size distribution determined from N_2 adsorption/desorption studies. Separate experiments analyzed: **(a)** pore size distribution in the micropore range (< 2nm) calculated by the Hovarth Kawazoe (HK) method; and **(b)** in the mesopore range (between 2 and 20) calculated by the Barrett Joyner Halenda (BJH) method. Materials were 400 cycles of MLD coated electrospun PVA fibers after calcinations at 400 °C for 48 hours. The microtubes are predominantly microporous with an average pore size of ~5 Å, with few mesopores present.

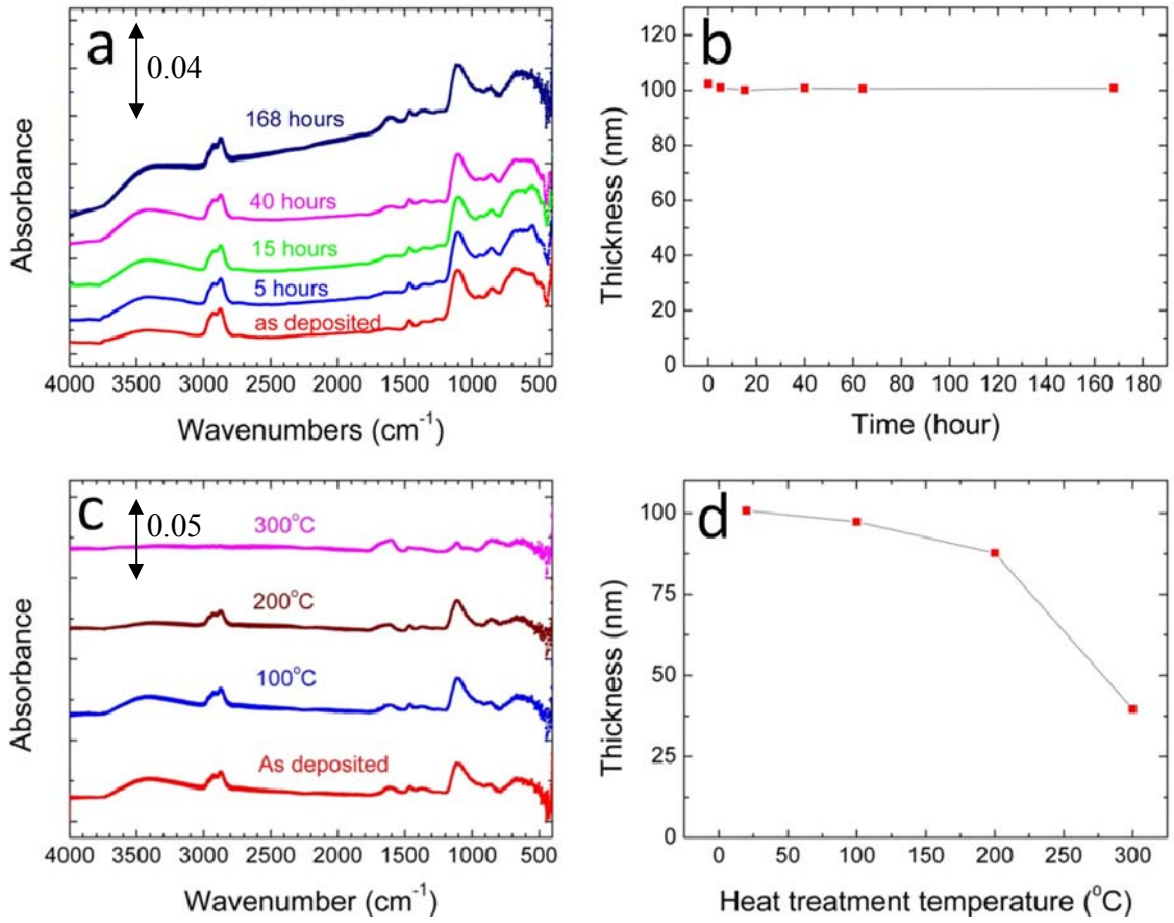


Figure 4.13. The stability of hybrid materials under ambient environment and thermal annealing conditions. **(a)** Ex-situ FTIR spectra and **(b)** thickness of deposited TMA/glycidol films (100 cycles at 120 °C) on silicon, with different ambient exposure time. **c)** Ex-situ FTIR spectra and **(d)** thickness of the same TMA/GLY films on silicon annealed in air at the indicated temperature for 2 hours. The data showed the hybrid network polymer films are stable in ambient environment for more than 1 week. Thermal treatment at temperatures above 200 °C eliminates the organic components in the films.

References

1 M. Ruben; D. Payer; A. Landa; A. Comisso; C. Gattinoni; N. Lin; J. P. Collin; J. P. Sauvage; A. De Vita; K. Kern; 2D supramolecular assemblies of benzene-1,3,5-triyl-tribenzoic acid: Temperature-induced phase transformations and hierarchical organization with macrocyclic molecules, *Journal of the American Chemical Society,* **2006**. *128*, 15644.

2 F. Tancini; D. Genovese; M. Montalti; L. Cristofolini; L. Nas; L. Prodi; E. Dalcanale; Hierarchical Self-Assembly on Silicon, *Journal of the American Chemical Society,* **2010**. *132*, 4781.

3 J. A. Theobald; N. S. Oxtoby; M. A. Phillips; N. R. Champness; P. H. Beton; Controlling molecular deposition and layer structure with supramolecular surface assemblies, *Nature,* **2003**. *424*, 1029.

4 D. Zacher; O. Shekhah; C. Wöll; R. A. Fischer; Thin films of metal-organic frameworks, *Chemical Society Reviews,* **2009**. *38*, 1418.

5 G. Decher; Fuzzy nanoassemblies: Toward layered polymeric multicomposites, *Science,* **1997**. *277*, 1232.

6 M. Altman; A. D. Shukla; T. Zubkov; G. Evmenenko; P. Dutta; M. E. van der Boom; Controlling structure from the bottom-up: Structural and optical properties of layer-by-layer assembled palladium coordination-based multilayers, *Journal of the American Chemical Society,* **2006**. *128*, 7374.

7 K. B. Blodgett; Films built by depositing successive monomolecular layers on a solid surface, *Journal of the American Chemical Society,* **1935**. *57*, 1007.

8 R. A. Fischer; C. Woll; Layer-by-Layer Liquid-Phase Epitaxy of Crystalline Coordination Polymers at Surfaces, *Angewandte Chemie-International Edition,* **2009**. *48*, 6205.

9 D. B. Mitzi; Thin-film deposition of organic-inorganic hybrid materials, *Chemistry of Materials,* **2001**. *13*, 3283.

10 B. H. Lee; M. K. Ryu; S. Y. Choi; K. H. Lee; S. Im; M. M. Sung; Rapid vapor-phase fabrication of organic-inorganic hybrid superlattices with monolayer precision, *Journal of the American Chemical Society,* **2007**. *129*, 16034.

11 X. H. Liang; M. Yu; J. H. Li; Y. B. Jiang; A. W. Weimer; Ultra-thin microporous-mesoporous metal oxide films prepared by molecular layer deposition (MLD), *Chemical Communications (Cambridge, United Kingdom),* **2009**. 7140.

12 Q. Peng; X. Y. Sun; J. C. Spagnola; G. K. Hyde; R. J. Spontak; G. N. Parsons; Atomic layer deposition on electrospun polymer fibers as a direct route to Al2O3 microtubes with precise wall thickness control, *Nano Letters,* **2007**. *7*, 719.

13 S. M. George; A. W. Ott; J. W. Klaus; Surface chemistry for atomic layer growth, *Journal of Physical Chemistry,* **1996**. *100*, 13121.

14 M. Leskela; M. Ritala; Atomic layer deposition (ALD): from precursors to thin film structures, *Thin Solid Films,* **2002**. *409*, 138.

15 T. Suntola; Atomic Layer Epitaxy, *Thin Solid Films,* **1992**. *216*, 84.

16 A. A. Dameron; D. Seghete; B. B. Burton; S. D. Davidson; A. S. Cavanagh; J. A. Bertrand; S. M. George; Molecular layer deposition of alucone polymer films using trimethylaluminum and ethylene glycol, *Chemistry of Materials,* **2008**. *20*, 3315.

17 Y. Du; S. M. George; Molecular layer deposition of nylon 66 films examined using in situ FTIR spectroscopy, *Journal of Physical Chemistry C,* **2007**. *111*, 8509.

18 P. W. Loscutoff; H. Zhou; S. B. Clendenning; S. F. Bent; Formation of Organic Nanoscale Laminates and Blends by Molecular Layer Deposition, *ACS Nano,* **2010**. *4*, 331.

19 Q. Peng; B. Gong; R. M. VanGundy; G. N. Parsons; "Zincone" Zinc Oxide-Organic Hybrid Polymer Thin Films Formed by Molecular Layer Deposition, *Chemistry of Materials,* **2009**. *21*, 820.

20 B. Yoon; J. L. O'Patchen; D. Seghete; A. S. Cavanagh; S. M. George; Molecular Layer Deposition of Hybrid Organic-Inorganic Polymer Films using Diethylzinc and Ethylene Glycol, *Chemical Vapor Deposition,* **2009**. *15*, 112.

21 B. Yoon; D. Seghete; A. S. Cavanagh; S. M. George; Molecular Layer Deposition of Hybrid Organic-Inorganic Alucone Polymer Films Using a Three-Step ABC Reaction Sequence, *Chemistry of Materials,* **2009**. *21*, 5365.

22 D. C. Miller; R. R. Foster; S. H. Jen; J. A. Bertrand; D. Seghete; B. Yoon; Y. C. Lee; S. M. George; M. L. Dunn; Thermomechanical properties of aluminum alkoxide (alucone) films created using molecular layer deposition, *Acta Materialia,* **2009**. *57*, 5083.

23 H. Sugimoto; C. Kawamura; M. Kuroki; T. Aida; S. Inoue; Lewis Acid-assisted Anionic Ring-Opening Polymerization of Epoxide by the Aluminum Complexes of Porphyrin, Phthalocyanine, Tetraazaannulene, and Schiff-base as initiators, *Macromolecules,* **1994**. *27*, 2013.

24 T. Suzuki; H. Saimoto; H. Tomioka; K. Oshima; H. Nozaki; Regioselective and Stereoselective Ring-Opening of Epoxy Alcohols with Organo-Aluminum Compounds leading to 1,2-Diols, *Tetrahedron Letters,* **1982**. *23*, 3597.

25 J. S. Jur; J. C. Spagnola; K. Lee; B. Gong; Q. Peng; G. N. Parsons; Temperature-Dependent Subsurface Growth during Atomic Layer Deposition on Polypropylene and Cellulose Fibers, *Langmuir,* **2010**. *26*, 8239.

26 J. C. Spagnola; B. Gong; S. A. Arvidson; J. S. Jur; S. A. Khan; G. N. Parsons; Surface and sub-surface reactions during low temperature aluminium oxide atomic layer deposition on fiber-forming polymers, *Journal of Materials Chemistry,* **2010**. *20*, 4213.

27 C. A. Wilson; R. K. Grubbs; S. M. George; Nucleation and growth during Al2O3 atomic layer deposition on polymers, *Chemistry of Materials,* **2005**. *17*, 5625.

28 D. Seghete; R. A. Hall; B. Yoon; S. M. George; Importance of Trimethylaluminum Diffusion in Three-Step ABC Molecular Layer Deposition Using Trimethylaluminum, Ethanolamine, and Maleic Anhydride, *Langmuir,* **2010**. *26*, 19045.

29 M. D. Groner; F. H. Fabreguette; J. W. Elam; S. M. George; Low-temperature Al2O3 atomic layer deposition, *Chemistry of Materials,* **2004**. *16*, 639.

30 J. W. Elam; M. D. Groner; S. M. George; Viscous flow reactor with quartz crystal microbalance for thin film growth by atomic layer deposition, *Review of Scientific Instruments,* **2002**. *73*, 2981.

31 S. M. George, in *Semiconductor Surface Chemistry* (Telluride, Colorado, 2010).

32 R. Joso; S. Reinicke; A. Walther; H. Schmalz; A. H. E. Muller; L. Barner; Facile Access to Hydroxy-Functional Core-Shell Microspheres via Grafting of Ethylene Oxide by Anionic Ring-Opening Polymerization, *Macromolecular Rapid Communications,* **2009**. *30*, 1009.

33 F. Lee, et al.; Decomposition of Trimethylgallium on Si(100) - Spectroscopic Identification of the Intermediates *Surface Science,* **1989**. *216(1-2)*, 173.

CHAPTER 5 is a reprint of a manuscript in preparation.

CHAPTER 5. A Two-Step Lewis Acid-Catalyzed ε-Caprolactone Ring-Opening Molecular Layer Deposition Process for Hybrid Organic-Aluminum Oxide Polymer Thin Films

Bo Gong, and *Gregory N. Parsons

Department of Chemical and Biomolecular Engineering, North Carolina State University

*Corresponding author: parsons@ncsu.edu

Abstract

New nanoscale hybrid organic-inorganic coordination polymer films are of interest for electronics, biomedical, chemical protection, and energy storage systems applications. Common methods for polymer film fabrication utilize organic solvents, which will degrade, swell and dissolve substrates, and raise safety and environmental concerns. Molecular layer deposition (MLD) proceeds by exposing a surface to a sequence of two or more reactant species, where each half-reaction goes to completion before the next reactant exposure. This method is a solvent-free vapor phase thin film deposition technique capable of precise thickness and composition control at the nanometer scale. However, in a typical binary MLD process, homo-bifunctional reactants such as ethylene glycol commonly undergo a "double" reaction, which impedes further reaction by consuming excess reactive surface sites. This work demonstrates a new binary MLD reaction scheme that employs ε-caprolactone (LAC) as one of reagent with tri-methyl-aluminum (TMA) in a simple A/B reaction scheme. Infrared absorbance confirms that the TMA/ ε-caprolactone combination produces an organic-inorganic coordination polymer with composition $(\text{-Al-O-}(C_8H_{16})\text{-O-})_n$ over a range of substrate temperature between 60 and 120°C. We show using in-situ infrared absorption spectroscopy that the growth mechanism includes a temperature dependent Lewis acid-catalyzed ring-opening reaction between an aluminum-methyl terminated surface and the ester group in ε-caprolactone. These results demonstrate a new method to fabricate organic-inorganic hybrid thin films, and present new insight into surface-catalytic vapor-phase thin film deposition mechanisms.

5.1. Introduction

New thin film materials and processes are of interest for surface passivation and stabilization, electronic and chemical sensing, catalytic functionalization, energy conversion and storage, and biomedical coatings and templates. In particular, thin film coordination polymers offer unique combinations of functionality and surface porosity,[1-3] but these materials are mostly fabricated through liquid solvent methods which can dissolve or otherwise degrade polymer substrates, making thin film integration a challenge. Solvent-based processes also generally raise safety and environment concerns. Vapor phase methods for organic coatings, including thermal evaporation,[4] vapor deposition polymerization[5-7] and chemical vapor deposition[8-11] commonly rely on physical or chemical transport to modify the structure of the deposited film. It is generally difficult in these methods to achieve uniform coatings on high aspect ratio features. Vapor phase molecular layer deposition, built on the principles of atomic layer deposition, is performed by exposing a surface to a sequence of two or more precursor or reactant species. The complete sequence constitutes one reaction cycle, and using sufficient precursor exposure during each step, the extent of reaction is identical to the number of available reactive sites on the growth surface. This progression of self-limiting surface reactions allows the film to be built with monolayer precision in film thickness on surfaces with arbitrary shape and surface area.[12-14] The process can proceed with many different organic linkers and inorganic components.[15,16] Organic films including polyamides, [17,18] polyimides[19] and polyureas[20] can be formed. Reports show formation of polyamide nylon 66 [17] using adipoyl chloride (ClOC-$(CH_2)_4$-COCl) and 1, 6-hexanediamine (H_2N-$(CH_2)_6$-NH_2), as well as formation of poly (p-phenylene terephthalamide) films.[18] In-

situ infrared (IR) transmission analysis confirms the sequence of proposed sequential steps. Recent work also report polyurea MLD using 1,4-phenylene diisocyanate(PDIC) and ethylene diamine(ED).[20]

In addition to pure organic films, several hybrid organic-inorganic polymer films can be synthesized by MLD. Trimethyl aluminum reacts readily with ethylene glycol to form a coordination polymer of the form $(Al\text{-}O\text{-}CH_2\text{-}CH_2\text{-}O)_n$. In-situ IR and quartz crystal microgravimetry (QCM) provided insight into the growth reaction mechanism.[21] In addition to well defined vertical film growth, results demonstrate that homo-bifunctional organic reactants, such as ethylene glycol, undergo a "double reaction",[16,21,22] where both hydroxyl groups on the ethylene glycol react with surface. The double reaction decreases the reactive site density and result in low growth rates and films with low density and poor stability under ambient exposure. To avoid double reactions associated with homo-bifunctional reactants, Yoon et al. used two hetero-bifunctional reactants, ethanolamine and maleic anhydride, along with trimethyl aluminum in a three-reactant sequence to form aluminum oxide organic hybrid films.[23] The same report also shows that maleic anhydride can undergo a ring-opening reaction with trimethyl aluminum in a binary reaction sequence. [23]

Trimethyl aluminum acts as a Lewis acid, and it will attack nucleophilic groups such as C=O[24] and epoxide rings[25] to form an aluminum alky oxide bond. Trimethyl aluminum is also an active catalyst for many solution phase reactions, including epoxide ring-opening,[26,27] and it can also function in vapor phase surface film growth reactions, to catalyze SiO_2 deposition from tri(tert-butoxy)silanol.[28] Nanolaminates of ZrO_2/Silica and HfO_2/SiO_2 have also been reported by the similar catalytic ALD process.[29,30]

The present work demonstrates TMA as a Lewis acid catalyst and precursor for ring-opening of ε-caprolactone in a two step MLD process, forming an Al-O/organic polymer. The process works over a range of substrate temperature between 60 and 120 °C. In-situ differential infrared transmission spectra show the surface reaction is strongly temperature dependent.

5.2. Experimental Details

Chemicals and Materials

All chemicals and materials were purchased commercially and used without further purification. Trimethylaluminum (TMA) 95 % was purchased from Strem chemical. ε-caprolactone (LAC) 97 % was purchased from Sigma-Aldrich. Deionized water (DI–H_2O) was used as the water source, and high purity argon (99.999 %) (National Welders Supply Co.) was used as the purge gas and carrier gas for reactants. Infrared transmission analysis employed high resistivity (50-100 ohm·cm) n-type double-side-polished silicon (100) substrates, producing uniform ~60 % transmittance over the middle infrared region. Anodisc™ Anodic aluminum oxide (AAO) membranes (60 μm thickness, 0.1 μm pore size and 13 mm diameter) were purchased from Whatman. For QCM analysis, unpolished quartz crystals with gold coating (SC-101, 6 MHz) were purchased from Inficon and used as received.

Deposition Reactors and Processes

Molecular layer deposition was carried out in homemade viscous flow vacuum reactor described previously.[16] The TMA precursor was stored in a low pressure carbon-steel cylinder and evaporated at room temperature (~20 °C). The DI–H_2O and LAC were also

stored in stainless steel containers and evaporated at room temperature and 60˚C respectively. The flow rate of Argon carrier gas is ~200 sccm with a steady-state process pressure of ~1.1 Torr monitored by a Baratron pressure gauge (MKS Instrument Inc.). The reaction system was pumped using a rotary mechanical pump. The metal organic and DI-water vapors were bled into the argon carrier flow and into the reactor through a needle valve with a computer–controlled ALD solenoid valve. During the TMA and H_2O pulses, the pressure measured increased 150 mTorr and 50 mTorr respectively. The LAC container was connected to the system using a bubbler, and the pressure increase during LAC doses were also ~50 mTorr. The reactant dose was adjusted by either changing pulse time or by changing the flow through the needle valve orifice. The reactor was designed to allow simple transitions between deposition of Al_2O_3 ALD and MLD by switching easily between H_2O and LAC reactant flow.

For a typical ALD Al_2O_3 deposition cycle, the gas exposure time for the TMA and H_2O were 1 second each, with an Ar purge time of 40 s between each reactant pulse. This process cycle is denoted as TMA/Ar/H_2O/Ar = 1/40/1/40 s. For a typical MLD deposition cycle, ε-caprolactone exposure was 2 seconds and the process cycles are denoted as TMA/Ar/LAC/Ar = 1/40/2/40 s. Silicon wafer pieces were used as substrates. Before loading into the reactor, Si wafer was wet cleaned by BakerClean® JTB-100 solution (Mallinckrodt Baker Inc), followed by rinse with DI-H_2O and blown-dry with N_2. A second reactor was designed and equipped for in-situ infrared transmission analysis.[25]

In-situ Quartz Crystal Microgravimetry

In situ quartz crystal microgravimetry (QCM) was used during ALD and MLD to monitor mass uptake during the reactant exposures. The QCM crystal was mounted to the QCM holder using conductive silver epoxy and attached onto the system through the load lock of the reactor. The sensor head was modified to allow inert gas purging (~ 10 sccm) to the backside of the QCM crystal to prevent film deposition on the back side, and protect the electrical contacts.[16] The mass change signals were detected and recorded by a film thickness monitor (Maxtek TM-400), using a home designed LABVIEW program to record the data.[16,25]

In-situ Fourier Transform Infrared Spectroscopy

A Thermal Scientific Nicolet 6700 IR system with an external MCT-A detector was used for in-situ FTIR experiment, the spectrometer was operated at transmittance mode in the frequency range from 4000 to 650 cm^{-1}, a mid-IR KBr beam splitter was installed for the measurement, spectra were collected at 4 cm^{-1} resolution using 200 scans. To increase the signal strength from the surface reaction, an IR wafer with a high surface area AAO porous membrane disk was used as the substrate for the In-situ IR measurement, and 20 cycles of TMA/Water ALD sequence was first used to cover the entire substrate with Al_2O_3. A reference IR spectrum of the substrate was collected before the initial reactant dose. To better visualize the surface chemistry upon reactant exposure, spectra are displayed in differential mode by subtracting the most recent spectrum as the reference. In differential mode, positive-going features are modes added since the previous exposure step, and negative-going features indicate modes that are removed.

Ex-situ Characterization

After deposition, we used Fourier transform infrared spectroscopy (FTIR) and X-ray photoelectron spectroscopy (XPS) to examine chemical composition and ambient stability of MLD films. FTIR measurements employed a ThermoNicolet 6700 IR bench in transmission mode using a deuterated triglycine sulfate (DTGS) detector (KBr beam splitter), typically with 2050 scans at 4 cm^{-1} resolution. Purified dry air continuously purged the measuring chamber, and the substrates were flat silicon wafers with high resistivity. XPS analysis utilized a Kratos Analytical Axis Ultra tool with a monochromatic Al Kα source. For all samples, we normalized the C 1s peak to 248.5 eV as the reference, and the pass energies for the survey and detail scans were 160 and 20 eV, respectively.

We analyzed surface morphology using a Dimension 3000 atomic force microscope (Digital Instruments) in tapping mode. A variable-angle alpha-SE spectroscopic ellipsometry (J.A. Woollam Co., Inc.), including a three-layer (MLD film/native oxide/silicon) Cauchy model, allowed for film thickness and reactive index measurement. In the model, thickness of native oxide was 20 Å, and the Si substrate was 400 microns.

5.3. Experimental Results

Film Thickness versus MLD Cycle

Figure 5.1 displays a plot of the thickness of the TMA/LAC MLD films on a silicon wafer (determined by ellipsometry) versus number of MLD cycles for deposition at several temperatures. For each temperature studied, the film thickness increased with the number of deposition cycles. A nucleation period is observed for all the deposition temperatures. The thickness measurement from MLD film on Si wafer showed the growth rate of TMA/LAC film decreased with an increase in the substrate temperature. For example, at 60 °C, the

deposition rate is 0.75 Å/cycle, which is nine times larger than 0.08 Å/cycle at 120 °C. This temperature dependence of the film growth is consistent with other hybrid MLD materials, and can be explained by excess precursor absorption on the substrate at lower temperature.[16,21]

Figure 5.2(a) shows FTIR spectra of typical MLD films collected ex-situ after deposition at 60 °C. Spectral features include the characteristic CH_2 symmetric and asymmetric stretching modes at 2865 and 2925 cm^{-1}, respectively, C-O stretching at 1100 cm^{-1}, and Al-O stretching mode near 700 cm^{-1}, consistent with the expected polymer structure $(\text{-Al-O-}(C_8H_{16})\text{-O-})_n$. Increasing the number of cycles produced a corresponding increase in intensity for each peak. Figure 5.2(b) shows a trace for the absorbance of CH_2 stretching mode at 2925 cm^{-1} plotted versus number of ALD cycles. The intensity of this peak is increased with the number of MLD cycles.

Film thickness measurements provide data on the ambient stability of the hybrid films. For this study, we deposited films using TMA/LAC at 60 °C and we analyzed film stability concurrently. Air exposure produced negligible changes.

In-situ QCM Analysis of TMA/LAC MLD Processes

Figure 5.3 shows in-situ QCM data collected during the TMA/LAC MLD process at different temperature. At 60 °C, the average mass uptake for TMA is ~30 ng/cm^2, and for LAC the value is ~20 ng/cm^2. The larger initial mass uptakes for both precursors were observed for the MLD process. After about 600 seconds (corresponding to 10 cycles), a steady state growth was achieved. This indicates an induction period for TMA/LAC MLD

film growth on ALD Al_2O_3. Plots also include data collected at 60 and 120 °C, demonstrating the decrease in growth rate as temperature increased, consistent with the ellipsometry results.

In-situ FTIR Analysis of TMA/LAC MLD

To better understand the mechanism behind this MLD process, in-situ differential FTIR spectra were collected for TMA/LAC sequences at 60°C and at 120°C. Figure 5.4 shows the spectra collected for TMA/LAC sequence at 60°C. The data is presented in differential mode, starting from the bottom-most spectrum. Each scan corresponds to the spectrum collected after each exposure step, using the spectrum collected just before each step as reference. The bottom spectrum shows the effect of TMA exposure on the Al-OH terminated surface. The coupled OH stretching mode near 3700 cm^{-1} decreases, and the CH_3 symmetric and asymmetric stretching modes at 2895 and 2940 cm^{-1}, respectively, increase, consistent with TMA reacting with surface OH groups to create Al-CH_3 surface species.[14] Differential spectra collected after 1st LAC dose shows increase of CH_2 modes at 2865 and 2928 cm^{-1} , aluminum carbonate mode (O-C-O asymmetric stretching)[31,32] at 1610 cm^{-1} and very little decrease of CH_3 absorbance at 2895 cm^{-1} and 2940 cm^{-1}, which indicate the reaction of (C=O)-O on LAC with Al-CH_3 and form aluminum carbonate. As discussed below, the mechanism likely involves an Lewis acid base adduction reaction between surface Al-CH_3 and ester group.[26] Upon the next TMA exposure, the methyl groups appear, and aluminum carbonate features decrease in intensity, indicating reaction of TMA with available Al-O-C in aluminum carbonate to form Al-CH_3 terminations. In the second LAC dose, the aluminum carbonate absorbance and C=O features increased. This indicated the surface reaction between Al-CH_3 and ester groups on the LAC molecular to form aluminum

carbonate. Also, some LAC is expected physicsorped on the surface at lower temperatures. Which resulted in the Increase of C=O absorbance. During the 3rd TMA exposure, the removing of aluminum carbonate absorbance is indicate the TMA could also react with Al-O-C in aluminum carbonate during the TMA exposure. The decrease of characterization peak of C=O indicate the TMA could also react with the carbonyl groups in the physisorped LAC molecular on the surface. The 3rd LAC exposure again results in an increase in CH_2 and C=O, consistent with a repeat of the previous surface reaction with Al-CH_3 and physisorption. Figure 5.5 shows the IR absorbance spectra after each deposition cycle for the MLD process at 60°C. The present of C=O corresponding to the incorporation of C=O in the film, which is attribute to the physisorption of LAC on the surface during the MLD process, Moreover, at 60 °C, TMA could not fully react with ester groups in the physisorped LAC.

Figure 5.6 displays a similar data set obtained during the TMA/LAC sequence at 120 °C. Differential spectra collected after LAC dose showed an increase of CH_2 modes at 2865 and 2928 cm^{-1} ,O-C-O asymmetric stretching in aluminum carbonate at 1610 cm^{-1} and very little decrease of CH_3 absorbance at 2895 cm^{-1} and 2940 cm^{-1}, which indicate the reaction of (C=O)-O on LAC with Al-CH_3 and form aluminum carbonate. Upon the next TMA exposure, the methyl groups appear, and asymmetric O-C-O stretching decreases in intensity, indicating reaction with available Al-O-C in aluminum carbonate to form Al-CH_3 units. In the second LAC dose, the increase of aluminum carbonate features. Indicate the surface reaction between Al-CH_3 and ester groups on the LAC molecular. The absent of C=O implied there is limited physisorped LAC on the surface. During the 3rd TMA pulse, the removing of aluminum carbonate absorbance (O-C-O) is indicating the TMA could also react

with Al-O-C during the TMA exposure. Figure 5.7 shows the IR absorbance spectra after each deposition cycle for the MLD process at 120°C. The absent of C=O absorbance indicated the limited C=O in the deposited film. There are limited physisorption of LAC on the surface during the LAC exposure.

Based on the IR and QCM data presented above, Figure 5.8 shows the proposed scheme for the TMA/LAC MLD reaction sequence at 120 °C. After TMA reaction with available hydroxyl species to form surface Al-CH_3 groups, LAC exposure leads to interaction between the aluminum-methyl as a Lewis acid site and a lone pair Lewis base site on the LAC oxygen. This catalyzes the ring-opening of (C=O)-O-C producing Al-O and C-CH_3 bonds upon transfer of the methyl from the aluminum to the alkyl chain, with no other vapor product. The Al-O-C group is then accessible for reaction during the next TMA exposure step. At 60 °C, in addition to the surface reaction, LAC molecule is expected physisorped on the surface during the exposure. This would result in the reaction between TMA and ester groups in adsorbed LAC during the following TMA pulse. This also explained the higher growth rate at lower temperature.

Film Component Analysis from XPS

X-ray photoelectron spectra data in Figure 5.9 shows composition and bonding structure of films deposited using the TMA/LAC processes at 60 °C. A survey scan indicates 45 atomic % carbon and 12 at.% aluminum. The detail scan of C 1s peak shows C-C, C=O and C-O-Al related features. As shown in Figure 5.10, samples deposited at 90 °C show an Al fraction of 15 atomic %, indicating increased aluminum incorporation at higher temperature.

Surface Morphology Measurement from AFM

Figure 5.11 displays surface structure images obtained from scanning probe microscopy of a 400 cycle MLD film deposited at 120 °C. The MLD film show a smooth surface, with a root mean square roughness of approximately ~5 Å, as compared to ~1.0 Å for the Al_2O_3 ALD film.

5.4. Conclusions

This work demonstrates that a cyclic ester LAC reagent can react with tri-methyl-aluminum in a vapor-phase molecular layer deposition binary reaction scheme at substrate temperatures between 60 and 120°C to form metal-organic hybrid coordination polymer thin films of the form $(\text{-Al-O-}(C_8H_{16})\text{-O-})_n$ that are relatively stable in ambient air. Ex-situ infrared transmittance spectra confirmed that films consist of Al-O and ethylene oxide units, and the deposited film showed good stability in ambient over 7 days in laboratory air. The good ambient stability will make this material of interest for applications in gas diffusion barriers, biomedical scaffold and porous coatings. Because this catalytic mechanism depends mainly on the Lewis acid properties of the aluminum-methyl, we expect many other metals organics will show the similar catalytic activity. These results show a new method to fabricate air stable organic-inorganic hybrid materials, and novel pathways to initiate surface ring opening reactions from the vapor phase.

Acknowledgments

This work was supported by the National Science Foundation project #0626256, and DOE project #08NT0001925. We are grateful to Dohan Kim and Mark D Walters for assistance with AFM, XPS data collection, respectively.

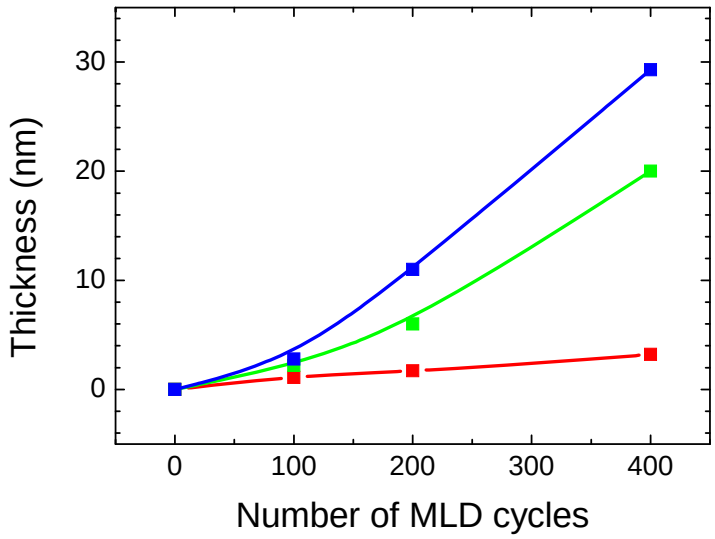


Figure 5.1. Film thickness for TMA/LAC MLD films on silicon wafers is plotted versus number of MLD cycles at various growth temperatures. Film thickness was determined using ellipsometry. For all the samples on Si wafer the deposition sequence was TMA/Ar/LAC/Ar = 1/40/2/40 seconds. The growth rate decreased from 0.75 Å /cycle to 0.08Å/cycle as the substrate temperature increased from 60 to 120°C.

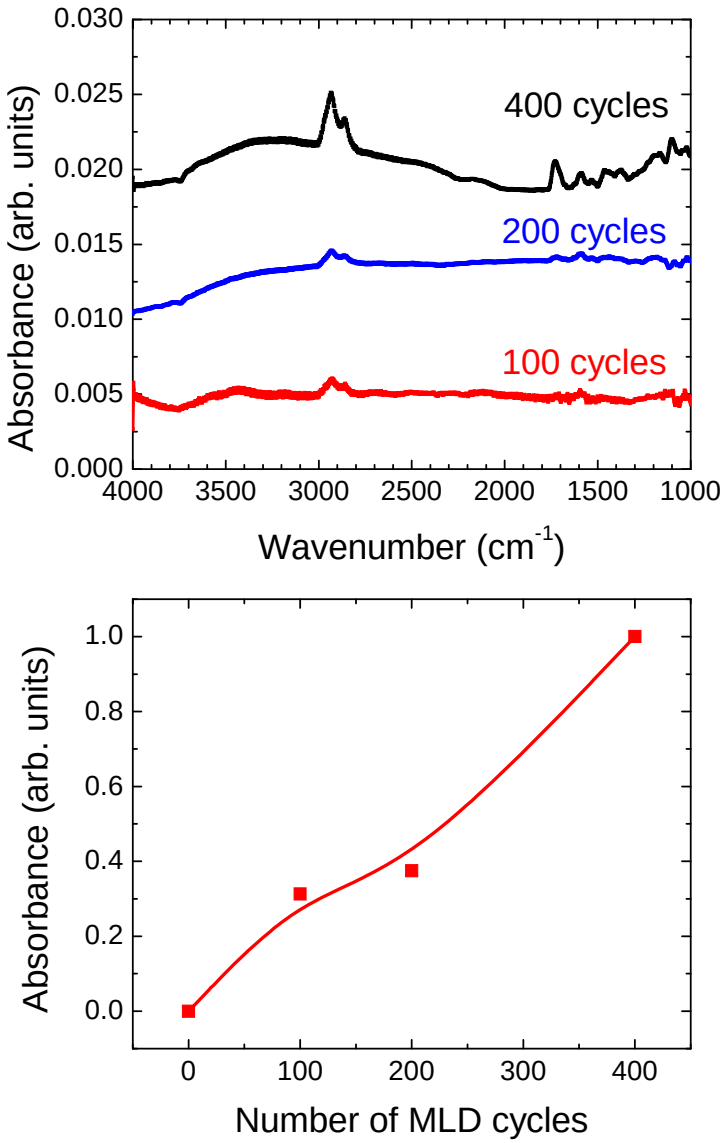


Figure 5.2. (a) Ex-situ FTIR spectra collected after deposition from MLD films on Si wafers using TMA/Ar/LAC/Ar = 1/40/2/40 seconds at 60°C. Spectra show modes associated with -CH_2- asymmetric and symmetric stretching at 2928 $cm^{-1}$and 2865cm^{-1}, C-O at 1100 cm^{-1} and Al-O stretching near 700cm^{-1} consistent with the polymer composition: (-Al-O-(C_8H_{16})-O-)$_n$. Mode intensity increased with the number of deposition cycles. (b) The intensity of the CH_2 asymmetric stretching mode at 2928 cm^{-1} is plotted versus number of MLD cycles, was selected as a characterization absorbance for MLD film, and the intensity of this peak is increased with the number of MLD cycles.

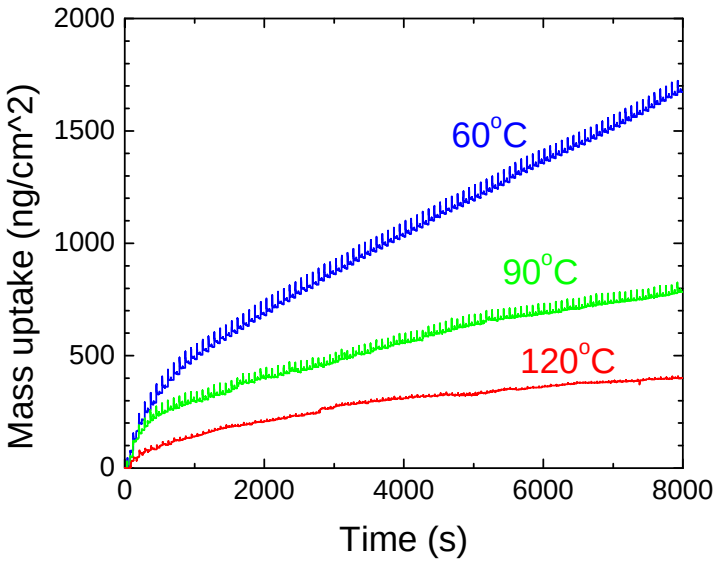


Figure 5.3. In-situ QCM mass uptake results for TMA/LAC MLD sequences. Gas pulse and purge times were 1/40/2/40 seconds. 100 cycles of TMA/GLY MLD at 60 to 120 °C on Al-OH surface formed using the TMA/water ALD process.

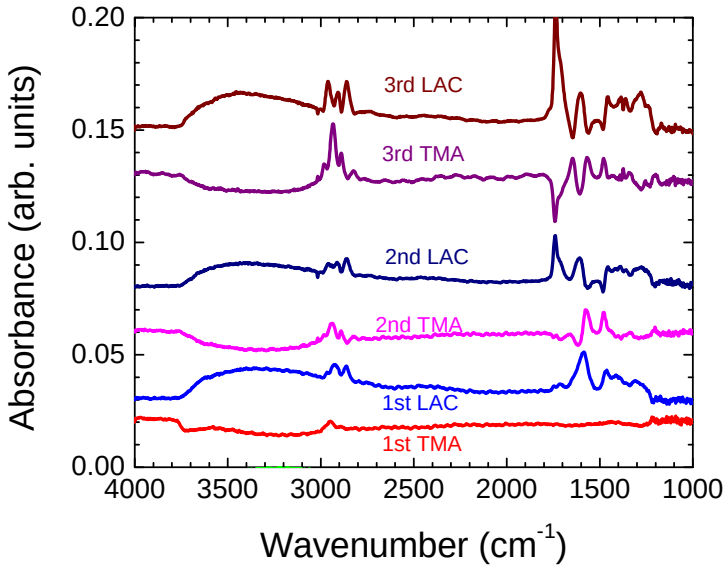


Figure 5.4. In-situ differential FTIR spectra collected during TMA/LAC sequence at 60°C. Differential spectra collected after LAC dose showed an increase of CH_2 modes at 2865 and 2928 cm^{-1} ,C=O mode at 1732 cm^{-1} and very little decrease of CH_3 absorbance at 2895 cm^{-1} and 2940 cm^{-1}, which indicate the selective reaction of C-O-C on LAC with Al-CH_3.

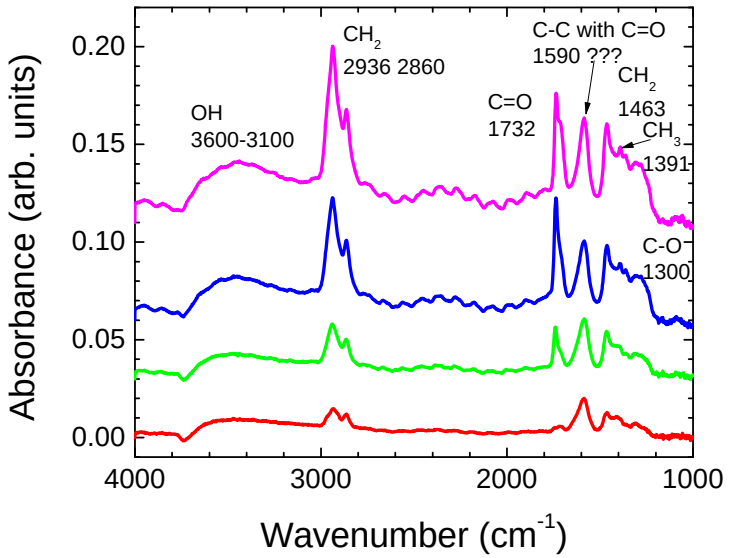


Figure 5.5. In-situ differential FTIR spectra collected after each TMA/LAC cycle at 60°C. Differential spectra collected after LAC dose showed an increase of CH_2 modes at 2865, 2928 and 1463 cm^{-1} ,OH mide at 3100-3600 cm^{-1}, C=O mode at 1732 cm^{-1}. Absorbance increase with deposition cycles.

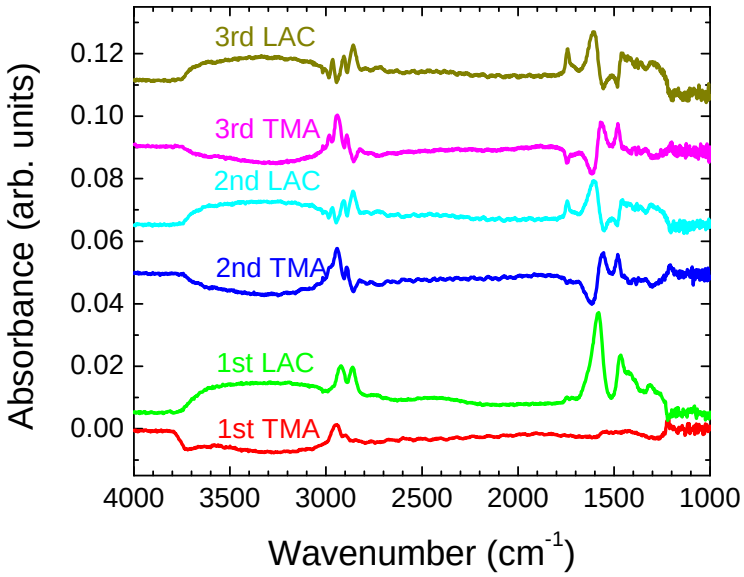


Figure 5.6. In-situ differential FTIR spectra collected during TMA/LAC sequence at 120°C. Differential spectra collected after LAC dose showed an increase of CH_2 modes at 2865 and 2928 cm^{-1} ,C-O-C mode at 1600 cm^{-1} and very little decrease of CH_3 absorbance at 2895 cm^{-1} and 2940 cm^{-1}, which indicate the selective reaction of C=O on LAC with Al-CH_3. Or both C-O-C and C=O on LAC will react with Al-CH_3.

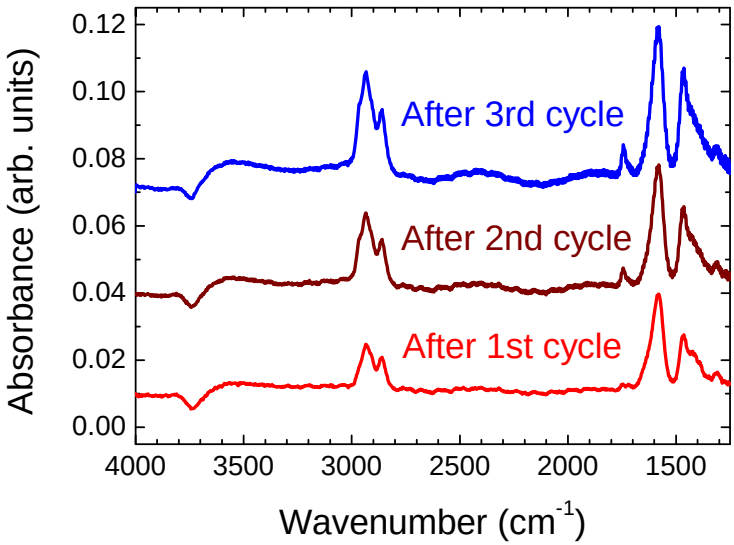


Figure 5.7. In-situ differential FTIR spectra collected after each TMA/LAC cycle at 120°C. Differential spectra collected after LAC dose showed an increase of CH_2 modes at 2865, 2928 and 1463 cm^{-1} ,OH mide at 3100-3600 cm^{-1}, C=O mode at 1732 cm^{-1}. Absorbance increase with deposition cycles.

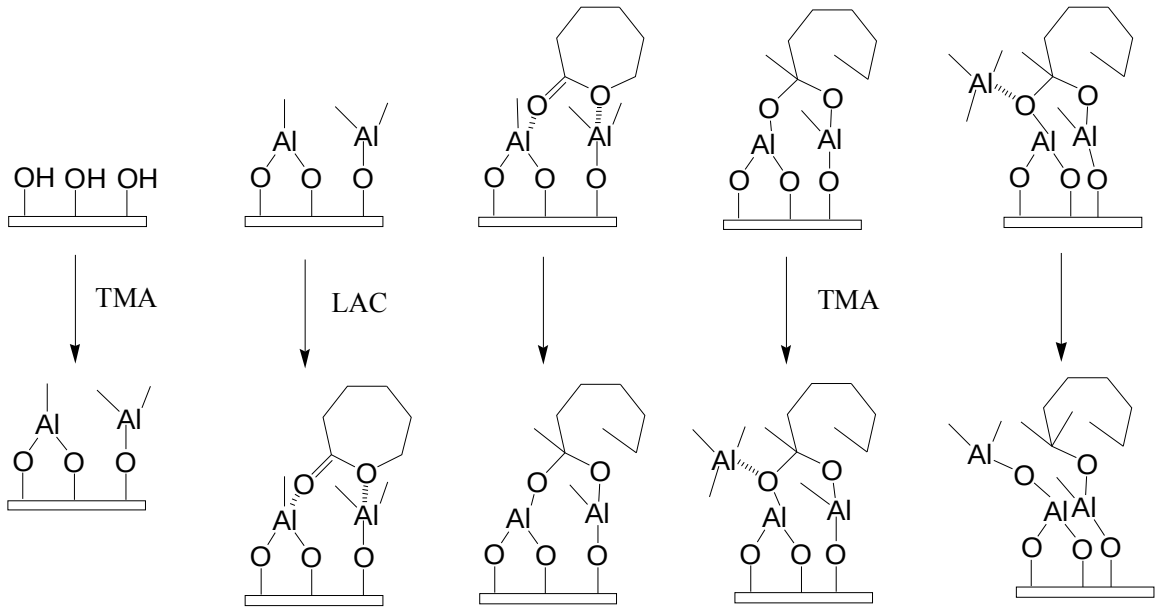


Figure 5.8. Schematic of the surface reactions during TMA/LAC MLD process at 120°C. Exposing the –OH surface to TMA produced Al-CH_3 features visible in the IR in Figure 5.6. Upon exposure to LAC, the IR data showed increase of CH2 related features, O-C-O aluminum carbonate absorbance and no obvious increase of carbonyl absorbance, indicating the surface Al-CH_3 reacts with the (C=O)-O group on the LAC molecule to produce aluminum carbonate groups. During the following TMA dose, the O-C-O asymmetric stretching mode in aluminum carbonate decreased. This is imply the reaction between Al-O-C groups will TMA, and formation of Al-CH_3 terminations.

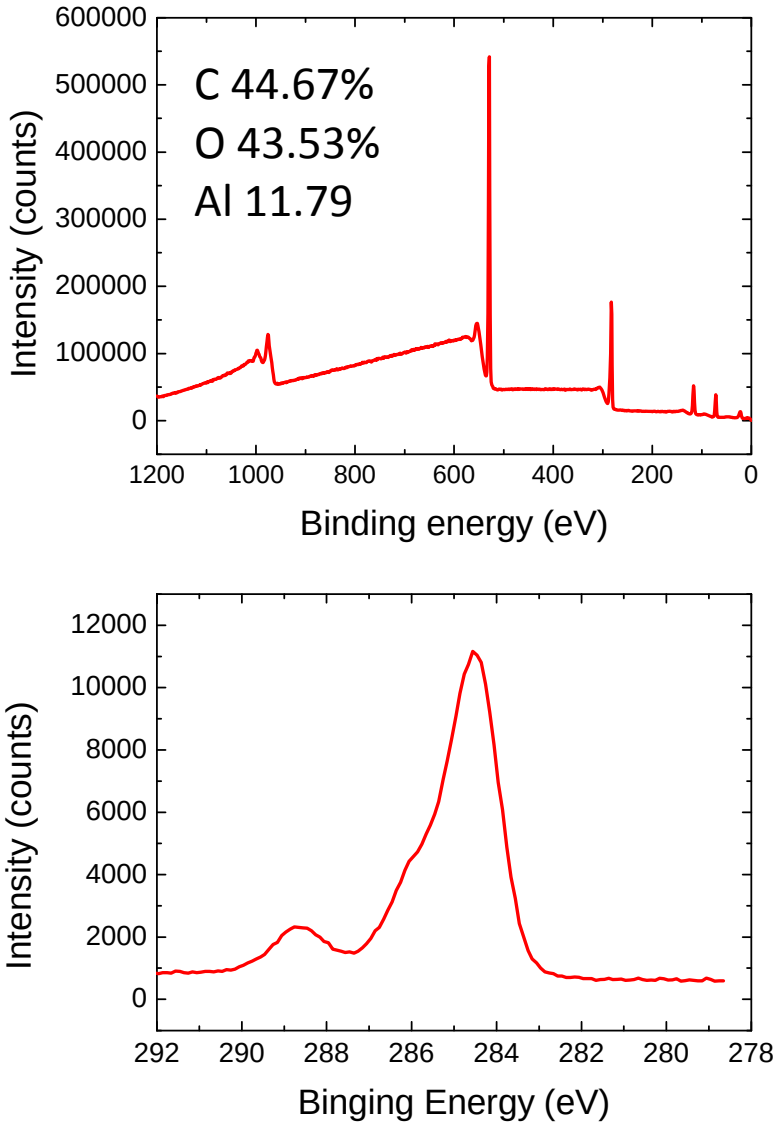


Figure 5.9. (a) XPS survey scan of the TMA/LAC MLD film on Si (400 cycles at 60°C). (b) The C 1s detail scan from the same sample showed a bonding distribution consistent with the polymer structure (Al-O-(C_4H_8)-), with little C=O present.

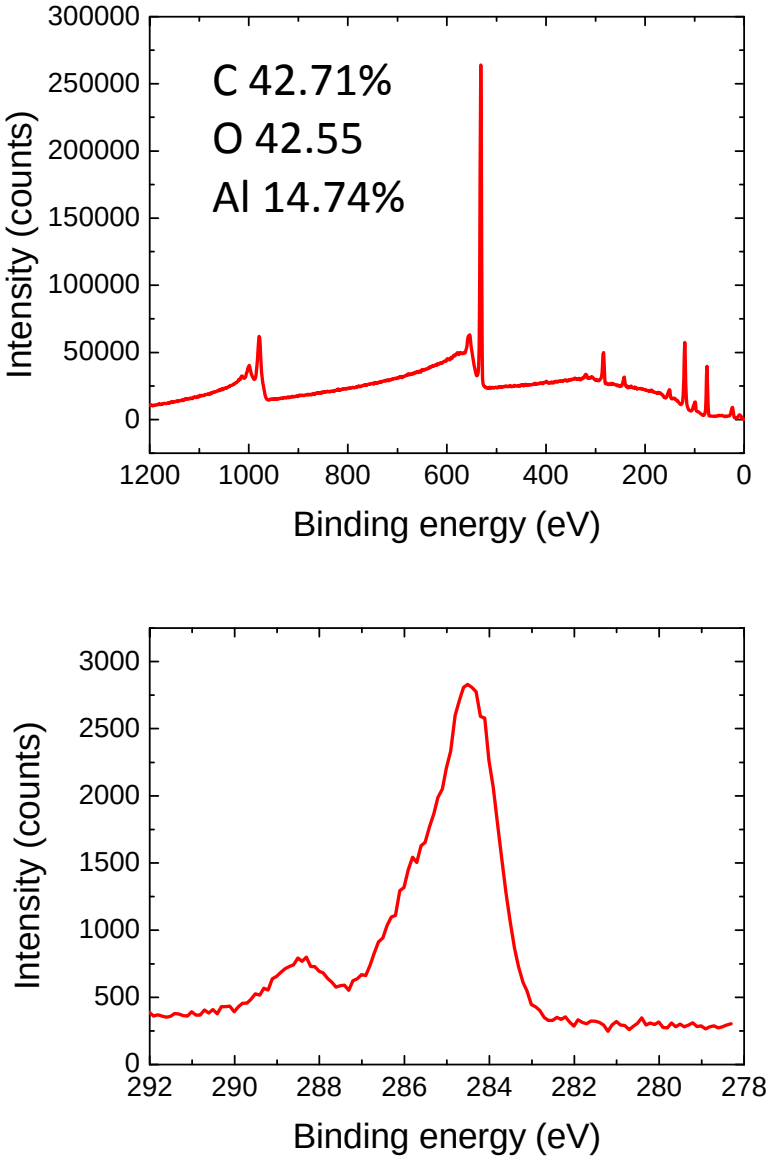


Figure 5.10. (a) XPS survey scan of the TMA/LAC MLD film on Si (400 cycles at 90°C). (b) The C 1s detail scan from the same sample showed a bonding distribution consistent with the polymer structure (Al-O-(C_4H_8)-), with little C=O present.

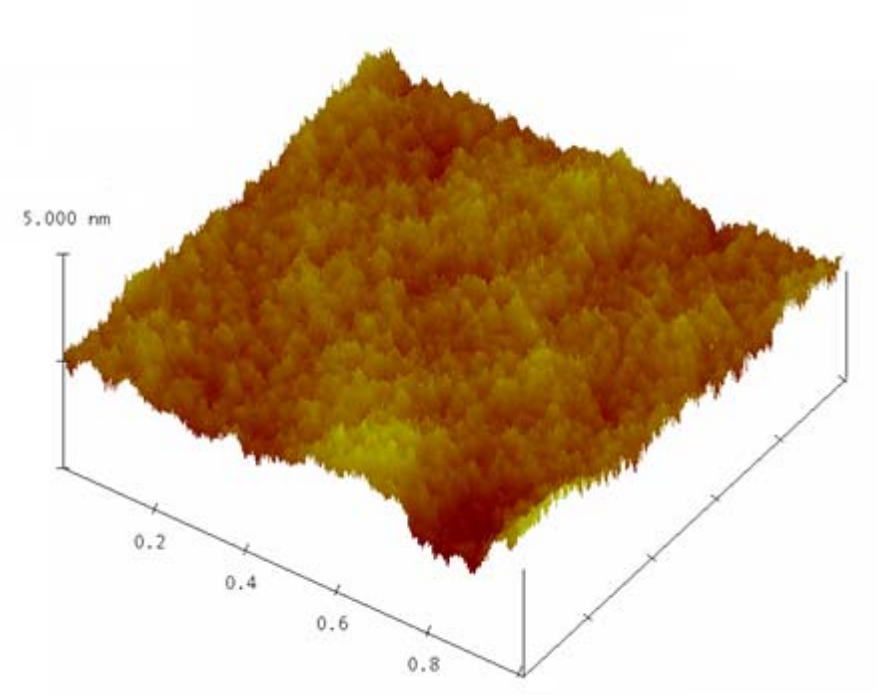


Figure 5.11. Atomic force micrographs of TMA/LAC MLD films (400 cycles at 120°C) on a Si wafer (1μm × 1μm). MLD film showed a larger surface roughness with RMS of ~5Å.

References

1 B. H. Lee; M. K. Ryu; S.-Y. Choi; K.-H. Lee; S. Im; M. M. Sung; Rapid Vapor-Phase Fabrication of Organic−Inorganic Hybrid Superlattices with Monolayer Precision, *Journal of the American Chemical Society,* **2007**. *129*, 16034.

2 X. Liang; A. Weimer; Photoactivity passivation of TiO2 nanoparticles using molecular layer deposited (MLD) polymer films, *Journal of Nanoparticle Research,* **2010**. *12*, 135.

3 X. H. Liang; M. Yu; J. H. Li; Y. B. Jiang; A. W. Weimer; Ultra-thin microporous-mesoporous metal oxide films prepared by molecular layer deposition (MLD), *Chemical Communications,* **2009**. 7140.

4 A. Kubono; N. Okui; Polymer Thin-Films Prepared By Vapor-Deposition, *Progress in Polymer Science,* **1994**. *19*, 389.

5 H. I. Shao; S. Umemoto; T. Kikutani; N. Okui; Layer-by-layer polycondensation of nylon 66 by alternating vapour deposition polymerization, *Polymer,* **1997**. *38*, 459.

6 Y. Takahashi; M. Iijima; Y. Oishi; M. Kakimoto; Y. Imai; Preparation Of Ultrathin Films Of Aromatic Polyamides And Aromatic Poly(Amide Imides) By Vapor-Deposition Polymerization, *Macromolecules,* **1991**. *24*, 3543.

7 T. Yoshimura; N. Terasawa; H. Kazama; Y. Naito; Y. Suzuki; K. Asama; Selective growth of conjugated polymer thin films by the vapor deposition polymerization, *Thin Solid Films,* **2006**. *497*, 182.

8 T. Yoshimura; S. Tatsuura; W. Sotoyama; A. Matsuura; T. Hayano; Quantum Wire And Dot Formation By Chemical Vapor-Deposition And Molecular Layer Deposition Of One-Dimensional Conjugated Polymer, *Applied Physics Letters,* **1992**. *60*, 268.

9 S. J. Limb; C. B. Labelle; K. K. Gleason; D. J. Edell; E. F. Gleason; Growth of fluorocarbon polymer thin films with high CF2 fractions and low dangling bond concentrations by thermal chemical vapor deposition, *Applied Physics Letters,* **1996**. *68*, 2810.

10 S. H. Baxamusa; S. G. Im; K. K. Gleason; Initiated and oxidative chemical vapor deposition: a scalable method for conformal and functional polymer films on real substrates, *Physical Chemistry Chemical Physics,* **2009**. *11*, 5227.

11 R. Sreenivasan; K. K. Gleason; Overview of Strategies for the CVD of Organic Films and Functional Polymer Layers, *Chemical Vapor Deposition,* **2009**. *15*, 77.

12 T. Suntola; Atomic Layer Epitaxy, *Thin Solid Films,* **1992**. *216*, 84.

13 M. Leskela; M. Ritala; Atomic layer deposition (ALD): from precursors to thin film structures, *Thin Solid Films,* **2002**. *409*, 138.

14 S. M. George; A. W. Ott; J. W. Klaus; Surface chemistry for atomic layer growth, *Journal of Physical Chemistry,* **1996**. *100*, 13121.

15 S. M. George; B. Yoon; A. A. Dameron; Surface Chemistry for Molecular Layer Deposition of Organic and Hybrid Organic-Inorganic Polymers, *Accounts of Chemical Research,* **2009**. *42*, 498.

16 Q. Peng; B. Gong; R. M. VanGundy; G. N. Parsons; "Zincone" Zinc Oxide-Organic Hybrid Polymer Thin Films Formed by Molecular Layer Deposition, *Chemistry of Materials,* **2009**. *21*, 820.

17 Y. Du; S. M. George; Molecular layer deposition of nylon 66 films examined using in situ FTIR spectroscopy, *Journal of Physical Chemistry C,* **2007**. *111*, 8509.

18 N. M. Adarnczyk; A. A. Dameron; S. M. George; Molecular layer deposition of poly(p-phenylene terephthalamide) films using terephthaloyl chloride and p-phenylenediamine, *Langmuir,* **2008**. *24*, 2081.

19 T. BitzerN. V. Richardson; Demonstration of an imide coupling reaction on a Si(100)-2x1 surface by molecular layer deposition, *Applied Physics Letters,* **1997**. *71*, 662.

20 P. W. Loscutoff; H. Zhou; S. B. Clendenning; S. F. Bent; Formation of Organic Nanoscale Laminates and Blends by Molecular Layer Deposition, *Acs Nano,* **2010**. *4*, 331.

21 A. A. Dameron; D. Seghete; B. B. Burton; S. D. Davidson; A. S. Cavanagh; J. A. Bertrand; S. M. George; Molecular layer deposition of alucone polymer films using trimethylaluminum and ethylene glycol, *Chemistry of Materials,* **2008**. *20*, 3315.

22 B. Yoon; J. L. O'Patchen; D. Seghete; A. S. Cavanagh; S. M. George; Molecular Layer Deposition of Hybrid Organic-Inorganic Polymer Films using Diethylzinc and Ethylene Glycol, *Chemical Vapor Deposition,* **2009**. *15*, 112.

23 B. Yoon; D. Seghete; A. S. Cavanagh; S. M. George; Molecular Layer Deposition of Hybrid Organic-Inorganic Alucone Polymer Films Using a Three-Step ABC Reaction Sequence, *Chemistry of Materials,* **2009**. *21*, 5365.

24 B. Gong; Q. Peng; J. S. Jur; C. K. Devine; K. Lee; G. N. Parsons; Sequential Vapor Infiltration of Metal Oxides into Sacrificial Polyester Fibers: Shape Replication and Controlled Porosity of Microporous/Mesoporous Oxide Monoliths, *Chemistry of Materials,* **2011**. *23*, 3476.

25 B. Gong; Q. Peng; G. N. Parsons; Conformal Organic−Inorganic Hybrid Network Polymer Thin Films by Molecular Layer Deposition using Trimethylaluminum and Glycidol, *The Journal of Physical Chemistry B,* **2011**. *115*, 5930.

26 H. Sugimoto; C. Kawamura; M. Kuroki; T. Aida; S. Inoue; Lewis Acid-assisted Anionic Ring-Opening Polymerization of Epoxide by the Aluminum Complexes of Porphyrin, Phthalocyanine, Tetraazaannulene, and Schiff-base as initiators, *Macromolecules,* **1994**. *27*, 2013.

27 M. Joubert; C. Delaite; E. Bourgeat-Lami; P. Dumas; Hairy PEO-silica nanoparticles through surface-initiated polymerization of ethylene oxide, *Macromolecular Rapid Communications,* **2005**. *26*, 602.

28 D. Hausmann; J. Becker; S. L. Wang; R. G. Gordon; Rapid vapor deposition of highly conformal silica nanolaminates, *Science,* **2002**. *298*, 402.

29 L. J. Zhong; F. Chen; S. A. Campbell; W. L. Gladfelter; Nanolaminates of zirconia and silica using atomic layer deposition, *Chemistry of Materials,* **2004**. *16*, 1098.

30 L. J. Zhong; W. L. Daniel; Z. H. Zhang; S. A. Campbell; W. L. Gladfelter; Atomic layer deposition, characterization, and dielectric properties of HfO2/SiO2 nanolaminates and comparisons with their homogeneous mixtures, *Chemical Vapor Deposition,* **2006**. *12*, 143.

31 D. N. Goldstein; J. A. McCormick; S. M. George; Al2O3 Atomic Layer Deposition with Trimethylaluminum and Ozone Studied by in Situ Transmission FTIR Spectroscopy and Quadrupole Mass Spectrometry, *The Journal of Physical Chemistry C,* **2008**. *112*, 19530.

32 M. Li; M. Dai; Y. J. Chabal; Atomic Layer Deposition of Aluminum Oxide on Carboxylic Acid-Terminated Self-Assembled Monolayers, *Langmuir,* **2009**. *25*, 1911.

CHAPTER 6 is a reprint of a manuscript published in Applied Catalysis A.

CHAPTER 6. Highly Active Photocatalytic ZnO Nanocrystalline Rods Supported on Polymer Fiber Mats: Synthesis Using ZnO Atomic Layer Deposition and Hydrothermal Crystal Growth

Bo Gong, Qing Peng, Jeong-Seok Na and Gregory N Parsons*

Department of Chemical and Biomolecular Engineering, North Carolina State University, Raleigh NC 27695, USA

Keywords: Atomic layer deposition, nonwoven fiber, diethyl zinc, zinc oxide, nanocrystals, nanorods, hydrothermal, zinc nitrate hexahydrate, hexamethylene tetramine, photocatalytic.

*Corresponding author: parsons@ncsu.edu

Abstract

Photocatalytically active zinc oxide nanocrystalline rods are grown on high surface area polybutylene terephthalate (PBT) polymer fiber mats using low temperature solution based methods, where the oxide crystal nucleation is facilitated using conformal thin films formed by low temperature vapor phase atomic layer deposition (ALD). Scanning electron microscopy (SEM) confirms that highly oriented single crystal ZnO nanorod crystals are directed normal to the starting fiber substrate surface, and the extent of nanocrystal growth within the fiber mat bulk is affected by the overall thickness of the ZnO nucleation layer. The high surface area of the nanocrystal-coated fibers is confirmed by nitrogen adsorption/desorption analysis. An organic dye in aqueous solution in contact with the coated fiber degraded rapidly upon ultraviolet light exposure, allowing quantitative analysis of the photocatalytic properties of fibers with and without nanorod crystals present. The dye degrades nearly twice as fast in contact with the ZnO nanorod crystals compared with samples with only an ALD ZnO layer. Additionally, the catalyst on the polymer fiber mat could be reused without need for a particle recovery step. This combination of ALD and hydrothermal processes could produce high surface area finishes on complex polymer substrates for reusable photocatalytic and other surface-reaction applications.

6.1. Introduction

The large band gap and strong exciton binding energy of zinc oxide make it a valuable semiconductor for many microelectronic and optoelectronic devices including solar cells,[1] photo-detectors[2] and light emitting diodes.[3,4] In addition, ZnO is one of many naturally oxygen deficient metal oxides that will photocatalytically decompose complex organic molecules in the presence of UV illumination.[5-7] Nanostructured ZnO crystals are particularly interesting for photocatalysis because of their high surface area increases the crystal/solution contact area. Recently, researchers have defined methods to create crystalline ZnO nanowires,[1,8,9] nanorods,[10] nanotubes,[11] nanobelts,[12,13] nanotowers,[14] dendritic hierarchical structures[15] and an assortment of other constructs.[16] However, few of these studies addressed issues in photocatalysis. A problem with free-standing ZnO nanostructures is that they could readily aggregate in aqueous solution. It is also a challenge to recycle and regenerate these nanostructures from the solution. Catalytically active particles with magnetic attraction show some promise in this regard.[17] Another promising approach is to attach ZnO nanostructures onto a three-dimension porous support. Polymer fiber mats are especially attractive as supports because they are inexpensive, readily available, and they are flexible and easy to use.

Aqueous hydrothermal techniques for ZnO nanorod crystal growth can proceed rapidly at relatively mild temperatures (<150 °C), and the processing permits surface-selective growth that drives nanostructure evolution.[18] For most hydrothermal methods, an oxide seed layer is essential to initiate and continue crystal evolution. The seed layer presents nucleation sites, lowering the thermodynamic barrier for ZnO nano- and micro-crystal growth and

further enhancing the growth direction selectivity and aspect ratio.[14,15] Previous researchers form nucleation sites by applying ZnO particles or a nanocrystalline film by dip coating, spin coating[15] or sputtering.[19] These approaches can work for deposition on planar surfaces, but for complex 3-D substrates, these methods are not expected to yield uniform seed layers and homogeneous seed layer distribution.

Atomic layer deposition (ALD) is a vapor phase thin film deposition technique which can deposit materials uniformly on complex 3D surfaces. In the ALD process, two co-reactants (e.g. diethyl zinc and water for ZnO formation) are introduced alternatively, separated by an inert gas purge step, allowing the surface to react with each reagent in a series of self-limiting adsorption/reaction steps.[16,20-23] Repeating this sequence builds up a coating with desired thickness on the substrate. Several research groups recently showed that this process yields uniform metal oxide thin film coatings on high aspect ratio polymer fiber substrates.[20-26] Some of these reports also show photocatalytic performance of the resulting polymer/oxide structures.[24,25] For this study, we show that the ALD layer provides an ideal seed layer for hydrothermal growth of ZnO nanorod crystals on fiber structures, and that these nanocrystal-coated fibers show high photocatalytic activity compared to previous structures.

In particular, we describe an ALD process to deposit a thin layer of ZnO onto a polybutylene terephthalate (PBT) nonwoven fiber mat, where the ZnO layer is then used as a seed layer for low temperature ZnO nanorod hydrothermal growth[16]. This sequence creates a hierarchical fiber/nanorod crystal composition with surface-normal ZnO nanorods on the

cylindrical fiber template. The final fiber cross section was imaged and physically characterized, and the photocatalytic properties of the fiber/nanorod construction were tested and compared to uncoated fibers and to fibers uniformly coated with ZnO ALD (i.e. without the hydrothermal growth step). The hierarchical structure shows superior photocatalytic performance, consistent with the expected enhanced surface area.

6.2. Experimental Procedures

ZnO Seed Layer Deposition by ALD

The substrate for ZnO nanocrystal growth was a multilayered nonwoven PBT fiber mat acquired from the Nonwoven Cooperative Research Center (NCRC) at NC State University. The SEM images of the fiber mat showed that it consisted of a mass of individual fibers (2-3 μm in diameter) with a total mat thickness of ~ 0.5 mm.[27] We monitored ALD growth by depositing simultaneously onto polished silicon wafer pieces. Figure 6.1 displays a schematic drawing of the homemade viscous flow hot wall vacuum reactor used for zinc oxide ALD.[28] The reaction system is composed of stainless steel tube ~3.5 cm in diameter, surrounded by a heating jacket to control the reactor temperature (100 °C for these studies). The carrier gas was ultrahigh-purity Ar (99.999% National Welders) flowing at ~200 standard cubic centimeters per minute (sccm). The reaction system was pumped using a rotary mechanical pump, and the steady-state process pressure was ~1.0 Torr, as monitored by a Baratron pressure gauge (MKS Instrument Inc.). One ZnO ALD cycle consisted of a 2 second exposure to diethyl zinc (DEZ, 98% Strem Chemical) followed by a 60 s Ar purge, a 2 s water exposure, and another 60 s Ar purge (the sequence is denoted as 2/60/2/60 s). The

reactant pulse produced a pressure increase of 50 mTorr in the reactor. The seed layers were deposited using either 100 or 200 ZnO deposition cycles. These cycles produce ~20 or 40 nm thick films, respectively, on planar silicon substrates. Refractive index and film thickness on silicon was measured by variable-angle alpha-SE spectroscopic ellipsometry (J.A. Woollam Co., Inc.).

Hydrothermal Growth of ZnO Nanorod Crystals on Seed Layer

After ALD coating, the PBT fibers and silicon control wafer were transferred into a teflon vessel containing 30 ml aqueous solution of equimolar (20mM) zinc nitrate hexahydrate ($Zn(NO_3)_2{\cdot}6H_2O$, 99% Aldrich) and hexamethylene tetramine ($C_6H_{12}N_4$, 99% Aldrich). The vessel was left open and held in an oven at 80 °C for 6 hr resulting in the growth of ZnO nanorod crystals on the ZnO coated silicon and PBT substrates. The silicon wafer was held face-down in the solution to prevent the precipitation of any ZnO particles that may have formed in the solution bulk. After growth, the PBT fiber mat and Si wafer were rinsed with deionized water for 2 mins, and then dried in N_2 flow at room temperature. Seed layer thicknesses of ~20 and 40 nm were investigated.

Microscopy and Surface Analysis

Images of the modified fibers were collected using an FEI XL30 Scanning Electron Microscope (SEM) operating at 7 kV with a working distance of 5 mm. Before SEM imaging, samples sputter-coated with 5 nm of Au/Pd to reduce surface charging. Transmission Electron Microscope (TEM) images of ZnO nanorod crystals on polymer fiber mats were collected using a Hitachi HF cold field emission TEM operated at 200 kV with 0.2

nm point resolution. The TEM samples were prepared by heating the treated fiber at 400 °C in air for 24 hr, resulting in calcination of the polymer. After calcination, the resulting materials were dispersed in methanol, sonicated for 1 min, and then transferred by pipette onto carbon film-coated TEM grids (Ted Pella, Inc.)

The static water contact angle on the starting and modified surfaces was collected using a Model 200 Rame Hart contact angle goniometer equipped with a CCD camera. We measured at least five different points on each sample and the average value is reported.

A Quantachrome Autosorb-1C surface area and pore size analyzer provided information on the Brunauer Emmett Teller (BET) surface area of the materials before and after processing. Before each analysis, samples were heated under vacuum at 100 °C for at least 4 hr to remove residual and moisture adsorbed. The recorded data was collected from ~ 200 mg samples using a seven point BET (P/P_0 range from 0.05 – 0.35) analysis.

Photocatalytic Characterization

Fiber samples with ZnO ALD coating, ZnO coating with subsequent hydrothermal nanocrystal growth, as well as untreated fibers were all cut into uniform sample pieces (1.8 cm × 1.8 cm) and placed into three glass vials, each containing 25 ml of deionized water with equal concentrations (3×10^{-4} volume%) of commercially available azo acid red 40 dye. We then exposed the vial (uncapped) to UV radiation from a shuttered Intell-Ray 400 Uvitron International UV floodlight (320-390 nm) providing 79 mW/cm^2 of energy flux impinging from the top. The incident power density was determined using a 1916-C Newport optical power meter. By monitoring the concentration of the dye in the vessel by UV-Vis absorbance

(measured by a Thermo Scientific Evolution 300 UV-Vis spectrophotometer) as a function of time, we were able to quantify the relative rate of dye degradation and hence analyze the effective photocatalytic activity of the different prepared samples.

6.3. Results and Discussion

Figure 6.2 presents SEM images of silicon wafers after hydrothermal ZnO nanorod crystal growth. The sample in panels (a) and (b) is prepared by hydrothermal growth directly on the silicon wafer (i.e. without the ZnO ALD seed layer), and the images in panels (c) and (d) were collected from a silicon wafer with the ALD ZnO seed layer. Without the seed layer, only small amount of sparsely distribute ZnO nanocrystals are present. They are also relatively large (~ 1 μm in diameter and ~ 3-5 μm long). When the substrate is pre-coated with 100 ZnO ALD cycles (producing a seed layer ~20 nm thick, as determined by ellipsometry), the hydrothermal growth step yields complete coverage of ZnO nanorod crystals with uniform size of ~ 50 nm diameter and ~500 nm long. We also note that the nanorods show predominantly surface-normal orientation, whereas more random orientation results without the seed layer. The ALD ZnO provides a good seed layer for the hydrothermal growth of ZnO nanocrystals. The detailed ALD condition could change the surface roughness of the PBT fiber mat, and further affect the morphology of coated ZnO nanorods. Future experiments were needed to verify this.

The effects of ZnO ALD seeding were also tested on polymer fiber mat. Figure 6.3 presents SEM images of PBT nonwoven fiber mats after ZnO nanorod crystal growth. For the bare PBT fiber mat, the images in 3(a) and (b) show only sparse and relatively large ZnO

clusters, similar to growth on untreated silicon wafer. Figures 6.3(c) and (d) show a PBT fiber mat after 20 nm (100 cycles) of ALD ZnO followed by hydrothermal growth. Interestingly, ZnO nanocrystals only grow on the outer surface of the substrate mat, and fibers in the middle layers of the substrate show almost no nanocrystal growth. This non-uniformity is particularly visible in Figure 6.3(d), in which fibers at the top of the mat appear to have a much larger diameter because of the nanorod crystals.

To understand this non-uniformity in nanorod growth, we examined water droplet contact angle and water penetration into the nonwoven fiber mat after the ALD coating.[22] As received, the PBT fibers appear hydrophobic. A water droplet placed on the fiber mat did not absorb and the average static water contact angle was ~120 °. After coating the mat with 100 cycles of ZnO ALD, water still did not readily penetrate, and the contact angle was ~ 100 °. We believe that the hydrophobic nature of the coated PBT fiber mat limits the penetration of the aqueous hydrothermal process solution into the mat, resulting in hydrothermal growth primarily on the outer fibers, as shown in Figure 6.3 (c) and (d). We find, however, that after 200 cycles of ZnO ALD, the PBT fiber mat became completely wetting (contact angle ~0 °), which will readily allow the aqueous hydrothermal solution to penetrate into the matrix. This wetting transition for ALD coated polymer fibers has been previously observed, and it is understood to result from a combination of changes in surface chemical termination and surface roughness.[22] As demonstrated in Figures 6.3(e) and (f) PBT fiber samples coated with 200 cycles ALD ZnO as a seed layer yielded a uniform coating of ZnO nanorod crystals deeper into the fiber mat. Several sample fibers extracted at random from the bulk of the mat

were examined by SEM, and all showed good coverage of ZnO nanocrystals after the hydrothermal growth with small variation in number and density of the crystallites.

High resolution TEM images presented in Figure 6.4 show nanorod crystals grown on PBT using the 200 cycles ZnO ALD seed layers. The PBT fiber has been removed by a calcination step at 400 °C for 24 hr. Figure 6.4 (a) clearly shows both the oriented ZnO nanorod crystals and the ZnO shell layer. The lattice fringe spacing of ~0.32 nm measured in Figure 6.4 (b) confirms the ZnO wurtzite structure. However, due to the relative high calcination temperature, the phase transition of ZnO nanorods could happen. The zincite structure could be formed during the hydrothermal growth,[29] and transformed to wurtzite during the calcinations. The particular sample shown in Figure 6.4 reveals a smaller number of nanocrystals. This could result from damage during sonication for the TEM sample preparation, or some non-uniformity in the hydrothermal growth step.

The surface area is critical for the catalytic performance of ZnO structures. The BET surface area measured by nitrogen adsorption/desorption analysis was ~0.73 m^2/g for the untreated PBT fiber mat, with a factor of 2-3 increase in surface area to ~ 1.79 m^2/g, after the ZnO seed layer and hydrothermal growth. This increase is rather modest on a per mass basis. However, we note that after hydrothermal growth, the net mass (per cm^2 of fiber mat sample) increased by a factor of four compared to the sample with ALD ZnO coating, which verifies a significant amount of hydrothermal ZnO deposition. The increase in mass, combined with an increase in surface area per unit mass basis means that on a per sample basis (i.e. for a fixed fiber mat sample size), the surface area of the fiber mat increases by at least a factor of

10 compared to the starting sample. An even larger increase in surface area could be expected if a fiber mat support with finer fibers was used, or if thinner and/or longer nanorods could be grown. The density and porosity of the fiber mat also likely play a role in determining the optimum conditions to achieve uniform nanocrystal growth and high surface area.

An organic dye in aqueous solution was used to test the photocatalysis performance of ZnO functionalized PBT fiber mats. The photocatalytic decomposition of organic materials in aqueous solution is generally believed to be initiated by photo-excitation of ZnO, producing hydroxyl radicals and holes with high oxidative potential, permitting rapid oxidation of organics in contact with the surface.[5,7] Figure 6.5 shows the photocatalytic performance of ZnO treated fiber mat samples where the UV-Visible absorbance measured at 525 nm, normalized to the starting absorbance of each dye solution sample, is plotted versus UV exposure time. Upon UV irradiation, the dye degraded in all sample vials, but the sample vial containing the nanocrystal-coated fibers in contact with the solution showed a substantially faster degradation rate compared with the other samples. In addition, we performed a control experiment without UV exposure where a similar sized nanocrystal-coated PBT fiber mat was placed into the dye solution and kept in dark for 2 hr. As expected, negligible UV-Vis absorbance change was observed from the dye solution, which confirmed that the decomposition is photocatalytic. Additionally, The dye solutions with and without PBT fiber mat showed very similar degradation curve, indicate that the UV PBT degradation has limited effect on the dye degradation.[30] However, the ZnO coating could catalysis the UV PBT degradation, and induces some degradation of acid red 40. The inset includes images of

three solution vials after a total of 2 hr UV exposure. The vial containing the control PBT fiber shows little degradation, and the vial with ALD ZnO coated PBT shows improved degradation compared to the vial with the uncoated PBT substrate. The vial containing the PBT with ALD ZnO and nanorod crystals showed the best performance, degrading ~ 90% of the dye within 2 hr. This superior performance is ascribed to the larger solution/photocatalyst contact area for the ALD/hydrothermal prepared materials.

The reusability of the ZnO coated PBT fiber mats were also tested with photocatalytic dye decomposition. As shown in Figure 6.6, both ZnO treated samples showed repeatable photocatalytic activity towards acid dye degradation. The higher final dye solution concentration indicated that the photocatalytic activity of the catalyst decreases in three consecutive 2 hours tests. Surface contamination or ZnO nanorods de-bond could be the cause of lower catalytic efficiency.

We also performed side-by-side comparisons of the same material sets using sunlight illumination in place of the laboratory UV lamp. While degradation under sunlight was less rapid than for the UV lamp, the experiment produced the same trend in photocatalytic performance. The fibers with nanorod crystals present showed substantially more degradation with the same exposure time. The integrated ALD/hydrothermal deposition method described here demonstrated an efficient way to further improve photocatalytic materials, and it would be a viable method to enhance other photoactive surface processes.

6.4. Summary and Conclusions

Photocatalytically active ZnO nanorod crystals are readily grown using a low temperature hydrothermal procedure on PBT fibers mats, when the fibers are first coated with a conformal ZnO nucleation layer using atomic layer deposition. The ALD efficiently functionalized the polymer fiber to facilitate hydrothermal nanorod crystal nucleation and subsequent growth. The process produces fibers with ~10× enhancement in total surface area (determined from BET analysis) on a per sample size (cm^2/cm^2) basis. We demonstrated that the ZnO film/nanorod composite will photocatalytically degrade an azo organic dye (acid red 40) in aqueous media at a rate that is nearly 2× faster than a similar fiber with only the ZnO film coating. More importantly, the functionalized polymer fiber mat could be reused very easily, and no additional particle recovery process is needed. This combination of ALD and hydrothermal processes may also be useful for other crystal growth systems, such as TiO_2, Fe_2O_3, SnO_2 and V_2O_5, where high area and ready solution access are desired.

Acknowledgements

We acknowledge support for this work from the US National Science Foundation under grant CBET-1034374.

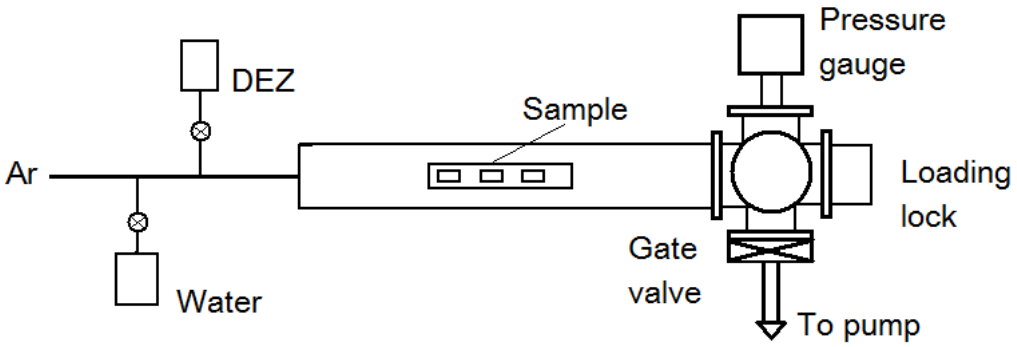


Figure 6.1. Schematic view of the viscous flow ALD reactor used for these studies. In one ALD cycle, two co-reactants (e.g. diethyl zinc and water for ZnO formation) are introduced alternatively, with an inert gas purge step in between, allowing formation of one atomic layer of ZnO. Desired thickness could be achieved by repeating the ALD cycles.

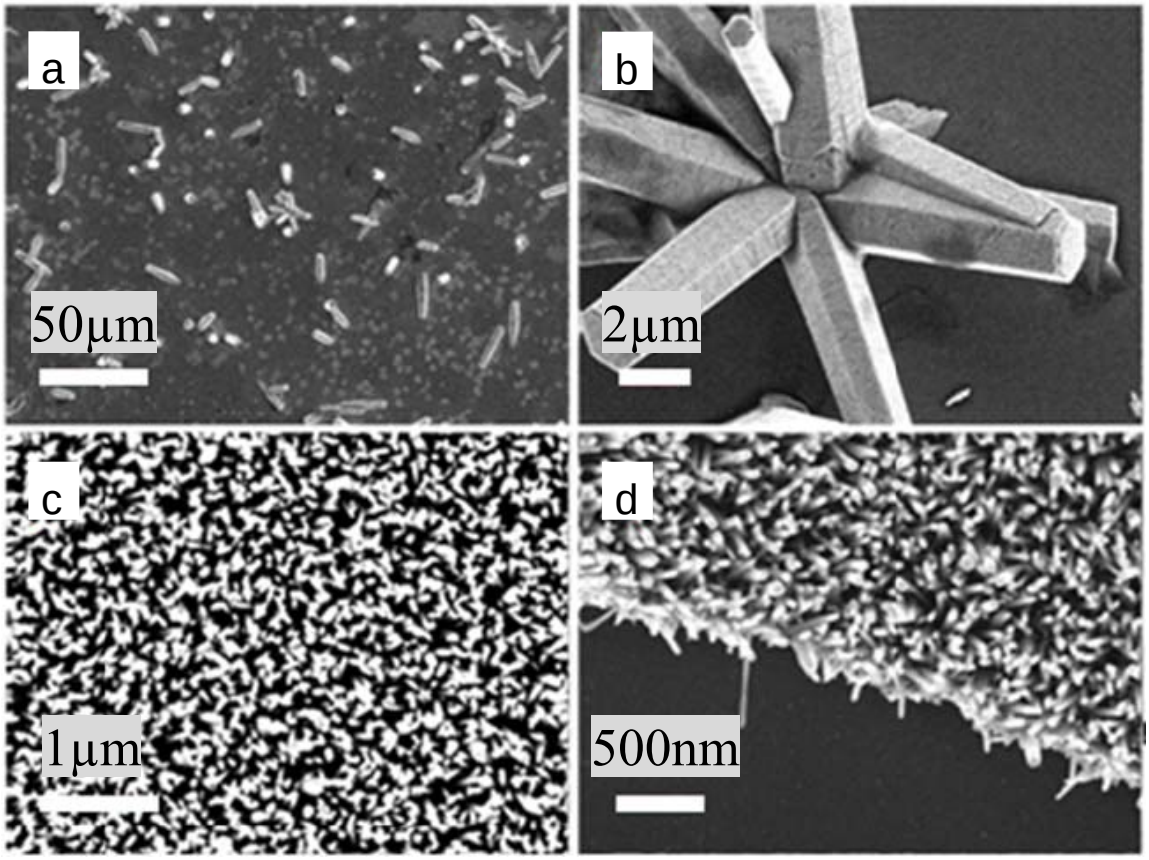


Figure 6.2. Scanning electron microscopy images of silicon wafers after ZnO hydrothermal growth. Images (a) and (b) were collected from samples without an ALD ZnO nucleation layer. Alternatively, images (c) and (d) were from silicon samples that were coated with 100 cycles of ALD ZnO before hydrothermal ZnO nanorod crystal growth.

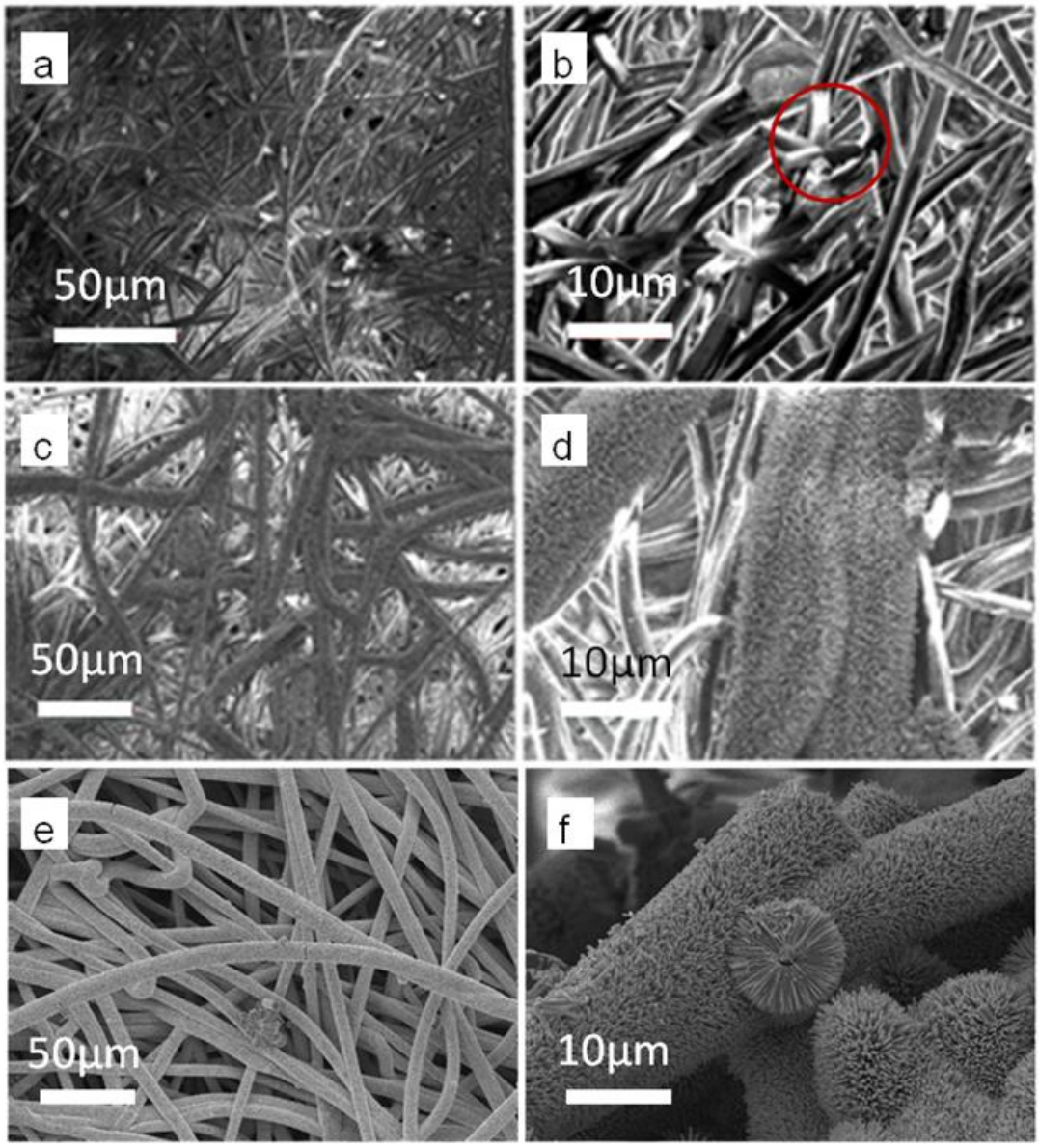


Figure 6.3. Scanning electron micrographs obtained from: (a) and (b), untreated PBT fibers after hydrothermal ZnO nanorod crystal growth; (c) and (d), PBT fibers after 100 ALD cycles of ZnO (~20 nm thick), followed by hydrothermal ZnO nanorod growth. Nanorod crystals are visible primarily on the top-most fibers in the fiber mat. Panels (e) and (f) show PBT fibers after 200 cycles (~40 nm) of ALD ZnO, followed by ZnO nanorod growth. Nanorod growth is visible on all the fibers. In panel (b) a circle highlights a large crystal, similar in size to the one shown in Figure 6.2(b), formed on the untreated fiber.

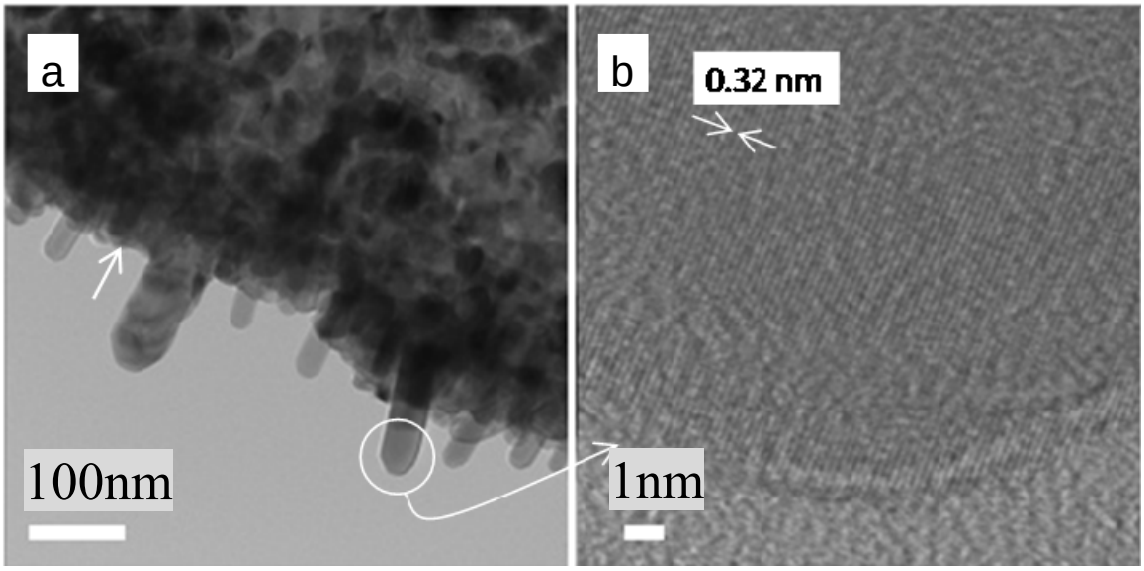


Figure 6.4. Transmission electron microscopy images obtained from ZnO nanorod crystals on PBT fibers where the polymer was removed by calcination before imaging. In image (a), the nanorods are visible protruding from the ZnO thin film layer that remains after calcination. The arrow on the left in image (a) points to a region of ALD ZnO coating without nanorod crystal growth. The image in (b) was collected from the tip of a nanocrystal rod, as indicated by the region circled in (a). The HRTEM image shows the lattice spacing is 0.32 nm, indicating wurtzite ZnO.

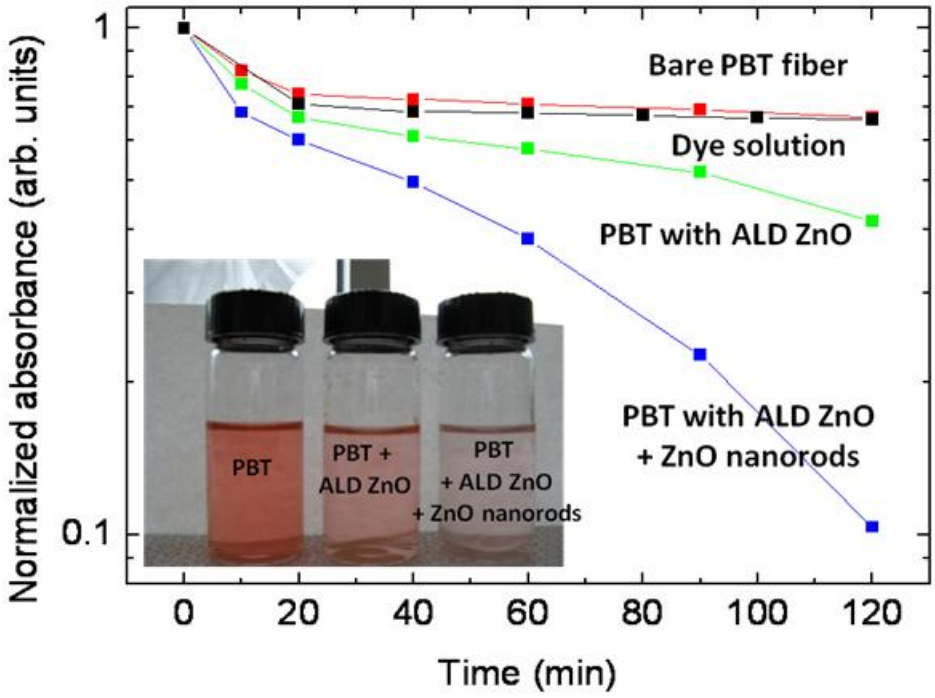


Figure 6.5. Normalized absorbance of organic dye at 525 nm plotted versus UV radiation exposure time. PBT fiber substrates with various surface treatments were immersed in the aqueous solution containing the azo dye (acid red 40), and illuminated using a UV lamp. The fibers with ALD ZnO and ZnO nanorod crystals produced the most rapid photocatalytic dye degradation. The inset shows a photograph of the dye solutions in contact with the different substrates after 2 hr of illumination. The red dye is nearly completely removed from the solution in contact with the nanorod-coated fibers.

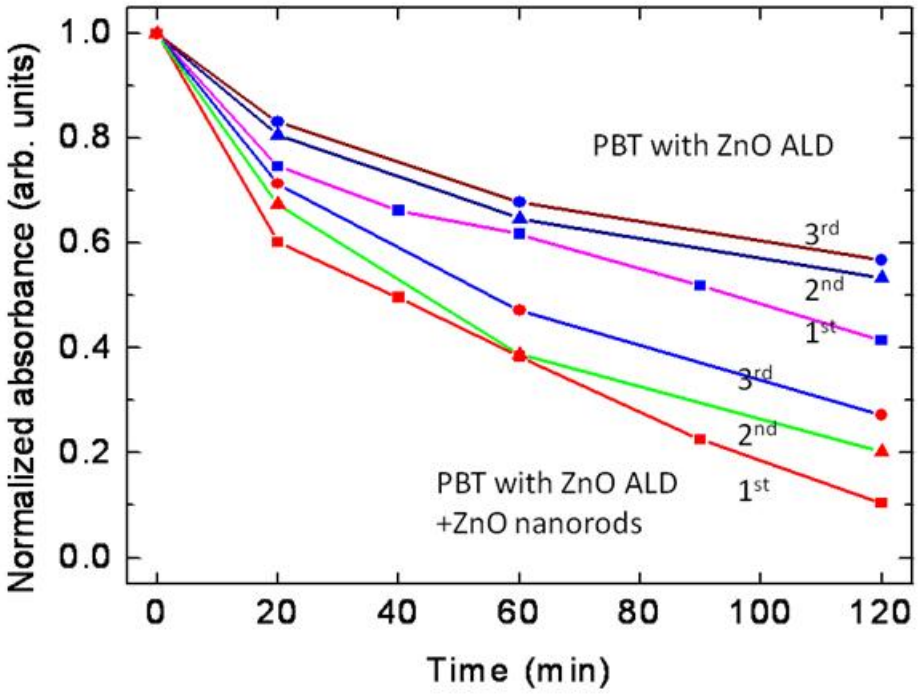


Figure 6.6. Reusability of ZnO treated PBT fiber mat for photocatalytic dye degradation. The PBT fiber mats with ZnO treatment showed repeatable photocatalytic activity. However, small decreases of efficiency were observed for both ZnO ALD coated and ZnO ALD/nanorods coated samples in three consecutive tests.

References

1 M. Law; L. E. Greene; J. C. Johnson; R. Saykally; P. D. Yang; Nanowire dye-sensitized solar cells, *Nature Materials,* **2005**. *4*, 455.

2 S. Liang; H. Sheng; Y. Liu; Z. Huo; Y. Lu; H. Shen; ZnO Schottky ultraviolet photodetectors, *Journal of Crystal Growth,* **2001**. *225*, 110.

3 H. Ohta; K. Kawamura; M. Orita; M. Hirano; N. Sarukura; H. Hosono; Current injection emission from a transparent p-n junction composed of p-SrCu2O2/n-ZnO, *Applied Physics Letters,* **2000**. *77*, 475.

4 J. Zhang; L. D. Sun; H. Y. Pan; C. S. Liao; C. H. Yan; ZnO nanowires fabricated by a convenient route, *New Journal of Chemistry,* **2002**. *26*, 33.

5 N. Daneshvar; D. Salari; A. R. Khataee; Photocatalytic degradation of azo dye acid red 14 in water on ZnO as an alternative catalyst to TiO2, *Journal of Photochemistry and Photobiology a-Chemistry,* **2004**. *162*, 317.

6 B. Pal; M. Sharon; Enhanced photocatalytic activity of highly porous ZnO thin films prepared by sol-gel process, *Materials Chemistry and Physics,* **2002**. *76*, 82.

7 C. S. Turchi; D. F. Ollis; Photocatalytic degradation of organic-water contaminants - Mechanisms involving hydroxyl radical attack, *Journal of Catalysis,* **1990**. *122*, 178.

8 L. E. Greene; M. Law; J. Goldberger; F. Kim; J. C. Johnson; Y. F. Zhang; R. J. Saykally; P. D. Yang; Low-temperature wafer-scale production of ZnO nanowire arrays, *Angewandte Chemie-International Edition,* **2003**. *42*, 3031.

9 Y. Li; G. W. Meng; L. D. Zhang; F. Phillipp; Ordered semiconductor ZnO nanowire arrays and their photoluminescence properties, *Applied Physics Letters,* **2000**. *76*, 2011.

10 J. J. Wu; S. C. Liu; Low-temperature growth of well-aligned ZnO nanorods by chemical vapor deposition, *Advanced Materials (Weinheim, Germany),* **2002**. *14*, 215.

11 L. F. Xu; Q. Liao; J. P. Zhang; X. C. Ai; D. S. Xu; Single-crystalline ZnO nanotube arrays on conductive glass substrates by selective dissolution of electrodeposited ZnO nanorods, *Journal of Physical Chemistry C,* **2007**. *111*, 4549.

12 M. S. Arnold; P. Avouris; Z. W. Pan; Z. L. Wang; Field-effect transistors based on single semiconducting oxide nanobelts, *Journal of Physical Chemistry B,* **2003**. *107*, 659.

13 Z. R. Dai; Z. W. Pan; Z. L. Wang; Novel nanostructures of functional oxides synthesized by thermal evaporation, *Advanced Functional Materials,* **2003**. *13*, 9.

14 Y. H. Tong; Y. C. Liu; C. L. Shao; R. X. Mu; Structural and optical properties of ZnO nanotower bundles, *Applied Physics Letters,* **2006**. *88*, 123111.

15 L. Vayssieres; K. Keis; S. E. Lindquist; A. Hagfeldt; Purpose-built anisotropic metal oxide material: 3D highly oriented microrod array of ZnO, *Journal of Physical Chemistry B,* **2001**. *105*, 3350.

16 J.-S. Na; B. Gong; G. Scarel; G. N. Parsons; Surface Polarity Shielding and Hierarchical ZnO Nano-Architecture Engineering using Sequential Hydrothermal Crystal Synthesis and Thin Film Atomic Layer Deposition, *ACS Nano,* **2009**. *3*, 3191.

17 E. Santala; M. Kemell; M. Leskela; M. Ritala; The preparation of reusable magnetic and photocatalytic composite nanofibers by electrospinning and atomic layer deposition, *Nanotechnology,* **2009**. *20*, 035602.

18 X. Y. Zhang; J. Y. Dai; H. C. Ong; N. Wang; H. L. W. Chan; C. L. Choy; Hydrothermal synthesis of oriented ZnO nanobelts and their temperature dependent photoluminescence, *Chemical Physics Letters,* **2004**. *393*, 17.

19 R. B. M. Cross; M. M. De Souza; E. M. S. Narayanan; A low temperature combination method for the production of ZnO nanowires, *Nanotechnology,* **2005**. *16*, 2188.

20 G. K. Hyde; K. J. Park; S. M. Stewart; J. P. Hinestroza; G. N. Parsons; Atomic layer deposition of Conformal inorganic nanoscale coatings on three-dimensional natural fiber systems: Effect of surface topology on film growth characteristics, *Langmuir,* **2007**. *23*, 9844.

21 G. K. Hyde; G. Scarel; J. C. Spagnola; Q. Peng; K. Lee; B. Gong; K. G. Roberts; K. M. Roth; C. A. Hanson; C. K. Devine; S. M. Stewart; D. Hojo; J. S. Na; J. S. Jur; G. N. Parsons; Atomic Layer Deposition and Abrupt Wetting Transitions on Nonwoven Polypropylene and Woven Cotton Fabrics, *Langmuir*, **2010**. *26*, 2550.

22 M. Kemell; V. Pore; M. Ritala; M. Leskela; M. Linden; Atomic Layer Deposition in Nanometer-Level Replication of Cellulosic Substances and Preparation of Photocatalytic TiO2/Cellulose Composites, *Journal of the American Chemical Society*, **2005**. *127*, 14178.

23 Q. Peng; X. Y. Sun; J. C. Spagnola; G. K. Hyde; R. J. Spontak; G. N. Parsons; Atomic layer deposition on electrospun polymer fibers as a direct route to Al2O3 microtubes with precise wall thickness control, *Nano Letters,* **2007**. *7*, 719.

24 M. Kemell; V. Pore; M. Ritala; M. Leskela; Ir/Oxide/Cellulose Composites for Catalytic Purposes Prepared by Atomic Layer Deposition, *Chemical Vapor Deposition,* **2006**. *12*, 419.

25 S. M. Lee; G. Grass; G. M. Kim; C. Dresbach; L. B. Zhang; U. Gosele; M. Knez; Low-temperature ZnO atomic layer deposition on biotemplates: flexible photocatalytic ZnO structures from eggshell membranes, *Physical Chemistry Chemical Physics,* **2009**. *11*, 3608.

26 S. M. Lee; E. Pippel; U. Gosele; C. Dresbach; Y. Qin; C. V. Chandran; T. Brauniger; G. Hause; M. Knez; Greatly Increased Toughness of Infiltrated Spider Silk, *Science,* **2009**. *324*, 488.

27 B. Gong; Q. Peng; J. S. Jur; C. K. Devine; K. Lee; G. N. Parsons; Sequential Vapor Infiltration of Metal Oxides into Sacrificial Polyester Fibers: Shape Replication and Controlled Porosity of Microporous/Mesoporous Oxide Monoliths, *Chemistry of Materials,* **2011**. *23*, 3476.

28 B. Gong; Q. Peng; G. N. Parsons; Conformal Organic−Inorganic Hybrid Network Polymer Thin Films by Molecular Layer Deposition using Trimethylaluminum and Glycidol, *The Journal of Physical Chemistry B,* **2011**. *115*, 5930.

29 C. Hariharan; Photocatalytic degradation of organic contaminants in water by ZnO nanoparticles: Revisited, *Applied Catalysis A: General,* **2006**. *304*, 55.

30 P. Gijsman; G. Meijers; G. Vitarelli; Comparison of the UV-degradation chemistry of polypropylene, polyethylene, polyamide 6 and polybutylene terephthalate, *Polymer Degradation and Stability*, **1999**. *65*, 433.

CHAPTER 7 is a reprint of a manuscript in preparation

CHAPTER 7. Layer by Layer Growth of HKUST-1 on Nonwoven Polypropylene Fiber Mat

Bo Gong and *Gregory N. Parsons

Department of Chemical and Biomolecular Engineering,

North Carolina State University,

Raleigh NC 27695, USA

***Corresponding author:** parsons@ncsu.edu

Abstract

Metal organic frameworks (MOFs) are a new generation of porous material. They are prepared by self-assembled of metal ions with organic bridging ligands. A range of promising properties have been reported for this new material, such as ultrahigh specific surface area, well defined pore structure, and the ability to control the surface chemistry. These properties enabled lots of advanced applications of the MOFs, such as gas storage, chemical sensing, separation, and catalyst. However, there is little report regarding the attachment of MOFs on high aspect ratio polymer systems, which would extend the applications of MOFs. In this work, we reported a promising route for the attachment of MOFs on polymer fiber mat substrates. Firstly, we used atomic layer deposition to coat the polymer substrates with a thin layer of Al_2O_3. This would give the surface a well defined Al-OH chemistry, which enabled the further attachment of MOFs by the Layer by Layer (LBL) technique. The X-ray diffraction was employed to confirm the crystal structure of the attached MOFs; SEM was used to monitor the morphology change during the attachment. The nitrogen adsorption/ desorption analysis (BET) was used to determine the surface area of the coated materials.

7.1. Introduction

Porous materials drew lots of research attentions due to their unique properties, and they have found a range of applications in our daily life and industry productions. [1-4] People use them for catalyst, energy storage materials, gas separation membranes, sensing materials, drug delivery carriers, and low-k dielectrics. For the last several decades, aluminosilicate zeolites were the key porous materials studied.[5] Because they have high surface area, good thermal stability, and well controlled porous structure. In the last decade, new generations of porous materials were developed. Such as metal organic frameworks (MOFs),[6,7] coordinate organic frameworks (COFs),[8,9] and porous polymers.[10] In these materials, MOFs attracted most researchers. A range of promising properties have been reported for this new material, such as ultrahigh specific surface area, well defined pore structure, and the ability to control the surface chemistry.[11-18] These properties enabled lots of advanced applications of the MOFs, such as gas storage, chemical sensing, separation, and catalyst.[14,16,17]

MOFs were conventionally synthesized by solvent thermal batch process, which result in the formation of MOFs in free standing particle morphology. However, more and more chemical sensing and adsorption applications required the attachment of MOFs on supporting materials, such as flexible polymer fiber mat.[19,20] Some developments of attachment of MOF on polymer fibers have been reported. Küsgen et al. reported the direct hydrothermal growth of MOFs on pulp fibers.[19] Rose et al. recently demonstrated a route to polymer fibers by electro-spin MOFs particles with the polymer solution.[20] However, these methods did not provide a very good control of MOFs attachment and the mechanical properties of the polymer substrates dramatically affected by these attaching processes.[19,20] A new method

developed by Shekhah, O et al. enabled the well controlled surface attachment of MOFs, which could enable the conformal attachment with precise thickness control.[21-26]

The surface chemistry of the supporting materials is critical for the formation of MOFs on surface. Previous research demonstrated that the NH_2 or COOH groups would help the nucleation on the surface, and affect the crystal growth orientation.[22,24-26] Other report showed that certain metal oxide or nitride surface could also enable the surface attachment of MOFs.[27] Previous research also showed Al_2O_3 coating on Si wafer could help with the nucleation during hydrothermal growth of MOF-5.[28]

Atomic layer deposition (ALD) is an ideal technique for the formation of conformal metal oxide surface. It is a chemical vapor phase deposition technique, which employed self-limiting surface reaction.[29,30] It could coat complex 3D substrates uniformly, and control the coating thickness precisely.[29,30] ALD is an ideal technique for surface functionalization of high aspect ratio substrates, such as polymer fiber mat. This has been demonstrated by the previous research in our group.[31-34] In this paper, we demonstrated a method for the surface attachment of MOFs on Polypropylene fiber mat by using Al_2O_3 ALD and LBL growth of MOFs. The metal organic framework HKUST-1 [Copper benzene-1,3,5-tricarboxylate $Cu_3(BTC)_2$] will be used as the demonstration material in this study.

7.2. Experimental

Chemicals

All chemicals were used as received without further purification. Copper (II) nitrate trihydrate [99%, $Cu(NO_3)_2 \cdot 3H_2O$], copper (II) acetate [98%, $Cu(CO_2CH_3)_2$], benzene tri-carboxylic acid (99%, BTC), (3-Aminopropyl)triethoxy silane (99% APTES), and ethanol

were purchased from Aldrich. Tri-methyl aluminum (98% TMA) was purchased from Strem Chemicals. A 4772-T-SS non-stirred pressured vessel from Parr Instrument was used for the hydrothermal growth. Non-woven polypropylene (PP) fiber mat (0.5 mm thick, with fiber diameter in the range of ~1-5 μm) was acquired from Nonwovens Cooperative Research Center (NCRC), North Carolina State University.

Al_2O_3 Seed Layer Deposition by ALD

Atomic layer deposition of Al_2O_3 was conducted in a homemade hot wall viscous flow vacuum reactor.[35] The ALD process was carried out at the pressure of ~1 Torr and the deposition temperature was kept at 60 °C. In a typical deposition cycle, the substrate was exposed to 2s of tri-methyl aluminum (TMA) and water vapor alternatively, with a 60s N_2 purge step in between. 50 deposition cycles was used to form the Al_2O_3 seed layer on PP fiber mat and Si wafers. The thickness of the Al_2O_3 coated on the Si wafer was measured by a J. A. Woollam alpha-SE elipsometry. For 50 deposition cycles at 60 °C, it builds up an Al_2O_3 layer approximately ~5 nm.

APTES Self-Assemble Layer Attachment

Some Al_2O_3 coated PP fiber mat were further treated with (3-Aminopropyl)triethoxy silane (APTES) before MOF attachment. The solution was prepared by disperse of 1gram of APTES in 100 gram of ethanol. The Al_2O_3 coated PP fiber mat was dipped into the solution for 12 hours at room temperature. After the treatment, PP fiber mat was removed from the APTES solution, and washed with ethanol thoroughly for 3 times before the further attachment of MOFs.

Layer by Layer Growth of HKUST-1

We attached the metal organic framework HKUST-1 [$Cu_3(btc)_2$] in a layer by layer (LBL) fashion.[21] The ALD seeded PP fiber mat was first dipped in a 1mM benzene tri-carboxylic acid (BTC) ethanol solution for 1 hour. After washed with ethanol for 5 mins, the PP fiber mat was then dipped in a 1mM copper acetate monohydrate [$Cu(CH_3COO)_2 \cdot H_2O$] ethanol solution for another 1 hour. Finally, the fiber mat was washed again with ethanol for 5 mins. This dip and wash process was considered as a growth cycle. Various MOF loading amount could be achieved by controlling the growth cycles.

Possibly, the BTC molecules were anchored to the Al_2O_3 seed layer by the covalent bond between the carboxyl groups on the BTC and the hydroxyls on the Al_2O_3. The residue carboxyl groups would react with Cu^{2+} during the next dipping. As the Cu^{2+} could coordinate with two carboxyl groups, thus the process cycle could continue in the following BTC deposition.[21,36]

Hydrothermal Growth of HKUST-1

Hydrothermal growth of HKUST-1 was conducted in a stainless pressured vessel. Firstly, 4mM of Benzene tri carboxylic acid (BTC) was dissolved in 24 ml of ethanol, and 7.2mM of copper nitrate trihydrate [$Cu(NO_3)_2 \cdot 3H_2O$] was dissolved in 24ml water. The two solutions were put together in the pressured vessel with the PP fiber samples. Then the pressured vessel was heated to 120 °C for 18 hours.[36] After cooled down, the sample was rinsed with ethanol for 3 times.

Materials Characterization

A FEI Phenom bench-top scanning electron microscope (SEM) was used to image the morphology of PP fiber mat with different MOFs coatings. 5-10 nm of Au-Pd was sputtered on the fiber samples before imaging.

XRD measurement was conducted on a Rigaku SmartLab X-ray diffraction tool with Cu Kα X-ray source.

Fourier transform infrared spectroscopy was used to monitor the LBL HKUST-1 growth on Si wafer. We used a Thermo Scientific Nicolet 6700 spectroscopy equipped with a KBr beam splitter and a Deuterated Triglycine Sulfate (DTGS) detector, which is capable of measuring the IR transmittance spectra in the mid-IR range ($4000cm^{-1}$ – $400cm^{-1}$)

A Quantachrome Autosorb-1C surface area and pore size analyzer was employed for the nitrogen adsorption/ desorption analysis. Before the measurement, the coated fiber was vacuum dried at 150°C for at least 4hours to remove water. Approximately 200 mg of sample was used for each measurement. BET surface area was calculated from the adsorption isotherm within relative pressure range of 0.05 - 0.35 P/P_0.

7.3. Experimental Results

The Fourier transform infrared (FTIR) spectra were collected from the LBL deposited HKUST-1 films on Al_2O_3 coated Si wafers. The symmetric (1645 and 1590 cm^{-1}) and asymmetric (1450 and 1370 cm^{-1}) stretching vibrations of carboxylate related absorbance was observed from the collected the spectrum,[37] which confirmed the chemical composition of the synthesized MOF. The carboxylate peak at ~1370 cm^{-1} was used as characterization absorbance to study the growth of HKUST-1 vs. deposition cycles. As shown in Figure 7.1, a

slow initial growth was found during the first 2 LBL growth cycles. After the initial stage, the linear increase of IR absorbance was observed with the increase of deposition cycles.

Optical images of HKUST-1 coated PP fiber mat were shown in Figure 7.2. Panel (a) shows the PP fiber mat with 10 LBL HKUST-1 with and without ALD pretreatment. The fiber mat on the left is the direct LBL growth of MOF on PP fiber mat. The mat on the right is the PP fiber mat pretreated with ALO, then coated with MOF by LBL technique. The pp fiber mat without ALD pretreatment showed almost no color change after LBL HKUST-1 growth. However, the fiber mat with Al_2O_3 ALD pretreatment showed the light green color, which is coming from the attached HKUST-1 crystals on the polymer surface. Panel (b) shows MOF coated PP fiber mat before vacuum dry in a glass tube. (c) MOF coated PP fiber mat after vacuum dry. After outgas, the color of the coated fiber changed from light green to dark blue, which is consistent with previous literature report.[7] The color change is attributed to the removing of Cu atoms coordinated water molecular.

To confirm the crystal structure of the coated MOFs, X-ray diffraction patterns were also collected from the PP fiber mat with LBL deposited HKUST-1. Figure 7.3(a) showed the XRD patterns collected from PP fiber mats with 10 cycles LBL deposited HKUST-1. Clear diffraction peaks from HKUST-1 was measured from PP fiber mat with Al_2O_3 seed layer. In contrary, very small peaks were collected from the PP fiber mat without the Al_2O_3 seed layer. The simulated XRD pattern from reported structure was also shown in Figure 7.3(b).[7] The diffraction peaks collected is matching the simulated XRD pattern, which confirmed we have made the HKUST-1.[7]

The BET surface area of the HKUST-1 crystals deposited by LBL approach on PP fiber mat was analyzed by N_2 adsorption/desorption method. PP fiber sample with Al_2O_3 seed layer was pre-weighed before the LBL attaching of HKUST-1. The weight of the HKUST-1 crystal attached could be calculated from the mass increase after the LBL growth and vacuum outgas (HKUST-1 absorbs ambient moisture). By measure the specific BET surface area of PP fiber mat and PP fiber mat with MOF, the specific BET surface area of HKUST-1 could be calculated.

Mass uptake and BET surface area data was summarized in Table 7.1. Without Al_2O_3 ALD treatment, very small mass uptake (~0.73 %) was measured after 20 LBL MOF growth on PP fiber mat. This implied that the Al_2O_3 ALD layer is serving as an important nucleation layer for the following MOF attachment. For the PP fiber mat with Al_2O_3 pretreatment and 20 LBL HKUST-1, the measured BET surface area is ~2.026 m^2/g. Considering the mass increase from the MOF coating is just ~5.52 %, we could calculate the specific BET surface area for the MOF coating, which equal to~15.34 m^2/g. The calculated specific surface area is much smaller than the reported HKUST-1 synthesized by hydrothermal approach.[7] This could because of the low process temperature of LBL technique, or there are trapped precursors in the pore structure. The APTES treatment of Al_2O_3 coated PP fiber mat could increase the LBL growth rate by a factor of ~2. We tried further treat of Al_2O_3 coated PP fiber mat with APTES solution. This treatment would introduce NH_2 amine groups on the surface, which reported would facilitate the nucleation of MOFs. After coating with 20 LBL MOF, the mass of the fiber mat increased by approximately ~10.26 % and the measure BET surface area is ~2.675 m^2/g. this is corresponding to the MOF has a specific BET surface area around

~16.16 m^2/g. The calculated specific surface area is very close to the LBL HKUST-1 attached on PP fiber mat with only Al_2O_3 coating. To increase the mass uptake of MOF, we also tested the a LBL and hydrothermal hybrid growth sequence for the $Cu_3(BTC)_2$ attachment. After we treated the Al_2O_3 coated PP with 10 LBL of HKUST-1, we did a hydrothermal growth on the treated fiber mat. The mass uptake of ~ 76.75 % was measured. The BET surface area of ~96.06 m^2/g was measured for the sample. The calculated specific BET surface area for the MOF coating is approximately ~219.54m^2/g. We also tried the direct hydrothermal method on the Al_2O_3 coated PP fiber mat. Large mass uptake (~92.46 %) was measured after hydrothermal growth. The calculated specific BET Surface area is ~709.8 m^2/g. It is very close to the reported specific BET surface area ~692m^2/g.[7]

The morphology of the MOF coated PP Fiber mat were monitored by the SEM, and displayed in Figure 7.4. Panel (a) showed the SEM image collected from untreated PP fiber mat. Smooth nonwoven PP fiber mat with diameter range from 1-5 μm were observed. (b) Al_2O_3 coated PP fiber mat with 20 LBL HKUST-1. We could clearly see the small HKUST-1 particles attached on the polymer surface. (c) APTES treated PP fiber mat with ALO, and 20 LBL HKUST-1. With APTES treatment, we found we were able to get continuous HKUST-1 coatings on the PP fiber surface. The SEM image shows the relative smooth surface after 20 LBL MOF attachment. (d) Direct hydrothermal growth of HKUST in ALO coated PP fiber mat. The direct hydrothermal growth will lead to the formation of large HKUST-1 crystals in the voids of the polymer fiber mat.

7.4. Conclusions

Ultra-thin film of Al_2O_3 deposited by ALD on inert PP fiber mat proved to be an ideal nucleation layer for the subsequent Layer by Layer growth of HKUST-1 metal organic frameworks. The FTIR analysis of LBL growth of MOF on Al_2O_3 ALD coated Si wafer demonstrated a linear growth of HKUST-1 vs. number of LBL cycles. The XRD patterns collected from the MOFs coated PP fiber mat confirmed that the crystal we attached is HKUST-1, and the Al_2O_3 nucleation layer is critical for this LBL attachment of MOFs. Interestingly, we found that the measured BET surface area for the HKUST-1 crystal grew by LBL technique is significantly smaller than the conventional hydrothermal method; this could due to the low processing temperature and the precursor residue in the pore structures. This is the first report using ALD technique for the formation of nucleation layers for LBL growth of HKUST-1 on polymer surface. This technique could be easily applied to other MOFs, and substrates, and enable a number of new applications.

Acknowlegment

We would like to thank our founding agency.

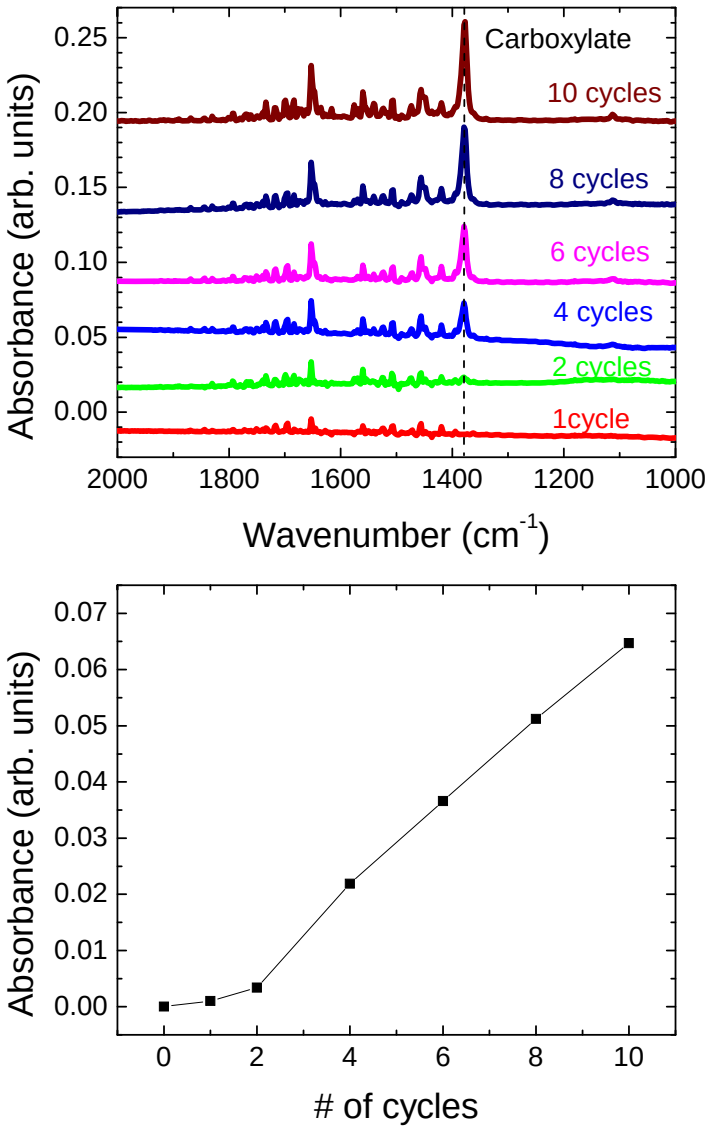


Figure 7.1. The Fourier transform infrared (FTIR) spectra collected from the HKUST-1 films on Al_2O_3 coated Si wafers. Slow growth was detected for the first 2 deposition cycles. Then the linear increase of IR absorbance vs. deposition cycles was observed.

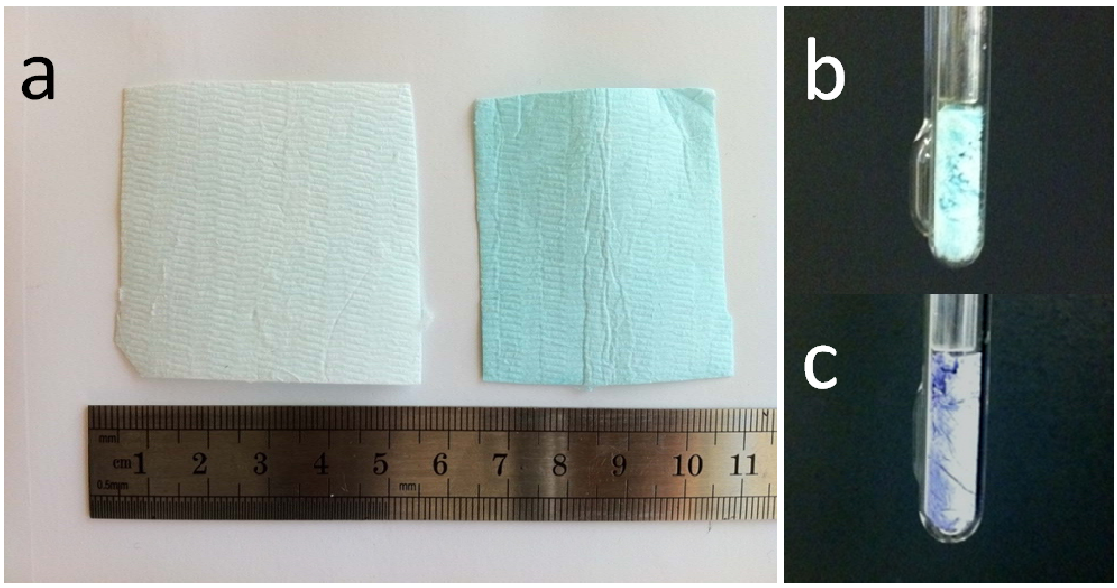


Figure 7.2. Optical images of HKUST-1 coated PP fiber mat. (a) The fiber mat on the left is the direct LBL growth of MOF on PP fiber mat. The mat on the right is the PP fiber mat pretreated with ALO, then coated with MOF by LBL technique. (b) MOF coated PP fiber mat before vacuum dry. (c) MOF coated PP fiber mat after vacuum dry.

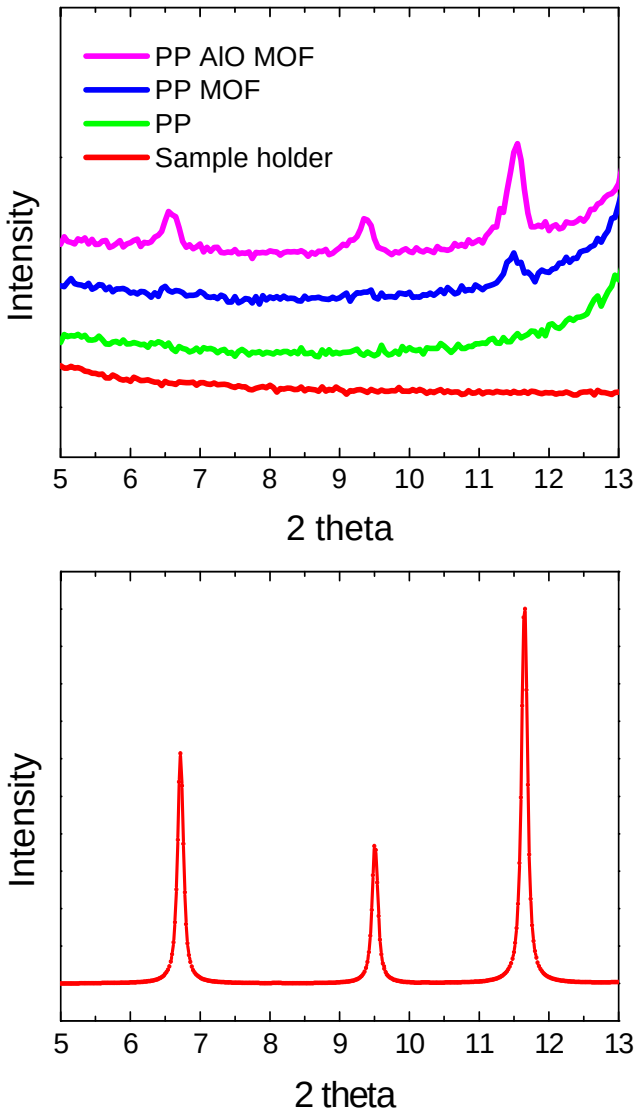


Figure 7.3. (a) The XRD patterns collected from the PP fiber mats. (b) The simulated XRD pattern from the reported HKUST-1 structure. Diffraction peaks from HKUST-1 was observed from PP fiber mat with Al_2O_3 seed layer. Very small diffraction peaks were measured from the PP fiber mat without the Al_2O_3 seed layer. The measured XRD pattern from the MOF coating match the reported HKUST-1 structure.

Table 7.1. Summary of mass increase from MOF coating and the measured BET surface area.

Samples	Mass increase from MOFs	Measure BET surface area	Caculated surface area for MOFs
20 LBL on PP	0.73%	-	-
20LBL on PP with ALO	5.52%	2.03 m^2/g	15.34 m^2/g
20LBL on APTES treated PP with ALO	10.26%	2.68 m^2/g	16.16 m^2/g
10LBL on PP with ALO + Hydrothermal growth	76.75%	96.06 m^2/g	219.54 m^2/g
PP with ALO + Hydrothermal growth	92.46%	341.00 m^2/g	709.80 m^2/g
PP with ALO	-	1.29 m^2/g	-

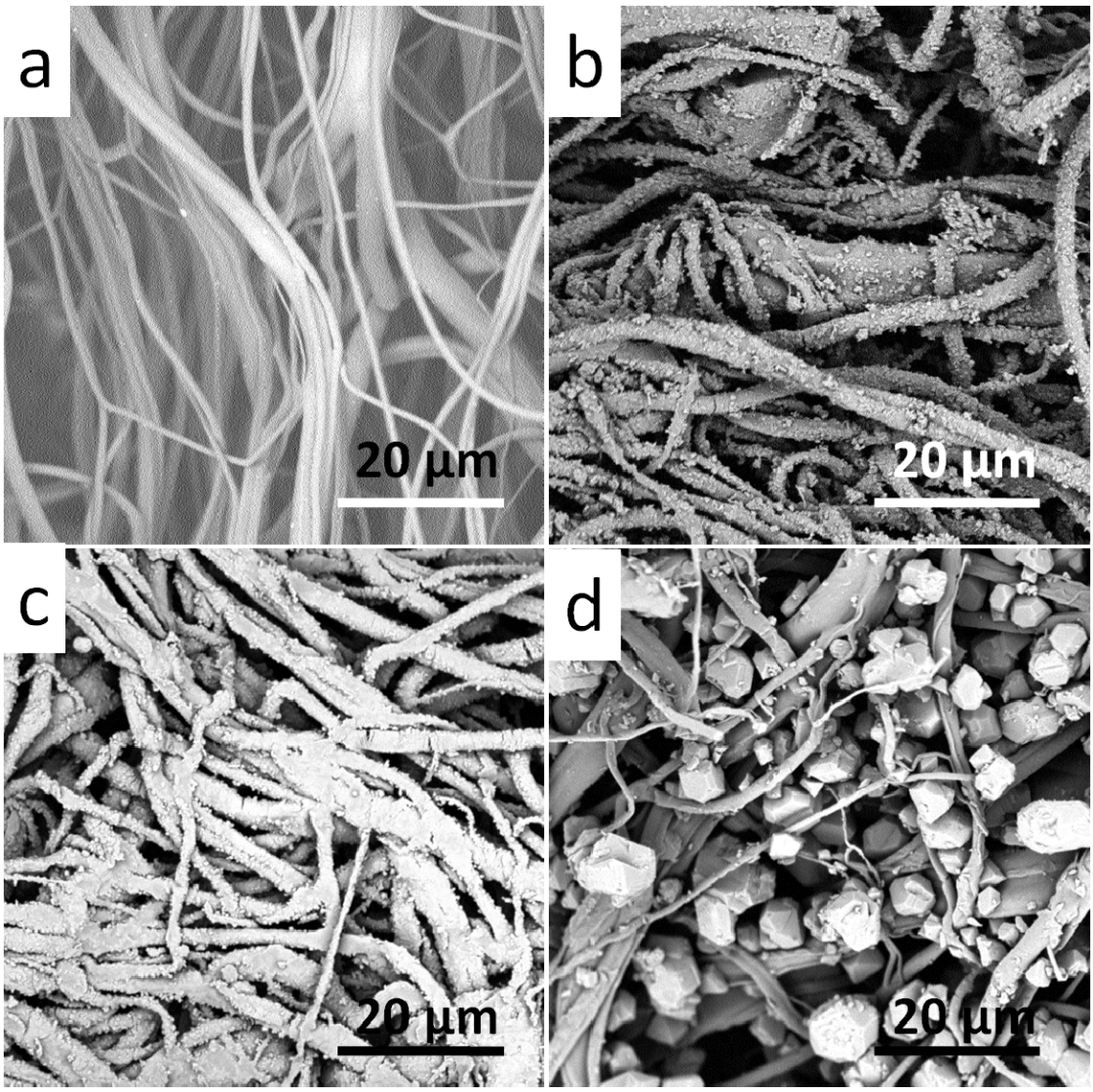


Figure 7.4. SEM images of PP fiber mat with different HKUST-1 coating. (a) untreated PP fiber mat. (b) ALO coated PP fiber mat with 20 LBL HKUST-1. (c) APTES treated PP fiber mat with ALO, and 20 LBL HKUST-1. (d) Direct hydrothermal growth of HKUST in ALO coated PP fiber mat.

References

1 M. Kruk; M. Jaroniec; C. H. Ko; R. Ryoo; Characterization of the porous structure of SBA-15, *Chemistry of Materials,* **2000**. *12*, 1961.

2 R. Ryoo; S. H. Joo; M. Kruk; M. Jaroniec; Ordered mesoporous carbons, *Advanced Materials,* **2001**. *13*, 677.

3 D. Y. Zhao; J. L. Feng; Q. S. Huo; N. Melosh; G. H. Fredrickson; B. F. Chmelka; G. D. Stucky; Triblock copolymer syntheses of mesoporous silica with periodic 50 to 300 angstrom pores, *Science,* **1998**. *279*, 548.

4 D. Y. Zhao; Q. S. Huo; J. L. Feng; B. F. Chmelka; G. D. Stucky; Nonionic triblock and star diblock copolymer and oligomeric surfactant syntheses of highly ordered, hydrothermally stable, mesoporous silica structures, *Journal of the American Chemical Society,* **1998**. *120*, 6024.

5 J. S. Beck; J. C. Vartuli; W. J. Roth; M. E. Leonowicz; C. T. Kresge; K. D. Schmitt; C. T. W. Chu; D. H. Olson; E. W. Sheppard; S. B. McCullen; J. B. Higgins; J. L. Schlenker; A new family of mesoporous molecular-sieves prepared with liquid-crystal templates, *Journal of the American Chemical Society,* **1992**. *114*, 10834.

6 S. L. James; Metal-organic frameworks, *Chemical Society Reviews,* **2003**. *32*, 276.

7 S. S. Y. Chui; S. M. F. Lo; J. P. H. Charmant; A. G. Orpen; I. D. Williams; A chemically functionalizable nanoporous material Cu-3(TMA)(2)(H2O)(3) (n), *Science,* **1999**. *283*, 1148.

8 A. P. Cote; A. I. Benin; N. W. Ockwig; M. O'Keeffe; A. J. Matzger; O. M. Yaghi; Porous, crystalline, covalent organic frameworks, *Science,* **2005**. *310*, 1166.

9 H. M. El-Kaderi; J. R. Hunt; J. L. Mendoza-Cortes; A. P. Cote; R. E. Taylor; M. O'Keeffe; O. M. Yaghi; Designed synthesis of 3D covalent organic frameworks, *Science,* **2007**. *316*, 268.

10 S. Kitagawa; R. Kitaura; S. Noro; Functional porous coordination polymers, *Angewandte Chemie-International Edition,* **2004**. *43*, 2334.

11 S. R. Batten; R. Robson; Interpenetrating nets: Ordered, periodic entanglement, *Angewandte Chemie-International Edition,* **1998**. *37*, 1460.

12 M. Eddaoudi; J. Kim; N. Rosi; D. Vodak; J. Wachter; M. O'Keeffe; O. M. Yaghi; Systematic design of pore size and functionality in isoreticular MOFs and their application in methane storage, *Science,* **2002**. *295*, 469.

13 M. Eddaoudi; D. B. Moler; H. L. Li; B. L. Chen; T. M. Reineke; M. O'Keeffe; O. M. Yaghi; Modular chemistry: Secondary building units as a basis for the design of highly porous and robust metal-organic carboxylate frameworks, *Accounts of Chemical Research,* **2001**. *34*, 319.

14 C. Janiak; Engineering coordination polymers towards applications, *Dalton Transactions,* **2003**. 2781.

15 H. Li; M. Eddaoudi; M. O'Keeffe; O. M. Yaghi; Design and synthesis of an exceptionally stable and highly porous metal-organic framework, *Nature,* **1999**. *402*, 276.

16 N. L. Rosi; J. Eckert; M. Eddaoudi; D. T. Vodak; J. Kim; M. O'Keeffe; O. M. Yaghi; Hydrogen storage in microporous metal-organic frameworks, *Science,* **2003**. *300*, 1127.

17 J. S. Seo; D. Whang; H. Lee; S. I. Jun; J. Oh; Y. J. Jeon; K. Kim; A homochiral metal-organic porous material for enantioselective separation and catalysis, *Nature,* **2000**. *404*, 982.

18 O. M. Yaghi; M. O'Keeffe; N. W. Ockwig; H. K. Chae; M. Eddaoudi; J. Kim; Reticular synthesis and the design of new materials, *Nature,* **2003**. *423*, 705.

19 P. Küsgens; S. Siegle; S. Kaskel; Crystal Growth of the Metal—Organic Framework Cu3(BTC)2 on the Surface of Pulp Fibers, *Advanced Engineering Materials,* **2009**. *11*, 93.

20 M. Rose; B. Böhringer; M. Jolly; R. Fischer; S. Kaskel; MOF Processing by Electrospinning for Functional Textiles, *Advanced Engineering Materials,* **2011**. *13*, 356.

21 O. Shekhah; H. Wang; S. Kowarik; F. Schreiber; M. Paulus; M. Tolan; C. Sternemann; F. Evers; D. Zacher; R. A. Fischer; C. Woll; Step-by-step route for the synthesis of metal-organic frameworks, *Journal of the American Chemical Society,* **2007**. *129*, 15118.

22 C. Munuera; O. Shekhah; H. Wang; C. Woell; C. Ocal; The controlled growth of oriented metal-organic frameworks on functionalized surfaces as followed by scanning force microscopy, *Physical Chemistry Chemical Physics,* **2008**. *10*, 7257.

23 O. Shekhah; J. Liu; R. A. Fischer; C. Woell; MOF thin films: existing and future applications, *Chemical Society Reviews,* **2011**. *40*, 1081.

24 O. Shekhah; H. Wang; M. Paradinas; C. Ocal; B. Schuepbach; A. Terfort; D. Zacher; R. A. Fischer; C. Woell; Controlling interpenetration in metal-organic frameworks by liquid-phase epitaxy, *Nature Materials,* **2009**. *8*, 481.

25 O. Shekhah; H. Wang; T. Strunskus; P. Cyganik; D. Zacher; R. Fischer; C. Woell; Layer-by-layer growth of oriented metal organic polymers on a functionalized organic surface, *Langmuir,* **2007**. *23*, 7440.

26 O. Shekhah; H. Wang; D. Zacher; R. A. Fischer; C. Woell; Growth Mechanism of Metal-Organic Frameworks: Insights into the Nucleation by Employing a Step-by-Step Route, *Angewandte Chemie-International Edition,* **2009**. *48*, 5038.

27 K. Yusenko; M. Meilikhov; D. Zacher; F. Wieland; C. Sternemann; X. Stammer; T. Ladnorg; C. Woell; R. A. Fischer; Step-by-step growth of highly oriented and continuous seeding layers of Cu(2)(ndc)(2)(dabco) on bare oxide and nitride substrates, *Crystengcomm,* **2010**. *12*, 2086.

28 S. Hermes; D. Zacher; A. Baunemann; C. Woell; R. A. Fischer; Selective growth and MOCVD loading of small single crystals of MOF-5 at alumina and silica surfaces modified with organic self-assembled monolayers, *Chemistry of Materials,* **2007**. *19*, 2168.

29 M. Leskela; M. Ritala; Atomic layer deposition (ALD): from precursors to thin film structures, *Thin Solid Films,* **2002**. *409*, 138.

30 R. L. Puurunen; Surface chemistry of atomic layer deposition: A case study for the trimethylaluminum/water process, *Journal of Applied Physics,* **2005**. *97*,

31 Q. Peng; X.-Y. Sun; J. C. Spagnola; G. K. Hyde; R. J. Spontak; G. N. Parsons; Atomic layer deposition on electrospun polymer fibers as a direct route to Al2O3 microtubes with precise wall thickness control, *Nano Letters,* **2007**. *7*, 719.

32 G. K. Hyde; G. Scarel; J. C. Spagnola; Q. Peng; K. Lee; B. Gong; K. G. Roberts; K. M. Roth; C. A. Hanson; C. K. Devine; S. M. Stewart; D. Hojo; J. S. Na; J. S. Jur; G. N. Parsons; Atomic Layer Deposition and Abrupt Wetting Transitions on Nonwoven Polypropylene and Woven Cotton Fabrics, *Langmuir,* **2010**. *26*, 2550.

33 B. Gong; Q. Peng; G. N. Parsons; Conformal Organic - Inorganic Hybrid Network Polymer Thin Films by Molecular Layer Deposition using Trimethylaluminum and Glycidol, *Journal of Physical Chemistry B,* **2011**. *115*, 5930.

34 B. Gong; Q. Peng; J. S. Na; G. N. Parsons; Highly active photocatalytic ZnO nanocrystalline rods supported on polymer fiber mats: Synthesis using atomic layer deposition and hydrothermal crystal growth, *Applied Catalysis a-General,* **2011**. *407*, 211.

35 Q. Peng; B. Gong; R. M. VanGundy; G. N. Parsons; "Zincone" Zinc Oxide-Organic Hybrid Polymer Thin Films Formed by Molecular Layer Deposition, *Chemistry of Materials,* **2009**. *21*, 820.

36 J. Nan; X. Dong; W. Wang; W. Jin; N. Xu; Step-by-Step Seeding Procedure for Preparing HKUST-1 Membrane on Porous α-Alumina Support, *Langmuir,* **2011**. *27*, 4309.

37 C. Petit; B. Mendoza; T. J. Bandosz; Hydrogen Sulfide Adsorption on MOFs and MOF/Graphite Oxide Composites, *ChemPhysChem,* **2010**. *11*, 3678.

CHAPTER 8 is a reprint of a manuscript in preparation.

CHAPTER 8. Atomic Layer Deposition of Aluminum Oxide on Metal Organic Framework $Cu_3(BTC)_2$

Bo Gong and Gregory N. Parsons

Department of Chemical and Biomolecular Engineering,

North Carolina State University, Raleigh, NC 27695

Corresponding author: Parsons@ncsu.edu

Abstract

Metal organic frameworks (MOFs) have a number of superior properties compare to pure inorganic porous materials, such as greater specific surface area, well-controlled pore structures, and custom-defined surface chemistry. These characteristics enabled many advanced applications of the MOFs. Many approaches have been developed to further adjust the pore structures and modify the surface chemistry of MOFs. Atomic layer deposition (ALD) is an ideal approach for the conformal thin film coating on porous materials. It is capable of fine tune the pore size and surface chemistry of the porous materials. In this work, we studied the ALD of aluminum oxide on MOF $Cu_3(BTC)_2$. In-situ QCM and FTIR were employed to study the ALD growth on the MOF. We also studied the microgravity moisture sensing by using the MOF. The sensitivity of the system could be fine tuned by ALD aluminum oxide.

8.1. Introduction

Metal organic frameworks (MOFs) are new emerging porous materials with advanced properties. Compare to pure inorganic porous materials, such as zeolite, MOFs have high specific surface area, regular pore structures and custom-defined surface chemistry.[1-4] These properties make MOFs find lots of applications in catalyst, gas separation, energy storage, and chemical sensing.[1,5,6]

In the last decade, a large number of MOFs has been developed and synthesized. In a typically MOF synthesis, metal centers and carboxylic acid linkers were self-assembled into ordered open frameworks. By selecting the different metal ions and organic ligands, MOFs with different structure and properties could be prepared. For example, metal ions with different coordination preference could induce the different structures by determine how many organic linker could connect to the metal center. A great number of structure can be synthesized by employing different metal ions and organic linkers.[5] Moreover, desired function groups can be easily incorporated in to the MOFs by selecting the organic linkers.

Another approach for MOFs with novel functionalities is to decorate MOFs with infiltration method. S. Kaskel recently demonstrated the decorating of MOF-5 with Pd nanoparticles by liquid phase infiltration of [$Pd(acac)_2$] and subsequent thermally activated hydrogenolysis of the imbedded precursor.[7] Another method is solvent free gas-phase infiltration with metal organic precurosor developed by R. A. Fischer. A range of metal and metal oxide has been imbedded into the MOFs by this technique. For example, Cu particles have been loaded into MOF-5 and used as catalyst for CO and water methanol synthesis.[8,9]

The loading of MOFs with inorganic nano-materials enabled lots of new applications in catalyst, sensing.[8-11]

Atomic layer deposition (ALD) is a vapor phase thin film deposition techniques, based on sequential self-limiting surface reactions.[12,13] It is capable of deposition thin films uniformly with atomic scale thickness control. It is also capable of coating complex 3D substrates with high aspect ratio.[14-16] These characteristics of ALD make it an ideal technique for the functionalization of MOFs.

In this paper, we studied the Al_2O_3 ALD growth from trimethyl aluminum/water on HKUST-1 or $Cu_3(BTC)_2$, which is a well studied MOF will good stability.[3] The MOF is also well known for its reversible binding of water molecules to the copper coordinate center.[17] Base on this reversible binding behavior, a micro gravity sensor was assembled from the $Cu_3(BTC)_2$, and it has been demonstrated for moisture sensing. ALD technique was used to fine tune the sensitivity of the sensor.

8.2. Experimental

Chemicals and Materials

All chemicals were used as received without further purification. Copper nitrate tri-hydrate (99%, $Cu(NO_3)_2 \cdot 3H_2O$), benzene tricarboxylic acid (99%, BTC) and anhydrous ethanol are purchased from Aldrich. Trimethyl aluminum (98%, TMA) was purchased from Strem Chemicals. Unpolished QCM crystals were purchased from Inficon. The 4772-T-SS non-stirred autoclave was purchased from Parr Instrument.

Hydrothermal Synthesis of $Cu_3(BTC)_2$

4 mmol of bebzene tricarboxylic acid (BTC) was first mixed with 24 ml of anhydrous ethanol. 7.2 mmol of copper nitrate trihydrate ($Cu(NO_3)_2 \cdot 3H_2O$) was dissolved in 24 ml of DI water. The two solutions were stirred separately by glass rods until the chemicals fully dissolved. The solutions were then mixed together and transferred into a Teflon lined autoclave, and heated in oven to 120 °C for 18 hours. After cooled down at room temperature, the formed blue crystals were collected by using a PP fiber mat as filter. The collected crystals were then rinsed thoroughly with ethanol for 3 times.

Material Characterizations

$Cu_3(BTC)_2$ crystals were placed on a microscope glass slide. The optical images were collected using an Olympus BX60 optical microscopy. Scanning electron microscope images of $Cu_3(BTC)_2$ crystals were collected from a FEI Phenom bench-top SEM.

A Quantachrome autosorb-1C surface area and pore size analyzer was employed for the nitrogen adsorption/ desorption analysis. Before the measurement, the $Cu_3(BTC)_2$ particles were vacuum dried at 150 °C for at least 4 hours to remove adsorbed moisture. Approximately 100 mg of sample was loaded for each measurement. BET surface area was calculated from the adsorption isotherm within relative pressure range of 0.05 - 0.35 P/P_0.

The X-ray diffraction patterns of $Cu_3(BTC)_2$ was collected from a Ragaku SmartLab XRD. The XRD tool was equipped with a Cu Kα X-ray source, which produced X-ray with wavelength of ~0.1541 nm. The 2θ diffraction patterns were collected from 5 to 25 degrees. The reported XRD pattern of $Cu_3(BTC)_2$ was simulated using Mercury software. The structure file was acquired from reported literature.[3]

Atomic Layer Deposition Tools and In-situ QCM and FTIR Setups

The ALD reactor with QCM in-situ analysis ability was used for the experiment, and previous described in detail.[18,19] In a typical ALD cycle, TMA and water were pulsed for 2 seconds, with 60 seconds Ar purge in between (2/60/2/60 TMA/Ar/water/Ar). Pressure increase for TMA and water is ~ 200 mTorr during pulse. In the QCM setup, the QCM crystal were held in the reactor chamber during the ALD growth. The back side of the QCM crystal was purged with Ar carrier gas to prevent the deposition on the back side of the crystal. $Cu_3(BTC)_2$ crystals were attached on the QCM crystal by the drop cast. Crystals were first dispersed in ethanol solutions (1% wt). 1 drop (~1/200 ml) of the ethanol solution was then applied on the QCM crystal. The mass loading of $Cu_3(BTC)_2$ is ~ 40 μg.

The in-situ FTIR analysis was conducted in another reactor.[19] $Cu_3(BTC)_2$ crystals were dispersed in ethanol solutions ~10% wt, 2 - 3 drops of the solution was then applied on the IR Si wafer (~ 2 × 3cm). Approximately 1mg of $Cu_3(BTC)_2$ was attached on the IR Si. During the in-situ FTIR experiments, a typical TMA/water deposition cycle involved TMA and water exposure for 5 seconds, with 120 seconds Ar purge and 150 s IR data collection period after each vapor exposure. The MOF coated IR Si was hold vertically in the IR beam during in-situ FTIR experiment. Before each precursor exposure, a reference spectrum was collected. The differential spectra were displayed to stress the chemistry change after each precursor exposure.

Microgravity Moisture Sensing by QCM

The microgravity moisture sensing was conducted in the ALD reactor by using QCM analysis. The MOF loaded QCM crystal was first exposed to 2 seconds of water exposure, and then purged with Ar for 60 seconds (2/60 water/Ar). The reactor was kept at 90 °C, and ~

200 mTorr pressure increase was monitored during water pulse. To study the effect of ALD coating on the MOF, the $Cu_3(BTC)_2$ coated QCM crystal was further treated with Al_2O_3 ALD coating. The microgravity moisture sensing experiment was also performed on the ALD treated MOF.

8.3. Results and Discussion

Characterization of Synthesized $Cu_3(BTC)_2$

The macro morphology of synthesized $Cu_3(BTC)_2$ was summarized in Figure 8.1. The molecular structure of the $Cu_3(BTC)_2$ crystal was displayed in panel(a). Panle (b) showed the optical images collected from the MOF crystals dispersed on a glass slide. Green crystals were observed. Panel (c) displayed SEM images of the MOF particles. Square bipyramid crystal morphology was observed, consistent with previous literature report.[3]

Figure 8.2. showed the nitrogen adsorption/desorption analysis results collected from $Cu_3(BTC)_2$ crystals. Figure 8.2(a) showed the nitrogen adsorption/desorption isotherm. The shape of the curve is corresponding to isotherm type I, which is corresponding to microporous solids with small external surfaces.[20] Figure 8.2(b) displayed the pore size distribution calculated from the nitrogen adsorption/desorption isotherm by the DFT method using As1win software package. The mode pore size for the synthesized crystals was ~ 2 nm. The calculated BET surface area is approximately ~528 m^2/g. The $Cu_3(BTC)_2$ MOF we synthesized has similar surface area and pore size distribution compare with literature report.[3]

Figure 8.3. showed the XRD patterns collected from the $Cu_3(BTC)_2$ crystals. The very bottom curve is from the uncoated glass substrates. No diffraction peaks were observed

from the substrate. The following curve is from the XRD pattern collected from the synthesized $Cu_3(BTC)_2$ crystals supported on the glass substrate. The very top pattern is the reported XRD pattern for $Cu_3(BTC)_2$. The measured XRD pattern matches the reported XRD pattern very well.

In-situ QCM and FTIR

The in-situ QCM data collected from the Al_2O_3 ALD process was shown in Figure 8.4. The bottom curve is collected from the typical ALD growth on untreated QCM crystals. Step-wise mass uptake behavior was monitored from the TMA and water pulses. The mass uptake for TMA and water were ~ 60 and 30 ng/cm^2 respectively, which is consistent with previous report at 90 °C.[19] The top curve is from the ALD growth on $Cu_3(BTC)_2$ coated QCM crystal. Approximately 40 μg of MOF was loaded onto the QCM crystal. Large mass uptake was monitored for the first TMA pulse, followed by a large mass decease from water pulse. This large mass uptake is probably corresponding to the high surface area of the MOF. ALD precursor could chemically or physically adsorb in the MOF crystals. $Cu_3(BTC)_2$ is also reported as good carrier for methane storage.[5,21] It is likely the methane formed as a byproduct in the ALD process could trap in the MOF crystals during the first TMA pulse. The large mass decrease during the water pulse is likely due to the remove of methane adsorbed in the MOF. We will discuss the methane adsorption in detail in the following section. As the number of ALD cycle increases, less mass uptake was observed. The decreasing of the mass uptake is probably due to the shrinking of pore openings by ALD.

Figure 8.5 showed the in-situ FTIR spectra collected from during the Al_2O_3 ALD growth on MOF crystals. The very bottom spectrum is from the MOF crystals supported on

the Si wafer. The symmetric (1645 and 1590 cm^{-1}) and asymmetric (1450 and 1370 cm^{-1}) stretching vibrations of carboxylate related absorbance was observed from the collected the spectrum,[22] which confirmed the chemical composition of the synthesized MOF particles. The following differential spectrum is collected after the first TMA pulse onto the MOF particles. Small increase of CH_3 related feature at 2940 and 1200 cm^{-1} is corresponding to the adsorption of TMA on the MOF surface[19,23,24]. More interestingly, we found strong CH_4 related absorbance around 3020 and 1306 cm^{-1} after the TMA pulse[25]. This is likely related to the trapped methane in the MOF. The methane was from by the reaction between TMA and surface OH. [13] These CH_4 could be coming from the reaction in the MOF crystals, or it could be coming from the reactor upstream. [23,24] The TMA could react with OH on the reactor wall, and forming CH_4. $Cu_3(BTC)_2$ is known to be a good supporting material for the CH_4 storage.[21,26] This also explained the large mass uptake in the QCM data during the first TMA pulse. The mass uptake is likely also from the CH_4 adsorption. In the following water pulse, most of CH_4 related absorbance removed from the spectrum. This implies the water would prefer to coordinate with Cu center in MOF crystals,[17,27] and result in the removing of CH_4 gas. The bonded water molecules could then be removed from the MOF during the following Ar purge step. Small decrease of CH_3 related absorbance corresponding to the water react with surface adsorbed TMA. In general, FTIR showed the ALD process does not react with MOF backbone dramatically, and the observation of CH_4 confirmed the MOF's ability to storage CH_4. It also confirmed the formation of methane in the TMA/water ALD process. It also supported that the porous structure did not get destroyed after small number of Al_2O_3

ALD cycles on the $Cu_3(BTC)_2$. Water pulse will remove the adsorbed CH_4 on the MOF. This is likely due to water would prefer to coordinate with Cu center in MOF.

QCM Moisture Sensing

Figure 8.6. showed the QCM data collected from the microgravity moisture sensing experiments. The very bottom curve is related to the (2/60 water/Ar) moisture exposure to untreated QCM crystal. No detectable mass uptake was observed during the water exposure. For the QCM crystal supported with MOF particles, dramatic increase of mass detected during water dose, and followed with a quick decrease of mass during the Ar purge. After we applied 5 cycle of Al_2O_3 ALD coating on MOF, we tried the moisture sensing experiment again. At the same experimental conditions, small mass uptake from water pulse was detected. The ALD coating seems reduced the sensitivity of the MOF particles, which is corresponding to the reduced surface area or pore size of the MOF.

8.4. Conclusion

We have successfully synthesized the $Cu_3(BTC)_2$ crystals from the hydrothermal method. The structure and the surface area of the prepared MOF was confirmed by XRD and BET analysis. In this paper, we conducted Al_2O_3 ALD process on the $Cu_3(BTC)_2$ MOF for the first time. In-situ QCM was used to monitor the mass change during the ALD process. A large mass uptake was detected during the precursor pulse, which is corresponding to large surface area and porosity of the $Cu_3(BTC)_2$. In-situ FTIR spectra was also collected to study the surface chemistry. The spectra did not show strong reaction between TMA and the $Cu_3(BTC)_2$ during ALD growth. Interestingly, CH_4 IR absorbance was observed after TMA dose. This is corresponding to the adsorption of CH_4 in the MOF crystals. In the following

water pulse, H_2O molecule would prefer to bind to the metal center in $Cu_3(BTC)_2$ and remove the CH_4 gas.

We also tested the moisture sensing properties of $Cu_3(BTC)_2$ by QCM. Interestingly, after we coat the MOFs with just 5 cycle of Al_2O_3 ALD process, we found the sensitivity of this microgravity sensor decreased. This is corresponding to the shrinking of pore size and the pore volume of MOFs after the ALD. It implied we could use ALD to fine tune the moisture sensing. It also confirmed we did not destroy the MOF structure by apply thin ALD coatings.

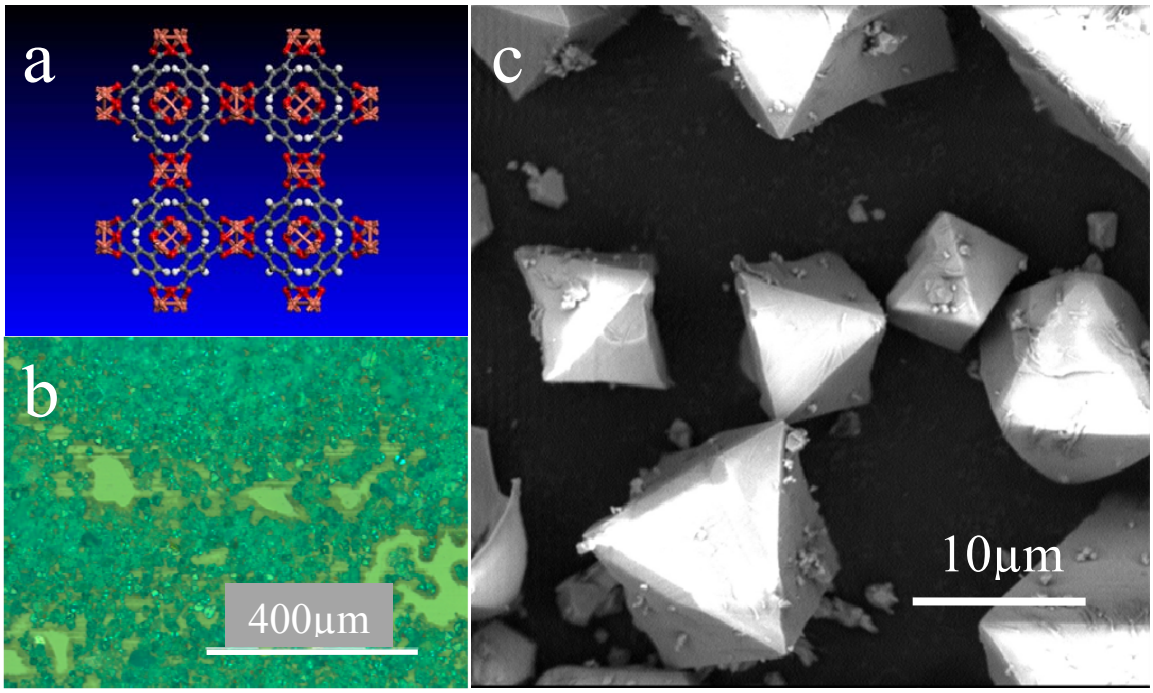


Figure 8.1. Structure and images of HKUST-1 (or $Cu_3(BTC)_2$). (a) The schematic diagram of the molecular structure of the $Cu_3(BTC)_2$. (b) Optical image collected from $Cu_3(BTC)_2$ crystals supported on a glass slide. (c) Scanning electron microscope image collected from the synthesized $Cu_3(BTC)_2$ crystals.

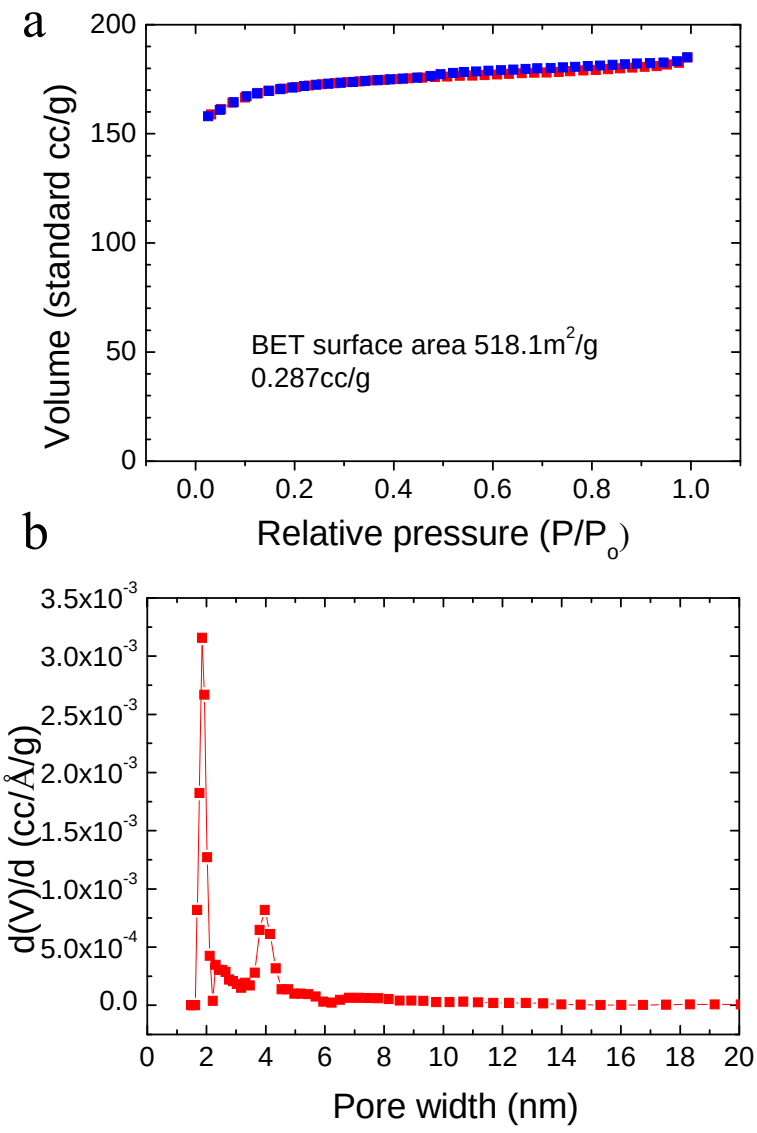


Figure 8.2. Nitrogen sorption data collected from the HKUST particles. (a) The adsorption/ desorption isotherm curve of the outgassed $Cu_3(BTC)_2$. (b) Pore size distribution of $Cu_3(BTC)_2$ calculated from the isotherm curve. (DFT method)

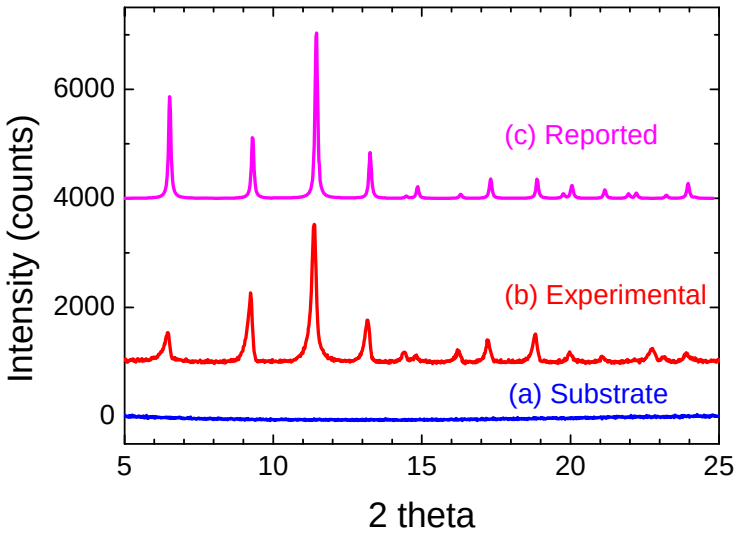


Figure 8.3. X-ray diffraction patterns collected from the (a) glass substrate and (b) $Cu_3(BTC)_2$ particles supported on the glass substrate. The curve (c) was simulated from the reported molecular structure of $Cu_3(BTC)_2$. The collected XRD pattern fits very well with the literature report, which confirmed the formation of $Cu_3(BTC)_2$.

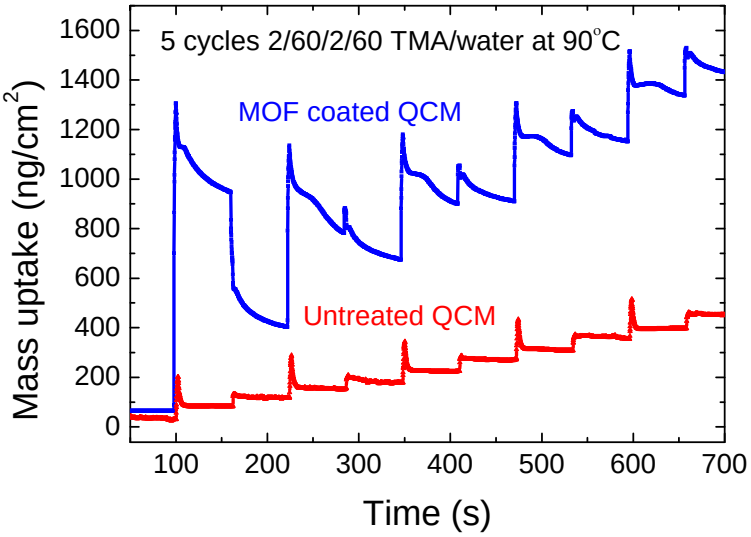


Figure 8.4. In-situ QCM and FTIR analysis of Al_2O_3 ALD on $Cu_3(BTC)_2$. The bottom curve related to the in-situ QCM data collected from TMA/water ALD process on the untreated QCM crystal. The top trace is corresponding to the TMA/water ALD on $Cu_3(BTC)_2$ supported QCM crystal. Much larger mass uptake was observed on MOF coated QCM, which consistent with the larger amount of TMA and water diffuse and reaction in the particles.

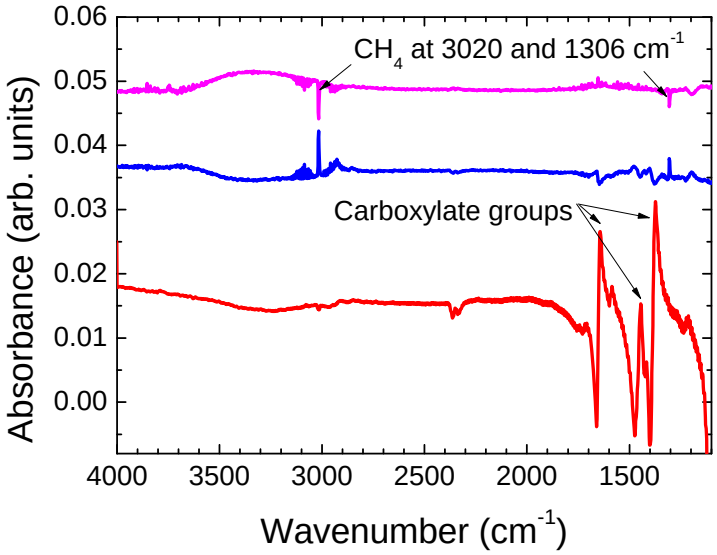


Figure 8.5. In-situ FTIR spectra collected during ALD on MOFs, The spectrum from $Cu_3(BTC)_2$ showed symmetric (1645, 1590 cm-1) and asymmetric (1450, 1370 cm-1) stretching of carboxylate groups, which is consistent with the reported chemical composition. TMA/water showed small reaction with MOFs, and the features around (3020 and 1306 cm^{-1}) corresponding to the formed methane trapped in MOFs.

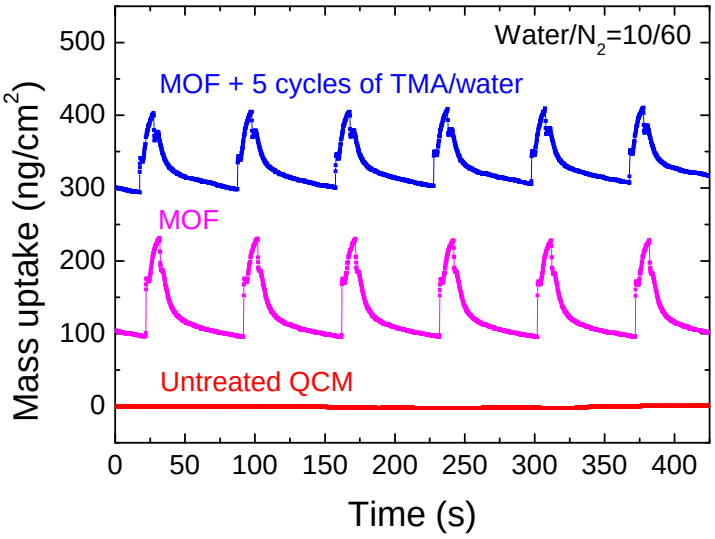


Figure 8.6. In-situ QCM data collected from water/Ar process on bare QCM and $Cu_3(BTC)_2$ particle coated QCM. Bare QCM crystal showed negligible mass uptake during water exposures, while the $Cu_3(BTC)_2$ coated QCM crystal showed very large mass uptake and decreasing. The MOF with 5 cycles of TMA/water ALD process showed smaller mass uptake during water exposure, and this could be explained by the shrinking of pore volume and size after ALD.

References

1 S. Achmann; G. Hagen; J. Kita; I. M. Malkowsky; C. Kiener; R. Moos; Metal-Organic Frameworks for Sensing Applications in the Gas Phase, *Sensors,* **2009**. *9*, 1574.

2 H. K. Chae; D. Y. Siberio-Perez; J. Kim; Y. Go; M. Eddaoudi; A. J. Matzger; M. O'Keeffe; O. M. Yaghi; A route to high surface area, porosity and inclusion of large molecules in crystals, *Nature,* **2004**. *427*, 523.

3 S. S. Y. Chui; S. M. F. Lo; J. P. H. Charmant; A. G. Orpen; I. D. Williams; A chemically functionalizable nanoporous material Cu-3(TMA)(2)(H2O)(3) (n), *Science,* **1999**. *283*, 1148.

4 N. W. Ockwig; O. Delgado-Friedrichs; M. O'Keeffe; O. M. Yaghi; Reticular chemistry: Occurrence and taxonomy of nets and grammar for the design of frameworks, *Accounts of Chemical Research,* **2005**. *38*, 176.

5 M. Eddaoudi; J. Kim; N. Rosi; D. Vodak; J. Wachter; M. O'Keeffe; O. M. Yaghi; Systematic design of pore size and functionality in isoreticular MOFs and their application in methane storage, *Science,* **2002**. *295*, 469.

6 N. L. Rosi; J. Eckert; M. Eddaoudi; D. T. Vodak; J. Kim; M. O'Keeffe; O. M. Yaghi; Hydrogen storage in microporous metal-organic frameworks, *Science,* **2003**. *300*, 1127.

7 M. Sabo; A. Henschel; H. Frode; E. Klemm; S. Kaskel; Solution infiltration of palladium into MOF-5: synthesis, physisorption and catalytic properties, *Journal of Materials Chemistry,* **2007**. *17*,

8 S. Hermes; F. Schroder; S. Amirjalayer; R. Schmid; R. A. Fischer; Loading of porous metal-organic open frameworks with organometallic CVD precursors: inclusion compounds of the type LnM (a)@MOF-5, *Journal of Materials Chemistry,* **2006**. *16*, 2464.

9 S. Hermes; M. K. Schroter; R. Schmid; L. Khodeir; M. Muhler; A. Tissler; R. W. Fischer; R. A. Fischer; Metal@MOF: Loading of highly porous coordination polymers host lattices by metal organic chemical vapor deposition, *Angewandte Chemie-International Edition,* **2005**. *44*, 6237.

10 R. A. Fischer; C. Woll; Functionalized Coordination Space in Metal-Organic Frameworks, *Angewandte Chemie-International Edition,* **2008**. *47*, 8164.

11 F. Schroder; R. A. Fischer, in *Functional Metal-Organic Frameworks: Gas Storage, Separation and Catalysis*; *Vol. 293* (2010), p. 77.

12 M. Leskela; M. Ritala; Atomic layer deposition (ALD): from precursors to thin film structures, *Thin Solid Films,* **2002**. *409*, 138.

13 R. L. Puurunen; Surface chemistry of atomic layer deposition: A case study for the trimethylaluminum/water process, *Journal of Applied Physics,* **2005**. *97*,

14 G. K. Hyde; K. J. Park; S. M. Stewart; J. P. Hinestroza; G. N. Parsons; Atomic layer deposition of Conformal inorganic nanoscale coatings on three-dimensional natural fiber systems: Effect of surface topology on film growth characteristics, *Langmuir,* **2007**. *23*, 9844.

15 Q. Peng; X. Y. Sun; J. C. Spagnola; G. K. Hyde; R. J. Spontak; G. N. Parsons; Atomic layer deposition on electrospun polymer fibers as a direct route to Al2O3 microtubes with precise wall thickness control, *Nano Letters,* **2007**. *7*, 719.

16 B. Gong; Q. Peng; J. S. Na; G. N. Parsons; Highly active photocatalytic ZnO nanocrystalline rods supported on polymer fiber mats: Synthesis using atomic layer deposition and hydrothermal crystal growth, *Applied Catalysis a-General,* **2011**. *407*, 211.

17 P. Kusgens; M. Rose; I. Senkovska; H. Frode; A. Henschel; S. Siegle; S. Kaskel; Characterization of metal-organic frameworks by water adsorption, *Microporous and Mesoporous Materials,* **2009**. *120*, 325.

18 Q. Peng; B. Gong; R. M. VanGundy; G. N. Parsons; "Zincone" Zinc Oxide-Organic Hybrid Polymer Thin Films Formed by Molecular Layer Deposition, *Chemistry of Materials,* **2009**. *21*, 820.

19 B. Gong; Q. Peng; G. N. Parsons; Conformal Organic - Inorganic Hybrid Network Polymer Thin Films by Molecular Layer Deposition using Trimethylaluminum and Glycidol, *Journal of Physical Chemistry B,* **2011**. *115*, 5930.

20 S. Petr; Adsorption isotherms of microporous-mesoporous solids revisited, *Applied Catalysis A: General,* **1995**. *129*, 157.

21 J. Getzschmann; I. Senkovska; D. Wallacher; M. Tovar; D. Fairen-Jimenez; T. Duren; J. M. van Baten; R. Krishna; S. Kaskel; Methane storage mechanism in the metal-organic framework Cu(3)(btc)(2): An in situ neutron diffraction study, *Microporous and Mesoporous Materials,* **2010**. *136*, 50.

22 C. Petit; B. Mendoza; T. J. Bandosz; Hydrogen Sulfide Adsorption on MOFs and MOF/Graphite Oxide Composites, *ChemPhysChem,* **2010**. *11*, 3678.

23 A. C. Dillon; A. W. Ott; J. D. Way; S. M. George; Surface-chemistry of Al2O3 Deposition Using Al(CH3)(3) and H2O in a Binary Reaction Sequence, *Surface Science,* **1995**. *322*, 230.

24 S. M. George; A. W. Ott; J. W. Klaus; Surface chemistry for atomic layer growth, *Journal of Physical Chemistry,* **1996**. *100*, 13121.

25 J. P. Cooley; The infra-red absorption bands of methane, *Astrophysical Journal,* **1925**. *62*, 73.

26 J. Moellmer; A. Moeller; F. Dreisbach; R. Glaeser; R. Staudt; High pressure adsorption of hydrogen, nitrogen, carbon dioxide and methane on the metal-organic framework HKUST-1, *Microporous and Mesoporous Materials,* **2011**. *138*, 140.

27 J. M. Castillo; T. J. H. Vlugt; S. Calero; Understanding Water Adsorption in Cu-BTC Metal-Organic Frameworks, *Journal of Physical Chemistry C,* **2008**. *112*, 15934.

CHAPTER 9 is a reprint of a manuscript submitted to Journal of Materials Chemistry.

CHAPTER 9. Quantitative Analysis of Reaction of Trimethyl-aluminum towards Polymer Substrates during Al_2O_3 Atomic Layer Deposition by In-situ FTIR

Bo Gong, Jesse S. Jur, Joseph C. Spagnola, Kyoungmi Lee, and Gregory N. Parsons*

Department of Chemical and Biomolecular Engineering,

North Carolina State University, Raleigh NC 27695, USA

*Corresponding author: parsons@ncsu.edu

Keywords: Atomic layer deposition, trimethyl aluminum, FTIR, aluminum oxide. polypropylene, polyvinyl alcohol, polybutylene terephthalate, polyethylene terephthalate, polylactic acid, polyethylene oxide, polycarbonate, polymethyl methacrylate, nylon, polyester, polyamide.

Abstract

The reactions of trimethylaluminum (TMA) toward substrates during the Al_2O_3 atomic layer deposition (ALD) on a variety of polymers were studied by in-situ Fourier transform infrared spectroscopy (FTIR). The experiments demonstrate that TMA reacts with certain nucleophilic functional groups on the polymer surface during the first several ALD cycles. For some polymer substrates, TMA vapor penetrates into the polymer and reacts in the polymer bulk. In both cases, the initial reaction plays an important role in the nucleation and growth of Al_2O_3. For chemical inert polymers, such as polypropylene, nucleation of Al_2O_3 ALD is relative slow at the initial stage due to the lack of reactive groups on substrate. However, polyester, polyamide and polyether are more reactive, and in-situ FTIR spectra showed a larger extent of reaction with TMA, facilitating the nucleation of ALD film on these polymers. By comparing FTIR spectra, we quantitative estimate the extent of TMA reaction towards different polymers, and results were confirmed using X-ray photoelectron spectroscopy and scanning electron microscopy. Results give insight into the importance of polymer structure in determining the nature and extent of reaction during ALD film processing on polymer substrates.

9.1. Introduction

Coating of polymer substrates with thin layer of inorganic materials has attracted significant research attention, in part because of potential applications in flexible electronics[1-3], solar cells[4,5], chemical resistant layers, antimicrobial coatings and gas diffusion barriers,[6] and others. Common techniques to deposit inorganic materials on polymer substrates include sol-gel,[7,8] hydrothermal,[9,10] and other solvent chemical routes. However, the introduction of water or organic solvent can lead to swelling and other degradation of polymer substrates. Moreover, it is particularly challenging to achieve defect free thin films with precise thickness and composition control using solvent methods. These downsides often limit the use of solvent methods in many advanced applications.

Atomic layer deposition (ALD) is a vapor phase thin film deposition technique based on sequential self-limiting surface reactions. In the typical ALD process, two reactants are introduced alternatively to the substrate, and forming a single layer of molecular each time. Conformal films with desired thickness and composition can be deposited by control reaction cycles.[11-14] Recently developed low temperature ALD processes, which can be conducted at temperature as low as room temperature, make coating of a variety of thermal sensitive substrates possible. An array of ALD deposition processes have been conducted on polymers substrates. For examples, polymer substrates were serving as templates for ALD to replicate complex 3D structures, such as polyethylene particles[15], patterned polystyrene spheres [16], electro-spun PVA fiber [17], block copolymers[18,19] , and virus shells.[20] Other research was focused on the surface fictionalization of polymer substrates by ALD coatings, for example, butterfly wing[21], polymer fibers[22] and water stride leg were coated by Al_2O_3 ALD to tune the

surface energy of these structures.[23] More interestingly, researchers found that ALD process does not just limited to deposit on the surface, it could be used to modify the polymer bulk.[24,25] ALD precursors could diffuse into the polymer substrates, and result in the subsurface diffuse and reaction during the ALD growth. For example, spider silk has been modified by multi pulse infiltration ALD process to improve the mechanical tensile strength. [26] Similarly, diethyl-zinc/water ALD process has also been used to prepare coordinate metal organic dyes by the multi pulse infiltration process[27].

Although lots of research has been focused on the ALD on polymer substrates, the interaction between precursors and polymer substrates, and mechanism of nucleation and growth of ALD film on polymer substrates has not been carefully studied. The Al_2O_3 film deposited by trimethy-aluminum (TMA) and water is the most studied ALD process. In which you first exposed the substrate to TMA vapor, TMA will react with surface OH and form Al-CH_3 terminated surface. In the following water pulse, these Al-CH_3 groups will react with water and change the surface back the OH terminated. By repeating the deposition cycles, Al_2O_3 film with desired thickness can be deposited.[11,13] The hypothesis is based on a OH terminated substrate, however, for many chemical inert polymers, such as polypropylene[22,24] and Polytetrafluoroethylene (PTFE)[28], this cannot explain the nucleation and growth of Al_2O_3 on these substrates. Wilson et. al has studied the quartz crystal microbalance (QCM) analysis of Al_2O_3 deposition on various polymer substrates.[29] The study showed that different polymer showed different mass uptake during first several ALD cycles before a steady state growth is achieved. They attributed this difference to the different porosity and solubility of polymers, and the nucleation mechanism involves the

diffusion and reaction of TMA/water in the subsurface region of polymer substrates. Moreover, previous research also found that this subsurface growth is a function of process temperature, precursor exposure and interactions between ALD precursor and polymer substrate.[24,25] However, just the QCM mass uptake data cannot show enough information of how the ALD precursors interact and react with the polymer substrate. [29]

In this paper, in-situ Fourier Transform Infrared Spectroscopy (FTIR) was employed to study the interactions between precusros and substrates during ALD deposition of Al_2O_3 from TMA/water on different polymer substrates, such as polypropylene, poly vinyl alcohol, polybutylene terephthalate, polyethylene terephthalate, polylactic acid, polyethylene oxide, polycarbonate, and polyamide. By compare the absorbance value between these FTIR spectra, a model have been developed to quantitatively analysis the reactivity of TMA towards different polymer substrates by examine the absorbance increase per surface area, which could further estimate the aluminum incorporation amount during TMA pulses. X-ray photoelectron spectroscopy (XPS) was employed to understand the composition change of polymer substrates at the initial stage of Al_2O_3 ALD deposition. Scanning Electron Microscope (SEM) was used to monitor the morphology change of the polymer substrates.

9.2. Experimental Section

Chemicals and Materials

All materials and chemicals were purchased commercially and used as received. Trimethylaluminum (TMA 98%) was purchased from Strem Chemicals, and deionized water (DI-H_2O) was used as the oxygen source for Al_2O_3 ALD. Ultra high purity argon (99.999 %, National Welders Supply Co.) was further purified by an inert gas filter (Gatekeeper® inert

gas purifier, Entegris) and used as the purge and reactant carrier gas. For IR substrates, we used double-side-polished n-type Si (100) with resistivity ~0-100 Ω·cm. These provided a uniform ~ 60% transmittance over the middle infrared (MIR) region.

A set of polymer materials, including polypropylene (PP), polybutylene terephthalate (PBT), and polyethylene terephthalate (PET) nonwoven fiber mats were acquired from nonwovens cooperative research center (NCRC) at NC State University. Poly vinyl alcohol (PVA) nanofibers (diameter ~200 nm) were electrospun as described previously.[18] Other polymers, including polybutylene terephthalate (PBT pellets, MW ~38,000), polyethylene oxide (PEO powder, MW ~100,000), polymethylmethacrylate (PMMA powder, MW~350,000), and polylactic acid (PLA powder, MW 60,000) were purchased from Sigma Aldrich. Porous membranes including Cyclopore polycarbonate membrane (0.2 μm pore, 25mm diameter) and Anodized aluminum oxide (AAO) membrane (0.2 μm pore, 13mm diameter) were purchased from Whatman. Organic solvents including decahydronaphthalene (DHN, mix of trans and cis, 97%), trifluoroacetic acid (TFA, 99%), formic acid (>95%), Toluene (99%) and chloroform (99%) were also attained from Sigma-Aldrich.

We formed polymer films on Si wafers by spin coating the dissolved the polymer 3000 rpm at room temperature. Before casting, the silicon was first dipped into a JTP cleaning solution for 2 min, and rinsed under DI water for 5 min, followed by drying under a flow of high purity N_2 (99%). For example, the PP film was prepared from PP fibers dissolved in DHN at 80 °C producing a 1 w% solution for spin casting. Similarly, PVA and PEO were dissolved in water, PBT and PET were dissolved in TFA, PLA was dissolved in chloroform,

PMMA was dissolved in toluene and nylon-6 was dissolved in formic acid before casting. Cast film thickness was typically several hundred nanometers.

ALD Process and In-situ Transmission FTIR Spectroscopy

The vapor delivery and surface analysis for ALD of Al_2O_3 on the polymer surfaces was carried out in a homemade viscous flow vacuum reactor including capability for in-situ transmission infrared spectroscopy, described previously.[34] The reaction system is composed of stainless steel tube ~3.5 cm in diameter maintained with a uniform deposition zone temperature of 80 °C. Two CsI IR windows allow IR transmission through the deposition zone, and two gate valves isolate the reaction zone during reactive vapor exposure. Data is collected between each ALD half-cycle during the inert gas purge step. We use a Nicolet 6700 FTIR spectrometer, where the beam transmits linearly through the sample under test and the IR windows, and is focused using a gold parabolic mirror onto an external MCT-A detector. The spectrometer operated in the frequency range from 4000 to 650 cm^{-1} using a mid-IR KBr beam splitter. Spectra were collected at 4 cm^{-1} resolution using 200 scans per spectrum (corresponding to a data collection time of 2 minutes per spectrum). To highlight the changes in the spectrum upon exposure, data was collected, processed and presented in differential mode, using the previous collected spectrum as the reference.

Samples for IR analysis were polymer films spun-coated onto high resistivity IR transparent silicon wafers and mounted in the IR beam with surface normal parallel to the beam path. The AAO membranes were mounted onto high resistivity silicon and centered on a sample holder with a 1 cm^2 circular aperture, ensuring that the entire sampled IR beam passed through the membranes. For all the in-situ FTIR measurements, samples were loaded

into the reactor, heated to 80°C, and pumped overnight to remove moisture or other vapor contaminants from the samples.

The surface reaction and coating experiments were all performed at 80°C. In a typical TMA/water deposition cycle, the TMA and H_2O each vapor flowed into the reactor for 5 seconds, followed by a chamber isolation step (i.e. the input and pumping valves were closed) for 60 seconds. This was followed by 120 seconds of Ar purge, 150 second of IR data collection (Ar continued to flow), followed by 10 more seconds of purge. For some samples (typically for XPS and SEM analysis) longer vapor exposure steps (TMA/Ar/H_2O/Ar = 60/30/60/30 minutes) were used to promote vapor infiltration into the polymers. For the discussion below, we refer to the cycle with 5 second TMA and water exposure as the "short cycle", whereas the 60 min exposure is the "long cycle" sequence.

Ex-situ characterization

After depositing several ALD cycles on each polymer film, a Riber XPS at the NC State Analytical Instrumentation Facility was used for surface element analysis. The tool is equipped with an Mg-Al dual source and a Mac 2 cylindrical mirror analyzer. Survey scans from 0 to 1200 eV were collected with a step size of 1.0 eV and a dwell time of 0.1 s. Detail element scans were acquired with a step size of 0.1 eV and a dwell time of 0.2 s. Samples were loaded one day before analysis to allow the chamber to pump down and remove any significant organic contaminants.

For the fiber samples, a FEI XL30 SEM was used to image the morphology change of polymer fibers after ALD coating and after post-deposition annealing in air at 450 °C overnight. Before imaging, samples were loaded into a bench top sputter coater, and a ~5 nm

thick gold/ palladium was coated on to the sample. The SEM was operated at a voltage of 7 kV with a working distance of ~5 mm.

The surface area of the AAO membrane was measured by nitrogen sorption analysis using a Quantachrome Autosorb-1C surface area and pore size distribution analyzer. The Brunauer Emmett Teller (BET) method was used to calculate the specific surface area by using the adsorption points in the pressure range of $0.05 < P/P_0 < 0.35$. For AAO membrane, the surface area of a single disk membrane (diameter = 1.3 cm) is found to be ~ 630 cm^2. This means that the overall surface area of the membrane is ~475× larger than a flat circle with the same diameter.

9.3. Experimental Results

Al_2O_3 ALD on Anodic Aluminum Oxide

A key reaction step upon TMA exposure to a hydroxylated alumina surface at low temperature is the TMA methyl/proton exchange with OH to form O-Al-$(CH_3)_2$ or $(Al\text{-}O)_2$-Al-(CH_3) units and volatile methane. Results in Figure 9.1 show IR transmission data collected in situ after saturation TMA exposure and saturation water exposure during steady state ALD processing on AAO. The data is plotted to show the change in IR absorbance relative to the previous saturated surface. The dominant IR modes include asymmetric and symmetric C-H stretches $\nu_a(CH_3)$ and $\nu_s(CH_3)$ at 2939 and 2898 cm^{-1} respectively.[35] On these thick AAO membranes, the strong Al-O substrate absorbance extends to up to 1300 cm^{-1}, masking features in low wavenumber range. This means that the Al-CH_3 symmetric bending or deformation mode[35] $\delta_s(CH_3)$ at ~1200 cm^{-1} is not readily visible. After TMA exposure on

a hydroxylated surface, positive-going features at 2800-3000 cm^{-1} correspond to the addition of asymmetric and symmetric C-H stretches. The positive-going feature at 2827 cm^{-1} is assigned to an overtone of the Al-CH_3 bending mode.[36,37] The increase in CH modes is consistent with TMA reacting with surface OH to from $(O-)_2Al-CH_3$ and $O-Al-(CH_3)_2$ surface groups. Reactions between TMA and bridging Al-O-Al can also produce -Al-CH_3 surface groups. Upon water exposure, C-H features are removed (corresponding to negative-going modes) and positive features are added. The broad mode between ~3600 and 3000 cm^{-1} is due to O-H stretching of hydrogen bonded Al-OH units as well as adsorbed molecular water.[38,39] Water-related bending modes are also expected in the 1400-1600 cm^{-1} range. [36]

To test if the IR mode intensity scales linearly with deposition surface area, we put 1, 2 or 3 AAO membranes in the beam path then exposed them to TMA for 1 minute. The 1 minute TMA exposure is expected to saturate the surface reaction with AAO. Similar IR features are observed for each case. Figure 9.1(b) shows the absorbance intensity of the CH_3 asymmetric stretching mode $\nu_a(CH_3)$ at ~2939 cm^{-1} plotted versus total surface area. The intensity scales linearly with the overall AAO surface area in the beam path. Based on the linear slope, the CH_3 groups on each AAO membrane (with 475× surface area than a flat surface) contribute ~0.008 in absorbance intensity. This means that the absorbance for the $\nu_a(CH_3)$ mode at 2939 cm^{-1} corresponding to a single planar monolayer is ~ 0.008/475 ≈ 1.7×10^{-5}. Therefore, for absorbance sensitivity limit of ~1-2 × 10^{-4}, the equivalent of ~10 planar monolayers of Al-CH_3 units is needed in the beam path for a measurable absorbance signal under the data collection process used here. We can thereby conclude that when a planar polymer film is exposed to TMA, a measurable change in $\nu_a(CH_3)$ mode intensity indicates that much more

than a single monolayer Al-CH_3 groups is present in the beam path. Since more than a single monolayer is not expected to react on a flat surface, the measurable absorbance is ascribed to TMA that has diffused and reacted within the polymer forming Al-CH_3 groups dispersed through the polymer film.

For the AAO substrate, trimethylaluminum reacts and adsorbs only on the solid surface, and as shown in Figure 9.1 (b), the $\nu_a(CH_3)$ mode intensity scales linearly with AAO surface area in the beam path. We note that mode intensities in the C-H stretching region can be impacted by several effects, including multiple mode coupling, overtones, back-bonded species and changes in local dielectric environment that will depend on the polymer studied, so the C-H stretching peak absorption is not always expected to scale strictly with C-H bond density. The lower energy $\delta_s(CH_3)$ mode provides an additional independent probe of the changes in C-H bond density upon TMA exposure. However, this mode is masked on the AAO substrates by the strong Al-O stretching feature. On the other hand, the $\delta_s(CH_3)$ signal is readily observed during ALD on the polymer substrates, and therefore, we can compare changes in the intensity of the $\delta_s(CH_3)$ mode relative to that for the $\nu_a(CH_3)$ mode for polymers exposed to TMA. As discussed below, the stretching and bending mode intensities correlate well with each other for our samples, so the changes in $\nu_a(CH_3)$ measured in-situ after TMA exposure provide a reasonably good quantitative probe for the relative extent of TMA sub-surface diffusion and reaction with the polymers studied here.

In the following sections, we explore TMA exposure on various polymer thin films and compare the $\nu_a(CH_3)$ mode intensity to estimate a relative propensity for TMA to react with the polymer to produce IR active Al-CH_3 units. This data, along with changes in other IR

modes, is used to identify possible mechanisms for TMA reaction with the polymers. These results therefore provide a starting point to quantitatively compare ALD reactions on polymers and identify common reaction sequences that may occur within different polymer materials.

Polyolefin (PP)

A polypropylene film spun-cast on silicon was used as substrate for in-situ FTIR analysis during TMA/water ALD, and the resulting spectra are plotted in Figure 9.2. The bottom spectrum is from the substrate alone, and the other spectra are plotted in differential mode to highlight the change in features after TMA or water exposure. The substrate was loaded one day before the analysis to remove any adsorbed water. The sample was held at 80 °C and exposed to TMA for 1 min followed by 2 min of Argon purge and IR data collection. The sample was then exposed to water vapor for 1 min, followed by a similar purge/IR data collection step. The absorbance of the untreated PP film shows characteristic peaks associated with the CH_3, CH_2 asymmetric (2947 and 2863 cm^{-1}) and symmetric (2911 and 2831 cm^{-1}) stretching features, and the CH_3, CH_2 bending features at ~1372 and 1452 cm^{-1}. After the TMA pulse, the differential FTIR spectrum showed no observable change of the IR peaks, and any change in the $\nu_a(CH_3)$ region was also less than the detection limit of ~ 2×10^{-4}. The subsequent water pulse also produced no detectable change in IR signal.

A spun-coated PP film on a silicon wafer was analyzed by XPS before and after one long vapor exposure cycle (TMA/Ar/H_2O/Ar = 60/30/60/30 minutes), and Figure 9.3 shows the resulting spectra. Consistent with the lack of reaction observed by IR, we observe no signal corresponding to the aluminum 2p peak at ~73 eV. Moreover, the C 1s peak detail scan

shows almost the identical characteristic shape before and after TMA/water cycle, also confirming that the PP is not reactive under TMA/water cycles. We also exposed polypropylene nonwoven fibers to the same long exposures of TMA and water in the same reactor system. We collected SEM images after coating and after calcining the fibers in air at 450 °C for 48 hour to remove the polymer. The calcination step results in minimal residue visible in the SEM, further confirming very little Al_2O_3 deposition. Based on these results, we could conclude that during Al_2O_3 ALD on PP substrate, TMA/water vapor does not react directly with polymer substrate. However, we do find that Al_2O_3 can be deposited on polypropylene during ALD.[26] In this case, therefore, the deposition proceeds by TMA diffusing sub-surface into the polypropylene, followed by incomplete removal of TMA during the subsequent purge cycle. Remaining TMA readily reacts with water during the water exposure step, producing Al-O bonding units on the surface and/or in the polymer bulk. These small clusters then provide sites for subsequent reactions with TMA and water during following cycles, eventually leading to film overgrowth.[25]

Polyvinyl alcohol (PVA)

In-situ FTIR spectra collected during ALD on a PVA film are plotted in Figure 9.4. Again, the bottom spectrum provides the substrate spectrum, and the other traces are differential spectra collected after TMA or water exposure. The untreated PVA film shows characteristic peaks for the hydroxyl feature at ~3400 cm^{-1}, the CH_2 asymmetric and symmetric stretching features at ~2930 and 2860 cm^{-1}, and ester features at ~1700 cm^{-1} (C=O stretching) and 1250 cm^{-1} (C-O stretching). The first TMA dose produces a decrease of OH at ~3700 cm^{-1} and carbonyl at ~1700 cm^{-1}, as well as an increase of CH_3 stretching at ~2935 cm^{-1} and Al-CH_3

deformation at ~1200 cm^{-1}. Based on the IR data, TMA reacts with available OH as well as carbonyl groups present on un-hydrolyzed acetate groups on the polymer chain. The peak intensity of CH_3 stretching at ~2935 cm^{-1} after first TMA pulse is ~ $4.0\pm0.5\times10^{-4}$. The following water pulse removes the CH_3 stretching and Al-CH_3 deformation modes.

Figure 9.5 shows SEM images collected after a PVA electrospun fiber mat is exposed to one "long" TMA/water cycle at 80 °C. The fiber template was removed by annealed in a furnace in air at ~450 °C overnight. The Figure 9.5(b) shows that after burning out the polymer, a double layered alumina "belt" was formed. This suggests that TMA reacts easily with the PVA fiber, producing a continuous film that collapses into flat shapes observed by SEM. In this case, the high density of hydroxyl groups at or near the PVA surface likely react with TMA to form O-Al-$(CH_3)_2$ units at or near the surface that block further TMA diffusion. Reaction with water then produces a continuous and conformal thin oxide coating.[18,40]

The spun-cast PVA films on silicon were also measured by XPS. A survey scan showed 55.1 atomic % carbon, 37.3 % oxygen, and 7.6 % silicon for untreated PVA, whereas after TMA/water treatment the film showed 9.1 atomic % aluminum, along with 44.7 % carbon, 39.7 % oxygen and 6.6 % silicon. The high aluminum content is consistent with some sub-surface TMA reaction. The C 1s detail scan in Figure 9.6 shows a dramatic decrease of C-OH and C=O related features after TMA/water, indicating TMA reaction with OH and carbonyl groups in the polymer backbone. This is consistent with the IR results.

Polyamide (Nylon-6)

Figure 9.7 shows in-situ IR data collected from a nylon-6 film on silicon after exposure to TMA and water at 80 °C. The absorbance of an untreated nylon-6 film shows characteristic

modes associated with N-H stretching at ~3304 cm^{-1}, the CH_2 asymmetric and symmetric stretching features at ~2930 and 2860 cm^{-1}, and amide features at ~1640 cm^{-1}, 1541 cm^{-1} and 1280 cm^{-1}. Upon TMA exposure, the $\nu_a(CH_3)$ mode at ~2941 cm^{-1} increased by ~$1.0\pm0.3\times10^{-2}$, showing a much larger extent of reaction for TMA with polyamide as compared to PP or PVA. Upon TMA exposure, the deformation mode at 1200 cm^{-1} also becomes visible and the intensity of N-H feature at 3304 cm^{-1} and amide feature at 1640 cm^{-1} decrease. The data shows that TMA readily reacts with the amide bonding unit. Upon water exposure, the Al-CH_3 features disappear and there is a corresponding increase in Al-O stretching mode in the 700 cm^{-1} range.

Another nylon-6 film on silicon was exposed to one "long" TMA/water cycle at 80 °C. XPS survey scan showed 3.1 % aluminum, 69.8 % carbon, 14.9 % oxygen, and 10.7 % nitrogen for the treated sample, compared to 77.7 % carbon, 10.7 % oxygen, and 11.6 % nitrogen for the untreated nylon-6 film. The aluminum content indicates significant diffusion of TMA into the nylon. The 3% aluminum after TMA exposure on PA-6 is less than the ~9% measured after the same TMA exposure on PVA. Because the XPS is sensitive to surface concentration, the relatively small Al fraction on the PA-6 is ascribed to a higher rate of subsurface diffusion on the PA-6 relative to the PVA. This is confirmed by the larger $\nu_a(CH_3)$ intensity in PA-6 compared to PVA after TMA exposure. The C 1s peak detail scan on the PA-6 (Figure 9.8) shows almost no change upon TMA exposure, consistent with increased sub-surface diffusion.

Polyesters (PBT, PET, PLA)

In-situ FTIR spectra for TMA and water exposure on a polybutylene terephthalate (PBT) film are plotted in Figure 9.9. The spectrum for untreated PBT displays modes for C=O stretch at ~1720 cm^{-1}, C-O stretch at ~1270 cm^{-1}, C-O-C stretch at ~1100 cm^{-1} and CH_2 symmetric and asymmetric stretching at ~2860 and 2925 cm^{-1}, respectively. The next trace shows the absorbance change after TMA exposure at 80 °C. Negative-going modes at ~1720 and 1260 cm^{-1} correspond to removal of carbonyl stretching units, and the decrease at ~1100 cm^{-1} shows removal of C-O-C groups. Positive signals at ~2960 cm^{-1} and 1200 cm^{-1} indicate appearance Al-CH_3 stretching and deformation modes. The mode appearing at 680 cm^{-1} is ascribed to Al-C bonds formed upon the TMA reaction. These changes demonstrate that TMA reacts with the carbonyl group on the PBT. TMA is a strong Lewis acid, and it is likely attacking nucleophilic carbonyl or ether groups in the polyester to form an aluminum-oxygen-alkyl units. The top-most spectrum was collected after exposing the sample to water vapor. This shows removal of Al-CH_3 related modes and formation of Al-O and OH features. The magnitude of the $\nu_a(CH_3)$ absorbance change at ~2960 cm^{-1} is measured to be ~ 0.30±0.05, consistent with very deep penetration and reaction of TMA in the PBT polymer.

The SEM images in Figure 9.10(a) and (b) were collected from a PBT nonwoven fiber mat before treatment, and after long TMA/water exposure followed by calcination at 450 °C in After calcination, the TMA/water treated fibers were brittle, and broken edges in panel (b) show the fiber to be a cylindrical solid. This results from TMA penetrating and reacting throughout the polymer fiber.[31] Removing the organic component by calcination yields a porous alumina structure surface area as high as 440 m^2/g, depending on the detailed process conditions.[31]

After the extended TMA/water treatment XPS spectra show 12.7 % aluminum, 37.2 % carbon, 45.9 % oxygen, and 4.2 % silicon, compared to 49.5 % carbon, 33.1 % oxygen, and 17.4 % silicon for the untreated PBT. The detail scan of C 1s peak (Figure 9.11) shows a decrease in C=O related features at 289.3 eV and an increase in C-O-Al at 283.5 eV after TMA/water, consistent with the IR data.

We also examined polyethylene terephthalate (PET) films, and the IR data is plotted in Figure 9.12. The PET has a chemical composition similar to PBT, and the differential spectra show PET has similar extent of reaction with TMA. After the first TMA exposure, the $\nu_a(CH_3)$ mode intensity increases by ~ 1.42±0.1 indicating significant penetration and reaction of TMA in PET.

Similar results from a polylactic acid (PLA) thin film exposed to TMA/water are presented in Figure 9.13. The untreated PLA shows ester bonds at ~1720 cm^{-1} and 1260 cm^{-1}, CH_3, CH_2 stretching features at ~2900 and the bending feature at ~1400 cm^{-1} and the C-O-C features at ~1100 cm^{-1}. After TMA exposure, the IR spectra shows clear evidence for TMA reaction with C=O and C-O-C groups. The change in the $\nu_a(CH_3)$ absorbance is ~ 5.3±0.5× 10^{-2}, which is smaller than for PBT and PET. An additional peak in PLA at 1600 cm^{-1} is assigned to aluminum carbonate,[41] which is more likely to be formed in the aliphatic PLA as compared to the aromatic PBT and PET. The peak disappears upon water exposure, consistent with carbonate hydroxylation.

Polycarbonate (PC)

We also studied reactions between TMA and polycarbonate (PC) using a track-etched polycarbonate membrane mounted on a silicon wafer. As received, the PC membranes

contained high density of sub-micron holes vertically etched through the membrane, resulting in a large surface area. The large area will enhance TMA adsorption and reaction compared to the other planar polymer films studied here. The IR results are shown in Figure 9.14. The PC substrate shows C-O stretch modes at ~1270 cm^{-1}, C=O stretch at ~1770 cm^{-1}, C-O-C stretch at ~1100 cm^{-1}, CH_3 stretching at ~2960 and CH_3 bending at ~1500 cm^{-1}. The PC membrane was relatively thick, so the C=O stretch and C-O stretch modes are topped due to the large absorbance. Upon TMA exposure, C=O (1770 cm^{-1}) decreases and CH_3 features (~2900 cm^{-1} and 1200 cm^{-1}) increase, showing reaction between TMA and the carbonyl groups, as expected from the analysis of the polyester materials. After TMA exposure on the PC membrane, the $\nu_a(CH_3)$ absorbance increased by ~0.31±0.06. According to the specification of the PC membrane, it has an array of holes, 200 nm in diameter with pore density of ~$3\times10^8/cm^2$. For a membrane ~10 μm thick, we estimate the total surface area is ~20× larger than a flat planar polymer disk with the same diameter. Therefore the increase in $\nu_a(CH_3)$ absorbance may be enhanced by a factor of 20 or more compared with the data collected from the other planar polymer film materials. The absorbance change of 0.31 corresponds to a relatively small extent of reaction for PC with TMA.

Poly methyl methacrylate (PMMA)

Infrared spectra from TMA/water exposure on a ~200 nm thick PMMA film are shown in Figure 9.15. The PMMA film shows characteristic peaks associated with CH_2 asymmetric and symmetric stretching at 2930 and 2860 cm^{-1}, and the carbonyl and ester stretching features at 1720 cm^{-1} and 1260 cm^{-1}, respectively.[42] Upon TMA exposure, we note an increase in $\nu_a(CH_3)$ peak intensity, but the magnitude is only ~ $1.7\pm0.3\times10^{-2}$ indicating

relatively small extent of reaction between TMA and PMMA. The TMA also leads to a decrease in C=O at 1720 cm^{-1} and C-O at 1260 cm^{-1}. Similar to the PLA system described above, a mode appears at 1600 cm^{-1} ascribed to formation of aluminum carbonate (O-C-O asymmetric stretching).[43] The water exposure removes Al-CH_3 modes as well as aluminum carbonate at 1600 cm^{-1}, and produces the expected increase in Al-O mode at ~700 cm^{-1}.

Polyethylene oxide (PEO)

Data from polyethylene oxide polymer films are shown in Figure 9.16. The spectra of untreated PEO film shows characteristic peaks associated with CH_2 asymmetric and symmetric stretching features at 2930 and 2860 cm^{-1}, and the ether stretching features at ~1100 cm^{-1}.[13] The differential spectrum collected after first TMA pulse shows a decrease in C-O-C stretching at 1100 cm^{-1} and an increase in both C-O stretching at ~1050 cm^{-1} and CH_3 stretching and deformation at ~2960 cm^{-1} and 1200 cm^{-1}. This indicates that TMA reacts with the ether groups in PEO, likely forming C-O-Al linkages. The intensity change for the $\nu_a(CH_3)$ mode is ~ 1.10±0.1, indicating a large extent of reaction for TMA with PEO. Upon water exposure, Al-CH_3 units react to form Al-OH. Water can also hydrolyze the C-O-Al bond yielding C-OH and Al-OH groups. These reactions are supported by the decrease of CH_3 absorbance and increase in both -OH at 3300-3700cm^{-1} and C-OH at ~1100 cm^{-1} upon water exposure.

9.4. Discussion

A. Extent of Reaction

For TMA exposure on the polymers, differential spectra can readily evaluate the changes in the C-H stretching and bending features. As noted above, mode intensities are often modulated by local environment which will vary with polymer structure and reaction. Any hydroxyl units at the surface of the polymer are expected to react with TMA. Other reactive sites including carbonyls, esters, ethers, vinyls, and others will also react with TMA to produce Al-CH_3 and C-CH_3 units. In addition, TMA can insert into Al-O-Al bridging sites to form O-Al-$(CH_3)_2$ and $(-O)_2$-Al-CH_3. If the local bonding environment for the CH_3 units formed in these materials is sufficiently consistent, it is reasonable to expect a relatively constant ratio between the CH_3 stretching and bending mode strengths. This means that upon reaction with TMA the change in $\nu_a(CH_3)$ mode intensity in the polymer should scale relatively well with changes in $\delta_a(CH_3)$ intensity. The IR data allows us to track the change in $\nu_a(CH_3)$ intensity at 2939 cm^{-1} and $\delta_a(CH_3)$ intensity at 1200 cm^{-1} upon TMA exposure for the various polymers studied, and Figure 9.17 shows the resulting correlation. The plot shows a good linear relation, with zero intercept, between the change in $\nu_a(CH_3)$ and $\delta_a(CH_3)$ mode intensities extending over a large absorbance range. Previous IR studies of Al_2O_3 ALD using ozone show quantitative correlation between changes in C-H stretching and Al-CH_3 deformation mode intensities.[43]

Since the IR data was collected for similar TMA exposure conditions on the polymers, the magnitude of the $\nu_a(CH_3)$ and $\delta_a(CH_3)$ intensity change data in Figure 9.17 also displays the relative extent of reaction between the various polymers and TMA. It is important to note that a smaller number of Al-CH_3 groups observed by in-situ IR (i.e. a smaller extent of reaction) could result from a low reactivity for the precursor with the polymer, or it could be

due to a relatively high reactivity leading to relatively rapid film formation that blocks subsequent precursor diffusion and sub-surface reaction. The trend in extent of reaction depicted in Figure 9.17 is influenced by relative reaction rates for TMA with various functional groups, as well as the rates and thermodynamic driving force for precursor diffusion and/or dissolution within the polymers. Therefore, the trend is not expected to scale simply with thermodynamic reaction energetics. We also note that the trend in extent of surface and sub-surface reaction will also likely be strongly affected by reaction temperature. Higher temperatures may promote diffusion in non-reactive polymers, whereas in other polymers an increased temperature may promote surface reactions that form layers that act to block sub-surface diffusion. The data in Figure 9.17 was collected for one fixed temperature, providing a preliminary quantitative guide for the degree of surface and subsurface reactivity to be expected during TMA/water ALD on these materials.

Clearly, the propensity for TMA or other ALD precursors to react on the surface or diffuse sub-surface depends on polymer structure. The extent reaction of TMA with some polymers such as PP and PVA is very small, whereas PET and PEO show much more reaction. It is interesting to note that PET and PMMA show very different extent of reaction, even though they contain similar -(C=O)-O- characteristic polymer groups.

The XPS and SEM results collected after Al_2O_3 ALD on polymer films are consistent with the trends determined from IR data analysis. For TMA on polypropylene, no aluminum is detected, whereas a significant Al-C peak is present in the detailed C 1s peak after ALD on PVA, nylon-6 and PBT. The SEM results showed little Al-O residue after calcination of the TMA/H_2O treated PP fibers, whereas calcining the treated PVA and PBT fibers produced

tubular structures and solid cylinders, respectively, showing a much larger reaction extent. These findings track with the IR results in Figure 9.17, showing more reaction for TMA with PBT compared with PVA, and minimal reaction with PP.

B. Quantitative Analysis of TMA reaction on AAO

To further analyze the extent of TMA reaction with the polymers studied, we can compare the $\nu_a(CH_3)$ absorbance intensity measured on the polymers to that measured on the high surface are AAO. After a saturation dose of TMA on AAO, we estimate the surface concentration of aluminum atoms to be $[Al] = \rho \bullet N_A \bullet t_{Al\text{-}O}/M_{Al\text{-}O} \approx 4.8/nm^2$, where film density $\rho = 3.5\ g/cm^3$, $N_A = 6.02x10^{23}\ mol^{-1}$, and the thickness and molecular weight of one "Al-O monolayer" are $t_{Al\text{-}O} = 0.11$ nm and $M_{Al\text{-}O} = M_{Al} + 3/2\ M_O = 50.98$ g/mol, respectively. If on average each Al has 1 or 2 CH_3 groups, then the surface density of Al-CH_3 units on a TMA saturated surface is $(^3/_2)*[Al] \approx 7.1\times10^{14}/cm^2$. The thickness of one "Al-O monolayer" is given by $t_{Al\text{-}O} = [\rho/(M_{Al\text{-}O} \bullet N_A)]^{1/3} \approx 0.29$ nm, so growth of 1.1 Å/cycle corresponds to about 30-40% of one monolayer, which roughly corresponds to the packing of Al-CH_3 groups in $(O\text{-})_2Al\text{-}CH_3$ and $O\text{-}Al\text{-}(CH_3)_2$ units on the surface after the TMA exposure step.[14]

When the AAO substrate is saturated with Al-CH_3, the IR beam probes a total of 475 "Al-CH_3 monolayers". Based on the data fit in Figure 9.1 (b), the absorbance of the $\nu_a(CH_3)$ mode at 2939 cm^{-1} for a single planar monolayer is $\sim 0.008/475 \approx 1.7\times10^{-5}$. The analysis above shows that upon TMA saturation, the density of a monolayer of Al-CH_3 units on a *planar* surface is $\approx 7.1\times10^{14}/cm^2$. Therefore, the absorptivity of Al-CH_3 will be $= 1.7\times10^{-5}/7.1\times10^{14} \approx 2.4\times10^{-20}\cdot cm^2$.

By comparing $\nu_a(CH_3)$ absorbance intensity measured on the polymers, we could quantitatively analyze the extent of reaction for TMA with these different polymer substrates. For example, upon the first TMA pulse, the PVA film shows an $\nu_a(CH_3)$ absorbance intensity increase of ~ 0.0004. The Al-CH_3 concentration is estimated to be $0.0004/2.4\times10^{-20}\cdot cm^2 \approx 1.7\times10^{16}/cm^2$, which is corresponding to $1.7\times10^{16}/7.1\times10^{14} \approx 24$ "Al-CH_3 monolayers", primarily within the polymer subsurface. The OH groups on the PVA could result in rapid formation of Al_2O_3 at the near surface, and prevent the precursor from penetrating deep into the polymer bulk. However, for TMA exposure on PET, the corresponding $\nu_a(CH_3)$ absorbance intensity increase shown in Figure 9.12 is ~1.42. This relates to an Al-CH_3 concentration of $1.42/2.4\times10^{-20}\cdot cm^2 \approx 5.9\times10^{19}/cm^2$, which is approximately equivalent to $5.9\times10^{19}/7.1\times10^{14} \approx 8.3\times10^4$ "Al-CH_3 monolayers". This shows that a large number of TMA molecules infuses and reacts in the PET bulk. By similar analysis on the other polymers, the "number of monolayers" could be used to quantitatively evaluate the extent of subsurface diffusion and reaction. This data is collected for each polymer and summarized in Table 1.

As the results in Table 1 show, the extent of subsurface diffusion and reaction with TMA strongly depends on polymer chemistry. TMA will attack nucleophilic functional groups in the polymer, such as C=O in the polyesters and polyamide, and C-O-C in the polyethers. These groups will have different propensities for reaction. Many polymers contain these groups, but the location of these reactive groups within the polymer also appears to be important. For example, PET and PMMA have similar -(C=O)-O- characteristic groups, but they show more than 10× difference in extent of reaction with TMA. In PET the ester is in the main chain so the reaction with TMA will more likely promote chain scission, facilitating

further TMA infusion and reaction. In PMMA however, the ester is limited to the side chain, so reaction is less likely to break the chain, helping to maintain the polymer structure and thereby limiting diffusion. Other factors such as the overall polymer molecular weight and crystallinity may also influence the reaction extent in these and other polymer/precursor reaction systems.

9.5. Summary

This work quantitatively analyzed the extent of reaction for TMA with various polymer substrates during Al_2O_3 ALD at low temperature (80 °C). The TMA as a strong Lewis acid showed a high reactivity towards nucleophilic functional groups in polymer chain, such as amide, ester and ether bonds. The extent of subsurface diffusion of the TMA precursor depended markedly on the polymer studied.

The in-situ FTIR data also provides insight to chemical reaction mechanisms. For inert polymers, like PP, reaction with TMA is nearly negligible. Nucleation and growth during ALD can occur, but it appears to be mostly through precursor diffusion and kinetic confinement in the polymer. Polyesters, polyamide and polyethylene oxide are much more reactive with TMA. In this case, the results are consistent with the Lewis acid/base interaction forming adducts of TMA and oxygen in the carbonyl or ether bonds followed by ligand exchange.

The quantitative study would help the understanding the chemical interactions of the ALD precursors with polymer substrates and the nucleation of ALD films, which is very important for many advanced applications of ALD films on polymers.

Acknowledgements

This work was supported by the National Science Foundation project number CBET-1034374. We are grateful to Michelle Gignac at SMIF (Duke University) for SEM measurements, Fred Stevie at AIF (NCSU) for XPS measurement, and Giovanna Scarel at James Madison University for FTIR data analysis.

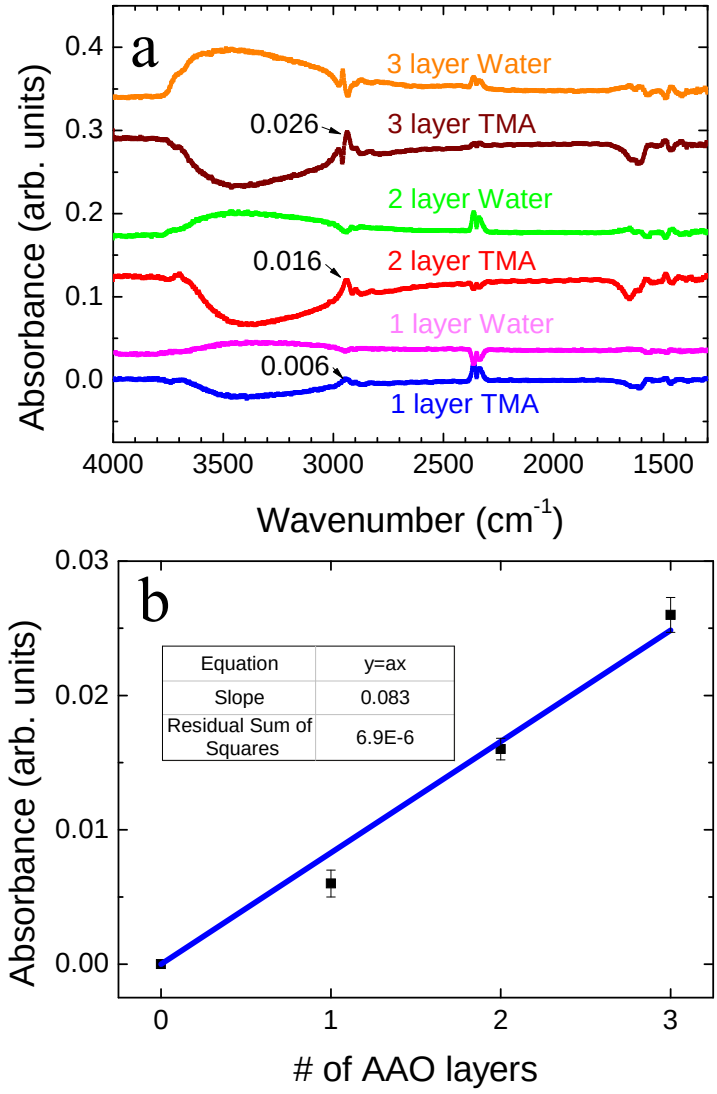


Figure 9.1. In-situ differential FTIR spectra of TMA/water deposition on AAO membranes. After TMA pulse, we observe the absorbance increase of CH_3 stretching feature at ~2960 cm^{-1} and the decrease of -OH related features between 3700 and 3000 cm^{-1}. In the following water pulse, we can see a mirrored spectrum, which corresponding to increase of -OH and decrease of CH_3 on the surface. Multiple layers of AAO membrane were used to quantitative analysis the relation between the absorbance and surface area. A linear relation between number of AAO membrane and CH_3 asymmetric stretching absorbance has been measured and plotted in panel (b).

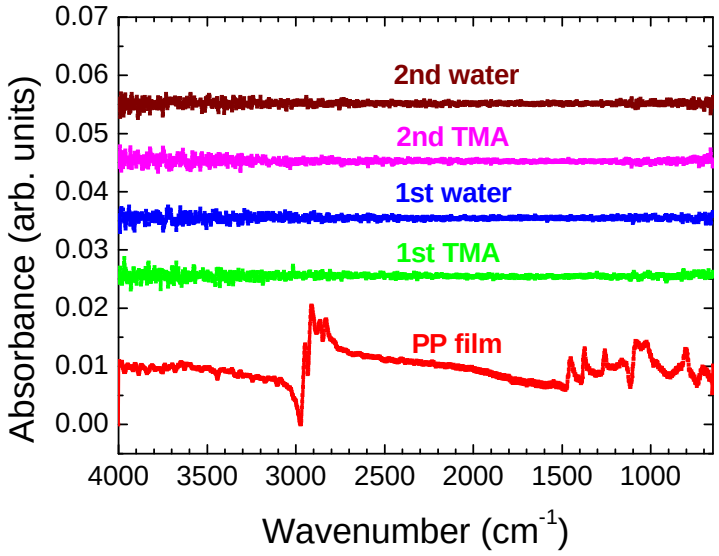


Figure 9.2. In-situ FTIR differential Spectra of TMA/water deposition on spin coated PP film. Negligible interactions between TMA and PP were observed. The peak intensity of CH_3 asymmetric stretching at ~2960cm^{-1} is not detectable (< 2×10^{-4}) after 1st TMA exposure.

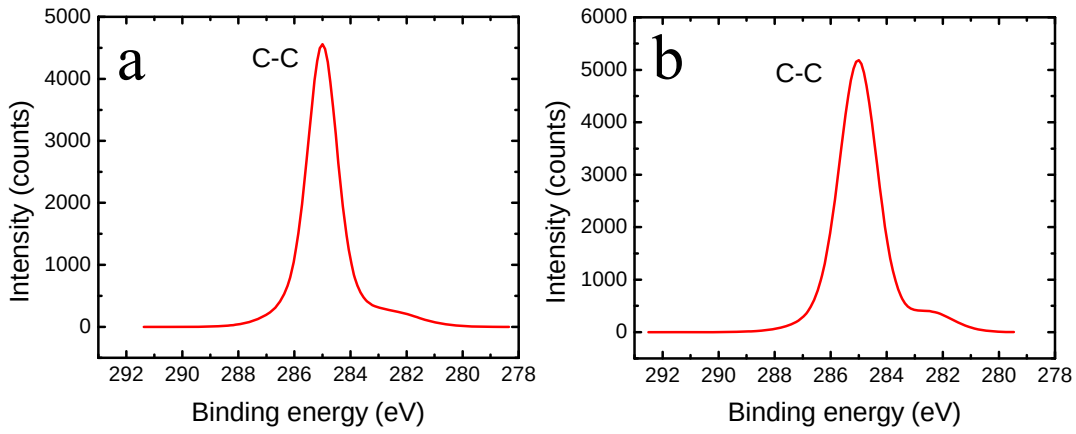


Figure 9.3. C 1s peak detail scan of PP film on Si wafer, before (a) and after (b) TMA/water soaking. No observable change in peak shape. The TMA/water soaked PP film showed no detectable Al.

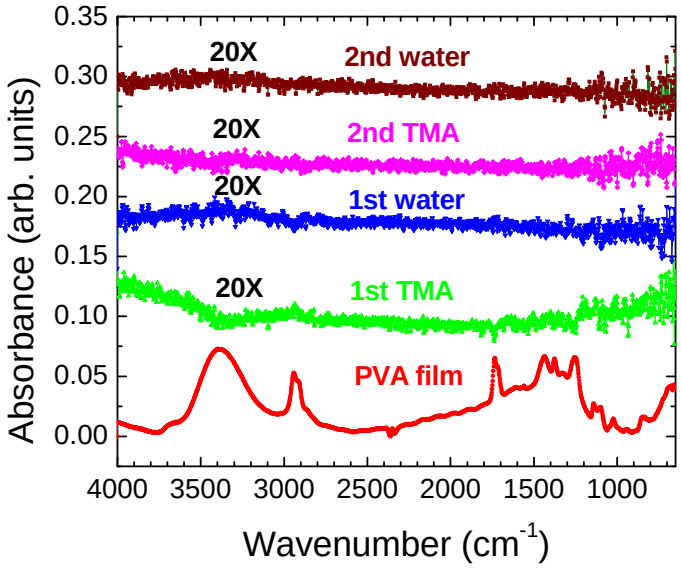


Figure 9.4. In-situ FTIR differential spectra of TMA/water deposition on spin coated PVA film. For clarity, differential spectra after precursor dose were magnified 20 times. We found TMA will react with C-OH and C=O on the PVA fiber in the first ALD cycle. The peak intensity of CH_3 stretching at ~2960 cm^{-1} is ~ 4.0±0.5× 10^{-4} after the first TMA exposure.

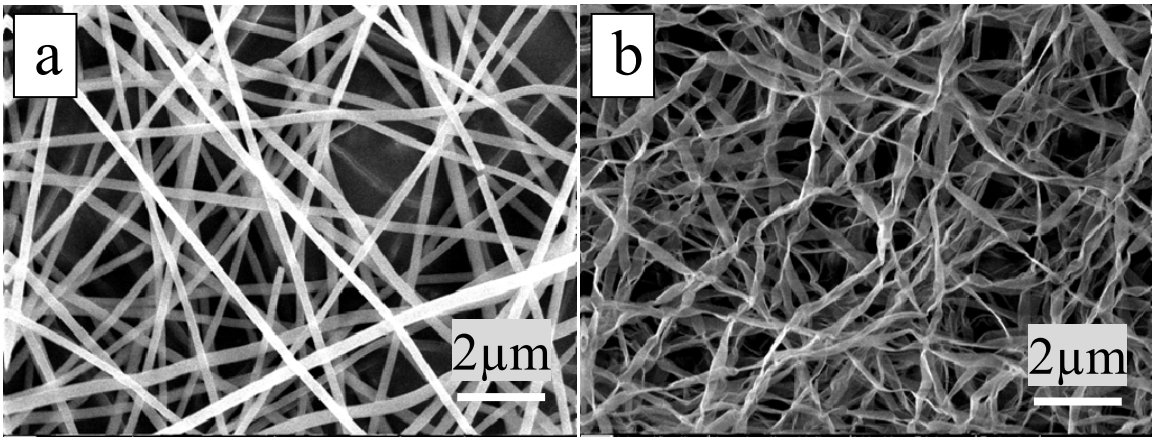


Figure 9.5. SEM images of electrospun PVA fiber before (a) and after (b) 1 cycle of TMA/water "long exposure" cycle, and annealing at 450 °C overnight. Alumina "nanobelts" are observed after annealing, indicating the formation of a thin layer of continuous film on the PVA electro-spun fiber.

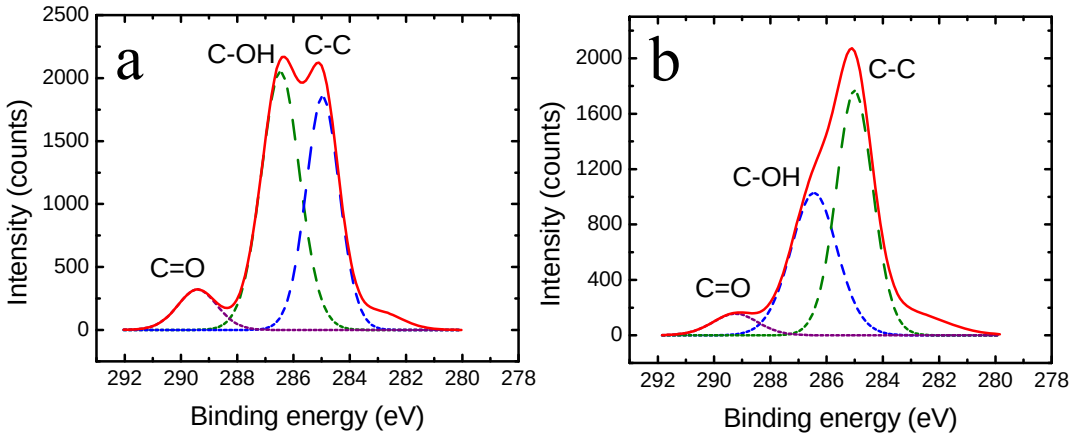


Figure 9.6. C 1s peak analysis of PVA film on Si wafer, before (a) and after (b) 1 cycle of TMA/water soaking. Significant decrease of C=O and C-OH features support the conclusion that TMA reacts with C-OH and C=O in the PVA.

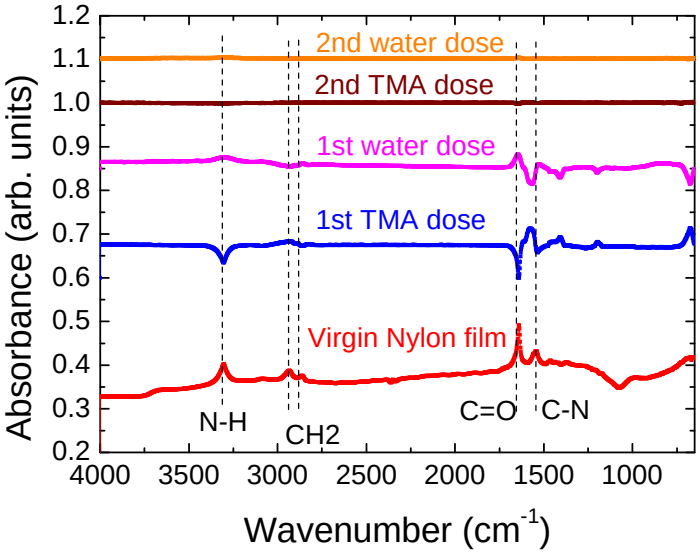


Figure 9.7. In-situ FTIR differential spectra of TMA/water deposition on spin coated Nylon-6 film. The absorbance scale is the same for all spectra. The spectra show hydrogen bonded NH stretching (3304 cm^{-1}), CH_2 stretching (2930 cm^{-1}), amide I (CO stretching) (1640 cm^{-1}), C-H stretching (2860-2930 cm^{-1}), CH_3 bending (1437 cm^{-1}, 1190 cm^{-1}) and CH_3 rocking (690 cm^{-1}). The large signal strength is consistent with a larger extent of reaction between Nylon-6 and TMA during the first ALD cycle. The peak intensity of CH_3 stretching at ~2960 cm^{-1} is ~ $1.0\pm0.3\times10^{-2}$ after the first TMA exposure.

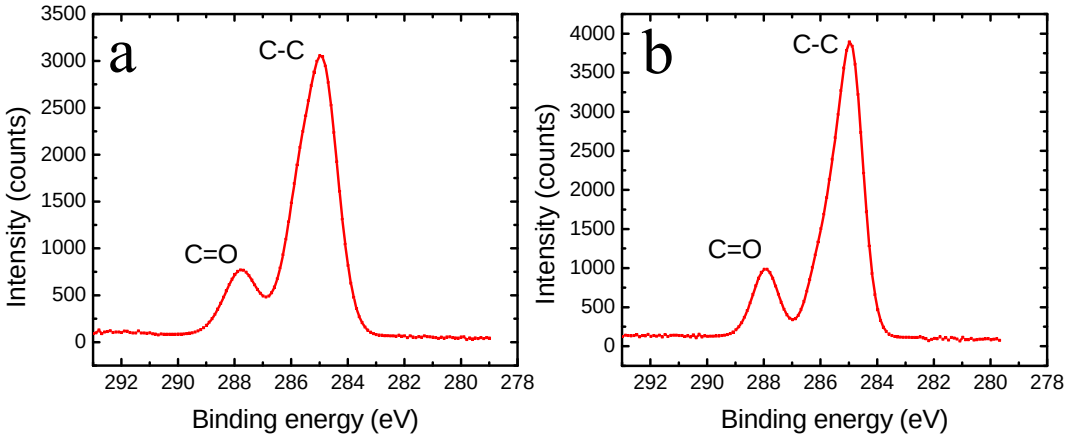


Figure 9.8. C 1s peak analysis of Nylon-6 film on Si wafer, before (a) and after (b) 1 cycle of TMA/water soaking.

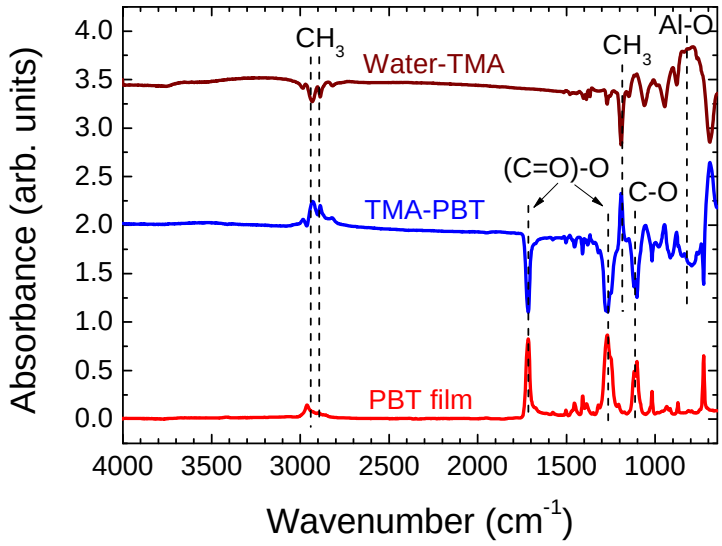


Figure 9.9. In-situ FTIR differential spectra of TMA/water deposition on PBT film on Si. After the TMA pulse, almost all the ester characteristic peaks (1720 cm^{-1} and 1260 cm^{-1}) are removed, indicating high reactivity of ester groups towards TMA vapor. The ether bond, which has a characteristic frequency of 1100 cm^{-1}, also dramatically decreased. This implies that the TMA vapor will also attach the ether bonds in PBT film. During water pulse, removal of the CH_3 related features (~2960 cm^{-1} and 1200 cm^{-1}) indicates the reaction between Al-CH_3 and water vapor. The peak intensity of CH_3 stretching at ~2960 cm^{-1} is ~0.30±0.05 after the TMA exposure.

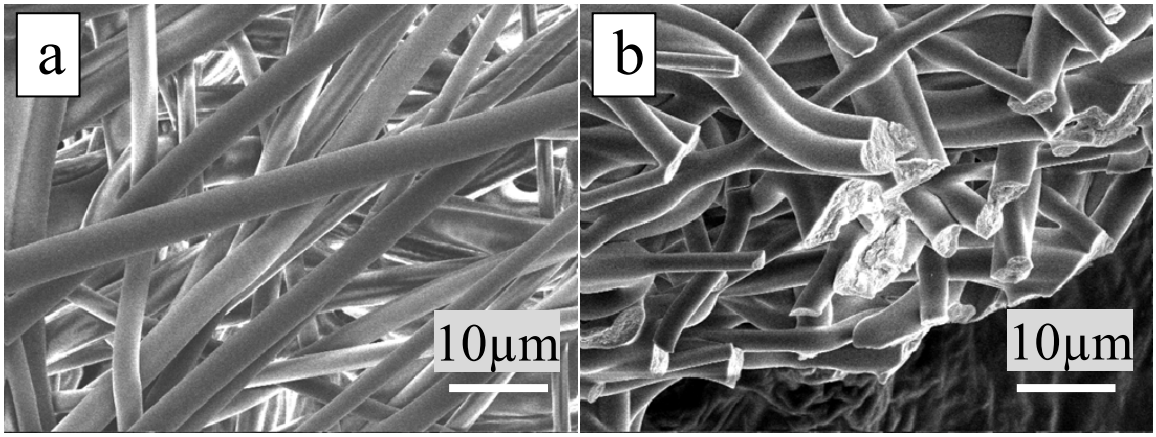


Figure 9.10. SEM images of nonwoven PBT fiber before (a) and after (b) 1 cycle of TMA/water soaking, and annealing at 450 °C overnight. Solid fibers were recovered after calcination, which indicated the TMA vapor penetrated all way through into the PBT fiber. A porous alumina fiber structure was formed which has been confirmed by N_2 adsorption/desorption analysis.

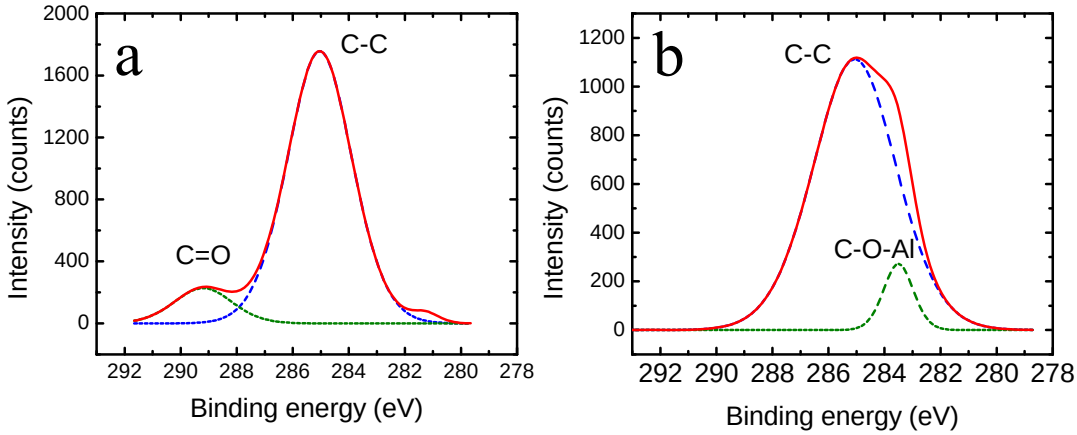


Figure 9.11. C 1s peak analysis of PBT film on Si wafer, before (a) and after (b) 1 cycle of TMA/water soaking. Complete removal of C=O and the formation of C-O-Al is consistent with the in-situ FTIR analysis.

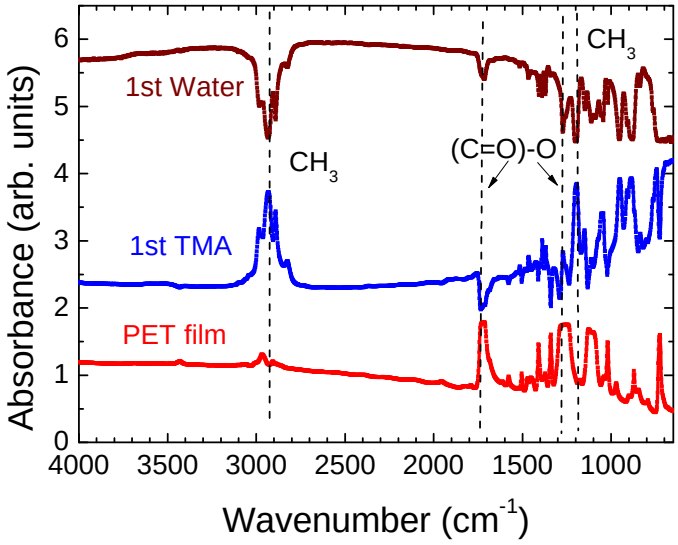


Figure 9.12. In-situ FTIR differential Spectra of TMA/water deposition on PET film on Si. Similar differential spectra were collected compared with PBT film. After the first TMA pulse, the peak intensity of CH_3 stretching at ~2960 cm^{-1} is ~ 1.42±0.1.

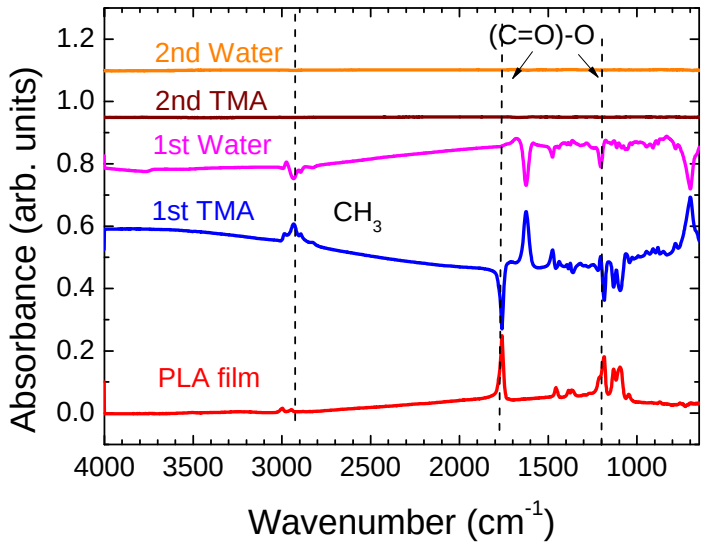


Figure 9.13. In-situ FTIR differential spectra of TMA/water deposition on spin coated PLA film on Si. Total removal of the ester characteristic peaks after TMA pulse, and new features at 1600 cm^{-1} are observed related to aluminum carbonate. After the water pulse, the CH_3 related features are removed, and the new mode at 1600 cm^{-1} is consistent with the reaction with water. The peak intensity of CH_3 asymmetric stretching at ~2960 cm^{-1} is ~ 5.3±0.5× 10^{-2}.

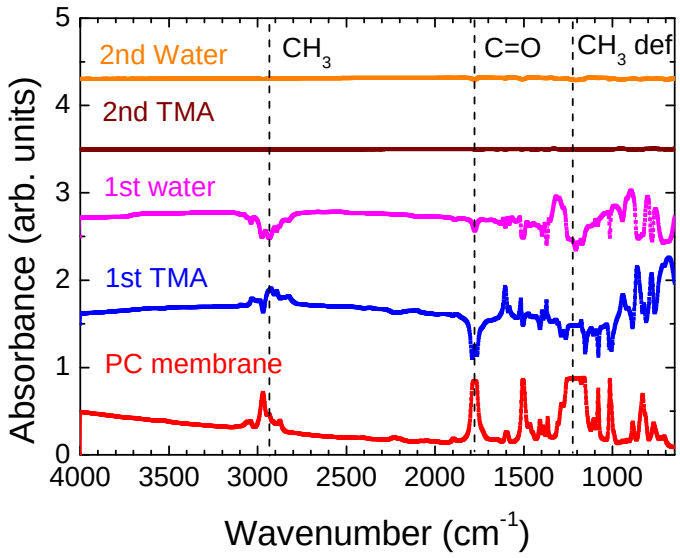


Figure 9.14. In-situ FTIR differential spectra of TMA/water deposition on polycarbonate membranes on Si. The data shows complete removal of ester characteristic peaks after the TMA pulse, and new features at 1600 cm^{-1} associated with the carbonyl-aluminum complex. After water pulse, the remove of CH_3 related features and the new mode at 1600 cm^{-1} is consistent with the reaction between Al-CH_3 and water. The peak intensity of CH_3 stretching at ~2960 cm^{-1} is ~0.31±0.06.

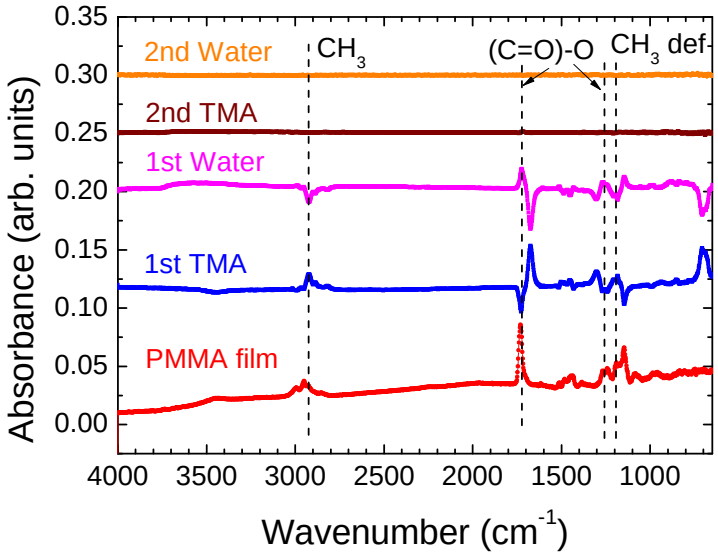


Figure 9.15. In-situ FTIR differential spectra of TMA/water deposition on PMMA film on Si. After TMA pulse, we find partial removal of the ester peaks, and again, Al-C mode at 1600 cm^{-1}. In the following water pulse, the Al-CH_3 groups react with water and form Al-OH. The peak intensity of CH_3 stretching at ~2960 cm^{-1} is ~ 1.7±0.3× 10^{-2} after the first TMA pulse.

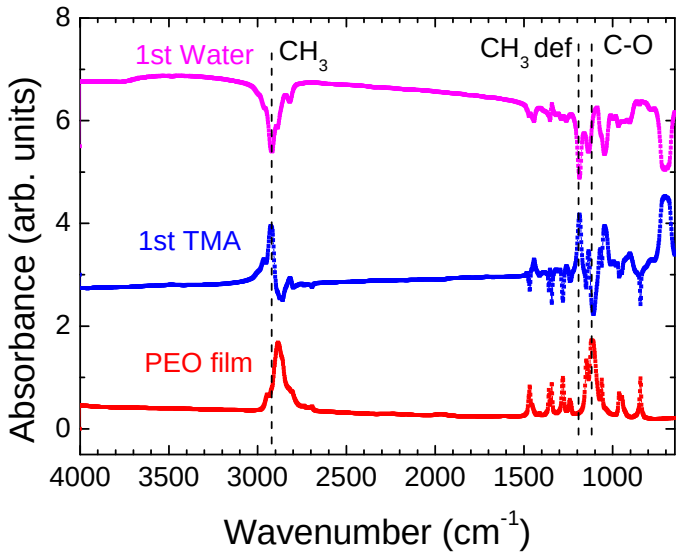


Figure 9.16. In-situ FTIR differential spectra of TMA/water deposition on PEO film on Si. Removal of ether bond at 1100 cm^{-1} shows the TMA inserts to break the C-O-C linkage in the polymer. Similarly, after the water pulse, the decrease of CH_3 stretching mode corresponds to the reaction of Al-CH_3 with water to form Al-OH. The peak intensity of CH_3 stretching at ~2960 cm^{-1} is ~ 1.10±0.1 after the first TMA exposure.

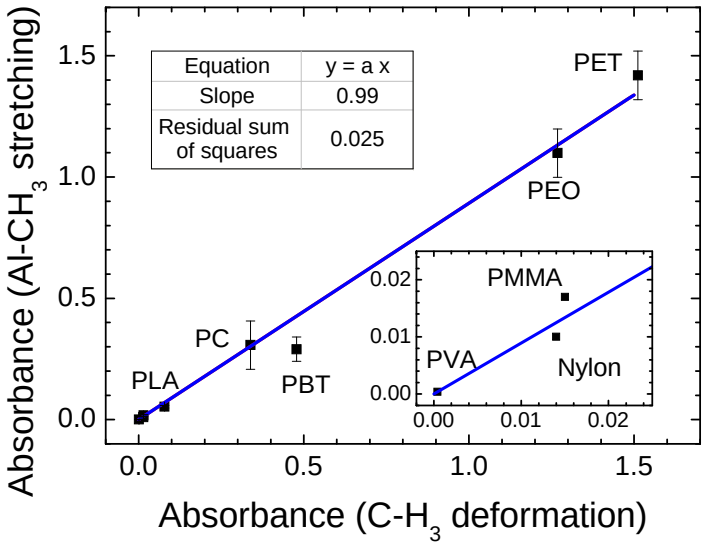


Figure 9.17. The Al-CH_3 deformation (~1200 cm^{-1}) and CH_3 asymmetric stretching (~2960 cm^{-1}) absorbance increase after first TMA pulse on different polymer substrate. The magnitude of the $\nu_a(CH_3)$ and $\delta_a(CH_3)$ intensity also displays the relative extent of reaction between the various polymers and TMA.

Table 9.1. Summary of polymer substrates studied, characteristic functional groups, and reactivity toward TMA/water ALD process. For each polymer, the TMA exposure was approximately 60seconds at 2 Torr.

Polymer	Characteristic group	# of Al-CH_3 monolayers
Polyolefin (PP fiber)	C-C	< 10
Polyvinyl Alcohol (PVA fiber)	C-OH	~ 24±6
Polyamide (PA 6)	C-(C=O)-NH-C	~ 5.9±0.9 $\times 10^2$
Polyester (PBT)	C-(C=O)-O-C	~ 1.8±0.3 $\times 10^4$
Polyester (PET)		~ 8.3±0.6 $\times 10^4$
Polyester (PLA)		~ 3.1±0.3 $\times 10^3$
Polycarbonate (PC)	C-O-(C=O)-O-C	~ 9.1±1.8 $\times 10^2$
Poly methyl methacrylate (PMMA)	C-(C=O)-O-C	~ 1.0±0.2 $\times 10^3$
Polyethylene Oxide (PEO)	C-O-C	~ 6.5±0.6 $\times 10^4$

References

1 K. Nomura; H. Ohta; A. Takagi; T. Kamiya; M. Hirano; H. Hosono; Room-temperature fabrication of transparent flexible thin-film transistors using amorphous oxide semiconductors, *Nature,* **2004**. *432*, 488.

2 J. A. Rogers; Z. Bao; K. Baldwin; A. Dodabalapur; B. Crone; V. R. Raju; V. Kuck; H. Katz; K. Amundson; J. Ewing; P. Drzaic; Paper-like electronic displays: Large-area rubber-stamped plastic sheets of electronics and microencapsulated electrophoretic inks, *Proceedings of the National Academy of Sciences of the United States of America,* **2001**. *98*, 4835.

3 D. H. Kim; J. H. Ahn; W. M. Choi; H. S. Kim; T. H. Kim; J. Z. Song; Y. G. Y. Huang; Z. J. Liu; C. Lu; J. A. Rogers; Stretchable and foldable silicon integrated circuits, *Science,* **2008**. *320*, 507.

4 D. Kuang; J. Brillet; P. Chen; M. Takata; S. Uchida; H. Miura; K. Sumioka; S. M. Zakeeruddin; M. Gratzel; Application of highly ordered TiO2 nanotube arrays in flexible dye-sensitized solar cells, *Acs Nano,* **2008**. *2*, 1113.

5 F. C. Krebs; S. A. Gevorgyan; J. Alstrup; A roll-to-roll process to flexible polymer solar cells: model studies, manufacture and operational stability studies, *Journal of Materials Chemistry,* **2009**. *19*, 5442.

6 H. Chatham; Oxygen diffusion barrier properties of transparent oxide coatings on polymeric substrates, *Surface & Coatings Technology,* **1996**. *78*, 1.

7 L. L. HenchJ. K. West; The Sol-gel Process, *Chemical Reviews,* **1990**. *90*, 33.

8 J. Livage; M. Henry; C. Sanchez; Sol-gel chemistry of Transition-metal oxides, *Progress in Solid State Chemistry,* **1988**. *18*, 259.

9 C. Y. Lee; S. Y. Li; P. Lin; T. Y. Tseng; ZnO nanowires hydrothermally grown on PET polymer substrates and their characteristics, *Journal of Nanoscience and Nanotechnology,* **2005**. *5*, 1088.

10 S. H. Yi; S. K. Choi; J. M. Jang; J. A. Kim; W. G. Jung; Low-temperature growth of ZnO nanorods by chemical bath deposition, *Journal of Colloid and Interface Science,* **2007**. *313*, 705.

11 M. Leskela; M. Ritala; Atomic layer deposition chemistry: Recent developments and future challenges, *Angewandte Chemie-International Edition,* **2003**. *42*, 5548.

12 T. Suntola; J. Hyvarinen; Atomic layer epitaxy, *Annual Review of Materials Science,* **1985**. *15*, 177.

13 S. M. George; A. W. Ott; J. W. Klaus; Surface chemistry for atomic layer growth, *Journal of Physical Chemistry,* **1996**. *100*, 13121.

14 R. L. Puurunen; Surface chemistry of atomic layer deposition: A case study for the trimethylaluminum/water process, *Journal of Applied Physics,* **2005**. *97*,

15 G. N. Parsons, in *Atomic Layer Deposition of Nanostructured Materials* (Wiley-VCH Verlag GmbH & Co. KGaA, 2011), p. 271.

16 J. D. Ferguson; A. W. Weimer; S. M. George; Atomic layer deposition of Al2O3 films on polyethylene particles, *Chemistry of Materials,* **2004**. *16*, 5602.

17 D. W. Xu; E. Graugnard; J. S. King; L. W. Zhong; C. J. Summers; Large-scale fabrication of ordered nanobowl arrays, *Nano Letters,* **2004**. *4*, 2223.

18 Q. Peng; X. Y. Sun; J. C. Spagnola; G. K. Hyde; R. J. Spontak; G. N. Parsons; Atomic layer deposition on electrospun polymer fibers as a direct route to Al2O3 microtubes with precise wall thickness control, *Nano Letters,* **2007**. *7*, 719.

19 R. H. A. Ras; M. Kemell; J. de Wit; M. Ritala; G. ten Brinke; M. Leskela; O. Ikkala; Hollow inorganic nanospheres and nanotubes with tunable wall thicknesses by atomic layer deposition on self-assembled polymeric templates, *Advanced Materials,* **2007**. *19*, 102.

20 Y. Wang; Y. Qin; A. Berger; E. Yau; C. C. He; L. B. Zhang; U. Gosele; M. Knez; M. Steinhart; Nanoscopic Morphologies in Block Copolymer Nanorods as Templates for Atomic-Layer Deposition of Semiconductors, *Advanced Materials,* **2009**. *21*, 2763.

21 M. Knez; A. Kadri; C. Wege; U. Gosele; H. Jeske; K. Nielsch; Atomic layer deposition on biological macromolecules: Metal oxide coating of tobacco mosaic virus and ferritin, *Nano Letters,* **2006**. *6*, 1172.

22 J. Y. Huang; X. D. Wang; Z. L. Wang; Controlled replication of butterfly wings for achieving tunable photonic properties, *Nano Letters,* **2006**. *6*, 2325.

23 G. K. Hyde; G. Scarel; J. C. Spagnola; Q. Peng; K. Lee; B. Gong; K. G. Roberts; K. M. Roth; C. A. Hanson; C. K. Devine; S. M. Stewart; D. Hojo; J. S. Na; J. S. Jur; G. N. Parsons; Atomic Layer Deposition and Abrupt Wetting Transitions on Nonwoven Polypropylene and Woven Cotton Fabrics, *Langmuir,* **2010**. *26*, 2550.

24 Y. Ding; S. Xu; Y. Zhang; A. C. Wang; M. H. Wang; Y. H. Xiu; C. P. Wong; Z. L. Wang; Modifying the anti-wetting property of butterfly wings and water strider legs

by atomic layer deposition coating: surface materials versus geometry, *Nanotechnology,* **2008**. *19*,

25 J. C. Spagnola; B. Gong; S. A. Arvidson; J. S. Jur; S. A. Khan; G. N. Parsons; Surface and sub-surface reactions during low temperature aluminium oxide atomic layer deposition on fiber-forming polymers, *Journal of Materials Chemistry,* **2010**. *20*, 4213.

26 J. S. Jur; J. C. Spagnola; K. Lee; B. Gong; Q. Peng; G. N. Parsons; Temperature-Dependent Subsurface Growth during Atomic Layer Deposition on Polypropylene and Cellulose Fibers, *Langmuir,* **2010**. *26*, 8239.

27 S. M. Lee; E. Pippel; U. Gosele; C. Dresbach; Y. Qin; C. V. Chandran; T. Brauniger; G. Hause; M. Knez; Greatly Increased Toughness of Infiltrated Spider Silk, *Science,* **2009**. *324*, 488.

28 L. B. Zhang; A. J. Patil; L. Li; A. Schierhorn; S. Mann; U. Gosele; M. Knez; Chemical Infiltration during Atomic Layer Deposition: Metalation of Porphyrins as Model Substrates, *Angewandte Chemie-International Edition,* **2009**. *48*, 4982.

29 T. K. Minton; B. H. Wu; J. M. Zhang; N. F. Lindholm; A. I. Abdulagatov; J. O'Patchen; S. M. George; M. D. Groner; Protecting Polymers in Space with Atomic Layer Deposition Coatings, *Acs Applied Materials & Interfaces,* **2010**. *2*, 2515.

30 C. A. Wilson; R. K. Grubbs; S. M. George; Nucleation and growth during Al2O3 atomic layer deposition on polymers, *Chemistry of Materials,* **2005**. *17*, 5625.

31 B. Gong; Q. Peng; J. S. Jur; C. K. Devine; K. Lee; G. N. Parsons; Sequential Vapor Infiltration of Metal Oxides into Sacrificial Polyester Fibers: Shape Replication and

Controlled Porosity of Microporous/Mesoporous Oxide Monoliths, *Chemistry of Materials,* **2011**. *23*, 3476.

32 K. Jayaraman; M. Kotaki; Y. Z. Zhang; X. M. Mo; S. Ramakrishna; Recent advances in polymer nanofibers, *Journal of Nanoscience and Nanotechnology,* **2004**. *4*, 52.

33 M. Ulbricht; Advanced functional polymer membranes, *Polymer,* **2006**. *47*, 2217.

34 B. Gong; Q. Peng; G. N. Parsons; Conformal Organic-Inorganic Hybrid Network Polymer Thin Films by Molecular Layer Deposition using Trimethylaluminum and Glycidol, *Journal of Physcial Chemistry B,* **2011**.

35 G. A. Atiya; A. S. Grady; D. K. Russell; T. A. Claxton; Vibrational-spectra of monomeric trimethylaluminum and trimethylgallium, *Spectrochimica Acta Part a-Molecular and Biomolecular Spectroscopy,* **1991**. *47*, 467.

36 G. S. Higashi; L. J. Rothberg; C. G. Fleming; Vibrational spectroscopy of growth surfaces during photochemical deposition of aluminum from trimethylaluminum vapor, *Chemical Physics Letters,* **1985**. *115*, 167.

37 A. C. Dillon; A. W. Ott; J. D. Way; S. M. George; Surface-chemistry of Al2O3 deposition using Al(CH3)3 and H2O in a binary reaction sequence, *Surface Science,* **1995**. *322*, 230.

38 J.-J. Max; C. Chapados; Isotope effects in liquid water by infrared spectroscopy. III. H2O and D2O spectra from 6000 to 0 cm(-1), *The Journal of chemical physics,* **2009**. *131*, 184505.

39 T. L. Tso; E. K. C. Lee; Role of hydrogen-bonding studied by the FTIR spectroscopy of the matrix-isolated molecular-complexes, dimer of H2O, H2O.CO2, H2O.CO, and H2O2.NCO in solid O-2 at 12-17-k, *Journal of Physical Chemistry,* **1985**. *89*, 1612.

40 M. D. Groner; F. H. Fabreguette; J. W. Elam; S. M. George; Low-temperature Al2O3 atomic layer deposition, *Chemistry of Materials,* **2004**. *16*, 639.

41 M. Li; M. Dai; Y. J. Chabal; Atomic Layer Deposition of Aluminum Oxide on Carboxylic Acid-Terminated Self-Assembled Monolayers, *Langmuir,* **2009**. *25*, 1911.

42 R. H. G. Brinkhuis; A. J. Schouten; Thin-film behavior of poly(methyl methacrylates) .2. an FT-IR study of langmuir-blodgett-films of isotactic PMMA, *Macromolecules,* **1991**. *24*, 1496.

43 D. N. Goldstein; J. A. McCormick; S. M. George; Al2O3 Atomic Layer Deposition with Trimethylaluminum and Ozone Studied by in Situ Transmission FTIR Spectroscopy and Quadrupole Mass Spectrometry, *Journal of Physical Chemistry C,* **2008**. *112*, 19530.

CHAPTER 10 is a reprint of a manuscript published in Chem. Mater.

CHAPTER 10. Sequential Vapor Infiltration of Metal Oxides into Sacrificial Polyester Fibers: Shape Replication and Controlled Porosity of Micro/Mesoporous Oxide Monoliths

Bo Gong, Qing Peng, Jesse S. Jur, Christina K. Devine, Kyoungmi Lee

and Gregory N Parsons

Department of Chemical and Biomolecular Engineering,

North Carolina State University,

Raleigh NC 27695, USA

Abstract

Preparation of microporous and mesoporous metal oxide materials continues to attracted considerable attention because of their possible use in chemical separations, catalyst support, chemical sensors, optical and electronic devices, energy storage and solar cells. While many methods are known for the synthesis of porous materials, researchers continue to seek new methods to control pore size distribution and macroscale morphology. In this work, we show that sequential vapor infiltration (SVI) can yield shape-controlled micro/mesoporous materials with tunable pore size using polyesters a sacrificial template. The reaction proceeds by exposing polymer fibers templates to a controlled sequence of metal organic and co-reactant vapor exposure cycles in an atomic layer deposition (ALD) reactor. The inorganic and co-reactant infuse sequentially, and thereby distribute and react uniformly within in the polymer, to yield an organic-inorganic hybrid material that retains the physical dimensions of the original polymer template. Subsequent calcination in air results in an inorganic micro/mesoporous material that again retains the macroscopic physical shape of the starting polymer matrix. The micro/mesoporous structure is confirmed by microscopy and nitrogen adsorption/desorption analysis, and the resulting pore size is controlled by the size of the starting polymer repeat unit and by the kinetics of the infiltration/annealing process steps. In-situ infrared transmission and quartz crystal microbalance results confirm the chemical reaction mechanisms. The chemical transformation that occurs during sequential vapor infiltration could be important for a range of applications that utilize well-defined porous nanostructures.

10.1. Introduction

Nano-porous materials are critical in many advancing technologies, including chemical separations, catalysis, chemical sensors, optical and electronic devices, energy storage and solar energy conversion cells.[1,2] Porous materials are often prepared by solution based methods, including sol-gel and hydrothermal processes, using structure directed templates, such as surfactants and amphiphilic block-copolymers, to control pore size distribution and surface area.[3,4] In addition, self-recognition and self-assembly chemistry can readily integrate with these process to prepare new types of porous materials including organic frameworks[5-8], covalent organic frameworks,[9-11] intrinsic porous polymers[12-14] and porous molecular cages.[15-18] A common drawback is that most methods require aqueous or organic solvents and long synthesis and processing times. Moreover, the material morphology that results from these methods is limited to films, i.e. formed by casting, or to powders.[19] New methods that can produce continuous porous materials with well-defined pore size distribution, while simultaneously enabling material structures with predetermined macro-scale size, shape and contour could enable new device functionality, such as defect free gas separation modules and structured porous materials for drug delivery, chemical sensing and energy storage and conversion.

Organic-inorganic hybrid templates are known to work well as sacrificial templates for inorganic porous structures with predefined macro morphology.[20,21] Calcination of the hybrid material generates a purely inorganic compound, with form and shape that replicates the starting polymer. In order to prepare hybrid materials from solid polymer templates, researchers have developed several solution based infiltration methods.[22,23] Unfortunately,

solvents often lead to swelling and dissolution of the starting polymer, and careful control of the pH and humidity are needed to slow down the reactions to uniformly disperse the metal oxide within the polymer matrix.

Vapor processing provides a solvent free environment for the chemical modification of organic structures where water can be controlled at the parts per million scale or better. Reagent exposure pressure, time, and temperature are also readily adjusted. Recent studies of vapor phase surface modification of polymers by inorganic atomic layer deposition[24-26] (ALD) demonstrated that metal oxide precursors often diffuse sub-surface into the polymer, creating a graded organic/inorganic interface region. The extent of subsurface diffusion and deposition during ALD on polymers is known to be affected by reaction temperature, extent of precursor exposure and the specific chemical interactions between the precursors and reactive groups in the polymer.[24-26] Other studies show that vapor infiltration alters the chemical and mechanical properties of natural polymer materials.[27,28] We can promote subsurface species diffusion and reaction during vapor exposure, for example by carefully selecting the polymer template, metal organic precursor, and the extent of precursor exposure. In this work we show that by allowing the subsurface precursor diffusion/reaction and sequence co-reactant diffusion to approach saturation, we can produce a homogeneous organic-inorganic hybrid material that retains the form and shape of the starting polymer template. Calcination yields a porous inorganic solid with pore size and pore size distribution controlled by the details of the infiltration and calcination process steps, where again, the shape of the resulting solid matrix directly mimics the starting nonwoven polymer

fiber web. Specifically, we examine the detailed reaction processes during the infiltration and reaction of metal organic precursors (such as trimethyl aluminum and titanium tetrachloride) with various polyester fibers, resulting in a set of different covalently coordinated organic-inorganic solid cylindrical matrices. The reaction proceeds in common ALD processing equipment, in an environment with well-controlled pressure and temperature, where the metal organic exposure is typically followed by an inert gas purge and a subsequent co-reactant exposure step. We also report the relationship between reactant exposure time, temperature and extent of reaction between the polymer and the reactants, and how the details of the reaction and annealing conditions affect pore distribution. Using higher temperature and longer infiltration times during metal organic exposure we find that the pore size shrinks and the size distribution narrows, where the size approaches the monomer unit dimension in the starting polymer. This indicates that polymer structure acts to template the porous oxide structure. Thus, by choosing the starting polyester monomer length, the pore size could be pre-selected and adjusted which will be useful for separations, vapor and other important applications.

10.2. Experimental Procedures

Chemicals and Materials

All materials and chemicals were purchased commercially and used as received. Trimethyl aluminum (TMA, 95%) and diethyl zinc (DEZ, 98%) were purchased from Strem chemicals, and titanium tetrachloride (TCl_4, 99%) was purchased from Gelest. The oxygen source was deionized water. The reactant carrier and purge gas was ultra high purity Argon

(99.999%) (National Welders), and it was further purified using a Gatekeeper inert gas purifier (rated to <100 parts per trillion H_2O and O_2) before flowing into the reactor. For infrared transmission studies on planar deposited films, we used double-side-polished high resistivity (50-100 ohm-cm) n-type Si (100) wafer substrates to provide uniform 60% infrared transmittance over the middle infrared region. Before use, all silicon wafers were first cleaned by dipping into a JTP cleaning solution for 2 minutes, followed by 5 minute deionized water flow rinse then dried under high purity (99%) nitrogen flow. Polybutylene terephthalate (PBT), polyethylene terephthalate (PET), polylactic acid (PLA) and poly ethylene naphthalate (PEN) nonwoven fiber mats were acquired from the Nonwoven Cooperative Research Center at NC State University. Tri-fluorine acetic acid (TFA) and PBT pellets (MW ~38,000) were purchased from Sigma-Aldrich.

Reactor and In-situ Analysis

Sequential vapor infiltration (SVI) of TMA, $TiCl_4$ and water into the polymer substrates was carried out in a homemade viscous flow atomic layer deposition (ALD) reactor, described previously.[29] The working pressure in the reactor during gas purge cycle was ~ 1 Torr. A typical SVI process used a sequence of 60 exposure steps, where each exposure step included flowing TMA into the reactor for 10 seconds followed by sealing the reactor at fixed pressure (~ 2 Torr) for 60 seconds, then purging the reactor with argon for 20 seconds. This sequence corresponded to one TMA "soak" cycle. After 60 TMA soak steps (a total soak time of one hour), the reactor was purged with Ar for 15 mins, then 20 water soak steps were performed using the same timing sequence before removing the sample from the

reactor. For some fiber samples, a long continuous soak scheme was used, which included a exposure the sample to ~7 Torr of TMA or $TiCl_4$ vapor for ~ 18 hr, followed by a purge with Ar for 30 mins and a soak in 5 Torr of water vapor for ~1 hr.

We equipped the reactor with in situ quartz crystal microbalance (QCM) sensor, and used it to monitor mass uptake during the reactant exposures. For this experiment, PBT polymer pellets were dissolved in tri-fluorine acetic acid, and a ~ 200 nm thick PBT film was spun-coat onto a QCM crystal, then mounted to the QCM housing using conductive silver epoxy. The QCM head was then positioned in the reaction chamber at the center deposition site. The sensor head was modified to allow inert gas flow (~ 10 sccm) to the backside of the QCM crystal to locally prevent film deposition and protect the electrical contacts. A film thickness monitor (Maxtek TM-400) recorded the mass change using a Labview program. The QCM setup is very sensitive to temperature and environment pressure, so to ensure that the temperature and pressure were stable within the reactor, the reactor with the QCM setup was allowed to purge with Argon for several hours before collecting data.

A second reactor, also described elsewhere,[30] was designed and equipped for in-situ infrared transmission analysis. It permitted collection and analysis of Fourier transform infrared (FTIR) transmission spectra during the purge cycle after the soak steps, without removing the sample from the reactor. For these studies, we spun-coat PBT films on silicon IR substrates using PBT polymer pellets dissolved in tri-fluorine acetic acid. A Thermo Scientific Nicolet 6700 IR system with an external MCT-A detector was used for the in-situ FTIR analysis. The spectrometer operated in transmittance mode in the frequency range

from 4000 to 650 cm^{-1}. Spectra were collected at 4 cm^{-1} resolution using 200 scans, corresponding to a data collection time of ~ 2 minutes per spectrum. A reference IR spectrum of the substrate was collected before the initial reactant dose. To better visualize the chemical reactions upon reactant exposure, all spectra are displayed in differential mode where the previously collected spectrum was subtracted as the reference.

After infiltrating the polymer with the metal organic precursor, calcination removed the organic species to produce the porous inorganic solid. The samples were heated in air for 12 hours to achieve full calcination. During heating, the temperature was carefully ramped at 10 °C/min to ensure temperature uniformity.

Post-Reaction Characterization

The morphology of polymer fibers as received, after sequential vapor infiltration, and after calcination was imaged using a FEI XL30 Scanning Electron Microscope (SEM). Before imaging, samples were sputter-coated with ~5 nm of gold/ palladium to prevent charging. The SEM operated at a voltage of 7 kV with a working distance of 5 mm. For cross-sectional imaging, we used a Hitachi HF 2000 Cold Field Emission transmission electron microscope (TEM) capable of 0.2 nm point resolution operated at 200 kV. The TEM is also equipped with an Oxford Link INCA energy dispersive X-ray spectroscopy (EDS), which was used to evaluate elemental composition during TEM analysis. The TEM samples were prepared using a Quanta 200 3D Focused Ion Beam system.

The surface area, pore volume, and average pore size of the resulting materials were measured to quantify the nature of the porous material formed after sample calcination. We

measured pore size distribution and surface area using a Quantachrome Autosorb-1C equipped with the ASWin software package. Nitrogen adsorption/desorption isotherms were performed using ~ 30 mg of sample and a 40 point adsorption/desorption scheme with standard micropore analysis ($2\times10^{-6} \leq P/P_o \leq 1.0$). Before analysis, the sample was allowed to outgas at 350°C at the outgas port of the Autosorb 1 for more than 4 hours. Surface areas were calculated by applying Brunauer-Emmet-Teller (BET) theory over the linear region of the isotherm ($0.05 \leq P/P_o \leq 0.30$). Pore size distributions were calculated in the ASWin software package using the non-local density functional theory method with the slit pore carbon equilibrium transition kernel. In addition to the N_2 adsorption/desorption analysis, similar experiments employing hydrogen allowed us to evaluate the hydrogen storage capability of the porous oxides.

We performed X-ray photoelectron spectroscopy (XPS) analysis using a Riber XPS system with a monochromatic Al Kα source. The pass energies for the survey and detail scans were 160 and 20 eV, respectively. For normalization, we set the adventitious C 1s peak to 284.5 eV. X-ray diffraction studies employed a Philips Xpert Pro MRD HR X-ray diffraction system to determine the atomic structure of the starting PBT polymer, and the organic-inorganic materials.

We also performed differential scanning calorimetry (DSC) and thermal gravimetric analysis (TGA) on vapor phase infiltrated organic-inorganic materials. A TA-Instruments DSC Q2000 was employed to measure the heat flow of untreated PBT fiber and TMA/water soaked PBT fiber in the temperature range from 0 to 275°C. A TA-Instruments TGAs-Q5000

was used to test the mass loss upon heating for the untreated and TMA/water soaked PBT fiber up to 900°C. Before each set of TGA tests, calibration runs were recorded using 10-15 mg of platinum plate freshly cleaned and annealed under a propane torch. The temperature ramp speed was typically fixed at 10°C/min.

10.3. Results and Discussion

Imaging and Nitrogen Adsorption/Desorption Analysis of Post-annealed Materials

Figure 10.1(a) shows a photograph of an untreated PBT nonwoven fiber mesh, a similar piece of nonwoven fiber after sequential vapor infiltration, and a similar sized piece again after high temperature calcination. Note that each treatment step produces a decrease in overall sample dimension. The brownish color after annealing is likely due to a small amount of carbon residue remaining in the sample. Figure 10.1 (b) presents an SEM image of the untreated nonwoven PBT, showing a uniform mat of randomly distributed individual fiber units with diameter of ~ 5 m. Figures 10.1(c) and (d) show similar fibers after TMA (60 min) / H_2O (20 min) vapor soak at 80°C followed by 24 hr calcination in air at 450°C. After treatment, the macroscopic fiber diameter is smaller, but the overall macroscopic structure not significantly changed. Figure 10.1(c) shows some connectivity between fibers after treatment that is not present before. Some polymer flow could be expected due to polymer chain scission and/or local heating during TMA/polymer reaction. A broken fiber in Figure 10.1(d) clearly shows a uniform cross section after high temperature calcination. As will be shown below, the treatment process effectively converts the fibers from a polymer to a highly porous inorganic solid. The images in Figure 10.1 show that the materials transformation

maintains the macroscopic fibrous shape, and framework of the original starting polymer. The conversion process involves TMA/PBT reaction, followed by metal-organic ligand oxidation (during water exposure) and organic combustion (during post treatment calcination). The uniform cross section after high temperature calcination supports the conclusion that TMA permeates individual fibers and reacts throughout the PBT polymer fiber bulk.

Cross sectional TEM images in Figure 10.2 show the fiber cross section on a relatively large scale (panel a), as well on a more detailed level (panel b and inset) for PBT fibers after TMA/water SVI and calcination treatments. Some contrast in the fiber radial direction may be present in the image in Figure 10.2(a), suggesting a small density gradient. At higher magnification, Figure 10.2(b) shows a uniform distributed mesoporous structure. Upon closer inspection (inset in panel b), the pores with size in the 5-10 nm range are readily visible, consistent with pore size results discussed below. The EDS spectrum collected from the TEM sample shows aluminum, oxygen and trace amount of carbon. Altogether, the images show good microscopic uniformity after infiltration and thermal treatment.

We explored several metal-organic/polymer combinations and measured specific surface area and pore size distribution using N_2 adsorption/desorption analysis. Table 10.1 summarizes the results. Results show that the pore size and size distribution are influenced by soaking and calcination time and temperature. Figure 10.3(a) displays example nitrogen and hydrogen adsorption/desorption isotherms collected at 77K after a 100 mg PBT fiber mat was soaked in TMA (18 h) / water (1 h) at 80°C, then annealed for 12 h at 450°C in air. The

resulting Brunauer-Emmett-Teller (BET) surface area is ~439 m^2/g, which is significantly larger than 0.71 m^2/g measured on untreated PBT fibers. The loop between adsorption and desorption curve is correlated to type E hysteresis, which is attributed to the present of "ink bottle" pores.[31] In addition, at 77K under atmosphere pressure, the treated sample can absorb 24.4 cc/g of hydrogen (at standard state), corresponding to ~0.22 wt %. The top-most trace in Figure 10.3(b) provides information on the pore size distribution for this sample. The sample contains micropores with ~1 nm pore width, along with mesopores with diameter between 2 and 4 nm.

The TMA/water soak time strongly influences the final pore structure. The lower trace in Figure 10.3(b) shows that a 1 hr TMA soak period produces a 5.45 nm average pore size, which is larger than 3.23 nm measured after an 18 hr soak. This average pore size is consistent with the cross-section TEM image in Figure 10.2(b). We expect that the extended exposure time permits a more complete reaction between the metal-organic and the polymer, producing a tighter network with smaller pores. Smaller pores are also produced at higher infiltration/reaction temperature, as shown in Figure 10.3(c), also consistent with a larger extent of metal organic/polymer reaction. The results in Figure 10.3(d) show that at a fixed reaction temperature of 80°C, increasing the calcination temperature from 100 to 800°C increases the average pore size and pore volume substantially. The increased pore size at high temperature could be induced, for example, by a more completely removal of the organic component and/or by pore reconstruction induced by alumina crystallization.

Interestingly, we find that the starting polymer repeat unit provides a template that

shapes the pore size attained during calcination. Specifically, we treated PLA, PET, PBT and PEN polyesters to the TMA sequential vapor infiltration for 18 hours at 80°C followed by water exposure and calcination at 450°C. The starting repeat unit length in PLA, PET, PBT and PEN are 0.36, 0.86, 1.05 and 1.10 nm, respectively, and after processing, the corresponding average pore size was 1.41, 1.49, 3.22, and 2.68 nm, respectively. The polymers with larger repeat units tend to result in oxides with larger pores. In the set above, the exception is for PBT, where the pores are larger than the monomer size trend would suggest. The PBT polymer has a high crystalline density, and the crystal domains could impede TMA diffusion and reactivity leading to regions of polymer that remain unreacted. Hence, slower diffusion kinetics in the crystalline phase will lead to larger pores after calcination. We explored this further by allowing the TMA infiltration into PBT to proceed for a longer time at higher temperature. If the kinetic limitation holds true, then pushing the reaction toward equilibrium (and saturation), will produce smaller pores. The results in Figure 10.3(b) and (c) support this hypothesis. Increasing TMA soak time and/or temperature sharpens the peak and shifts it down in size, demonstrating smaller and more uniform pores. Soaking the PBT at 160°C for 18h produces pores that are ~ 1.75 nm which approaches the ~1.05 nm PBT repeat unit length. These results therefore point to an explanation for the change in pore shape with infiltration time and temperature, as well as suggest a practical approach to produce porous oxide materials with pre-determined pore size and size distribution.

We also infiltrated $TiCl_4$ and diethyl zinc vapors into PBT, followed by calcination and characterization. Figure 10.4 shows results from N_2 isothermal adsorption of

mesoporous titanium dioxide obtained by exposing PBT to $TiCl_4$/water at 160 °C and annealing at 450 °C in air. We find that under the same soak and calcination conditions, the $TiCl_4$ treatment produces a larger pore width (4.2 nm for $TiCl_4$ vs. 1.75 nm for TMA). A similar increase in pore size results when PEN is exposed to $TiCl_4$ vs TMA (3.6 vs 2.7 nm, respectively). We expect that a slower reaction between the polyester and the $TiCl_4$ compared to polyester/TMA could produce a larger pore diameter.

Exposing PBT, PEN and PBT to diethyl zinc and water vapor produced little reaction, and calcination yielded no measureable oxide residue. We hypothesize that the TMA or $TiCl_4$ adsorption sequence involves Lewis acid/base adduct formation at oxygen lone pair sites. The DEZ is a weaker Lewis acid and is less likely to form the adduct state. Also, its larger size compared to TMA and $TiCl_4$ also impedes diffusion into the polymer matrix.

In-situ Characterization of TMA/water Infiltration of PBT

We applied in-situ QCM and FTIR to monitor chemical interactions during vapor phase polymer infiltration. For the QCM analysis, PBT was spun coat onto quartz crystal substrates and mass uptake was measured upon exposure to a sequence of TMA and water vapor "micro-doses", consisting of 2 sec exposure followed by 40 sec argon purge at 80°C. After 400 TMA/argon micro-dose cycles, the reaction vessel was purged for 10 min, and then exposed to 100 water/argon micro-doses with the same duration. The QCM results in Figure 10.5(a) show an initial large mass uptake followed by saturation after ~ 400 micro-doses, indicating reaction completion. After this, exposure to water/argon micro-doses produces a net mass decrease followed by saturation after ~100 dose steps. A closer view of data from

the first 30 TMA/Ar cycles is displayed in Figure 10.5(b), showing each TMA dose produced mass uptake, followed by mass decrease during the purge step. The mass decrease is ascribed to desorption of TMA that is not tightly bound to the polymer. The total mass uptake recorded over 400 cycles is approximately 90 g which is significantly larger than ~40 ng measured for saturating exposure of TMA during Al_2O_3 ALD on a planar dense substrate.[30,32,33] The mass uptake confirms significant TMA absorption into the PBT film. The overall mass decrease during water exposure suggests loss of organic composition, possibly through combustion reactions, to form Al-O-Al linkages. Interestingly, we found that removing the TMA-exposed samples from the reactor and exposing them to air could lead to spontaneous sample ignition, which is expected with pyrophoric TMA remaining within the fiber matrix. On the other hand, samples exposed to both TMA and water were stable in air and safe to handle.

Infrared transmission results provide insight into the reaction mechanisms, and Figure 10.6 displays results collected in-situ during TMA and water soaking into a PBT film spun onto silicon. The spectrum for untreated polybutylene terephthalate (bottom-most trace) displays modes for C-O stretch at 1270 cm^{-1}, C=O stretch at 1720 cm^{-1}, C-O-C stretch at 1100 cm^{-1} and C-H_2 symmetric and asymmetric stretching at 2860 and 2925 cm^{-1}, respectively. The next trace shows the spectral change upon TMA exposure at 80°C. In this case, TMA was allowed to flow in the reactor for 10 sec, and then the reactor was sealed for 60 sec. The system was then purged with argon, and data was collected during the argon purge step. The previous collected spectrum was subtracted as background, producing a differential spectrum. Negative-going modes a 1720 and 1270 cm^{-1} correspond to removal of

carbonyl stretching modes, and negative features at 1100 cm^{-1} show removal of C-O-C groups. Positive signals at 2960 cm^{-1} and 1200 cm^{-1} indicate appearance C-H_3 stretching features, indicative of the methyl groups on TMA. A new mode at 680 cm^{-1} is ascribed to Al-C bonds formed upon the TMA reaction. These changes demonstrate that TMA reacted with the carbonyl group on the PBT to form C-O-Al-$(CH_3)_2$ and C-CH_3 groups. The top-most spectrum in Figure 10.6 was collected after the water vapor exposure step at 80°C, following the same cycle timing used for TMA/argon. This shows removal of Al-CH_3 modes and formation of Al-O and OH features. A simplified scheme showing possible reactions between the PBT, trimethyl aluminum and water is shown in Figure 10.7. Trimethyl aluminum could attack nucleophilic carbonyl groups in the polyester to break the C=O ester bond, resulting in a methyl group transfer to the carbonyl carbon and formation of aluminum alkyl oxide. Computational results from Derk et al.[34] predict that the reaction between TMA and the ester group in methyl acetate will react exothermically through 1,2 carbonyl addition with an overall heat of reaction of -32.7 kcal/mol. This is almost as large as the -36.8 kcal/mol heat of reaction they predict for the hydroxylation of TMA by water to produce methane. We speculate that an additional reaction between trimethyl aluminum and PBT may involve TMA insertion into ether linkages in the polymer backbone, to break the polymer chain and produce a methyl termination and a corresponding Al-$(CH_3)_2$ terminal group. Derk et al. also considered the reaction between TMA and dimethyl ether to form $(CH_3)_2$-Al-CH_2-CH_3 and ethane[34] and found it to be overall exothermic with overall heat of reaction of -38.7 kcal/mol. However, the reaction is predicted to proceed through a relatively high energy transition state which could impede the net reaction kinetics. During water pulses, the Al-CH_3 groups

readily react with water to form Al-OH, or undergo other reactions to form Al-O-Al network bonds.

Chemical and Thermal Analysis of Infiltrated Materials

After fully reacting PBT in TMA/water (before calcination), X-ray photoelectron spectroscopy showed nearly 1:3 Al:C atomic ratio (12.7 at.% Al : 37.2 at.% C), confirming significant aluminum infiltration. The C 1s spectral features collected before and after processing (Figure 10.8) confirm removal of C=O and formation of C-O-Al. The TMA/water soaked PBT fiber (before calcination) is X-ray amorphous, with no diffraction peaks detected. Figure 10.9 shows DSC and TGA analysis of untreated and SVI treated PBT fibers (without calcination). The DSC analysis of the untreated PBT shown in Figure 10.9(a) indicated a clear increase of heat flow at approximately 220°C, consistent with expected melting point (T_m) for PBT. The thermal gravimetric analysis of untreated PBT fibers (Figure 10.9(b)) exhibited >90% mass loss at ~400°C and 100 % loss by 525 °C. The DSC trace in Figure 10.9(c) for the SVI treated PBT showed no obvious T_m, further revealing disruption of the polymer structure by TMA/water infiltration. This sample also showed continuous mass loss with ~25% remaining after heating to 900°C. In principle, one may expect that if the TMA/water fully reacted with all the carbonyl groups in the polymer chain, it could result in a uniform microporous structure with average pore size comparable to the nanometer or sub-nanometer dimension of the remaining organic groups. The 25% remaining mass observed by TGA indicates a larger organic fraction, consistent with mesopores a few nanometers in size.

The thermal and ambient stability of the material after infiltration is also of interest. Figure 10.10 shows ex-situ FTIR analysis of a PBT film soaked in TMA/water at 80°C, immediately after removing it from the reactor and after several hours in ambient laboratory air. The as-soaked material shows modes associated with CH_3 and CH_2 stretching, and a broad absorbance band centered near 700 cm^{-1} due to Al-O stretching vibrations. After one hour of air exposure, significant hydroxyl group absorption is observed between 3000 and 3700 cm^{-1} due to moisture uptake from the ambient. With extended exposure, the hydroxyl group intensity stays relatively stable, but a continued decrease of organic-related mode intensity is evidence for continued volatilization of the organic component. The top-most spectrum in Figure 10.10 obtained from the sample after anneal in air at 450 °C for 120 min shows only Al-O stretching, demonstrating formation of an Al_2O_3 matrix.

10.4. Conclusions

This work demonstrates a new approach for synthesis of shape-controlled micro/mesoporous materials using polyesters as sacrificial templates. Vapor phase trimethyl aluminum and titanium tetrachloride precursors can diffuse into polyester fibers, including PBT, PET, PLA and PEN, and using water as a co-reactant produce a matrix network hybrid organic-inorganic polymer. This polymer readily transforms upon anneal in air to yield a porous inorganic Al_2O_3 or TiO_2 solid monolith. Moreover, the shape and macroscopic physical appearance of the inorganic solid faithfully duplicates that of the original starting polymer. The proposed reaction sequence during TMA/water exposure on PBT involves a large TMA mass uptake and removal of (C=O)-O bonding units through TMA interaction with the ester bond in the PBT backbone, likely through Lewis acid/base adducts.

Experiments using a relatively weak Lewis acid such as diethyl zinc as the metal source do not produce similar reactions, consistent with the proposed reaction mechanism. The micro/mesoporous structure is confirmed using cross-sectional transmission electron microscopy and nitrogen absorption/desorption experiments. The pore size and volume depend systematically on the detailed process conditions. The data shows that the starting polymer repeat unit acts to template the resulting inorganic pore size. The ability to prepare porous inorganic solids with tunable pore size, where the monolith shape is preselected by the shape of the starting polymer template could be useful for catalytic support structures, chemical and electrochemical separations, and other porous membrane systems. This process is also open to a wide range of inorganic components and a variety of different starting polymers, allowing significant versatility over the final product design.

Acknowledgments

This project was funded through the US National Science Foundation under grant # 1034374.

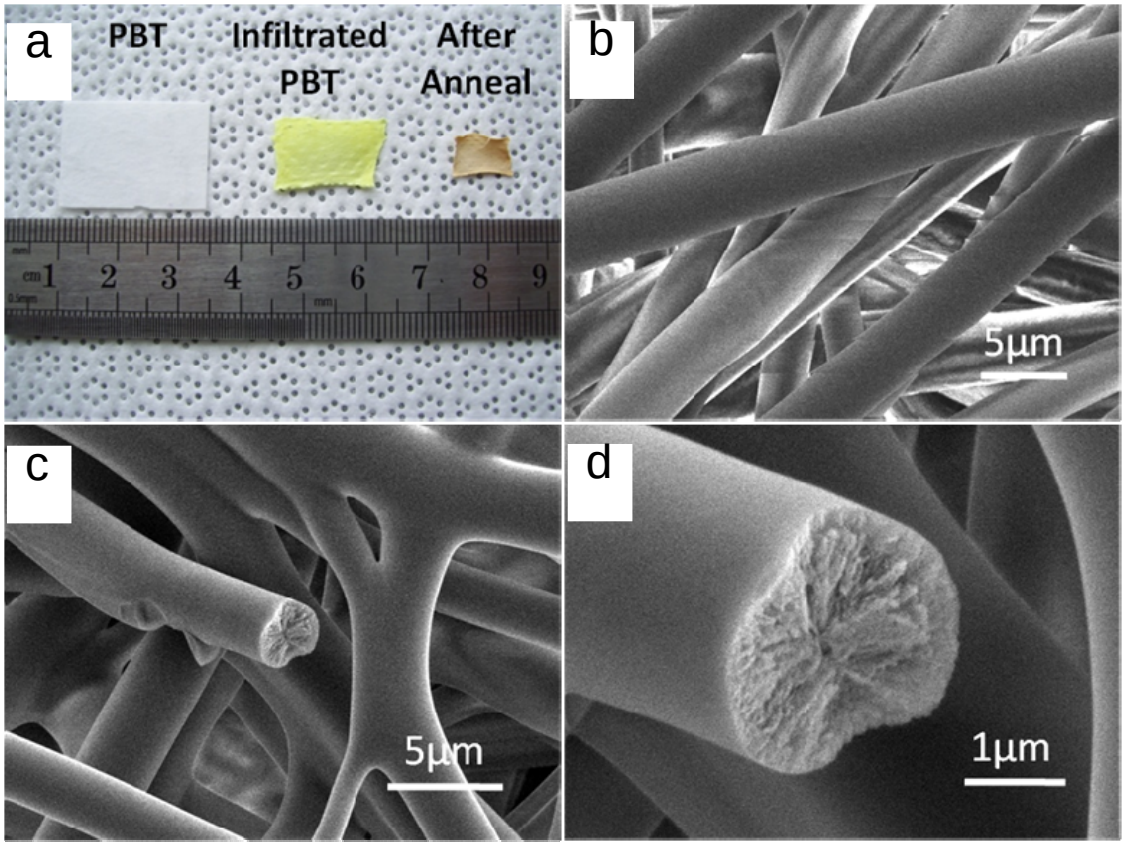


Figure 10.1. Panel (a) presents a picture of polybutylene terephthalate (PBT) nonwoven fiber mats: (left) as received; (middle) after TMA/water infiltration; and (right) after infiltration and anneal at 450°C. The starting size for all samples was approximately the same. After infiltration, the fiber mat becomes yellow in color, shrinks in size and becomes mechanically stiffer. Annealing causes more shrinkage, and the sample becomes more brittle, consistent with transformation of the polymer to micron-sized alumina fibers. Panel (b) shows a scanning electron microscope image of the as-received PBT nonwoven. Panels (c) and (d) show a similar sample after 1 h TMA/water soaking and 12 h 450°C anneal. The images in (c) and (d) show that the soaking and annealing preserves the starting fiber morphology. Some connectivity between the fibers likely results from polymer flow during the soaking process. More connectivity was observed with higher process temperature and longer precursor exposure. The cross-sectional view in panel (d) confirms that the fibers are uniform after calcination, indicating full penetration of the precursor throughout the 3 µm diameter starting fiber.

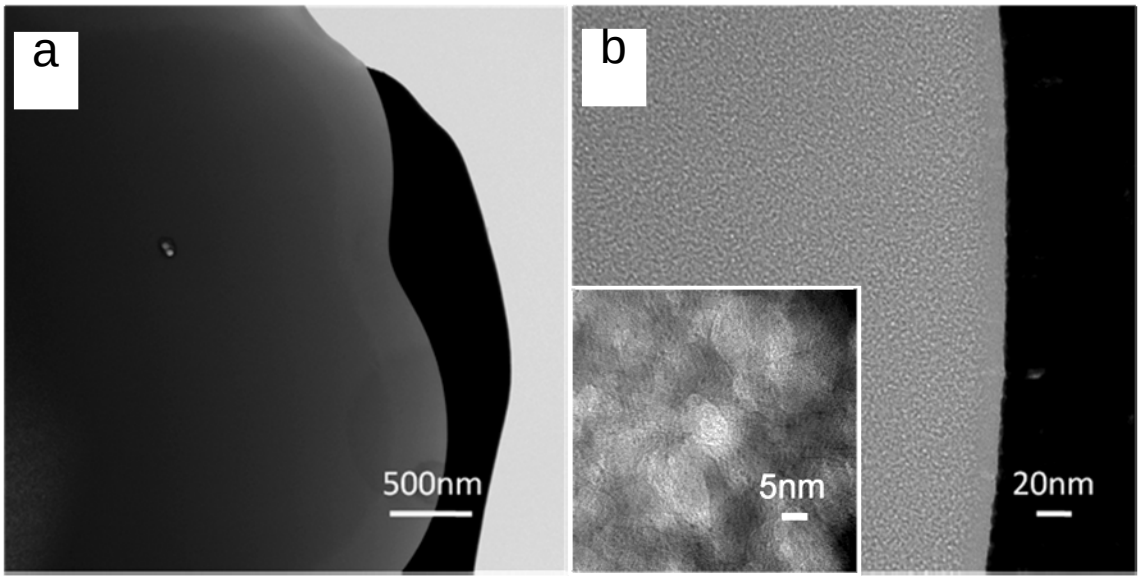


Figure 10.2. Cross-sectional TEM images of a PBT fiber after 1h TMA/water exposure at 80°C, and 450°C anneal. The dark region on the lower resolution image is platinum deposited during TEM sample preparation. Some contrast in image (a) in the radial direction may be present. A closer look of the outer edge of the fiber in figure (b) shows a uniform distributed mesoporous structure. The insect shows a high magnification of the mesoporous structure, and it is consistent with a pore diameter of 5-10 nm.

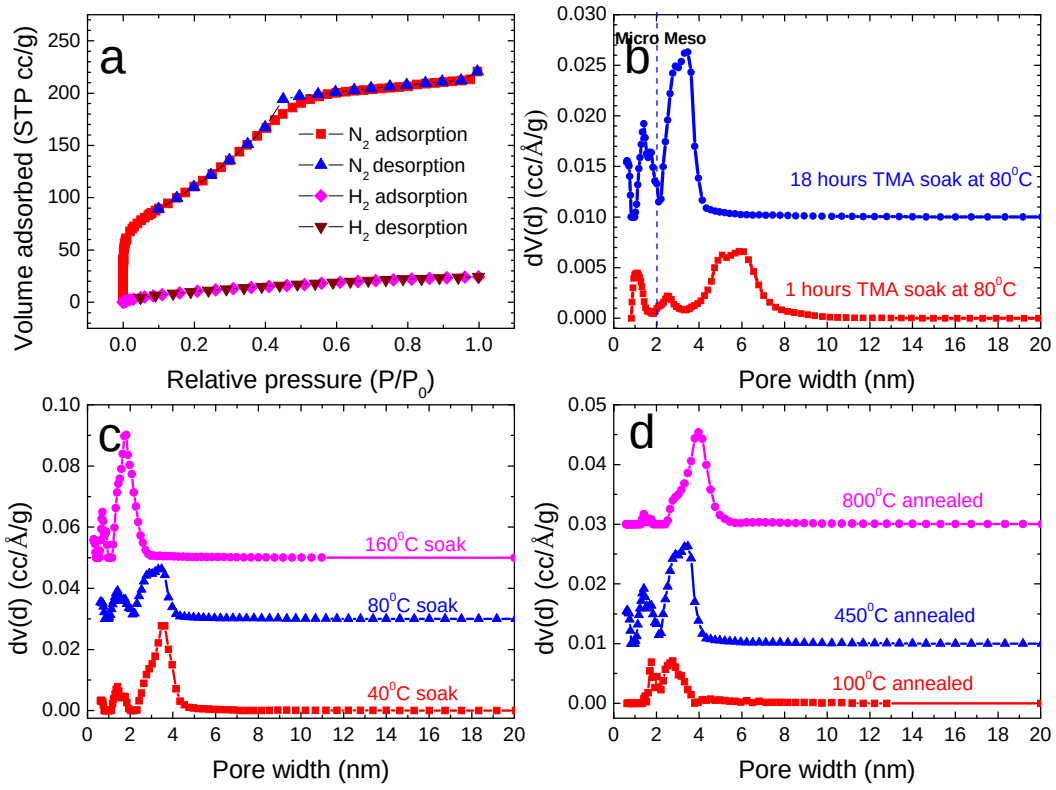


Figure 10.3. Nitrogen/hydrogen adsorption/desorption results collected at 77K from PBT samples. Figure (a) Nitrogen and hydrogen isotherm from PBT samples after 18 hr TMA/water soaking at 80°C and 24 hr anneal 450°C. The hydrogen adsorption/desorption analysis shows 24.4 standard cc/g adsorption at atmosphere pressure, corresponding to ~ 0.22 weight % hydrogen. Figure(b) Pore size distribution results from PBT soaked in TMA vapor with different duration, with fixed infiltration (80°C) and post annealing temperature (450°C). The longer soak time leads to smaller pores and higher pore volume, consistent with more TMA incorporation. Figure (c) Pore size distribution results from PBT soaked in TMA vapor at different temperatures, with other conditions fixed (Table 10.1). Higher soaking temperature also results in porous alumina with smaller pores, which is attributed to the increased reactivity between the TMA and the polymers. Figure (d) Additional pore size analysis for PBT samples annealed at different temperatures after soaking under same condition (details given in Table 10.1). The higher anneal temperature produces larger pores.

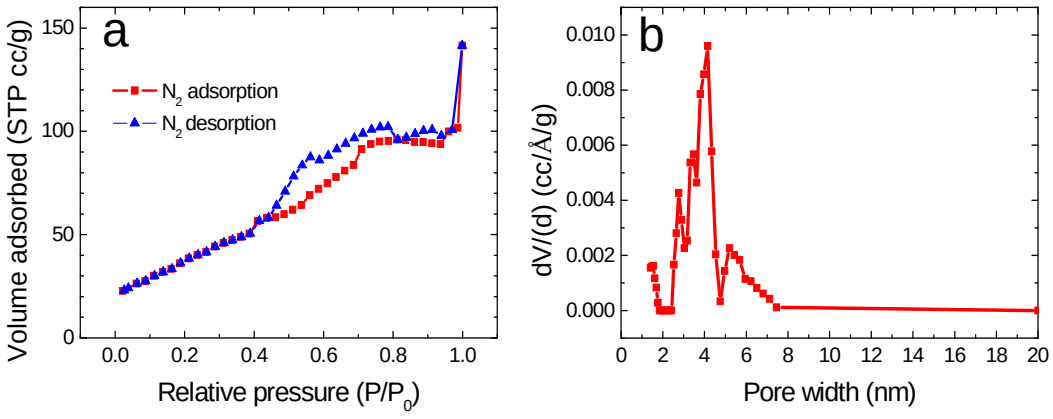


Figure 10.4. Panel (a): nitrogen isothermal adsorption/desorption data obtained from porous titania. The plot shows the amount of vapor adsorbed as a function of pressure up to one atmosphere. The sample was prepared by soaking of PBT polymer fibers at 160°C for 18 hr in $TiCl_4$, then annealing at 450 °C for 12 hr. Panel (b): pore size distribution of the porous titania calculated from the isotherm. The pore size is larger than obtained for the same polymer soaked in TMA and annealed under the same conditions.

Table 10.1. Summary of porous metal oxide samples prepared by vapor phase infiltration. BET surface area, total pore volume and mode pore width of TMA/water and $TiCl_4$/water soaked polyester fibers are listed.

Reactants	**Polymer fiber**	**Infiltration Temp (°C)**	**Anneal Temp (°C)**	**Soak time (hours)**	**BET surface area (m^2/g)**	**Pore volume (m^3/g)**	**Mode pore width (nm)**
--	PBT	--	--	--	0.71	--	--
TMA / water	PBT	80	100	18	182.6	0.139	2.69
		80	450	18	439.9	0.342	3.23
		80	800	18	167.6	0.237	3.88
		80	450	1	248.6	0.245	5.45
		40	450	18	394.6	0.398	3.54
		120	450	18	226.1	0.166	2.67
		160	450	18	384.6	0.413	1.75
	PLA	80	450	18	283.7	0.265	1.41
	PET	80	450	18	280.9	0.172	1.49
	PEN	80	450	18	396.1	0.289	2.68
$TiCl_4$ / water	PBT	160	450	18	149.5	0.220	4.19
	PEN	160	450	18	208.2	0.334	3.63

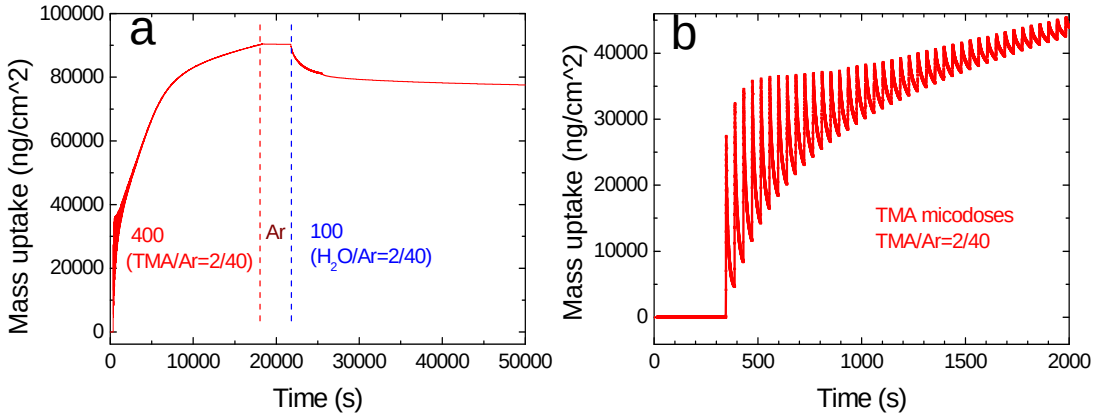


Figure 10.5. Mass increase during TMA/water infiltration at 80°C on a cast PBT film, measured in situ using a quartz crystal microbalance. Figure (a) shows that the mass increase saturates after 400 micro-doses (2 sec each) of TMA, with ~ 90 µg overall mass uptake. This amount of mass increase is more than 1000× larger than ~40 ng measured for a typical TMA/water ALD process on a planar solid substrate (i.e. with no subsurface reaction). Likewise, the water reaction saturates after ~ 100 micro-doses. Figure (b) shows a closer view of first 30 TMA micro-doses on a PBT film. A large mass uptake occurs for the first several cycles then decreases as exposure proceeds.

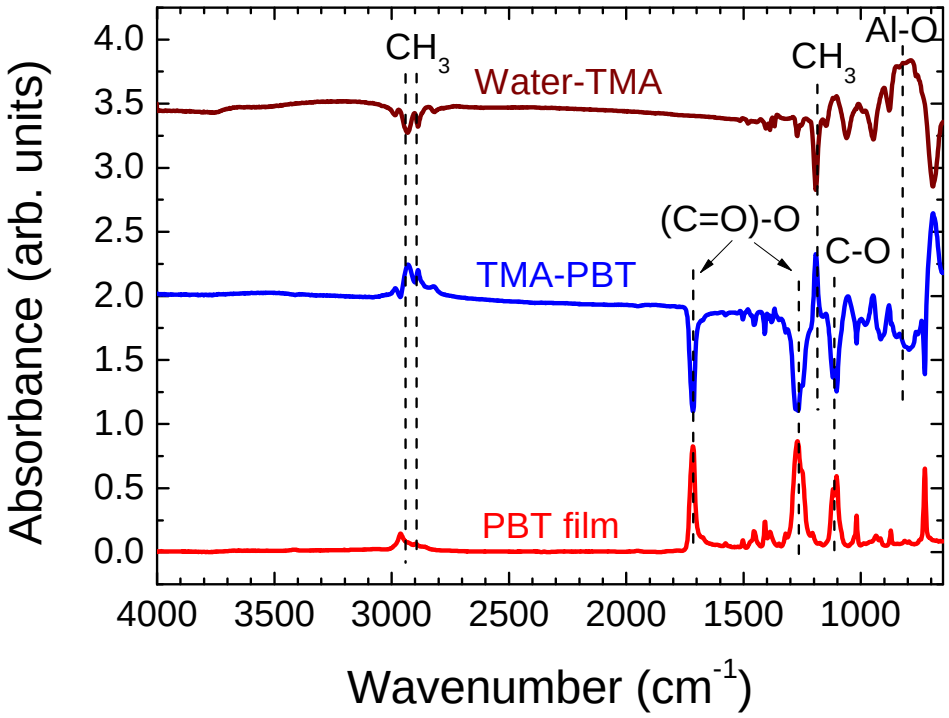


Figure 10.6. FTIR transmission spectra collected in situ from the a starting PBT film cast onto a silicon substrate (bottom trace) and after exposing the film to TMA (middle) and water (upper trace) at 80°C. The TMA exposure removes ester (1720 and 1270cm^{-1}) and ether (1100 cm^{-1}) bonding units indicating high reactivity between TMA and ester bonds in the PBT. The CH_3 (2860 and 2930 cm^{-1}) and Al-CH_3 modes (1200 cm^{-1}) increase upon TMA treatment, confirming Al-CH_3 present in the soaked PBT film. After water dosing, the decrease in CH_3 and Al-CH_3 absorbance and an increase in Al-O modes shows water reacting with the Al-CH_3 groups to form Al-OH.

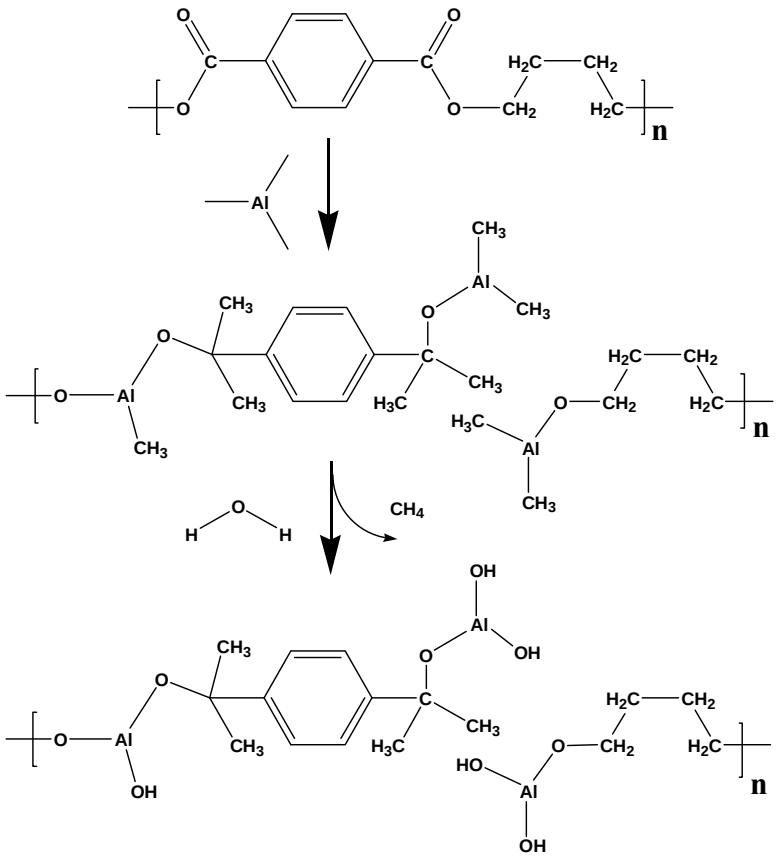


Figure 10.7. Proposed scheme for the PBT/TMA and PBT/TMA/water reactions consistent with the IR data shown in Figure 10.6. TMA is a strong Lewis acid and will likely attack nucleophilic carbonyl groups in the polyester to break the C=O ester bond and formation of aluminum alkyl oxide. Likewise, TMA can also insert into the C-O-C backbone linkage in the PBT to break the polymer chain and produce a methyl termination and a corresponding Al-$(CH_3)_2$ terminal group. During water pulses, the Al-CH_3 groups readily react with water to form Al-OH.

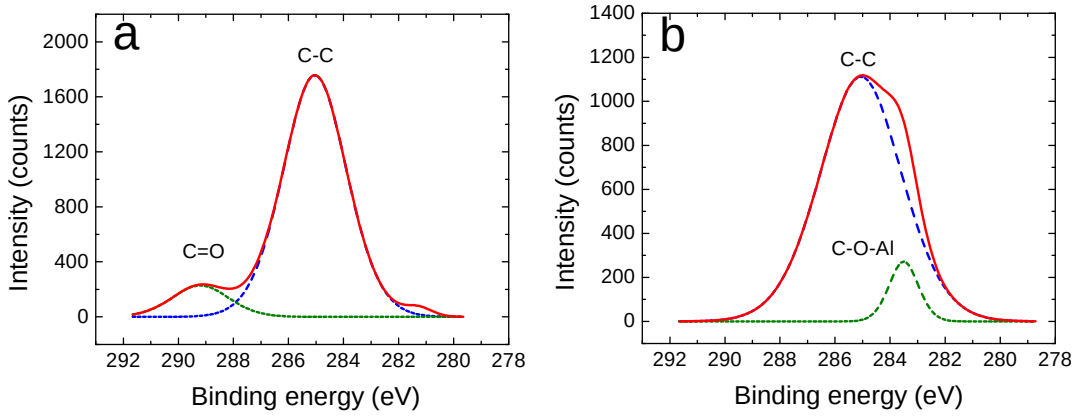


Figure 10.8. X-ray photoelectron spectra of the C 1s feature in: (a) an untreated PBT film; and (b) a PBT film after TMA/water infiltration. The spectra collected after TMA/water show negligible C=O at 289 eV and formation of Al-O-C at ~283.5 eV consistent with mechanism in Figure 10.7.

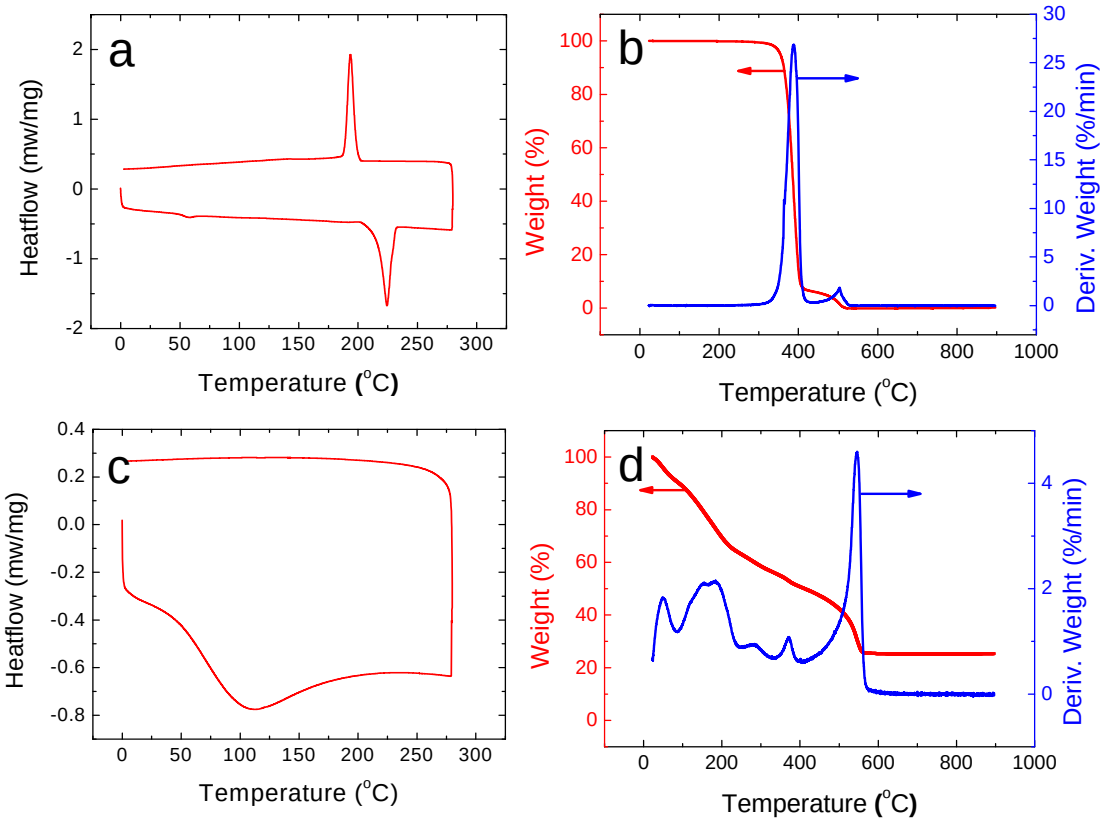


Figure 10.9. Differential scanning calorimetry and thermal gravimetric analysis of: (a), (b) untreated PBT fibers; and (c), (d) TMA/water infiltrated PBT fibers. Results in panel (a) show increased heatflow at approximately 220 °C, consistent with the PBT melting point. Whereas, in panel (c) for the TMA/water soaked PBT, no obvious T_m was observed up to 275 °C. The TGA curve for untreated PBT in panel (b) shows rapid mass decrease at ~400 °C, with ~0 % residue after 900 °C. However, after TMA/water soaking, panel (d) shows a more gradual mass loss, continuing until ~550 °C with ~25 % of mass remaining after 900 °C.

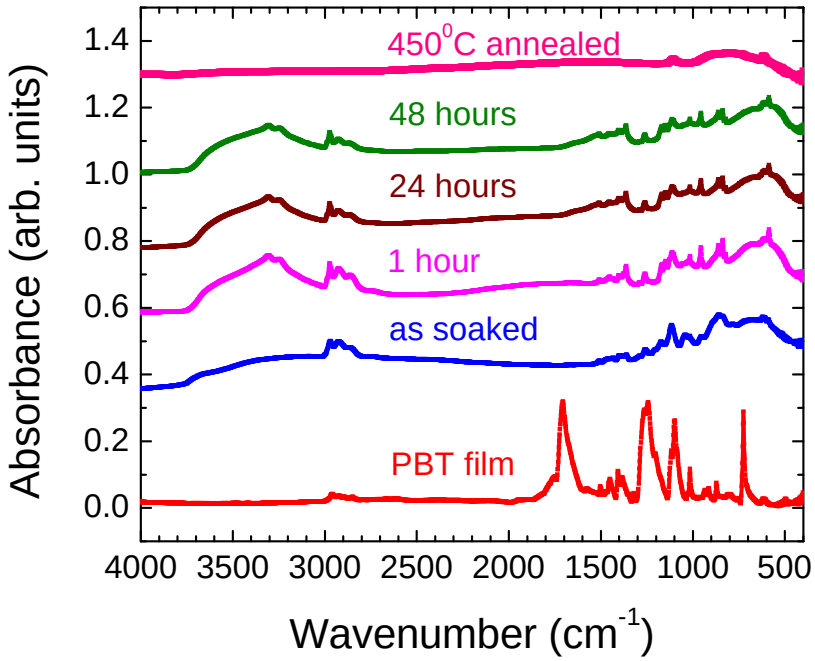


Figure 10.10. Ex-situ FTIR spectra showing the ambient and thermal stability of a TMA/water infiltrated PBT film. The TMA/water soaked PBT continues to absorb water from the ambient during one hour of air exposure. Annealing at 450 °C removes water and the organic component, leaving primarily Al-O modes near 700 cm^{-1}.

References

1 G. J. D. Soler-illia, C. Sanchez, B. Lebeau, and J. Patarin, *"Chemical strategies to design textured materials: From microporous and mesoporous oxides to nanonetworks and hierarchical structures"*, Chemical Reviews **102,** 4093-4138 (2002).

2 A. Corma, *"From microporous to mesoporous molecular sieve materials and their use in catalysis"*, Chemical Reviews **97,** 2373-2419 (1997).

3 D. Y. Zhao, J. L. Feng, Q. S. Huo, N. Melosh, G. H. Fredrickson, B. F. Chmelka, and G. D. Stucky, *"Triblock copolymer syntheses of mesoporous silica with periodic 50 to 300 angstrom pores"*, Science **279,** 548-552 (1998).

4 D. Y. Zhao, Q. S. Huo, J. L. Feng, B. F. Chmelka, and G. D. Stucky, *"Nonionic triblock and star diblock copolymer and oligomeric surfactant syntheses of highly ordered, hydrothermally stable, mesoporous silica structures"*, Journal of the American Chemical Society **120,** 6024-6036 (1998).

5 M. Eddaoudi, D. B. Moler, H. L. Li, B. L. Chen, T. M. Reineke, M. O'Keeffe, and O. M. Yaghi, *"Modular chemistry: Secondary building units as a basis for the design of highly porous and robust metal-organic carboxylate frameworks"*, Accounts of Chemical Research **34,** 319-330 (2001).

6 H. Li, M. Eddaoudi, M. O'Keeffe, and O. M. Yaghi, *"Design and synthesis of an exceptionally stable and highly porous metal-organic framework"*, Nature **402,** 276-279 (1999).

7 N. L. Rosi, J. Eckert, M. Eddaoudi, D. T. Vodak, J. Kim, M. O'Keeffe, and O. M. Yaghi, *"Hydrogen storage in microporous metal-organic frameworks"*, Science **300,** 1127-1129 (2003).

8 O. M. Yaghi, M. O'Keeffe, N. W. Ockwig, H. K. Chae, M. Eddaoudi, and J. Kim, *"Reticular synthesis and the design of new materials"*, Nature **423,** 705-714 (2003).

9 A. P. Cote, A. I. Benin, N. W. Ockwig, M. O'Keeffe, A. J. Matzger, and O. M. Yaghi, *"Porous, crystalline, covalent organic frameworks"*, Science **310,** 1166-1170 (2005).

10 H. M. El-Kaderi, J. R. Hunt, J. L. Mendoza-Cortes, A. P. Cote, R. E. Taylor, M. O'Keeffe, and O. M. Yaghi, *"Designed synthesis of 3D covalent organic frameworks"*, Science **316,** 268-272 (2007).

11 S. S. Han, H. Furukawa, O. M. Yaghi, and W. A. Goddard, *"Covalent organic frameworks as exceptional hydrogen storage materials"*, Journal of the American Chemical Society **130,** 11580-+ (2008).

12 C. D. Wood, B. Tan, A. Trewin, H. J. Niu, D. Bradshaw, M. J. Rosseinsky, Y. Z. Khimyak, N. L. Campbell, R. Kirk, E. Stockel, and A. I. Cooper, *"Hydrogen storage in microporous hypercrosslinked organic polymer networks"*, Chemistry of Materials **19,** 2034-2048 (2007).

13 P. M. Budd, B. S. Ghanem, S. Makhseed, N. B. McKeown, K. J. Msayib, and C. E. Tattershall, *"Polymers of intrinsic microporosity (PIMs): robust, solution-processable, organic nanoporous materials"*, Chemical Communications**,** 230-231 (2004).

14 J. Germain, J. Hradil, J. M. J. Frechet, and F. Svec, *"High surface area nanoporous polymers for reversible hydrogen storage"*, Chemistry of Materials **18,** 4430-4435 (2006).

15 T. Tozawa, J. T. A. Jones, S. I. Swamy, S. Jiang, D. J. Adams, S. Shakespeare, R. Clowes, D. Bradshaw, T. Hasell, S. Y. Chong, C. Tang, S. Thompson, J. Parker, A. Trewin, J. Bacsa, A. M. Z. Slawin, A. Steiner, and A. I. Cooper, *"Porous organic cages"*, Nature Materials **8,** 973-978 (2009).

16 C. G. Bezzu, M. Helliwell, J. E. Warren, D. R. Allan, and N. B. McKeown, *"Heme-Like Coordination Chemistry Within Nanoporous Molecular Crystals"*, Science **327,** 1627-1630 (2010).

17 P. Sozzani, S. Bracco, A. Comotti, L. Ferretti, and R. Simonutti, *"Methane and carbon dioxide storage in a porous van der Waals crystal"*, Angewandte Chemie-International Edition **44,** 1816-1820 (2005).

18 S. Lim, H. Kim, N. Selvapalam, K. J. Kim, S. J. Cho, G. Seo, and K. Kim, *"Cucurbit 6 uril: Organic molecular porous material with permanent porosity, exceptional stability, and acetylene sorption properties"*, Angewandte Chemie-International Edition **47,** 3352-3355 (2008).

19 D. Zacher, O. Shekhah, C. Woll, and R. A. Fischer, *"Thin films of metal-organic frameworks"*, Chemical Society Reviews **38,** 1418-1429 (2009).

20 D. Li, Y. L. Wang, and Y. N. Xia, *"Electrospinning of polymeric and ceramic nanofibers as uniaxially aligned arrays"*, Nano Letters **3,** 1167-1171 (2003).

21 S. Madhugiri, B. Sun, P. G. Smirniotis, J. P. Ferraris, and K. J. Balkus, *"Electrospun mesoporous titanium dioxide fibers"*, Microporous and Mesoporous Materials **69,** 77-83 (2004).

22 G. T. Roman and C. T. Culbertson, *"Surface engineering of poly(dimethylsiloxane) microfluidic devices using transition metal sol-gel chemistry"*, Langmuir **22,** 4445-4451 (2006).

23 G. T. Roman, T. Hlaus, K. J. Bass, T. G. Seelhammer, and C. T. Culbertson, *"Sol-gel modified poly(dimethylsiloxane) microfluidic devices with high electroosmotic Mobilities and hydrophilic channel wall characteristics"*, Analytical Chemistry **77,** 1414-1422 (2005).

24 C. A. Wilson, R. K. Grubbs, and S. M. George, *"Nucleation and growth during Al2O3 atomic layer deposition on polymers"*, Chemistry of Materials **17,** 5625-5634 (2005).

25 G. K. Hyde, G. Scarel, J. C. Spagnola, Q. Peng, K. Lee, B. Gong, K. G. Roberts, K. M. Roth, C. A. Hanson, C. K. Devine, S. M. Stewart, D. Hojo, J. S. Na, J. S. Jur, and G. N. Parsons, *"Atomic Layer Deposition and Abrupt Wetting Transitions on Nonwoven Polypropylene and Woven Cotton Fabrics"*, Langmuir **26,** 2550-2558 (2010).

26 L. B. Zhang, A. J. Patil, L. Li, A. Schierhorn, S. Mann, U. Gosele, and M. Knez, *"Chemical Infiltration during Atomic Layer Deposition: Metalation of Porphyrins as Model Substrates"*, Angewandte Chemie-International Edition **48,** 4982-4985 (2009).

27 S. M. Lee, E. Pippel, U. Gosele, C. Dresbach, Y. Qin, C. V. Chandran, T. Brauniger, G. Hause, and M. Knez, *"Greatly Increased Toughness of Infiltrated Spider Silk"*, Science **324,** 488-492 (2009).

28 S. M. Lee, E. Pippel, O. Moutanabbir, I. Gunkel, T. Thurn-Albrecht, and M. Knez, *"Improved Mechanical Stability of Dried Collagen Membrane after Metal Infiltration"*, ACS Applied Materials & Interfaces **2,** 2436-2441 (2010).

29 Q. Peng, B. Gong, R. M. VanGundy, and G. N. Parsons, *""Zincone" Zinc Oxide-Organic Hybrid Polymer Thin Films Formed by Molecular Layer Deposition"*, Chemistry of Materials **21,** 820-830 (2009).

30 J. C. Spagnola, B. Gong, S. A. Arvidson, J. S. Jur, S. A. Khan, and G. N. Parsons, *"Surface and sub-surface reactions during low temperature aluminium oxide atomic layer deposition on fiber-forming polymers"*, Journal of Materials Chemistry **20,** 4213-4222 (2010).

31 M. Thommes, B. Smarsly, M. Groenewolt, P. I. Ravikovitch, and A. V. Neimark, *"Adsorption hysteresis of nitrogen and argon in pore networks and characterization of novel micro- and mesoporous silicas"*, Langmuir **22,** 756-764 (2006).

32 J. W. Elam, M. D. Groner, and S. M. George, *"Viscous flow reactor with quartz crystal microbalance for thin film growth by atomic layer deposition"*, Review of Scientific Instruments **73,** 2981-2987 (2002).

33 M. Leskela and M. Ritala, *"Atomic layer deposition (ALD): from precursors to thin film structures"*, Thin Solid Films **409,** 138-146 (2002).

34 A. R. Derk, P. Zimmerman, and C. B. Musgrave, *"Reactivity of Trimethylaluminum Towards Organic Functional Groups for the Deposition of Hybrid Organic-Inorganic Films by Molecular and Atomic Layer Deposition"*, submitted (2010).

CHAPTER 11 is a reprint of a manuscript published in JVST-A.

CHAPTER 11. Hydrophilic Mechanical Buffer Layers and Stable Hydrophilic Finishes on Polydimethylsiloxane using Combined Sequential Vapor Infiltration and Atomic/Molecular Layer Deposition

Bo Gong†, Joseph C. Spagnola‡ and Gregory N. Parsons†*

† Department of Chemical and Biomolecular Engineering

‡ Department of Materials Science and Engineering

North Carolina State University, Raleigh, NC 27695

*Corresponding author: Tel: 919-515-7553, Email: parsons@ncsu.edu

Abstract

Polydimethylsiloxane (PDMS) is an important polymer material widely used for microfluidic device fabrication, micro-contact lithography, and surface morphology molding. However, the hydrophobic surface limits its functionality. Low temperature atomic layer deposition (ALD) has recently been used to functionalize a wide range of polymer surfaces. In our previous research, we were able to produce a uniform hydrophilic alumina film coating on PDMS using trimethyl aluminum/water ALD. However, the surface recovered its hydrophobicity after 24-48 hours in ambient air or under inert gas storage, which was ascribed to organic species out-diffusion through the ALD layer. In this paper, we report a stable hydrophilic ALD surface modification on the PDMS. Before metal oxide ALD, the PDMS substrate was first exposed to TMA(DEZ)/water sequential vapor infiltration. The infiltration will form a mechanical and diffusion buffer layer between the PDMS bulk and ALD deposited metal oxide film, preventing hydrophobic recovery due to organic out-diffusion. The new approach provides valuable insight into means to reliably modify the surface energy and mechanical properties of PDMS using vapor-phase precursor/polymer reactions. In addition, molecular layer deposition of "alucone" coatings was also investigated to modify the PDMS surface. The experiment result showed the vapor infiltration and MLD coatings can achieve a more stable hydrophilic surface on PDMS.

11.1. Introduction

Polydimethylsiloxane (PDMS) is a widely used material for many advanced applications, such as microfluidic devices, microstructure replication and soft lithography.[1-3] However, PDMS is natural hydrophobic which limits it use with aqueous solutions. It is also highly porous and readily swells upon exposure to organic solvents, making it hard to use in microfluidic applications.[4] There is significant interest therefore in surface modification of PDMS to increase its wetting properties and improve its stability in organic systems. Many approaches have been employed to tune the surface energy of PDMS, such as corona discharge,[5, 6] plasma exposure,[5, 7, 8] ultraviolet radiation with ozone (UV/O_3),[9-11] surface polymer grafting,[8, 12] layer-by-layer assembly of polyelectrolytes,[13] and physical vapor deposition.[14] In these methods, a thin layer of hydrophilic materials were formed on PDMS. However, the changes in surface wetting are not permanent, but result in a transition from hydrophilic back to hydrophobic in several hours.[6, 7, 10, 14] The hydrophobic recovery is ascribed to diffusion of uncured low molecular weight oligomers present in the PDMS bulk to the surface. Moreover, surface defects, buckling and cracks on PDMS, formed for example after UV/O_3 treatment, play an important role in accelerate the hydrophobic recovery.[6, 15, 16]

Low temperature atomic layer deposition (ALD) provides a promising approach to change the surface properties of a variety of polymer substrates.[17-21] The ALD process employs a binary sequence of self-limiting surface adsorption and reaction steps to deposit conformal films with excellent uniformity and thickness control. The use of ALD to coat polymer fiber structures as well as planar substrates suggests ALD may be a useful tool for the modification of highly complex 2D and 3D soft lithography masks and microfluidic

devices. The previous research in our group has demonstrated that uniform aluminum oxide ALD coating can be successfully deposited on the PDMS surface at various temperatures.[21] However, like other coatings, the surface recovered its hydrophobicity after 24-48 hours. Furthermore, buckles and cracks on the ALD coating induced by the thermal expansion mismatch between PDMS and the metal oxide accelerated this transition. Therefore, a more mechanically robust diffusion barrier would be attractive to help prevent organic transport and maintain a continuous layer without cracking.

During ALD on polymers, the metal organic precursor will often diffuse below the surface, resulting subsurface reaction and nucleation, and continued ALD then results in a graded organic/inorganic interface.[22-24] Recent studies[25, 26] promoting this species subsurface diffusion during ALD showed that the process can lead to creation of a well defined hybrid organic-inorganic solid. We believe that this process may provide a possibility to solve this hydrophobic recovery problem. The extent of this subsurface diffusion and reaction is determined by the process temperature, precursor exposure time, and the rate and driving force for the chemical interaction between the polymer and the metal organic precursor.[26, 27] By controlling vapor infiltration and sub-surface diffusion, and then separately defining an ALD process to create an overcoat, one could couple a well-defined interface layer with an inorganic overcoat, which could act as a robust mechanical and gas diffusion barrier. The hybrid organic-inorganic buffer layer will likely improve the thermal expansion matching between the polymer and inorganic, which could decrease the surface tension induced by the thermal expansion and chemical swelling. In addition, this buffer layer could also help prevent the small molecular weight PDMS units from diffusing out from the PDMS bulk, and

thereby impede the hydrophobic recovery. In this work, long "soaking" exposures of PDMS in a sequence of trimethylaluminum (TMA) and water vapors induces infiltration and reaction to form a thick oxide/polymer buffer layer, which is critical for permanent hydrophilic surface modification. After the interface layer is formed, the surface is treated with TMA/water ALD or TMA/glycidol molecular layer deposition[27] to produce a more hydrophilic surface.

11.2. Experimental Methods

A. Preparation of polydimethylsiloxane, sequential vapor infiltration, and ALD/MLD thin film coating

Polydimethylsiloxane (Sylgard 184, Dow Corning) was polymerized by mixing a silicone base and the cross-linking agent in a 10:1 mass ratio using a glass stir rod. Bubbles produced by the polymerization were removed by placing the mixture in a vacuum desiccator for ~20 mins. After the bubbles were removed, the mixture was poured into a petri dish and allowed to cure at room temperature for more than 48 hours. The thickness of the polymer layer is controlled by the amount of PDMS poured into the petri dish, and film thickness was typically ~0.5 mm. The PDMS thin films samples were cut in to strips of ~30 mm×10 mm before coating. For each coating run, a silicon wafer with native oxide coating was also coated as a control sample.

Atomic layer deposition of Al_2O_3 and molecular layer deposition of "alucone" were performed at temperatures between 60 °C and 120 °C at an operating pressure of ~1 Torr in a homemade hot wall reactor described previously.[26, 27] The metal-organic precursor used was trimethylaluminum (TMA, 98%, Strem Chemicals), or diethylzinc (DEZ, 95%, Strem

Chemicals) and the oxidizing agent was deionized water or glycidol. The glycidol (GLY, 96%, Aldrich) was loaded into a heated bubbler for consistent delivery. After loading, we opened the glycidol vessel to the MLD reactor and pumped on the bubbler for more than 30 minutes to remove air bubbles and residual water. Any residual water in the glycidol could produce a small amount of alumina ALD in parallel with the alucone MLD. Ultra-high purity Argon (Ar, 99.999%, National Welders Supply Co.) was used as the purge and carrier gas, and was further purified by an inert gas filter (Aeronex GateKeeper, Entegris) before entering the bubbler and reactor. In a typical metal organic vapor infiltration process, the PDMS substrate was first exposed to metal organic precursors for 5 hours, and then the reactor chamber was purged with Ar for 30 mins. Finally the infiltrated PDMS was exposed to water vapor for another 30 mins. In a typical ALD cycle, TMA (or DEZ) and water were dosed for 1 second and the exposures were separated by 30 seconds of argon gas purging. For the TMA/GLY MLD process, TMA and GLY were dosed for one second and two seconds respectively, and the pulses were separated by 40 seconds of Ar gas purging. A liquid nitrogen trap was attached in one of the exhaust lines to trap unreacted volatile organic precursors.

B. Materials Characterization

Advancing water contact angles of pristine and treated PDMS samples were obtained using a Model 200 Rame-Hart contact angle goniometer. Measurements were taken within a few minutes of atomic layer deposition and molecular layer deposition treatment in order to reduce possible effects of exposure to ambient lab air. After proper tool alignment, the water droplet was allowed to stabilize on the sample for a few seconds before more water was

added while measurements were recorded as the droplet size increased. In this way, contact angle was obtained as the interface between the water droplet and the surface of the substrate advanced. The values reported here correspond to averages from between 10 and 25 measurements of each sample, with typical uncertainty (one standard deviation) of less than 10 °. The optical images of the PDMS samples were collected by an Olympus BX60 optical microscope.

The mechanical properties of soaked PDMS were measured by a TA Instruments RSA III Micro Strain Analyzer. A transient analysis mode was selected to acquire the strain stress curves. The pristine and TMA/water soaked PDMS samples were calcinated at 400 ºC, and the Brunauer Emmett Teller (BET) surface area of the samples were measured by nitrogen sorption analysis using an autosorb-1C surface area and pore size analyzer.

11.3. Results and Discussion

The advancing water contact angle measured on a silicon wafer with native oxide and a PDMS film after exposure to 100 cycles of Al_2O_3 ALD at 120 °C is displayed in Figure 11.1. After aluminum oxide ALD coating, the Si wafer showed a hydrophilic surface with the water contact angle of ~20 °. Similarly, coating the PDMS surface with 100 cycles of Al_2O_3 ALD resulted in a decrease of the water contact angle from ~ 116 ° to 60 °, consistent with the surface composition transition from hydrophobic PDMS to more hydrophilic Al_2O_3. During storage in ambient air, the silicon wafer and PDMS with the ALD coating became more hydrophobic over ~ 48 hours after coating.[21] This is ascribed to oligomer out-diffusion from the polymer bulk onto the surface through cracks or other defects in the surface coating layer. The ALD coating on PDMS was not sufficient to maintain favorable wetting

characteristics for extended periods after thin film coating. We also note that the Si wafer with ALD coating also showed a similar trend for hydrophobic recovery. However, this is due to the adsorption of hydrocarbons from the lab ambient onto the surface. In addition to the ALD coatings, the silicon wafers were also coated with hybrid organic-inorganic MLD films. The MLD coatings on silicon produced a hydrophilic surface. More importantly, the contact angle stays low for more than 2 weeks in the lab ambient. As the MLD coating hydrolyzes, the surface transitions to a micro-porous alumina structure, similar to that observed after annealing of MLD films.[26-28] This surface microstructure can keep the surface hydrophobic.

The water contact angle measured on PDMS samples treated with metal organic vapor infiltration and ALD/MLD under several process conditions is plotted in Figure 11.2. Similar to the results plotted in Figure 11.1, water contact angle change was monitored over time to assess the stability of the surface treatment. After TMA/water infiltration and 100 cycles of Al_2O_3 ALD at 120 °C, the PDMS surface became hydrophilic, with an initial water contact angle of ~20°. After 48 hours exposure to lab air, the surface became more hydrophobic, and the water contact angle stabilized at ~65°. We also tested the same infiltration + ALD process at 60 °C. As a control experiment, we treated the sample at 60 °C then left the sample in the reactor at 60 °C under Ar purge for 48 hours. After storage, the ALD-modified surface was hydrophilic (contact angle ~20°), similar to samples tested immediately after deposition, but like the other samples, the contact increased with time after air exposure. We conclude therefore, that the lower temperature infiltration + ALD treatment produced a coating that successfully impeded the out-diffusion of oligomer species from the

bulk. The increased contact angle upon air exposure results from adventitious carbon (similar to the ALD coatings on silicon), possibly with some out-diffusion through defects or small cracks formed upon sample cooling. However, any cracks in samples coated at 60 °C were small enough to not be readily visible in optical microscope images (as shown below in Figure 11.3).

We also tested diethyl zinc for the metal infiltration and ALD experiments. The infiltration followed by 100 cycles of zinc oxide ALD at 60 °C resulted in a relatively high contact angle of ~60 °, and it increased to ~110 ° in a few hours. The DEZ infiltrated PDMS seems not sufficient enough to prevent the hydrophobic recovery. Compare to amorphous Al_2O_3, the deposited ZnO is crystalline. This could be the reason for the hydrophobic recovery of DEZ infiltrated PDMS. Interestingly, all of the PDMS samples just treated with TMA/water or DEZ/water infiltration showed hydrophobic surface (contact angle > 100 º).

We also noted that data in Figure 11.1 shows that a silicon wafer coated with a TMA/GLY MLD alucone film was more hydrophilic and stable compared to wafers coated with TMA/water ALD. Therefore, we examined the effect of a layer of alucone formed by molecular layer deposition after the infiltration + ALD process at 60°C. As displayed in Figure 11.2, the PDMS with infiltration + ALD + MLD shows the most hydrophilic and stable coating, with the contact angle staying low at ~40° for 200 hours in lab air. The treated PDMS was not as hydrophilic as silicon wafers with the same alucone finish coating. We note that although the time dependent results are not shown in Figure 11.2, PDMS films exposed to infiltration followed by the MLD coating (without the intermediate ALD layer) also showed good stable hydrophilicity and smooth surface structure. The multi-step

infiltration/ALD/MLD coating procedure is a promising means to control surface properties of reactive and unstable polymer films.

We performed further analysis on the infiltrated and ALD/MLD coated Si and PDMS samples. Ellipsometry analysis of the silicon wafers exposed to vapor infiltration and 100 TMA/water ALD cycles at 120 °C had a film coating of 118 Å thick. This is consistent with 100 cycles of aluminum oxide ALD. This is reasonable since the vapor infiltration process is not expected to have a significant effect on the hard silicon surface (i.e. it is similar to one ALD cycle with excess exposure). Ellipsometry analysis of the coated and modified PDMS samples did not yield reliable results.

Optical microscopy images of samples treated with infiltration and ALD coating are shown in Figure 11.3. Specifically, Figure 11.3(a) shows a sample after TMA/water infiltration and 100 cycles of aluminum oxide ALD at 120 °C. This sample shows a smooth surface morphology, but macroscopic buckles and cracks in the film are readily visible (image in Figure 11.3a). The buckling was previously observed during ALD on PDMS,[21] and is ascribed to compressive stress at the interface that arises upon sample cooling. The buckling could also be enhanced by subsurface precursor diffusion that acts to swell the polymer surface region during coating.[23] Figure 11.3(b) shows a sample after the same infiltration/ALD treatment at 60 °C. The lower temperature produced a more flat, defect free surface, consistent with less substrate expansion. Figure 11.3(c) shows the substrate after exposure to DEZ/water infiltration and DEZ/water ALD at 60 °C, using the same conditions as for the sample in 3(b). The DEZ infiltration/ALD process leads to a rough and cracked surface, suggesting a more serious problem with controlled infiltration and thermal expansion

for this system. Finally, Figure 11.3(d) shows the sample prepared with TMA/water infiltration followed by alumina ALD and TMA/glycidol MLD at 60 °C. Like the surface formed by infiltration + ALD in Figure 11.3(b), the surface in 3(d) formed with infiltration + ALD + MLD is smooth and flat. As displayed in Figure 11.2, this process with the MLD surface finish yielded the most stable and hydrophilic surface wetting character.

The mechanical properties of soaked PDMS samples were measured by a TA Instruments RSA III Micro Strain Analyzer, and results are plotted in Figure 11.4. A virgin PDMS film showed good elastic response with Young's module of ~2.7 MPa, and the sample was able to extend to 65% strain before yielding. After infiltration with TMA/water vapor at 120 °C, the PDMS became much stiffer. The modulus increased to ~29 MPa, and the film yielded with approximately 22% strain. The DEZ/water treatment at 120 °C also makes the PDMS stiffer, with a modulus of ~16 MPa, permitting up to ~53 % strain before yielding. The mechanical results show that the sequential vapor infiltration increases the Young's modulus, forming a mechanical buffer layer between the polymer and the subsequent ALD coating. This layer can therefore prevent film cracking and maintain the hydrophilic surface structure, as shown by the water contact angle and surface morphology results presented above.

After mechanical testing, the TMA- and DEZ-infiltrated PDMS samples were calcined in air at ~400 °C for several hours. This process removed the organic component, leaving behind the inorganic solid. Calcining the untreated PDMS yields a silica powder whereas the infiltrated samples produce mixed silica-alumina or silica-ZnO particles. We measured the pore size and pore size distribution of these materials using BET surface area

analysis. The specific BET surface area was ~36 m^2/g for the silica derived from the untreated PDMS. After TMA or DEZ sequential vapor infiltration, the calcined samples measured 253 and 90 m^2/g respectively, demonstrating that the infiltration significantly modifies the PDMS bulk chemical structure and network connectivity, consistent with vapor infiltration studies showing structural modification that depends on the starting polymer, infiltration precursor, and infiltration conditions. [26]

11.4. Summary and Conclusions

We exposed freshly cured polydimethylsiloxane polymer to sequential vapor infiltration of trimethylaluminum/water, then performed atomic layer deposition using TMA/water or molecular layer deposition using TMA/glycidol. Figure 11.5 presents a schematic rendering of the surface engineering process. We found that the TMA/water infiltration followed by ALD alumina and MLD alucone at 60 °C yields a hydrophilic coating on PDMS with advancing water contact angle of ~40 °, and the contact angle remains relatively stable in air for the ~14 day duration of our study. Vapor infiltration and reaction before the ALD + MLD increased the Young's modulus and strengthened the polymer, creating a mechanical buffer layer at the polymer/inorganic interface that helped maintain the resulting hydrophilic structure. The PDMS samples treated by infiltration and ALD (without the MLD finish layer) became hydrophobic within a few hours after exposure to air. Keeping the samples in inert Ar for up to 48 hours delayed the transition, showing that the infiltration + ALD process successfully impedes organic out-diffusion from the PDMS bulk. The ALD or MLD capping layer then provides a hydrophilic finish to the surface.

PDMS treated with only the ALD coating (without the buffer layer) or with only the infiltration process (without the finish layer) were also hydrophilic after coating, but they were much less stable and rapidly became hydrophobic over time. The alucone MLD finish coating produced a more hydrophilic finish as compared to the ALD alumina. The alucone and other hybrid organic-inorganic materials are known to take up some water after processing,[27] and some water absorption can help maintain the hydrophilic surface. The process described here, which combines sequential vapor infiltration combine with atomic layer deposition and/or molecular layer deposition on PDMS, can be a general method that could work to functionally engineer and tailor the mechanical and chemical performance polymer barriers and other important organic/inorganic material systems.

Acknowledgements

We acknowledge support for this work from the US National Science Foundation under CBET project #103437, and from DOE Project No.08NT0001925. We are grateful to Mark D Walters for assistance with mechanical tensile data collection.

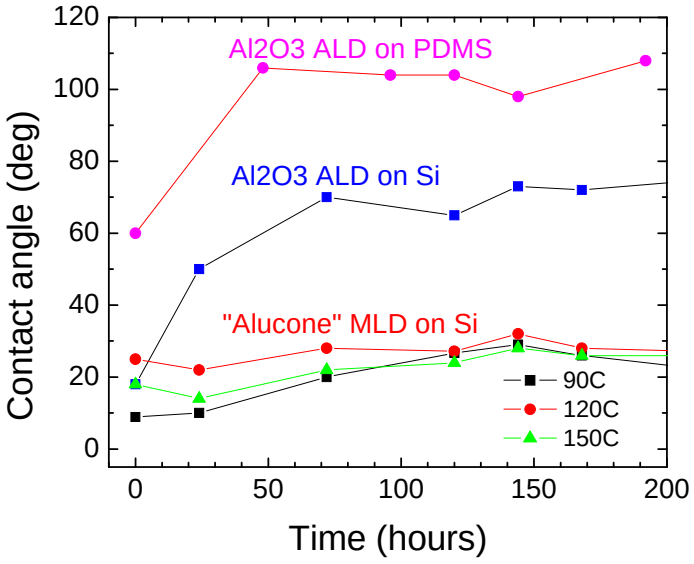


Figure 11.1. Water contact angle behavior measured over time. The symbols correspond to samples as follows: *purple dots:* PDMS with 100 cycles aluminum oxide ALD at 120 °C; *Blue squares:* Si wafer with 100 cycles aluminum oxide ALD at 120 °C; *Red dots:* Si wafer coated with liquid water soaked 200 cycles "alucone" at 120 °C; *Green triangles:* liquid water soaked 200 cycles "alucone" on Si wafer at 150 °C; *Black squares:* liquid water soaked 200 cycles "alucone" on Si wafer at 90 °C. All ALD treated samples showed increased contact angle over time during exposure to laboratory air. It is interesting to note the water contact angle is kept at a very low value for the MLD coatings, possible because of the micro porous morphology formed from the hydroxylation of the MLD coating.

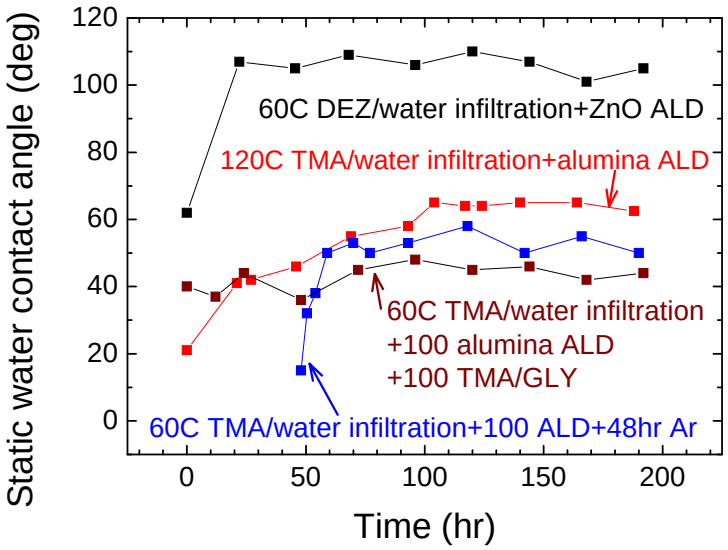


Figure 11.2. Water contact angle behavior measured over time. The symbols correspond to samples as follows: *Red squares:* TMA/water soak and 100 cycles aluminum oxide ALD at 120 °C; *blue squares:* TMA/water soak and 100 cycles aluminum oxide ALD at 60 °C and purge with Ar for 48 hours; *Black squares:* DEZ/water soak and 100 cycles Zinc oxide ALD at 60 °C: *Gray squares*: TMA/water soak + 100 cycles aluminum oxide ALD + 100 cycles "alucone" at 60 °C. All the treated samples showed increased contact angle over time during exposure to laboratory air, except the "alucone" coated sample.

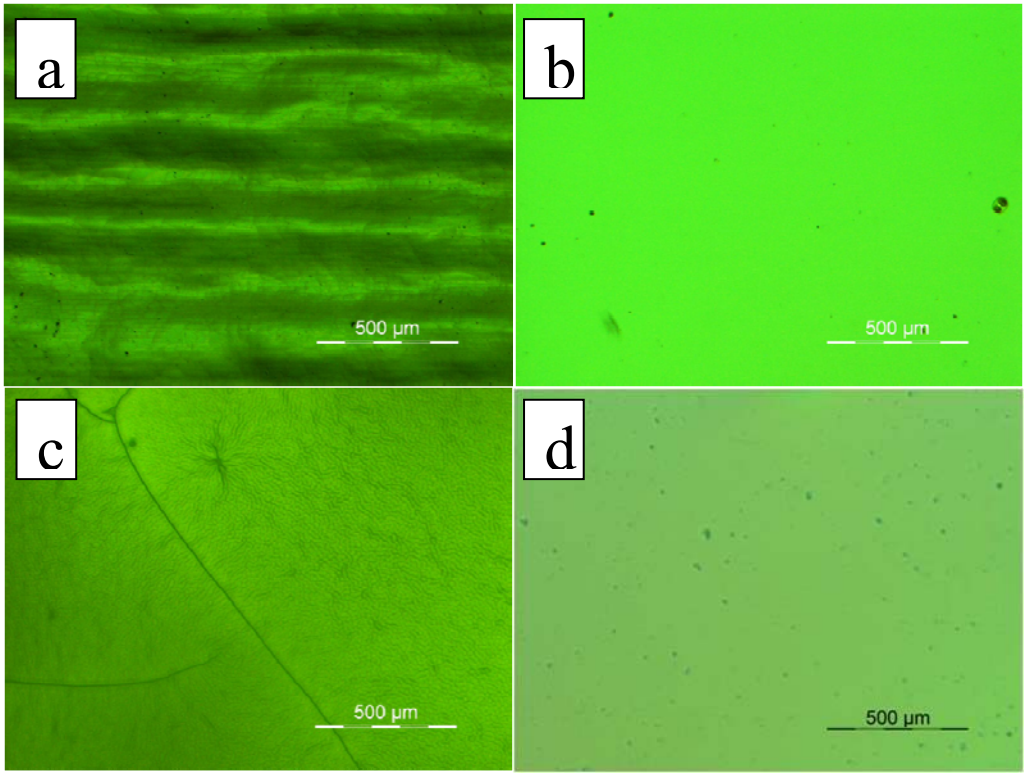


Figure 11.3. (a) Optical microscopy images of PDMS after TMA/water soak and 100 cycles aluminum oxide ALD at 120 °C. Visible cracks and buckle of the surface is observed. (b) Optical microscopy images of PDMS after TMA/water soak and 100 cycles aluminum oxide ALD at 60 °C. Smooth and crack free coating was formed on the PDMS, this could attribute to the smaller thermal expansion at lower process temperature. (c) Optical microscopy images of PDMS after DEZ/water soak and 100cycles Zinc oxide ALD at 60°C. Buckles and cracks were formed on the PDMS surface during the DEZ treatment.

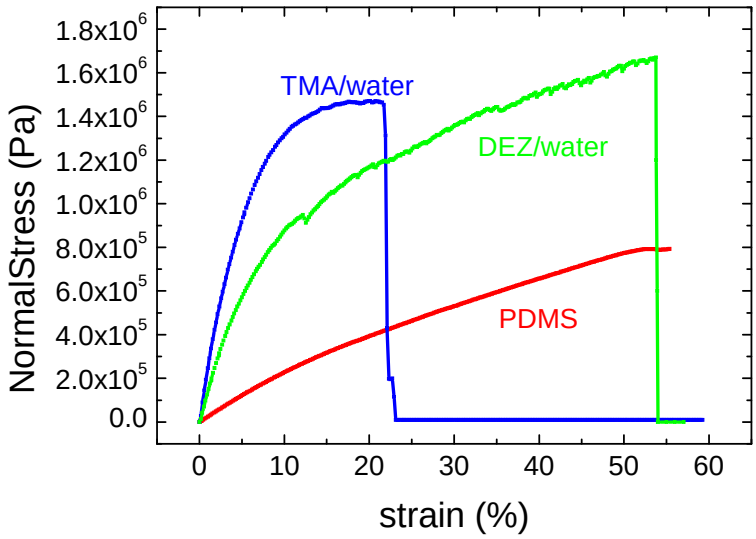


Figure 11.4. Stress strain curve of TMA/water and DEZ/water soaked PDMS and pristine PDMS. The slope of the stress strain curve is the measure of the Young's modules, we can see after soak with metal organic precursor, the modules of PDMS is significant increased. This increase of Young's modulus will form a mechanical buffer layer between ALD coating and bulk PDMS, which will stabilize the ALD coating and keep the ALD layer intact.

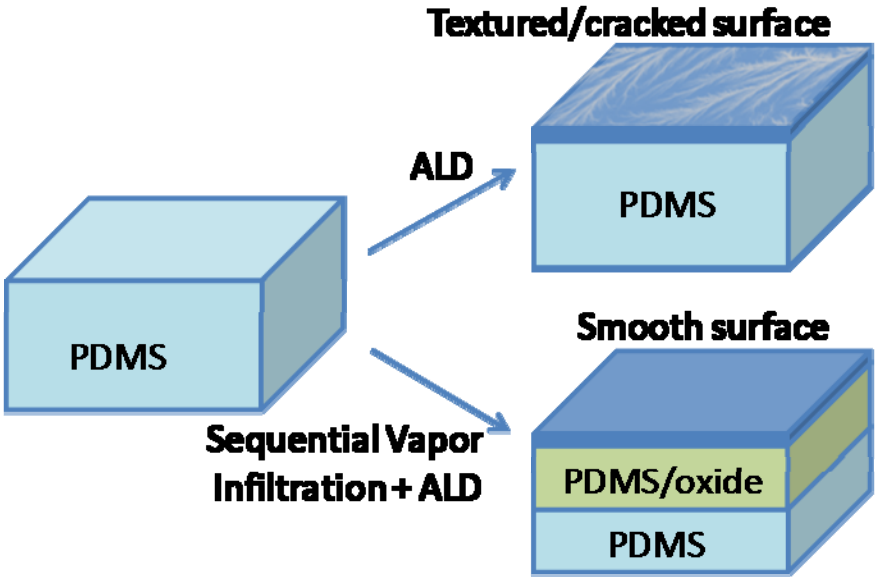


Figure 11.5. Schematic diagram of surface treatment of PDMS with ALD only or sequential vapor infiltration followed by ALD. The top scenario shows direct aluminum oxide ALD on PDMS resulting in cracked aluminum oxide coating. The bottom scenario shows ALD after sequential vapor infiltration, producing a smooth and uniform coating on the PDMS. The sequential vapor infiltration before the ALD helps maintain the surface in a hydrophilic state.

References

1 E. Delamarche, A. Bernard, H. Schmid, B. Michel, and H. Biebuyck, Science 276, 779-781 (1997).

2 Kim, Y. N. Xia, and G. M. Whitesides, Nature 376, 581-584 (1995).

3 J. C. McDonald, and G. M. Whitesides, Acc. Chem. Res. 35, 491-499 (2002).

4 J. N. Lee, C. Park, and G. M. Whitesides, Anal. Chem. **75,** 6544-6554 (2003).

5 G. A. Diaz-Quijada, and D. D. M. Wayner, Langmuir **20,** 9607-9611 (2004).

6 H. Hillborg, and U. W. Gedde, Polymer **39,** 1991-1998 (1998).

7 J. L. Fritz, and M. J. Owen, J. Adhes. **54,** 33-45 (1995).

8 J. Roth, V. Albrecht, M. Nitschke, C. Bellmann, F. Simon, S. Zschoche, S. Michel, C. Luhmann, K. Grundke, and B. Voit, Langmuir **24,** 12603-12611 (2008).

8 K. Efimenko, W. E. Wallace, and J. Genzer, J. Colloid Interface Sci. **254,** 306-315 (2002).

10 A. Olah, H. Hillborg, and G. J. Vancso, Appl. Surf. Sci. **239,** 410-423 (2005).

11 E. A. Waddell, S. Shreeves, H. Carrell, C. Perry, B. A. Reid, and J. McKee, Appl. Surf. Sci. **254,** 5314-5318 (2008).

12 S. W. Hu, X. Q. Ren, M. Bachman, C. E. Sims, G. P. Li, and N. Allbritton, Anal. Chem. **74,** 4117-4123 (2002).

13 Y. Liu, J. C. Fanguy, J. M. Bledsoe, and C. S. Henry, Anal. Chem. **72,** 5939-5944 (2000).

14 Z. Q. Niu, F. Gao, X. Y. Jia, W. P. Zhang, W. Y. Chen, and K. Y. Qian, Colloids and Surfaces A: Physicochem. Eng. Aspects **272,** 170-175 (2006).

15 N. Bowden, S. Brittain, A. G. Evans, J. W. Hutchinson, and G. M. Whitesides, Nature **393,** 146-149 (1998).

16 K. Efimenko, M. Rackaitis, E. Manias, A. Vaziri, L. Mahadevan, and J. Genzer, Nature Mater. **4,** 293-297 (2005).

17 A. A. Dameron, S. D. Davidson, B. B. Burton, P. F. Carcia, R. S. McLean, and S. M. George, J. Phys. Chem. C **112,** 4573-4580 (2008).

18 S. Ferrari, F. Perissinotti, E. Peron, L. Fumagalli, D. Natali, and M. Sampietro, Org. Electron. **8,** 407-414 (2007).

19 G. K. Hyde, G. Scarel, J. C. Spagnola, Q. Peng, K. Lee, B. Gong, K. G. Roberts, K. M. Roth, C. A. Hanson, C. K. Devine, S. M. Stewart, D. Hojo, J. S. Na, J. S. Jur, and G. N. Parsons, Langmuir **26,** 2550-2558 (2010).

20 M. Kemell, E. Farm, M. Ritala, and M. Leskela, Eur. Polym. J. **44,** 3564-3570 (2008).

21 J. C. Spagnola, B. Gong, and G. N. Parsons, J. Vac. Sci. Technol. A **28,** 1330-1337 (2010).

22 C. A. Wilson, R. K. Grubbs, and S. M. George, Chem. Mater. **17,** 5625-5634 (2005).

23 J. S. Jur, J. C. Spagnola, K. Lee, B. Gong, Q. Peng, and G. N. Parsons, Langmuir **26,** 8239-8244 (2010).

24 J. C. Spagnola, B. Gong, S. A. Arvidson, J. S. Jur, S. A. Khan, and G. N. Parsons, J. Mater. Chem. **20,** 4213-4222 (2010).

25 S.-M. Lee, V. Ischenko, E. Pippel, A. Masic, O. Moutanabbir, P. Fratzl, and M. Knez, Adv. Funct. Mater. **21(16),** 3047-3055 (2011).

26 B. Gong, Q. Peng, J. S. Jur, C. K. Devine, K. Lee, and G. N. Parsons, Chem. Mater. **23 (15),** 3476-3485 (2011).

27 B. Gong, Q. Peng, and G. N. Parsons, J. Phys. Chem. B **115(19),** 5930-5938 (2011).

28 X. H. Liang, M. Yu, J. H. Li, Y. B. Jiang, and A. W. Weimer, Chem. Commun. 7140-7142 (2009).

CHAPTER 12 is a reprint of a manuscript in preparation.

CHAPTER 12. Directed Mesoporous Metal Oxides by Vapor Phase Atomic Layer Deposition and Infiltration of Ordered Surfactant Thin Films

*Bo Gong, Do-han Kim and Gregory N. Parsons**

Department of Chemical and Biomolecular Engineering,

North Carolina State University, Raleigh, NC 27695

Corresponding author: Parsons@ncsu.edu

Abstract

Mesoporous materials are critical for lots of applications in catalyst, energy, and chemical separations. Surfactant molecules were always used as structure direct templates in the conventional solution based synthesis approaches. The specific surface area, pore structures, and pore size can be easily tuned by selecting various surfactants. In this work, mesoporous metal oxide material was prepared by the direct vapor phase infiltration of metal organic precursors (trimethyl aluminum and titanium tetrachloride) and water into the surfactants. After the post surfactant template removal, mesoporous metal oxide materials were synthesized. In-situ FTIR was used to monitor the chemistry reaction during the vapor infiltration. SEM and XRD were used to characterize the structure of the porous material. The nitrogen adsorption/desorption analysis was employed to measure the specific surface area and the pore size distribution of the resulted porous metal oxide. We demostrated a vapor phase infiltration approach for preparation of the mesoporous metal oxide from surfactant templates.

12.1. Introduction

Researchers continue to explore mesoprous metal oxide materials for applications including heterogeneous catalyst,[1-4] energy storage[5,6] and conversion,[7-9] and chemical separations.[10,11] Compared to conventional silica based mesoporous materials, metal oxide materials provide many advantages, such as superior acid catalytic activity, and advantageous electrical and optical properties.[12-15] It is well known that amphiphilic surfactant molecules will directly template metal oxide precursors from solution to produce porous metal oxide frameworks. The interaction between the hydrophilic head of the surfactants molecule and the metal oxide precursor helped the self-assembly of ordered micelles/metal oxide hybrids. Template removal by heat or dissolution then yields well defined porous materials.[13,14] However, precursors with high reactivity, including metal halides and metal alkyloxides which are advantageous for some systems, make it difficult to prepare the mesoporous metal oxide structures. The solution pH and the reaction humidity need to be carefully controlled to slow down the reaction and prevent bulk metal oxide growth.[12-14]

Polymers can be modified by exposing them to chemical vapors, incluidng metal-organic precursors, which will infuse into the struture to react. Introducing multiple reactant vapors periodically with long or short exposure steps, one can design a process to introduce metal species deep in the bulk or near the polymer surface. This periodic exposure method, sometimes called Sequential Vapor Infiltration (SVI),[16,17] has produced a variety of inorganic/organic hybrid and porous materials from organic template materals.[18,19] The vapor deposition process proceeds in a confined reactor, allowing precise control of moisture,

chemical exposure time, temperature and other process variables. Post fabrication annealing of infiltrated polymers is known to yield well-defined porous metal oxide solids.[18]

Recently, selective reactions between metal oxide precursors and distinct regions within multicomponent polymers has been reported and studied.[20,21] Based on these previous studies, we hypothesized that exposing an ordered amphiphilc surfactant molecule film to sequential vapor infiltration or ALD could yield a well-ordered inorganic/organic hybrid material. Removing the organic component could then generate a porous metal oxide film. Judicious choice of the starting material, precursors and reaction conditions would then provide a wide window to prepare ordered organic/inorganic hybrid films and porous metal oxide layers for multiple application areas.

In this work, we report preparation of mesoporous aluminum oxide and titanium oxide material by the vapor phase infiltration of trimethyl aluminum or titanium tetrachloride and water vapor into ordered surfactant molecule films. For some studies, we also directly compare vapor infiltration (using relatively long vapor exposure times) to atomic layer deposition processes that use a similar sequential exposure cycle, but on a shorter time scale. As starting surfactants, we start with the well known nonionic (F127 $EO_{106}PO_{70}EO_{106}$) and the ionic (cetyltrimethylammonium bromide CTAB and sodium dodecyl sulfate SDS) materials. We use in-situ FTIR spectroscopy to monitor the internal changes in bonding structure that occur upon vapor infiltration. After material formation, we use scanning electron microscopy (SEM), transmission electron microscopy (TEM) and X-ray diffraction (XRD) to characterize the morphology and structure of the materials. After organic

component removal, we employ nitrogen adsorption and desorption analysis to characterize the specific surface area and the pore size distribution of the resulting porous metal oxide.

12.2. Experimental Methods

Surfactant Thin Films

Nonionic poly(ethylene oxide)-poly(propylene oxide)-poly(ethylene oxide) amphiphilic triblock copolymer Pluronic F127 ($EO_{106}PO_{70}EO_{106}$ 99%, Aldrich) and ionic cetyltrimethylammonium bromide (CTAB 99%, Aldrich) and sodium dodecyl sulfate (SDS 99%, Aldrich) were used as structure template. The surfactant film was prepared on the silicon wafer by spin-coating at 6000 rpm for 2 minutes. The Pluronic F127 solution was prepared with F127, ethanol (EtOH), and deionized water (mole ratio: 0.03 Pluronic F127: 100 EtOH: 100 H_2O), and the CTAB solution was similarly prepared with CTAB, ethanol (EtOH), and deionized water (mole ratios 0.5 CTAB: 50 ETOH: 100 H_2O). The SDS solution contained SDS, ethanol (EtOH), and deionized water (mole ratio: 1 SDS: 100 EtOH: 100H_2O). In addition to surfactant films on flat silicon substrates, we also utilized fibrous nonwoven polypropylene (PP) polymer as a support membrane. The nonwoven material was composed of a randomly oriented 2-3 μm fibers tightly pressed in a mat with thickness of ~ 0.5 mm. The polymer substrate was coated with the surfactant film by dip coating followed by air drying, producing a thin surfactant layer on polymer fibers.

Atomic Layer Deposition and Vapor Infiltration

We performed atomic layer deposition (ALD) or vapor infiltration using trimethylaluminum (TMA 98 %, Strem Chemicals) and water, or titanium tetrachloride ($TiCl_4$ 99 %, Gelest) and water at 45 or 90 °C in a custom hot wall ALD reactor described

previously.[22,23] The low temperature promotes surface wettability of the surfactant films. Ultra-high purity argon (Ar 99.999 %, National Welders Supply Co.) was used as the purge and carrier gas, and was further purified by an inert gas filter (Aeronex GateKeeper, Entegris) before entering the reactor. In a typical sequential vapor phase infiltration process, the surfactant film on silicon wafer was first exposed to the metal organic (TMA or $TiCl_4$) for 80 min at pressure of ~7 Torr, and then the reactor chamber was purged with Ar for 30 min, followed by water vapor exposure for 30 min, and another Ar purge. Similarly, surfactants on PP fiber mat were treated with 4 hours TMA or $TiCl_4$ vapor exposure to promote full reaction between the surfactant and the metal organic precursors. For the ALD coating, we used a short ALD cycle sequence of 1 s TMA (or $TiCl_4$), 60 s Ar purge, 1 s water dose and 60 s Ar purge. Each sample coated received either 100 or 200 ALD cycles at 90 °C. The in-situ FTIR experiments were conducted in separate reactor using the same long-period exposure sequences.[23]

After ALD coating or infiltration, the samples prepared on polypropylene fibers were immersed in deionized water for 24 hours at room temperature to dissolve the surfactant. This step keeps the PP substrate intact during the surfactant template removal. After this, we placed both the PP and silicon substrates into an air furnace overnight. Starting from ambient temperature, the furnace temperature increases a rate of 5 °C/min and stabilizes at 400°C. The samples on silicon could then be imaged by SEM. From the PP substrate, the process yielded a free-standing metal oxide layer, or small flakes, typically < 100 nm thick. The free-standing layer was brittle, but it could be readily transported into the TEM or BET system for analysis.

Materials Characterization

A FEI XL30 scanning electron microscopy (SEM) was used to image the morphology of vapor soaked surfactant film before and after calcination. The samples were imaged as prepared, with no conductive coating added. The SEM was operated at a voltage of 10kV and working distance of 5 mm. Samples were prepared for TEM (FEI Tecnai G^2 TWIN operated at 200 kV) by heating the vapor infiltrated films on PP fibers at 400 °C for 24 h to remove the PP. The residue films were dispersed and sonicated in methanol, and applied on a carbon film coated TEM grid from Ted Pella.

We measured nitrogen adsorption/desorption isotherms at 77 K using an Autosorb-1C surface area and pore size analyzer from Quantachrome. Before experiments, samples were outgassed at 350 °C for at least 4 h to remove contaminants and moisture. The multipoint Brunauer Emmett Teller (BET) surface area of the mesoporous materials was calculated from the isotherm adsorption curve in the relative pressure range of 0.05 to 0.35. The pore size distribution was calculated using the BJH method from the isotherm desorption curve.

In-situ FTIR spectra were collected in a separate reactor. In the deposition zone, two single crystal CsI IR windows were integrated into the reactor wall, and each was isolated during the reactant exposure steps using a gate valve. The IR beam exited from the Nicolet 6700 FTIR system, through IR windows and the sample, and then focused into an external MCT-A detector using a gold parabolic mirror. [23] For each spectrum, data is presented using an uncoated silicon wafer (same as the film substrate) as the subtracted IR reference spectrum. For X-ray diffraction analysis, we used a Philips X' pert-MPD using Cu-Kα radiation with λ= 1.5418Å in the θ-2θ scan mode.

12.3. Results and Discussion

Mesoporous Aluminum Oxide from Vapor-Modified Nonionic Surfactant

Figures 12.1 (a) and (b) show SEM images collected from a TMA/water vapor-modified F127 surfactant film on a silicon substrate. The infiltrated surfactant film showed a very smooth top-surface. Panels (c) and (d) show SEM images collected from the similar films after calcination at 400 °C overnight. The top surface of the alumina film is very smooth, and opening of the pores appear mostly two-dimensional, parallel to the Si substrate. From the SEM analysis, the pore size is in the range of 3 nm - 10 nm. After calcination, the surface roughness increases, likely due to film shrinkage. Figure 12.2 shows transmission electron microscopy images of a flake of porous oxide collected from an F127 surfactant film after TMA/water infiltration and annealing in air. For this sample, the F127 film was originally formed on PP fiber. After infiltration and annealing, the TEM images show mesopores with diameter from 5-10 nm, consistent with the SEM results.

Figure 12.3 (a) shows N_2 adsorption/desorption isotherms for an F127 surfactant treated by TMA/water infiltration followed by annealing in air. Red squares correspond to adsorption and blue dots are the desorption data. From the N_2 adsorption isotherm, the BET surface area is calculated to be ~ 631.3 m^2/g. The pore size distribution was also calculated from the isotherm desorption curve using the BJH approach[24] and pore volume versus width is plotted in Figure 12.3 (c). The results show mesopores between 3 nm and 10 nm in size, consistent with the SEM and TEM images. Likewise, Figure 12.3(b) showed the nitrogen adsorption/desorption isotherms from F127 surfactant materials after exposure to 100 TMA/water ALD cycles at 90 °C. Figure 12.3(d) displays the pore size distribution

calculated from the isotherms. The measured BET specific surface area is ~417 m^2/g, which is less than obtained after the long-exposure steps. The shorter ALD sequence likely results in a more non-uniform infiltration and reaction, leading to smaller pores and less overall pore volume.

X-ray diffraction analysis of the as-formed F127 surfactant film shows a diffraction peak at 1.1 degrees, consistent with a laminar structured film on the Si substrate.[25] After the long vapor infiltration treatment, the resulting layers showed no clear diffraction peaks. The F127 structure consists of PEO and PPO segments chemically ordered in the polymer chain. It is likely that the lack of selectivity for the TMA reaction with PEO and PPO could lead to the observed disordered structure after vapor treatment.

The change in bonding structure upon long-cycle vapor infiltration and annealing was monitored using in-situ FTIR analysis, and results are plotted in Figure 12.4. The bottom spectrum in Figure 12.4 corresponds to the as formed F127 surfactant film. The characteristic peaks at 2960 and 2880 cm^{-1} correspond to CH_3, CH_2 stretching. The features at 1458 and 1372 cm^{-1} are related to the CH_2, CH_3 bending. Absorbance at 1100 cm^{-1} is attributed to the C-O-C stretching. These absorbance modes are consistent with the expected bonding in the poly ethylene oxide and poly propylene oxide within the F127 surfactant. Spectrum (b) shows IR data collected after exposing the F127 to TMA vapor. The vapor treatment produces an increase of CH_3 stretching at 2940 cm^{-1} and CH_3 deformation at 1200 cm^{-1} consistent with the expected addition of Al-CH_3 groups.[26] The decrease of C-O-C stretching at 1100cm^{-1} is related to the reaction between TMA with nucleophilic ether groups.[27] Data collected after exposing the sample to water is presented in spectrum (c). The CH_3 stretching

mode at 2940 cm^{-1} and the CH_3 deformation mode at 1200 cm^{-1} decrease, consistent with the hydroxylation of the aluminum methyl. After annealing at 400 °C, spectrum (d) shows no features related to the organic component. Features near 700 cm^{-1} correspond to Al-O stretching.

Surfactant Modification Using Other Vapors

In addition to the F127 surfactant on polypropylene, we also examined vapor infiltration using CTAB and SDS starting materials, where both TMA and $TiCl_4$ were used as reactive vapor species. Control experiments using the PP substrate alone, or PP with the ALD or infiltration exposure without surfactant present were also performed. The measured BET surface area, total pore volume, and the mode pore size from all the metal oxide materials prepared are summarized in Table 1. The data show interesting trends. For example, CTAB treated by TMA (by either infiltration or ALD) produce larger surface area than similarly treated F127, but CTAB reacted with $TiCl_4$ produces a smaller surface area than the F127. Also, the low temperature vapor infiltration using TMA produces larger pore volumes than the higher temperature TMA ALD treatment, for all of the surfactants studied.

We also note an important trend in pore size and volume with the starting material. Using CTAB as the starting material, the BET surface area after TMA infiltration is ~1044 m^2/g, which is larger than ~631 m^2/g attained after treating the F127 surfactant. The average pore size for the CTAB is also smaller, 2.14 nm versus 3.40 nm for the F127 template. This trend is consistent with the smaller molecular length in the CTAB. Figure 12.5 shows XRD patterns collected from (a) a CTAB surfactant film, (b) a CTAB film after long-cycle TMA/water vapor infiltration, and (c) a treated film after anneal at 400 °C. The

untreated surfactant film showed two diffraction peaks at ~3.4 and ~6.9° with similar intensity, corresponding to the laminar structure of the CTAB surfactant on the Si substrate.[28,29] After TMA infiltration, the treated surfactant film shows smaller diffraction peaks at ~2.2 and ~4.4°. The shift of the diffraction peaks upon infiltration corresponds to an increase of the d-spacing. The change in crystal dimension can be due to aluminum oxide forming in the hydrophilic layers of the surfactant films, pushing the layers apart. Moreover, diffraction peak at ~ 2.2° becomes much more intense than the peak at 4.4° after treatment, consistent with a phase transition from predominantly laminar to cylindrical hexagonal arrays within the surfactant film.[25,28,30,31] Figure 12.6 shows a schematic diagram for the phase transition. After calcination, the diffraction peaks disappear, indicating a disordered amorphous oxide is present after the organic removal.

In addition to TMA and $TiCl_4$, we also examined diethyl zinc vapor as a means to modify surfactant films. After exposing the surfactant film on PP fiber mat to one long cycle of DEZ/water at 45 °C, we recovered no measureable metal oxide after calcination. For the surfactants on PP exposed to the short-cycle ALD process, the measured BET surface area and pore volume was very close to the control PP fiber mat, suggesting that DEZ did not penetrate into the surfactant. The DEZ is a relatively poor Lewis acid, suggesting that it will not readily interact with reactive sites on the surfactants molecules.[23]

Application of Directed Mesoporous Titanium Oxide in a Dye Sensitized Photovoltaic Cell

We demonstrate functional performance of the infiltrated surfactant layer, we created mesoporous titanium oxide from the F127 surfactant using the long-cycle exposure of $TiCl_4$

and H_2O at 45°C and used it as a porous anode layer in a dye sensitized photovoltaic cell. We first prepared the surfactant film on fluorine doped tin oxide (FTO) coated glass using the doctor-blade method. Multiply layers of Scotch^{TM} tape were used as a spacer (thickness ~20 μm) to create a rectangular electrode ~ 1 cm × 0.5 cm in size. The surfactant film on FTO glass then transferred into an ALD reactor, where it was exposed to 4 hours of $TiCl_4$ and 2 hours of water alternatively at 45°C. Finally, the infiltrated surfactant film was annealed in air at 480 °C for 30 mins (ramp rate of 5 °C/ min). The thickness of the resulting porous TiO_2 layer was measured by a VEECO Dektak 150 profilometer to be ~150 nm. This thickness is much smaller than the surfactant layer (~20 μm), which implied that $TiCl_4$ did not infuse very deep into the surfactant layer during SVI. The electrode was then loaded with N719 dye and assembled with a Pt counter electrode into a solar cell configuration. Further details of the solar cell fabrication methods used in our lab are described elsewhere.[32] Photocurrent-voltage was measured using a solar simulator (M-9119, Newport) equipped with a 300 W Xenon lamp (AM 1.5G) and a source meter (Keithley 2400). Figure 12.7 shows the results. The device shows an overall solar energy conversion efficiency of 0.04%. Good quality TiO_2 based dye sensitized PV cells with efficiency between 5 and 12% typically utilize a mesoporous titania layer that is 5-10 μm thick to maximize solar energy collection while maintaining sufficiently high device conductivity. Devices from our lab with thicker active layers have overall efficiency of 5-8%.[32] The low efficiency of our fabricated device is associated with the thin ~150 nm electrode. In addition, the relatively small pore size may prevent the dye from penetrating throughout the titania layer. Never-

the-less, the functional performance of the infiltrated surfactant provides a starting point to advance applications for these nanostructured materials.

12.4. Summary and Conclusions

Ordered mesoporous metal oxide materials were succesfully prepared by exposing surfactant assembled films to atomic layer deposition and sequential infiltration vapor treatments. The nonionic (F127, PEO-PPO-PEO) and ionic (CTAB, SDS) surfactants were tested. SEM images showed the the F127 surfactant layer can be transferred into porous metal oxide layer by vapor infiltration of TMA/water and post annealing. The pore size was measured between 3 to 10 nm in the SEM images. TEM iamges collected from the similar samples also showed the formation of the porous aluminum oxide. Furthermore, the nitrogen adsorption/desorption analysis confirmed the formation of porus structures by measuring the specific surface area and the pore size distribution of the materials. The structure and chemistry changes of the surfactant layer during the sequential vapor phase infiltration were monitored by XRD and in-situ FTIR. XRD pattern collected from TMA/water infiltrated CTAB surfactant showed that the vapor infiltration of metal organic prursorsor could result in increase of d spacing of the surfactant layers. Further increase of TMA/water infiltration could result in phase transition of the surfactant layer from laminar struture to hexanol cylindrical arrays. In-situ FTIR results collected during the SVI of TMA/water on F127 surfactant showed that TMA could react with neoclephilic ether groups (C-O-C) in the surfactant during the vapor infiltration. Results demostrate a vapor phase approach to create ordered mesoporous metal oxide layers from a surfactant template. This method could

readily extend to a range of other surfactant and precrusor systems that utilize the a Lewis acid/base interaction to promote metal-organic/polymer functional group interaction.

Although we tried many surfactants and metal oxide chemistry, we haven't been able to get ordered porous metal oxide. One of the most promising combination is CTAB surfactant and Al_2O_3 (TMA/water). We were able to get ordered Al_2O_3/ CTAB surfactant hybrid materials, however, the structure got destroyed during the high temperature annealing. The possible reason is that there is not enough metal oxide dispersed into the surfactant layer. Upon calcination, the structure collapse. If we could get more metal organic precursor infuse into the surfactant layers, we should be able to get ordered metal oxide materials. To achieve this, the detailed process condition need to be fine tuned. Longer infiltration time and higher temperture might help. Moreover, alternative template removing methods can be tested on these materials, such as oxygen plasma and UV-Ozone techniques.

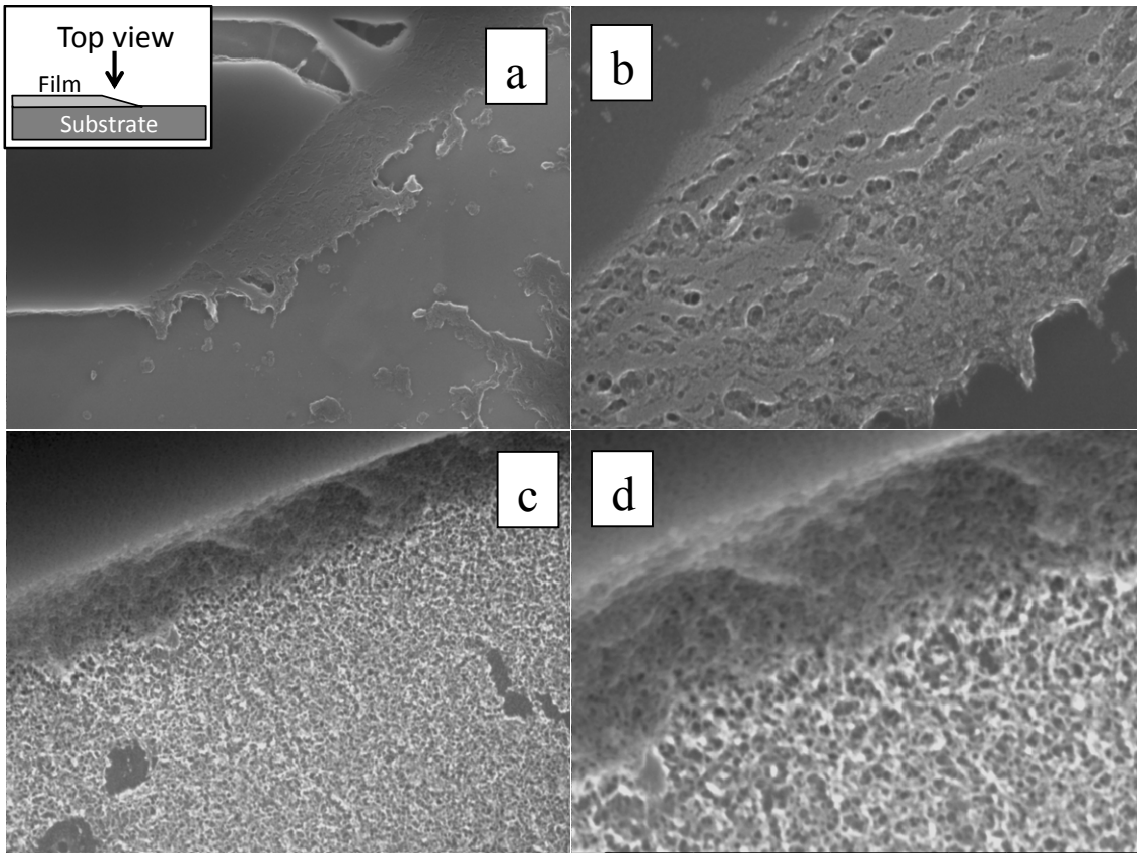


Figure 12.1. Scanning electron microscope images collected from the vapor phase infiltrated F127 surfactants film on the Si wafer. Panel (a), (b) showed the morphology of F127 surfactants film after TMA/water vapor infiltration. Panel (c), (d) showed the mesoporous aluminum oxide film formed on the Si wafer after calcinations of infiltrated film at 400 °C overnight. The pore size is measured from 3nm-10nm. The openings of the pores are mostly on the edge of the film.

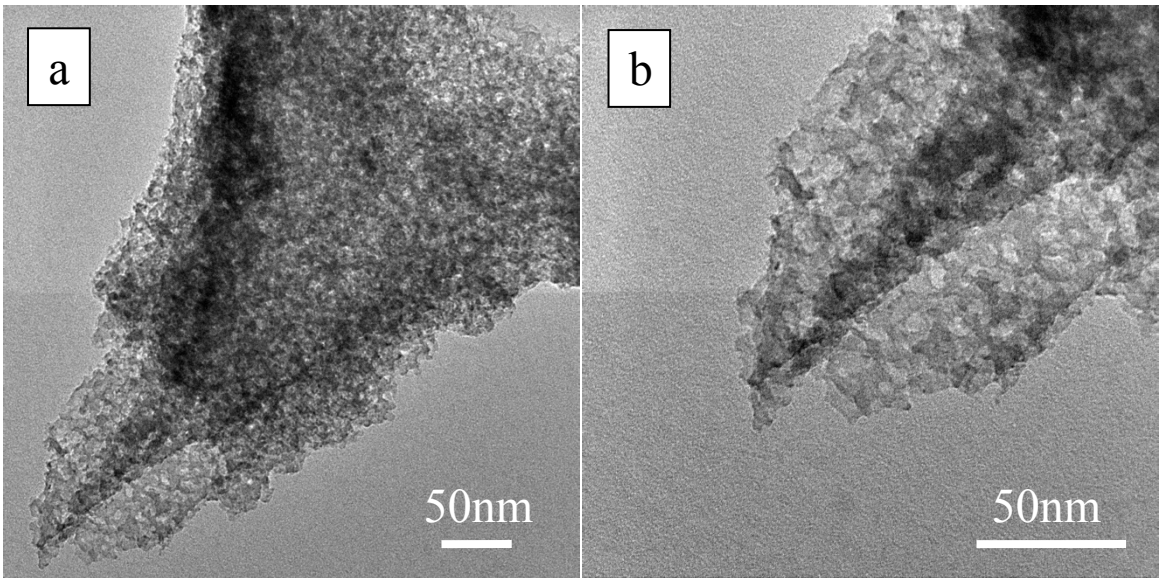


Figure 12.2. TEM images collected from the mesoporous aluminum oxide samples for N_2 adsoprtion/desorption analysis. The sample was prepared by TMA/water vapor phase infiltration of F127 surfactant dipcoated on PP fiber mat, and post calcinations at 400 °C overnight. PP fiber mat and surfactant template have been removed by the calcinations.

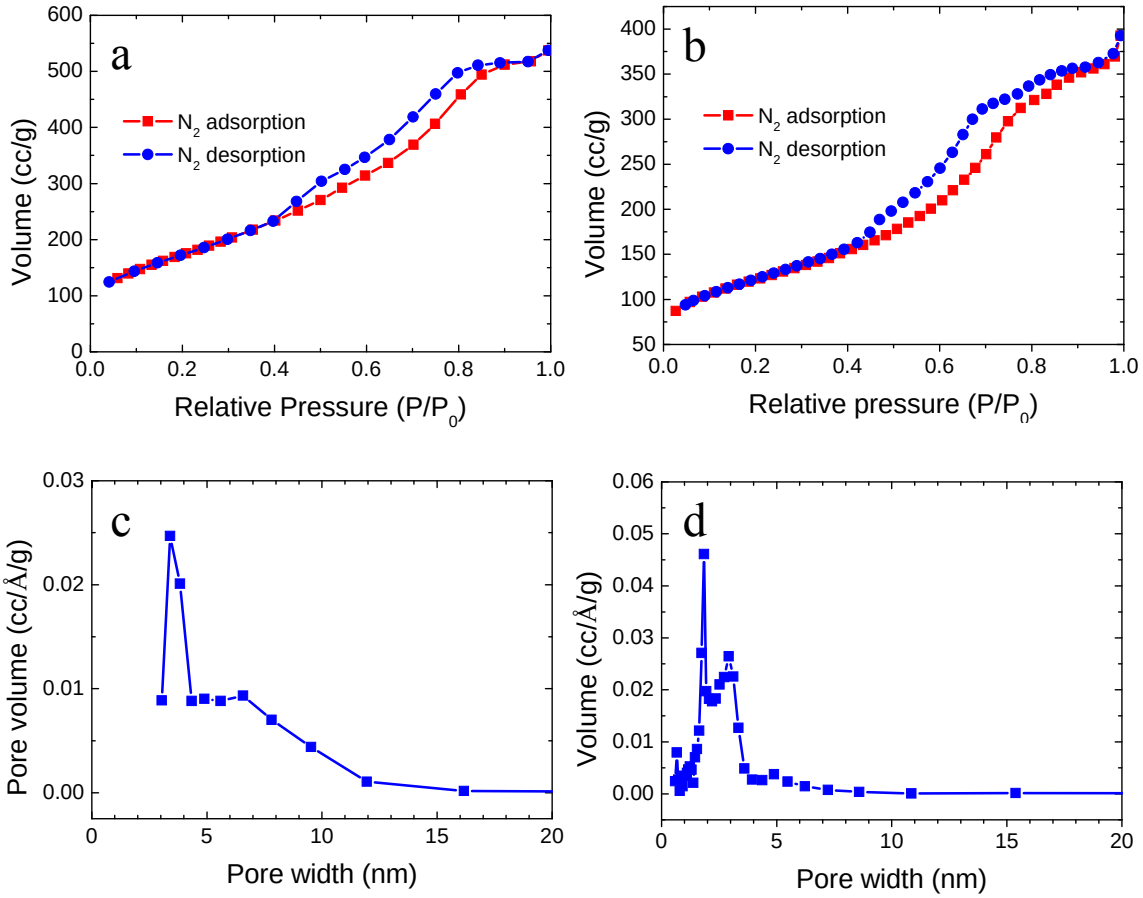


Figure 12.3. (a). Nitrogen adsorption/desorption isotherms for mesoporous alumina prepared by vapor phase infiltration of F127 surfactant with TMA/water. The BET surface area is measured 631.3 m2/g. **(b)** Nitrogen adsorption/desorption isotherms for mesoporous alumina prepared by 100 cycles of TMA/water (1/60/1/60) ALD on F127 surfactant. The BET surface area is measured as 417.3 m2/g. **(c)**, Pore sized distribution calculated from the N2 adsorption/desorption isotherm in Figure (a) with the BJH method. **(d)** Pore sized distribution of ALD coated F127 calculated from the N2 desorption isotherm with the BJH method.

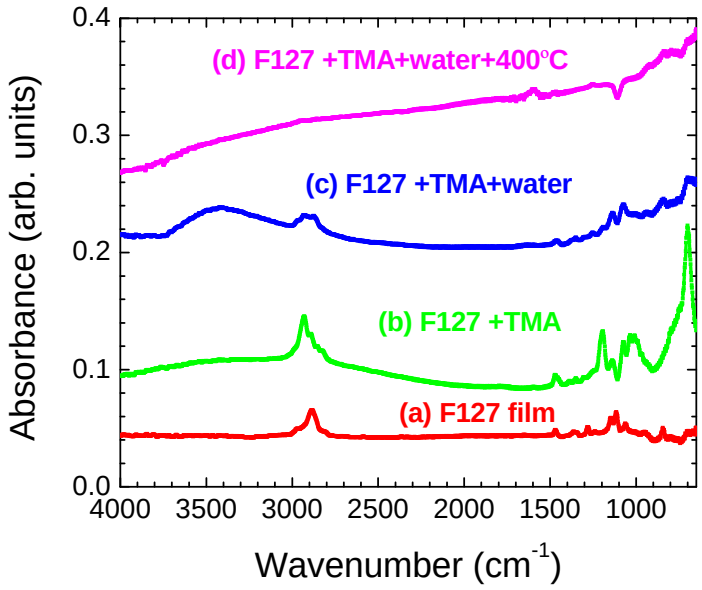


Figure 12.4. In-situ FTIR spectra collected from the **(a)** F127 surfactant film on Si wafer, **(b)** TMA vapor soaked F127 surfactant film, **(c)** TMA/water vapor soaked F127 surfactant film, and **(d)** 400 °C annealed mesoporous alumina film on silicon wafer. The increase of CH_3 related feature at 2930, 1200 and 700 cm^{-1} is corresponding to the large amount incorporation of TMA in the surfactant film. The removed of CH_3 related absorbance and the increase of hydroxyl related absorbance after water dose is related to the conversion of Al-CH_3 to Al-OH.

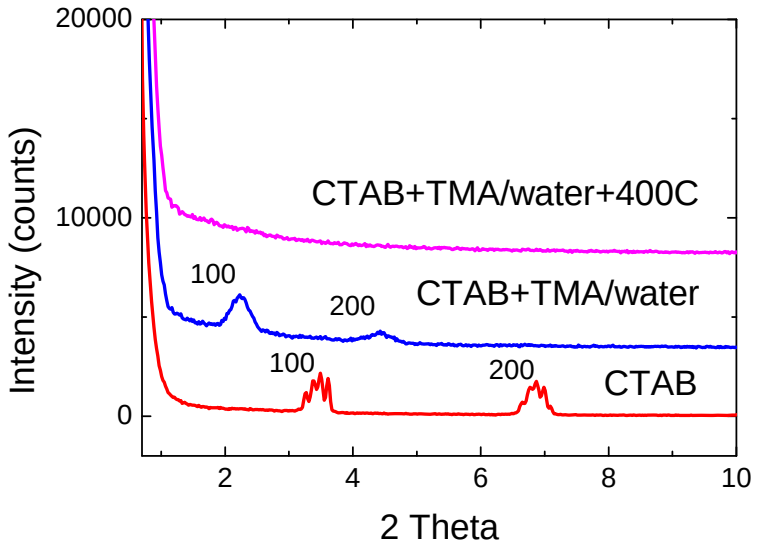


Figure 12.5. XRD patterns collected from **(a)** CTAB surfactant film, **(b)** TMA/water vapor infiltrated CTAB surfactant film, **(c)** A calcined mesoporous alumina film. Calcination temperature was 400 °C. A low angle diffraction peak is observed for CTAB films, corresponding to the laminar structures of the CTAB surfactant. However, the TMA/water vapor phase infiltration induced the phase changed from laminar to cylindrical structure. The formed mesoporous alumina is characterized as amorphous.

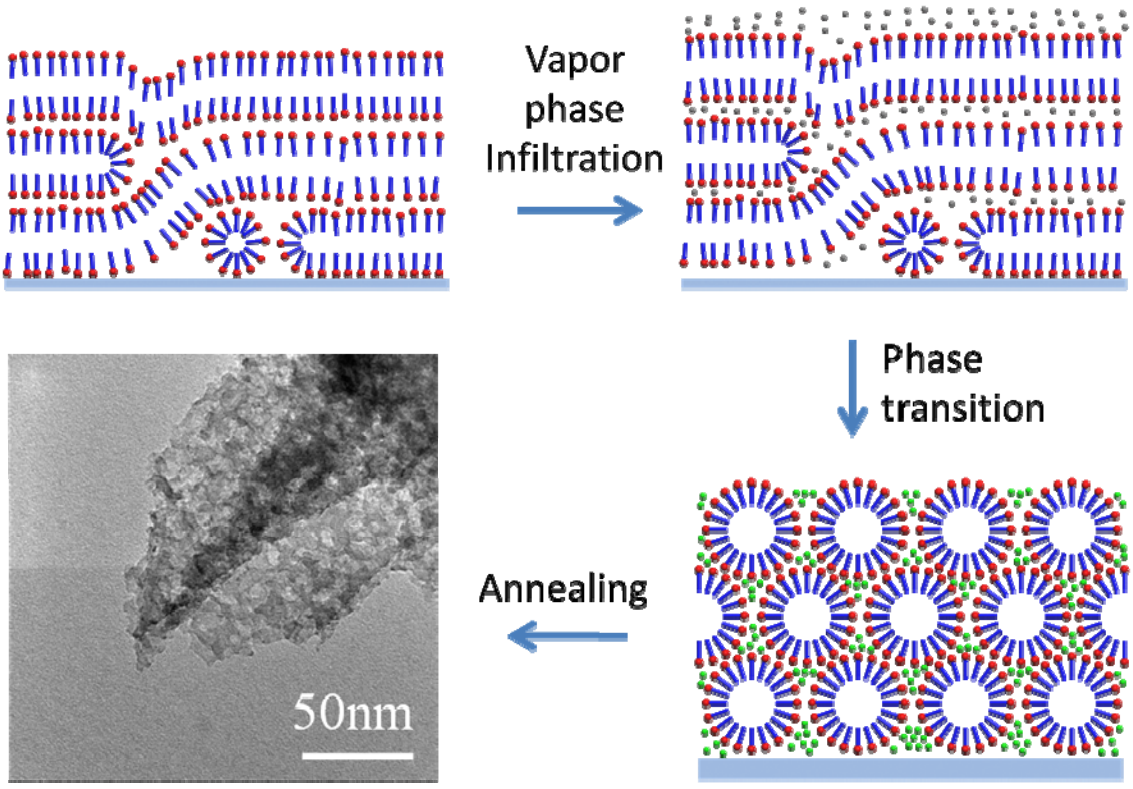


Figure 12.6, Schematic diagram for the preparation of mesoporous metal oxide materials from vapor phase infiltration method.

Table 12.1. Summary of porous metal oxide samples prepared by vapor phase infiltration and atomic layer deposition on surfactants after post annealing at 450 °C for 12hr. BET surface area, total pore volume and mode pore width are listed.

Method	Surfactant on PP fiber mat	Reagents	Template removal	BET surface area (m^2/g)	Pore volume (cc/g)	Mode pore size (nm)
Vapor phase infiltation @ 45 °C	F127	TMA	Calcination	631	0.83	3.40
		$TiCl_4$	Calcination	253	0.51	5.84
		TMA	Dissolution	77	0.10	3.68
	CTAB	TMA	Calcination	1044	1.22	2.14
		$TiCl_4$	Calcination	131	0.24	5.07
	SDS	TMA	Calcination	329	1.68	7.71
		TMA	Dissolution	59	0.35	4.65
Atomic layer deposition @ 90 °C	F127	100 TMA/water	Calcination	417	0.61	1.84
		100 $TiCl_4$/water	Calcination	254	0.76	5.42
	CTAB	100 TMA/water	Calcination	728	0.65	2.11
		100 $TiCl_4$/water	Calcination	157	0.39	7.27
	F127	200 DEZ/water	Calcination	21	0.12	15.2
	none	200 DEZ/water	Calcination	21	0.15	23.9
Uncoated PP	none	none	none	1.5	-	-

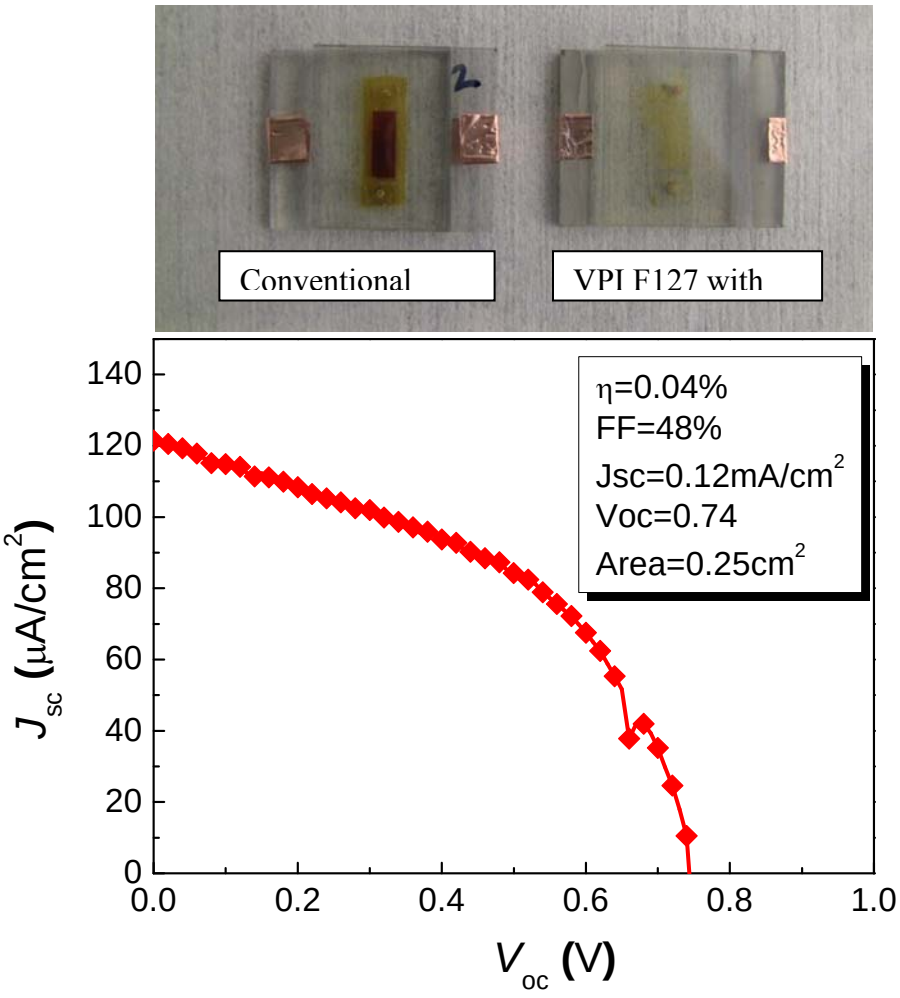


Figure 12.7. DSSC performance for mesoporous TiO_2 electrode by vapor phase infiltration of F127 surfactants with $TiCl_4$ vapor at 45 °C. The light color of the DSSC electrode is due to the small thickness of porous TiO_2 layer(~150 nm in thickness), which would inhibit the performance of the solar cell. An overall solar energy conversion efficiency of 0.04% was measured. The small pore size and the two-dimensionally pore structure could also have prevented the dye from diffuse in and adsorb on the TiO_2 porous electrode. The conventional DSSC made from TiO_2 nanoparticle electrode (~5-10 μm in thickness) showed ~5-8 % overall efficiency.

References

1 D. E. De Vos; M. Dams; B. F. Sels; P. A. Jacobs; Ordered mesoporous and microporous molecular sieves functionalized with transition metal complexes as catalysts for selective organic transformations, *Chemical Reviews,* **2002**. *102*, 3615.

2 T. Maschmeyer; F. Rey; G. Sankar; J. M. Thomas; Heterogeneous catalysts obtained by grafting metallocene complexes onto mesoporous silica, *Nature,* **1995**. *378*, 159.

3 A. Sayari; Catalysis by crystalline mesoporous molecular sieves, *Chemistry of Materials,* **1996**. *8*, 1840.

4 P. T. Tanev; M. Chibwe; T. J. Pinnavaia; Titanium-containing mesoporous molecular-sieves for catalytic-oxidation of aromatic-compounds, *Nature,* **1994**. *368*, 321.

5 J. W. Long; B. Dunn; D. R. Rolison; H. S. White; Three-dimensional battery architectures, *Chemical Reviews,* **2004**. *104*, 4463.

6 H. S. Zhou; D. L. Li; M. Hibino; I. Honma; A self-ordered, crystalline-glass, mesoporous nanocomposite for use as a lithium-based storage device with both high power and high energy densities, *Angewandte Chemie-International Edition,* **2005**. *44*, 797.

7 U. Bach; D. Lupo; P. Comte; J. E. Moser; F. Weissortel; J. Salbeck; H. Spreitzer; M. Gratzel; Solid-state dye-sensitized mesoporous TiO2 solar cells with high photon-to-electron conversion efficiencies, *Nature,* **1998**. *395*, 583.

8 A. Hagfeldt; M. Gratzel; Molecular photovoltaics, *Accounts of Chemical Research,* **2000**. *33*, 269.

9 M. Zukalova; A. Zukal; L. Kavan; M. K. Nazeeruddin; P. Liska; M. Gratzel; Organized mesoporous TiO2 films exhibiting greatly enhanced performance in dye-sensitized solar cells, *Nano Letters,* **2005**. *5*, 1789.

10 C. J. Brinker; T. L. Ward; R. Sehgal; N. K. Raman; S. L. Hietala; D. M. Smith; D. W. Hua; T. J. Headley; Ultramicroporous silica-based supported inorganic membranes, *Journal of Membrane Science,* **1993**. *77*, 165.

11 Y. H. Kim; C. M. Kim; I. H. Choi; S. Rengaraj; J. H. Yi; Arsenic removal using mesoporous alumina prepared via a templating method, *Environmental Science & Technology*, **2004**. *38*, 924.

12 F. Schuth; Non-siliceous mesostructured and mesoporous materials, *Chemistry of Materials,* **2001**. *13*, 3184.

13 P. D. Yang; D. Y. Zhao; D. I. Margolese; B. F. Chmelka; G. D. Stucky; Generalized syntheses of large-pore mesoporous metal oxides with semicrystalline frameworks, *Nature,* **1998**. *396*, 152.

14 P. D. Yang; D. Y. Zhao; D. I. Margolese; B. F. Chmelka; G. D. Stucky; Block copolymer templating syntheses of mesoporous metal oxides with large ordering lengths and semicrystalline framework, *Chemistry of Materials,* **1999**. *11*, 2813.

15 T. Maruo; S. Tanaka; H. W. Hillhouse; N. Nishiyama; Y. Egashira; K. Ueyama; Disordered mesoporous silica low-k thin films prepared by vapor deposition into a triblock copolymer template film, *Thin Solid Films,* **2008**. *516*, 4771.

16 J. S. Jur; J. C. Spagnola; K. Lee; B. Gong; Q. Peng; G. N. Parsons; Temperature-Dependent Subsurface Growth during Atomic Layer Deposition on Polypropylene and Cellulose Fibers, *Langmuir,* **2010**. *26*, 8239.

17 J. C. Spagnola; B. Gong; S. A. Arvidson; J. S. Jur; S. A. Khan; G. N. Parsons; Surface and sub-surface reactions during low temperature aluminium oxide atomic layer deposition on fiber-forming polymers, *Journal of Materials Chemistry,* **2010**. *20*, 4213.

18 B. Gong; Q. Peng; J. S. Jur; C. K. Devine; K. Lee; G. N. Parsons; Sequential Vapor Infiltration of Metal Oxides into Sacrificial Polyester Fibers: Shape Replication and Controlled Porosity of Microporous/Mesoporous Oxide Monoliths, *Chemistry of Materials,* **2011**. *23*, 3476.

19 B. Gong; J. C. Spagnola; G. N. Parsons; Hydrophilic mechanical buffer layers and stable hydrophilic finishes on polydimethylsiloxane using combined sequential vapor infiltration and atomic/molecular layer deposition, *Journal of Vacuum Science & Technology A,* **2012**. *30*,

20 B. Gong; J. C. Spagnola; S. A. Arvidson; S. A. Khan; G. N. Parsons; Structured Polymer/Inorganic Nanocomposites by Selective Vapor Infusion and Reaction during Atomic Layer Deposition on Bi-Component Polymer Fibers **2012**.

21 Q. Peng; Y.-C. Tseng; S. B. Darling; J. W. Elam; Nanoscopic Patterned Materials with Tunable Dimensions via Atomic Layer Deposition on Block Copolymers, *Advanced Materials,* **2010**. *22*, 5129.

22 Q. Peng; B. Gong; R. M. VanGundy; G. N. Parsons; "Zincone" Zinc Oxide-Organic Hybrid Polymer Thin Films Formed by Molecular Layer Deposition, *Chemistry of Materials,* **2009**. *21*, 820.

23 B. Gong; Q. Peng; G. N. Parsons; Conformal Organic - Inorganic Hybrid Network Polymer Thin Films by Molecular Layer Deposition using Trimethylaluminum and Glycidol, *Journal of Physical Chemistry B,* **2011**. *115*, 5930.

24 E. P. Barrett; L. G. Joyner; P. P. Halenda; The Determination of Pore Volume and Area Distributions in Porous Substances. I. Computations from Nitrogen Isotherms, *Journal of the American Chemical Society,* **1951**. *73*, 373.

25 S. Tanaka; N. Nishiyama; Y. Oku; Y. Egashira; K. Ueyama; Nano-architectural silica thin films with two-dimensionally connected cagelike pores synthesized from vapor phase, *Journal of the American Chemical Society,* **2004**. *126*, 4854.

26 A. C. Dillon; A. W. Ott; J. D. Way; S. M. George; Surface-chemistry of Al2O3 deposition using Al(CH3)(3) and H2O in a binary reaction sequence, *Surface Science,* **1995**. *322*, 230.

27 B. Gong; G. N. Parsons; Quantitative In-Situ Infrared Analysis of Reactions between Trimethylaluminum and Polymers during Al2O3 Atomic Layer Deposition *Journal of Materials Chemistry,* **2012**.

28 N. Nishiyama; S. Tanaka; Y. Egashira; Y. Oku; K. Ueyama; Vapor-phase synthesis of mesoporous silica thin films, *Chemistry of Materials,* **2003**. *15*, 1006.

29 T. Maruo; K. Nagata; N. Nishiyama; Y. Egashira; K. Ueyama; Synthesis of 3D pore mesostructured silica films by vapor infiltration of tetraethoxysilane, *Journal of Colloid and Interface Science,* **2008**. *328*, 120.

30 K. J. Lee; S. H. Min; J. S. Jang; Vapor-Phase Synthesis of Mesostructured Silica Nanofibers Inside Porous Alumina Membranes, *Small,* **2008**. *4*, 1945.

31 N. Nishiyama; J. Kaihara; Y. Nishiyama; Y. Egashira; K. Ueyama; Vapor-phase synthesis of mesoporous SiO2-P2O5 thin films, *Langmuir,* **2007**. *23*, 4746.

32 D. H. Kim; H.-J. Koo; J. S. Jur; M. Woodroof; B. Kalanyan; K. Lee; C. K. Devine; G. N. Parsons; Stable anatase TiO2 coating on quartz fibers by atomic layer deposition for photoactive light-scattering in dye-sensitized solar cells, **2012**.

CHAPTER 13 is a reprint of a manuscript in preparation.

CHAPTER 13. Core Sheath Nanocomposite Structures Enabled by Aluminum Oxide Atomic Layer Deposition on Bicomponent Polymer Fibers

*Bo Gong, Joe C. Spagnola, Sara A. Arvidson, Saad A. Khan and Gregory N. Parsons**

Department of Chemical and Biomolecular Engineering,

North Carolina State University, Raleigh, NC 27695

Corresponding author: Parsons@ncsu.edu

Abstract

Nanocomposite with desired local functionality has attracted lots of research for applications in drug delivery, energy storage and conversion, and separations. However, the preparation of this local functionalized nanocomposite is still a challenge for the conventional solution based method. In the previous research, we have demonstrated the preparation of hybrid materials from the organic polymer template by vapor phase infiltration of metal organic precursors. Moreover, different polymers showed different response toward vapor phase infiltration. By employing this selective reaction, we could enable the selective dispersed and reacted of metal oxide in the selective polymer segment. In this paper, a core sheath bi-component fiber was used for the demonstration, and the selective reaction between TMA and the fiber core is observed. This selective infiltration of metal oxide materials will enable many advanced application for the nanocomposite materials. New devices and applications would be enabled by this method.

13.1. Introduction

Nanocomposite materials composed of an organic host with inorganic flake or particle inclusions show unique prospects for use in drug delivery[1,2], chemical separation[3-5] and energy conversion and storage systems.[6-10] Polymer-based composites can retain the inherent mechanical properties and flexibility of the organic while also showing improved thermal, optical and electrical performance due to the added inorganic component.[11-15] Conventional solution based methods for nanocomposite materials synthesis typically require mechanical mixing of organic and inorganic precursors, and for the most part, result in inorganic clusters or particles uniformly distributed within the organic structure.[16-18] However, the ability to tune nanocomposite structure and component distribution will further extend the applications of the materials. As such, new means to prepare hybrid materials with desired local composition continue to attract research interest.[19,20]

Recent research shows that under some conditions, exposing polymers to vapor phase inorganic atomic layer deposition (ALD) reactions results in sub-surface metal oxide nucleation and particle growth. The particles are dispersed generally near the substrate surface, but the reaction depth depends strongly on the substrate and the specific reaction chemistry.[21-23] The different reactivity of metal organic precursors with different polymers can enable the selective reaction in multi-component polymers, which in turn could enable the preparation of the hybrid materials with desired local functionalities.[23,24]

In this paper, we demonstrate selective reaction between metal organic vapor and polymers in a multi-component polymer structure. Specifically, we used bi-component

fibers, approximately 12-15 μm in diameter. One fiber type was made up of a ~7-8 μm core of polylactic acid surrounded by a ~ 2-3 μm thick polypropylene sheath (referred to as PLA/PP fibers), and another fiber type had a polypropylene core surrounded by a polylactic acid sheath (i.e. PP/PLA fibers). We exposed the fibers to an aluminum oxide atomic layer deposition sequence using trimethylaluminum (TMA) and water. We found that the TMA could diffuse into the polymers to form well-defined inorganic inclusions within the polymer matrix. Furthermore we show that the location and structure (i.e. continuous film or isolated particles) of the inorganic component is controlled by the fiber structure and the detailed deposition and exposure conditions. In this manner, the vapor-phase ALD process enables very fine control of inorganic material integration with polymer matrices for advanced nanocomposite synthesis.

13.2. Experimental Section

Materials

Thin film polymers were formed on planar substrates for surface reaction characterization and analysis. To cast films, polylactic acid pellets (PLA, MW ~60,000) were purchased from Aldrich, and polypropylene was obtained in fiber form from the Nonwovens Cooperative Research Center at NC State University. To dissolve the polymers, decahydronaphthalene ($C_{10}H_{18}$, 99 % anhydrous) and chloroform ($CHCl_3$, 99 % anhydrous) solvents were obtained from Aldrich and used as received. For atomic layer deposition, trimethylaluminum (TMA, 98%) was purchased from Strem Chemicals, and ultra-high purity argon (Ar, 99.999 %, National Welders Supply Co.) was used as the purge and carrier gas. Polypropylene/polylactic acid (PP/PLA, 1:1) bi-component nonwoven core/sheath fiber mats

were also acquired from the Nonwovens Cooperative Research Center. Fibers with a PLA core and PP sheath were tested, as were similar fibers with PP core and PLA sheath.

Polymer Films Preparation

Thin films of polypropylene on silicon substrates were produced by drop casting polypropylene polymer solution (1% wt in decahydronaphthalene). The solution was prepared by dissolving polypropylene nonwoven fiber mat in decahydronaphthalene at 60 °C. The solution then transferred in a syringe. A syringe filter (polyvinylidene fluoride, 0.22 μm pore size, Fisher Scientific) was added to remove any particulates present in the polymer solution upon transfer to the substrate. Once several drops of the solution were placed on the Si wafer, spinning began at 6000 rpm for 60 seconds. The resulted PP film on Si is ~1.3 μm thick. The PLA polymer was dissolved in chloroform at room temperature, and the similar processing procedure is employed to make the PLA film.[23]

Atomic Layer Deposition

Atomic layer deposition of Al_2O_3 and TMA/water vapor phase infiltration were performed at constant temperature of 120 °C at an operating pressure of ~1 Torr in a homemade hot wall reactor described previously.[25] Ultra-high purity argon was further purified by an inert gas filter (Aeronex GateKeeper, Entegris) before entering the reactor. In a typical ALD cycle, TMA flowed into the reactor for 1 second followed by 60 seconds of argon gas purge. This was followed by a 1 second water dose and another 60 s Ar purge. This ALD sequence is one "short cycle". For some runs, we used a much longer precursor exposure sequence, which we refer to as a "long cycle" or more generally as "sequential vapor infiltration". For

one long cycle, we flow TMA for 5 seconds then isolate the chamber for an addition 60 s, resulting in an overall 65 s exposure. We then purge for 60 seconds, and repeat the 65 s flow/exposure step for water and the 60 s purge. Previous results show that the ALD precursors can diffuse deep into the surface of some polymers, and these long exposure times will promote more diffusion into the more porous or less reactive polymers.

For in-situ FTIR experiments, we mounted the planar films on the silicon wafers in another ALD reactor described previous in detail.[26,27] The reactor allowed the IR beam to pass through the polymer, and data was collected during the argon exposure step after TMA exposure, then again after the water exposure step. For these tests, the sample was exposed to TMA for 5 seconds, followed by chamber isolation for 60 s, and an argon purge for 280 s. The IR data was collected for ~150 s during the 280 s Ar purge step. This sub-cycle was then repeated for the water exposure step, and the overall cycle was repeated a few times for each polymer. The substrate temperature was held at 80 °C for all the IR experiments. Using the previously collected spectrum as the background, changes in IR modes provide information on the specific reaction mechanisms as well as the extent of precursor reactivity.[27]

Materials Characterization

The morphology of TMA/water treated core/sheath fiber mat samples were determined by scanning electron microscopy (SEM) and transmission electron microscopy (TEM). An FEI Phenom bench-top scanning electron microscope was used to collect relatively low magnification SEM images. A Hitachi HF 2000 transmittance electron microscope operated

at 200 kV was used for TEM imaging. The cross-section TEM of the bi-component core/sheath fiber was collected from microtomed samples. The fibers were first embedded in Spurr low-viscosity epoxy resin (Ladd Research Industries). After cured overnight at room temperature, the resins were then cut into thin layer of ~ 70 nm using a Lecia Ultracut diamond knife microtome. The thin layers were then transferred on Cu mesh grids for TEM imaging.

For higher magnification SEM imaging, a Hitachi S3200 SEM was also used to image the cross section of the bi-component fiber, which is prepared at the same time from the microtome samples. An Oxford Isis Energy-dispersive X-ray spectroscopy (EDS) system is also attached to the instrument which allows for elemental analysis. Before imaging, samples were loaded into a bench top sputter coater, and a 5nm layer of gold/platinum was coated on to the sample. Each EDS scan line consisted of 200 points with 10s collecting time for each point.

X-ray photoelectron spectroscopy (XPS) was performed in with a Kratos AXIS Ultra spectrometer equipped with an aluminum source and spherical mirror analyzer. Thin films of PP and PLA on silicon, approximately 1 cm × 1 cm were used for XPS experiments. Survey spectra were obtained from 1200 eV to 0 eV with 1 eV steps and a dwell time of 0.2 seconds. Atomic percentages were calculated using the survey scans and the CasaXPS software package. Detail scan for C 1s also performed on the same samples.

13.3. Experimental Results and Discussion:

We exposed both PLA/PP and PP/PLA core/sheath fibers to 100 "short" cycles of TMA and water ALD at 120 °C then imaged the samples under SEM. The results are shown in Figure 13.1. After ALD, the PLA/PP fiber retains its original morphology, with no significant visible change. However, the result is very different for the PP/PLA fiber. For these fibers, the PLA sheath appears to have reacted heavily during the TMA/water process, but the PP core remains intact. This is consistent with a much higher extent of reaction for TMA with PLA compared to TMA with PP.[27]

To characterize the precursor reaction with the different polymers, we performed in-situ FTIR analysis of TMA and water reaction with planar polymer films. Results in Figure 13.2 (a) show IR data collected during TMA/water exposure to PLA. The bottom spectrum is collected from the PLA polymer film, and it shows characteristic peaks for the ester groups (C=O stretching at 1751cm^{-1} and C-O stretching at 1188 cm^{-1}). The figure also shows differential spectra after the first TMA, first water, second TMA and second water exposure steps. After the first TMA exposure, we note an increase of the asymmetric and symmetric C-H stretches $\nu_a(CH_3)$ and $\nu_s(CH_3)$ at 2939 and 2898 cm^{-1} respectively, which is ascribed to reaction of TMA with the polymer substrates. Another increase of absorbance was (O-C-O stretching) detected at ~1600 cm^{-1},[28,29] which is corresponding to the formation of aluminum carbonate. We found that almost all the absorbance from ester groups was removed after TMA exposure. We believe the strong interaction between TMA and the ester groups on PLA polymer chain will enable the formation of aluminum carbonate. Similarly, another differential spectrum was collected after water pulse, and the differential spectrum were

presented. After water pulse, we found the aluminum carbonate absorbance (O-C-O stretching at ~1600^{-1}) reacted with water. This is like related to the hydroxylation of aluminum carbonate.

The in-situ FTIR analysis of TMA/water exposure on a PP film is shown in Figure 13.2 (b). The bottom-most spectrum shows the PP absorbance features, and the other spectra reflect the absorbance change upon exposure to TMA or water. After expose to TMA, no detectable IR signal is observed. Likewise, no observable change is present after the water exposure, consistent with the inert structure of the polypropylene.[23]

To further examine the reaction of PLA with TMA/water, we examined the PLA film and TMA/water treated PLA film using XPS. The XPS sample was prepared using the long precursor exposure sequence at 120 °C. Figure 13.3 shows survey and C 1s scans of PLA polymer film before and after infiltration. The survey scans clearly show an increase in aluminum and oxygen after TMA/water infiltration. For the C1s features, the peak near 289 eV present in the PLA is significantly reduced after TMA/water exposure, consistent with TMA reacting with C=O groups. XPS survey spectra collected on PP films after TMA/water exposure (not shown) indicated no detectable aluminum.

To physically investigate the TMA/water vapor diffusion into the PLA/PP bi-component fiber, we used cross sectional TEM. Figure 13.4 shows TEM image collected from the untreated and ALD treated PLA/PP fibers. The image in panel (b) was after 500 "short" ALD cycles, and panel (c) shows the structure after 100 "long" ALD cycles at 120 All images clearly show the core/sheath structure. The dark dots in the untreated PP sheath in

panel (a) are air bubbles formed during the fiber fabrication. After 500 short ALD cycles, image (b) shows a dark conformal aluminum oxide coating on outside PP layer, consistent with previous results of ALD on PP at low temperature. [22,23,30] A closer look at the TEM image shows formation of some aluminum oxide particles in the PP near the interface, consistent with some diffusion of TMA into the PP layer. [22,23] The cross sectional structure after 100 long ALD cycles is clearly different. Only a very thin, if any, conforomal coating is present. Rather, a graded contrast in the PP shell shows a darker region near the outer edge, consistent with particles in the near surface region.[22,23] The PLA core now shows a striking two-layer structure, consistent with a diffusion limited reaction into the PLA.

To confirm that TMA can diffuse through the PP sheath and react with the PLA core, we performed an EDS line scan experiment on three similarly prepared samples to detect the aluminum distribution in the cross sections. The results are presented in Figure 13.5. As expected, the untreated PP/PLA core/sheath fiber shows no detectable aluminum. After 500 short cycles at 120 °C, Al is limited to a thin outer coating. However, after 100 long ALD cycles, the Al is much more distributed through the PP and PLA. It is interesting to note that the a build-up of Al is present at the outer edge of both the PP and PLA, suggesting that as the TMA diffuses through the PP, it tends to react and "stick" in the PLA core. Figure 13.6 shows a schematic diagram of the selective reaction between TMA and PLA core, during TMA/water infiltration on PLA/PP core/sheath bi-component fiber. When the PLA/PP core/sheath fiber was exposed to "short" TMA/water exposures, precursor vapors were not given long enough time to diffuse into the PP layer. Minimal subsurface diffusion and reaction occurred, and thin Al_2O_3 ALD layer was deposited on PP surface. However, when

we use the “long” precursor exposures, TMA and water vapors could diffuse deep into the Once the TMA diffuse though the PP layer, it will react with PLA core. Because PP is inert to TMA/water reaction, excess TMA/water in the PP layer would be removed in the following Ar purges. By fine tune the precursor exposure time and purge time, we could enable selective functionalization of target polymer segment by ALD.

13.4. Conclusion

Al_2O_3 ALD on core/sheath bi-component fibers demonstrates the selective reactivity of TMA with PP and PLA; the PP acts as an inert polymer with little reaction with TMA/water, but TEM images confirm that a conformal film coating is attained using relatively short exposure times. In contrast, PLA shows high reactivity towards TMA vapor, with substantially more sub-surface reaction during long exposures. This difference in reactivity towards metal organic vapors enabled selective incorporation of aluminum oxide films and particles within different regions of bi-component PP/PLA and PLA/PP core/sheath fibers. For long exposures, TMA will diffuse through the inert PP layer and react with PLA. The ALD on bi-component polymers enables a new approach to selectively modify portions of multicomponent polymers to create unique organic/inorganic composite structures.

Acknowledgments

This work was supported by the National Science Foundation project number CBET-1034374.

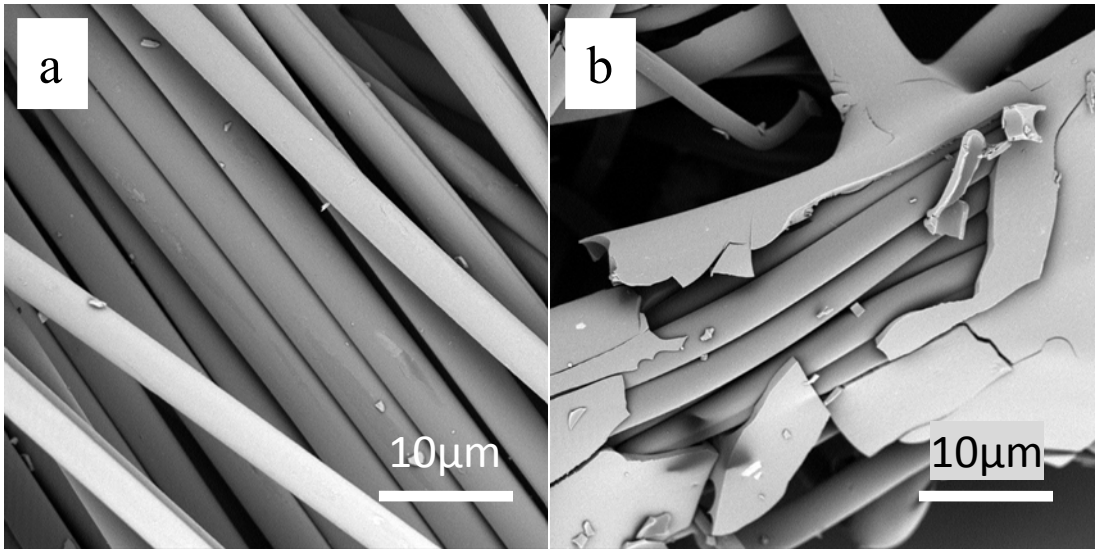


Figure 13.1. Scanning electron microscope images collected from core/sheath bi-component fibers with 100 "short" TMA/water ALD cycles. Image (a) is collected from coated PLA/PP core/sheath fibers. The coated fibers showed almost identical morphology to the untreated fibers (not shown). Image (b) is collected from coated PP/PLA core/sheath fibers. PLA sheath melted together with adjacent fibers resulting in a cracked and nonuniform coating, whereas the smaller the PP core fibers remained intact and are readily visible in the image.

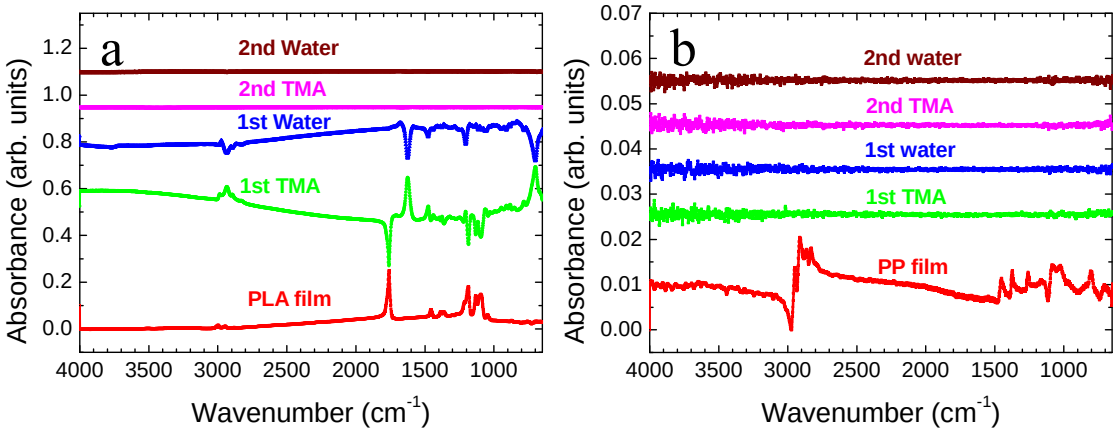


Figure 13.2. In-situ FTIR spectra collected during the first two "long" TMA/water ALD cycles on PLA and PP films. Panel (a) showed the IR spectra collected from the PLA. The spectrum at the very bottom is from the untreated PLA film on Si wafer. Differential spectra collected after each pulse of reagents were listed from bottom to the top. Significant reaction between TMA and carbonyls in PLA was measured. Panel (b) displayed the IR spectra collected from the PP. Similarly, the bottom spectrum is collected from the untreated PP film on Si wafer, and the differential spectra collected after each pulse of reagents were listed from bottom to the top. The minimal reaction between TMA and PP is not detectable.

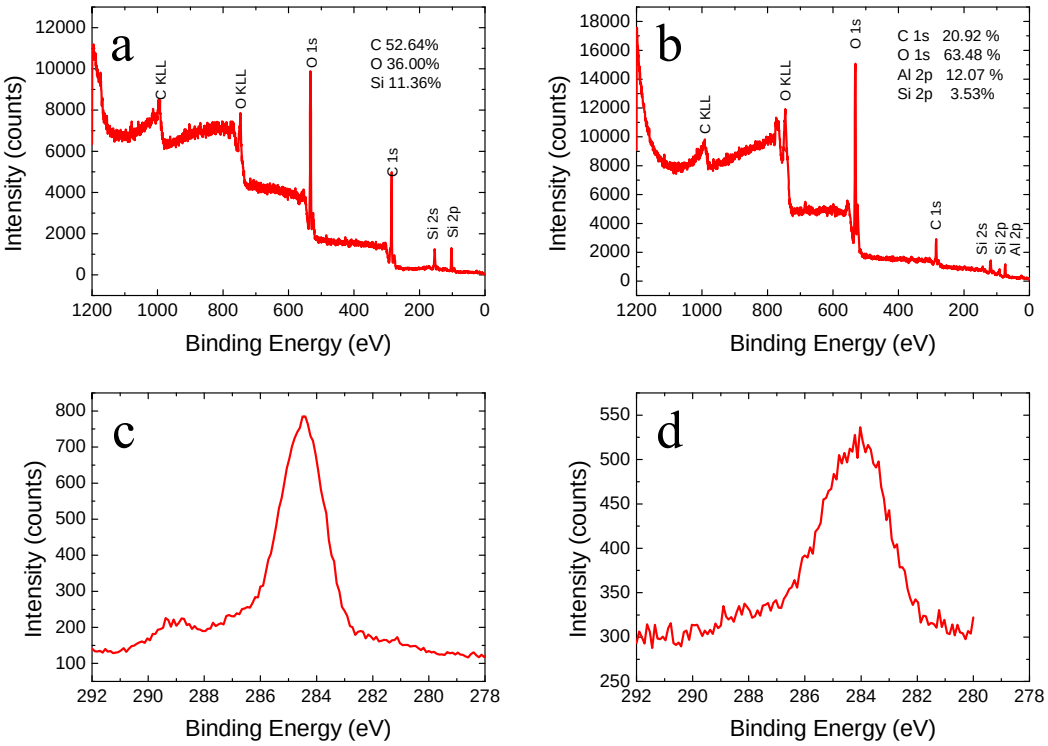


Figure 13.3. XPS spectra collected from the PLA film on Si wafer. The survey scans of (a) untreated and (b) treated PLA film were displayed on the top. After one "long" TMA/water ALD cycle, significant increase of Al atom percentage (12%) was measured. The detailed C 1s scan of untreated and treated PLA film were shown in figure (c) and (d). The spectrum of PLA film showed peaks at 284.5 eV (C-C) and 289 eV (C=O). After one "long" TMA/water exposure, the peak at 289 eV is removed, corresponding to the reaction between the TMA with C=O bond in the PLA.

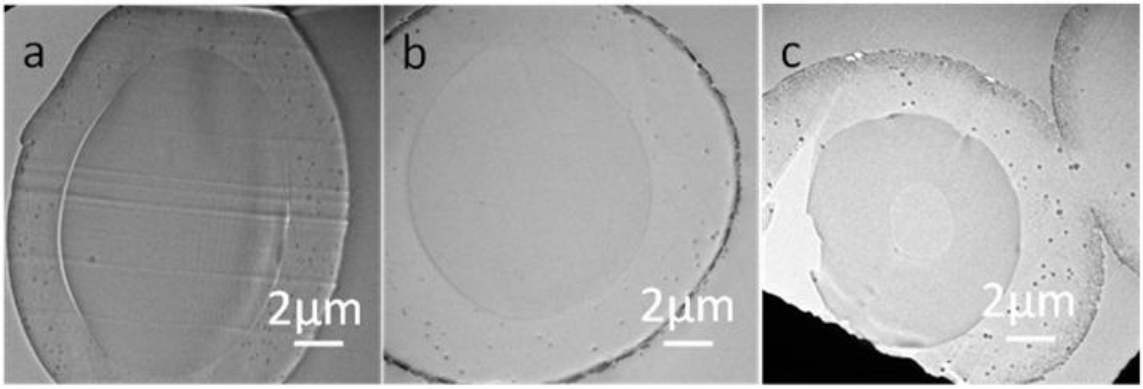


Figure 13.4. The cross-section TEM image collected from (a) untreated PLA/PP core/sheath fiber, (b) PLA/PP core/sheath fiber with 500 “short” TMA/water ALD cycles and (c) PLA/PP core/sheath fiber with 100 “long” TMA/water cycles. After 500 “short” ALD cycles, thin Al2O3 film was deposited on PP surface. However, for 100 “long” ALD cycles coated sample, different contrast in PLA core was observed.

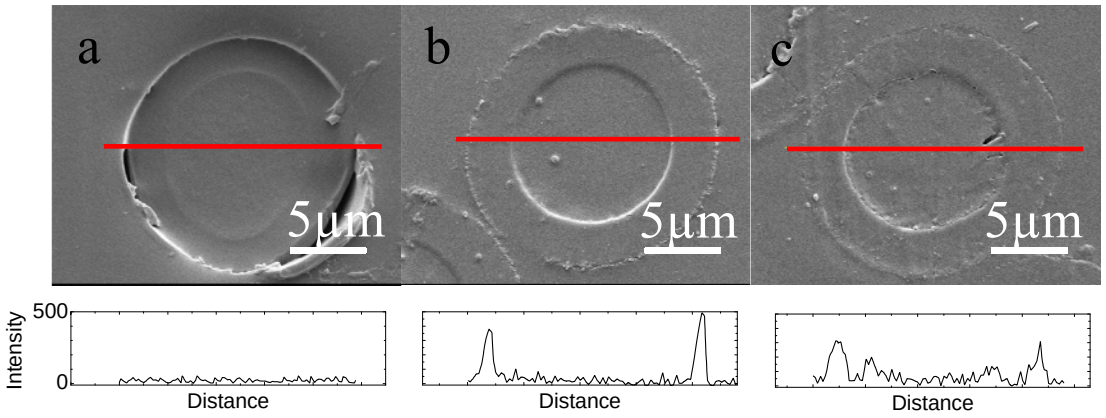


Figure 13.5. The SEM images and EDS line scans collected from the cross-section of PLA/PP core/sheath fibers. Figure (a) showed the cross-section of an untreated PLA/PP fiber. The EDS line scan along the diameter of the fiber showed no detectable aluminum. The SEM image in figure (b) was collected from the cross-section PLA/PP core/sheath fiber with 500 "short" TMA/water ALD cycles. The EDS line scan showed two distinctive aluminum peaks located on PP surface. This is consistent with conformal Al2O3 coating on PP. Figure (c) displayed the SEM image collected from the cross-section of 100 cycles of "long" TMA/water coated PLA/PP core/sheath fiber. In addition to the two aluminum peaks located on PP surface, the EDS line scan along the diameter showed aluminum peaks in PLA core. These additional aluminum peaks consistent with TMA diffuse through PP and react with PLA core.

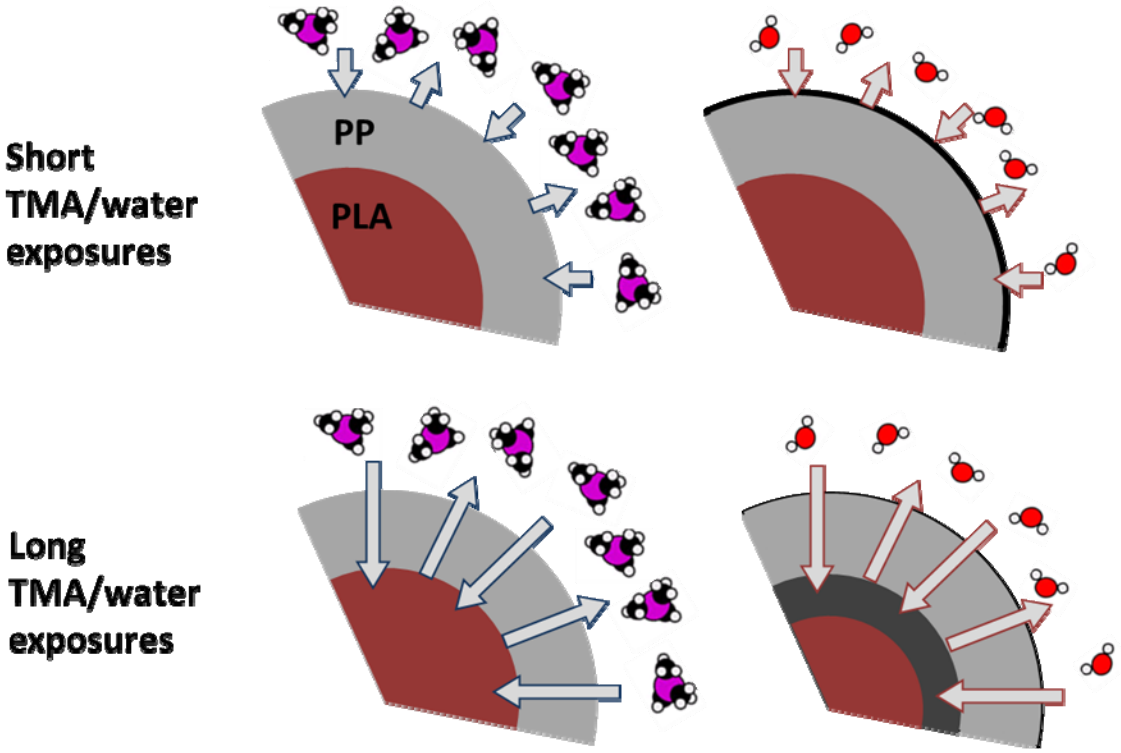


Figure 13.6. Schematic diagram of the "short" and "long" TMA/water ALD cycles on PLA/PP core/sheath bi-component fibers. When the core/sheath fiber was exposed to "short" TMA/water exposures, precursor vapors were not given enough time to diffuse into the PP layer. Minimal subsurface diffusion and reaction occurred, and thin Al2O3 ALD layer was deposited on PP surface. However, when the "long" precursor exposures were used, TMA and water vapors could diffuse through the PP, and react with PLA core.

References

1 S. R. Sershen; S. L. Westcott; N. J. Halas; J. L. West; Temperature-sensitive polymer-nanoshell composites for photothermally modulated drug delivery, *Journal of Biomedical Materials Research,* **2000**. *51*, 293.

2 N. K. Mal; M. Fujiwara; Y. Tanaka; Photocontrolled reversible release of guest molecules from coumarin-modified mesoporous silica, *Nature,* **2003**. *421*, 350.

3 X. S. Feng; R. Y. M. Huang; Liquid separation by membrane pervaporation: A review, *Industrial & Engineering Chemistry Research,* **1997**. *36*, 1048.

4 T. T. Moore; W. J. Koros; Non-ideal effects in organic-inorganic materials for gas separation membranes, *Journal of Molecular Structure,* **2005**. *739*, 87.

5 T. T. Moore; R. Mahajan; D. Q. Vu; W. J. Koros; Hybrid membrane materials comprising organic polymers with rigid dispersed phases, *Aiche Journal,* **2004**. *50*, 311.

6 P. Gomez-Romero; Hybrid organic-inorganic materials - In search of synergic activity, *Advanced Materials,* **2001**. *13*, 163.

7 P. V. Kamat; Meeting the clean energy demand: Nanostructure architectures for solar energy conversion, *Journal of Physical Chemistry C,* **2007**. *111*, 2834.

8 M. Law; L. E. Greene; J. C. Johnson; R. Saykally; P. D. Yang; Nanowire dye-sensitized solar cells, *Nature Materials,* **2005**. *4*, 455.

9 N. L. Rosi; J. Eckert; M. Eddaoudi; D. T. Vodak; J. Kim; M. O'Keeffe; O. M. Yaghi; Hydrogen storage in microporous metal-organic frameworks, *Science,* **2003**. *300*, 1127.

10 D. F. Sun; S. Q. Ma; Y. X. Ke; D. J. Collins; H. C. Zhou; An interweaving MOF with high hydrogen uptake, *Journal of the American Chemical Society,* **2006**. *128*, 3896.

11 C. Sanchez; F. Ribot; Design of hybrid organic-inorganic materials synthesized via sol-gel chemistry, *New Journal of Chemistry,* **1994**. *18*, 1007.

12 R. Gangopadhyay; A. De; Conducting polymer nanocomposites: A brief overview, *Chemistry of Materials,* **2000**. *12*, 608.

13 T. Kashiwagi; E. Grulke; J. Hilding; K. Groth; R. Harris; K. Butler; J. Shields; S. Kharchenko; J. Douglas; Thermal and flammability properties of polypropylene/carbon nanotube nanocomposites, *Polymer,* **2004**. *45*, 4227.

14 Y. X. Pan; Z. Z. Yu; Y. C. Ou; G. H. Hu; A new process of fabricating electrically conducting nylon 6/graphite nanocomposites via intercalation polymerization, *Journal of Polymer Science Part B-Polymer Physics,* **2000**. *38*, 1626.

15 D. R. Paul; L. M. Robeson; Polymer nanotechnology: Nanocomposites, *Polymer,* **2008**. *49*, 3187.

16 Y. Kojima; A. Usuki; M. Kawasumi; A. Okada; Y. Fukushima; T. Kurauchi; O. Kamigaito; Mechanical-properties of nylon 6-clay hybrid, *Journal of Materials Research,* **1993**. *8*, 1185.

17 P. C. LeBaron; Z. Wang; T. J. Pinnavaia; Polymer-layered silicate nanocomposites: an overview, *Applied Clay Science,* **1999**. *15*, 11.

18 B. M. Novak; Hybrid nanocomposite materials - between inorganic glasses and organic polymers, *Advanced Materials,* **1993**. *5*, 422.

19 R. A. Caruso; A. Susha; F. Caruso; Multilayered titania, silica, and Laponite nanoparticle coatings on polystyrene colloidal templates and resulting inorganic hollow spheres, *Chemistry of Materials,* **2001**. *13*, 400.

20 S. Srivastava; N. A. Kotov; Composite Layer-by-Layer (LBL) Assembly with Inorganic Nanoparticles and Nanowires, *Accounts of Chemical Research,* **2008**. *41*, 1831.

21 B. Gong; Q. Peng; J. S. Jur; C. K. Devine; K. Lee; G. N. Parsons; Sequential Vapor Infiltration of Metal Oxides into Sacrificial Polyester Fibers: Shape Replication and Controlled Porosity of Microporous/Mesoporous Oxide Monoliths, *Chemistry of Materials,* **2011**. *23*, 3476.

22 J. S. Jur; J. C. Spagnola; K. Lee; B. Gong; Q. Peng; G. N. Parsons; Temperature-Dependent Subsurface Growth during Atomic Layer Deposition on Polypropylene and Cellulose Fibers, *Langmuir,* **2010**. *26*, 8239.

23 J. C. Spagnola; B. Gong; S. A. Arvidson; J. S. Jur; S. A. Khan; G. N. Parsons; Surface and sub-surface reactions during low temperature aluminium oxide atomic layer deposition on fiber-forming polymers, *Journal of Materials Chemistry,* **2010**. *20*, 4213.

24 Q. Peng; Y.-C. Tseng; S. B. Darling; J. W. Elam; Nanoscopic Patterned Materials with Tunable Dimensions via Atomic Layer Deposition on Block Copolymers, *Advanced Materials,* **2010**. *22*, 5129.

25 Q. Peng; B. Gong; R. M. VanGundy; G. N. Parsons; "Zincone" Zinc Oxide-Organic Hybrid Polymer Thin Films Formed by Molecular Layer Deposition, *Chemistry of Materials,* **2009**. *21*, 820.

26 B. Gong; Q. Peng; G. N. Parsons; Conformal Organic - Inorganic Hybrid Network Polymer Thin Films by Molecular Layer Deposition using Trimethylaluminum and Glycidol, *Journal of Physical Chemistry B,* **2011**. *115*, 5930.

27 B. Gong; G. N. Parsons; Quantitative In-Situ Infrared Analysis of Reactions between Trimethylaluminum and Polymers during Al2O3 Atomic Layer Deposition *Journal of Materials Chemistry,* **2012**. *Submitted*,

28 D. N. Goldstein; J. A. McCormick; S. M. George; Al(2)O(3) Atomic Layer Deposition with Trimethylaluminum and Ozone Studied by in Situ Transmission FTIR Spectroscopy and Quadrupole Mass Spectrometry, *Journal of Physical Chemistry C,* **2008**. *112*, 19530.

29 M. Li; M. Dai; Y. J. Chabal; Atomic Layer Deposition of Aluminum Oxide on Carboxylic Acid-Terminated Self-Assembled Monolayers, *Langmuir,* **2009**. *25*, 1911.

30 G. K. Hyde; G. Scarel; J. C. Spagnola; Q. Peng; K. Lee; B. Gong; K. G. Roberts; K. M. Roth; C. A. Hanson; C. K. Devine; S. M. Stewart; D. Hojo; J.-S. Na; J. S. Jur; G. N.

Parsons; Atomic Layer Deposition and Abrupt Wetting Transitions on Nonwoven Polypropylene and Woven Cotton Fabrics, *Langmuir,* **2009**. *26*, 2550.